Orthogonal Self-Assembly of Bioactive Hydrogels

Vânia Margarida Pinto Vieira

PhD

University of York
Chemistry
September 2017

Abstract

Hydrogels are of great interest due to their ability to encapsulate and deliver bioactive molecules, mimic the extracellular matrix (ECM) and act as an artificial 3D scaffold. Here we report multi-component hydrogels based on low-molecular-weight gelators (LMWGs) and polymer gelators (PGs) incorporating heparin that can bind to self-assembled molecules, and their potential for controlled release and to mimic the ECM. These multi-component systems were characterised and the orthogonality of each individual component investigated.

Firstly, three cationic surfactants were synthesised and their ability to self-assemble and bind to polyanionic heparin was investigated. The systems consisted of an amine-based head group connected *via* an amide linkage to different saturated fatty acids. Self-assembled C14-DAPMA and C16-DAPMA formed highly organised polycrystalline assemblies with heparin, proving that the micelles remain intact during the hierarchical assembly process. C16-DAPMA proved to be the most charge-efficient heparin binder, also with the lowest critical aggregation concentration, with high stability when free and solution and when electrostatically interacting with heparin.

Two dibenzylidene-D-sorbitol (DBS) derivatives capable of forming hydrogels are then introduced: a pH-activated LMWG (DBS-COOH) and a thermally-activated LWMG (DBS-$CONHNH_2$). The incorporation and release of heparin from the LMWGs hydrogels in the presence and absence of C16-DAPMA, and from hybrid hydrogels consisting of one of the LMWGs and a PG - agarose is reported. The rate of heparin release can be controlled through network density and composition, and control of the release surface area to volume ratio, while the presence of C16-DAPMA inhibits heparin release. Characterisation of this multi-component complexes (LMWG + Heparin + C16-DAPMA) showed the orthogonal self-assembly of each individual component within one single system. Cytocompatilibity of the multi-component hydrogels is reported. Heparin was then incorporated and released from three different hydrogels based on triamide cyclohexane derivatives. From these, a positively charged LMWG able to directly interact with heparin, resulted in the triggered release of heparin by hydrogel disruption through enzymatic cleavage.

Table of Contents

List of Figures

List of Tables

List of Schemes

List of Equations

Dedication

To my father

Acknowledgements

I would like to thank my supervisor Professor David Smith for all the guidance and advice, for helping me building up my confidence and for the great scientific enthusiasm and ideas. I would also like to acknowledge Professor Jan van Esch and Dr Menno de Jong for welcoming me in Delft and Groningen for my placements, allowing me to improve my scientific experience and adaptability.

I am very grateful to all the members of Smith's group for the great work environment, making my adaptation to a new country so much easier. I would like to thank Stephen and Tunde for all the help and support when I started. Rex for the NMR advices and computer tips. I would also like to thank my brilliant MChem student Laura, for contributing to this thesis. Jorge for being a good neighbour, in country, fume hood and desk (por favor), and for together with Phill having the craziest conversations. To Lizzie for all the English lessons and allowing me to have some dog therapy moments. Nicole, my favourite Scottish person, for her great work and for bringing an industrial point of view to the group. Buthaina, the kindest person I ever met, for being a truly friend and for the nicest and funniest conversations. Ana for being more than a postdoc, a really good friend and for cheering me up when I feel like a 'pasa'. I would also like to thank all the SmartNet members for the amazing and unforgettable meetings around Europe. In addition, I would like to thank Vicent le Sage and Ana Catarina Lima for all the help and availability during my placements in Netherlands.

I must also acknowledge the collaborators who have contributed to this project; Professor Sabrina Pricl (Italy) and Professor Mauri Kostiainen (Finland). Additionally, I would like to thank all the technical support received from Karl Heaton (MS), Heather Fish (NMR), Andrew Leech (CD) and Meg Stark (TEM and SEM).

Finally, a special thanks to my family. To my mother for always supporting me in new adventures and encouraging me to explore the world. To my sister and Alexandre for giving me the best gift I could ever ask during my PhD, my little nephew Pedro. To Bruno, for being the most supportive boyfriend and for always being by my side. And lastly to my father, I am sure he would be proud of my achievements.

Declaration

I declare that the work presented within this thesis is entirely my own, except where otherwise acknowledged. This work has not been submitted in part or fully for examination towards any other degrees or qualifications.

Vânia Margarida Pinto Vieira

1. Introduction

1.1. Introduction to Gels

1.1.1. Supramolecular Chemistry

Supramolecular chemistry studies the noncovalent interactions between molecular building blocks which generate different self-assembled materials in different dimensions.[1,2] Back in the 1990s, Lehn as described it as 'the designed chemistry of the intermolecular bond'.[3] These intermolecular bonds include solvophobic effects, electrostatic interactions, hydrogen bonding, π-π interactions and van der Waals interactions. Despite non-covalent interactions being weaker than covalent interactions, they give supramolecular materials unique properties, such as mechanical tunability, responsiveness and directionality, allowing control over composition and functionality.[4] Additionally, supramolecular materials can play an important role in mimicking biological systems, as supramolecular assemblies are naturally present in biological systems from bilayer membranes to ribosomes and self-assembly of lipids in the formation of the cell membrane. The replacement of natural materials with biocompatible supramolecular scaffolds can be particularly useful for tissue engineering and in fact supramolecular materials can be used, for example, in the replication of the structure of collagen (the main component of the extracellular matrix (ECM)), or as muscle-like supramolecular polymers.[5–7] Hence, it is immediately noteworthy that this field requires a multidisciplinary knowledge across chemistry, physics and biology.

Supramolecular chemistry can be divided into two main categories: host-guest interactions and self-assembly (Figure 1.1). Host-guest complexes, as the name suggests, consist of a larger molecule (a host) that can surround a smaller molecule (a guest) via non-covalent interactions, forming a stable host-guest complex based on the interactions between them.[8,9] Self-assembly processes are based on non-covalent interactions between molecules, often with similar size and shape. In the present work, we will be focused on self-assembly processes, which will be explained in more detail in the next section and in section 1.6.

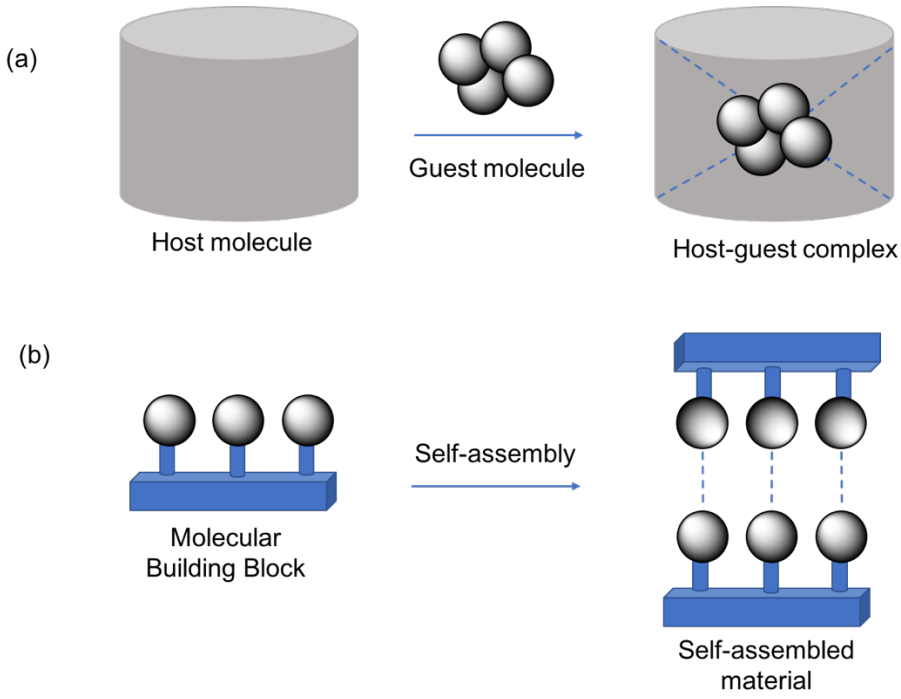

Figure 1.1 Supramolecular structures based on (a) host-guest complexes and (b) self-assembled materials. [Adapted from reference [10]]

1.1.2. Self-Assembly

Self-assembly refers to the spontaneous association of molecules under equilibrium conditions into stable, structurally well-defined, aggregates held together by non-covalent bonds.[11] Self-assembly processes are vital in nature and the use of weak non-covalent interactions, means that it is a reversible process with a thermodynamically stable final product. This allows natural systems to correct any errors that may arise from the multiple intermolecular interactions present in such complex structures.[10,12] A well-known example of a molecule spontaneously held together by non-covalent interactions is the DNA double-helix.[13,14] The two single strands come together by hydrogen bonding and π-π stacking interactions between complementary nucleobases of each strand. Assembly and disassembly allows the structure to correct any matching errors and to form the most thermodynamically stable structure.

The most common molecular structure used in self-assembled systems corresponds to amphiphilic molecules, which aggregate in aqueous solution in processes driven by the hydrophobic effect. As the non-polar regions of the molecule aggregate, their associated

surface water molecules become free in solution, resulting in an increase of entropy, which more than compensates the entropic cost associated with the aggregation of the hydrophobic components.[15] The type of aggregates formed from the assembly of the individual monomers depends on different factors, such as monomer concentration and morphology.[16] Israelachvili et al.[17] reported the effect of the degree of hydrophobicity of an amphiphile on the self-assembly process. The morphology of the aggregates changes with the relative sizes of the hydrophobic and hydrophilic components, in order to geometrically maximise packing and minimise unfavourable solvent interactions, resulting in different geometries (Figure 1.2). When hydrophilic heads are larger than the hydrophobic tails, this favours the formation of spherical micelles. As the hydrophilic heads become smaller in comparison to the hydrophobic tails, self-assembly into cylindrical shapes is favoured. With a further increase in hydrophobicity, usually by the addition of a second aliphatic tail, vesicles or liposomes become preferred. If the hydrophobic and hydrophilic domain are comparable in size it tends to form a planar bilayer structure. When the hydrophobic tails are larger than the hydrophilic heads, inverted micelles are formed.

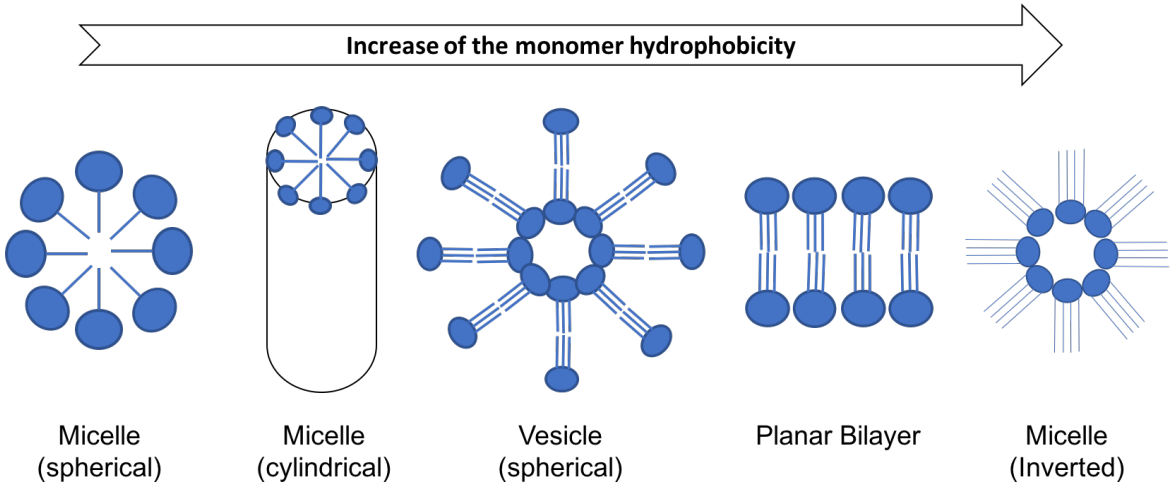

Figure 1.2. Morphology of amphiphilic aggregates in aqueous solution depending on the hydrophobic-hydrophilic balance of the monomers, by Isreaelachvili.

It is common for a self-assembled system to form after successive self-assembly processes where one stage of complexity cannot be achieved without the previous one. This process is called hierarchical self-assembly and can give rise to the design of multifunctional

structures. As an example, the hierarchical self-assembly of functionalised gold nanoparticles (AuNPs) with promising applications in theranostic tools has been reported. Firstly, the AuNPs functionalised with amphiphilic copolymers self-assembled into vesicles. With the slow addition of water into the system it was verified that the grafting density of the copolymers affected the hierarchical self-assembly. While high copolymer density resulted in the self-assembly of the hollow vesicles with membranes composed of two-dimensional (2D) AuNP arrays, when the grafting density was reduced the vesicles were composed of one-dimensional (1D) linear AuNP strings (Figure 1.3). This was found to be a result of the fact that the AuNPs with high grafting density of copolymer were interacting through solvophobic interactions that favoured the formation of 2D assemblies. On the other hand, AuNPs with low grafting density were primarily interacting through van der Waals interactions which favoured the formation of 1D strings. The different forms of assembly resulted in an important shift in the absorbance of the AuNPs from visible (AuNPs with high grafting density of polymer) to near-infrared (NIR) (AuNPs with low grafting density of polymer) - efficient probes for bioimaging are required to absorb at NIR.[18]

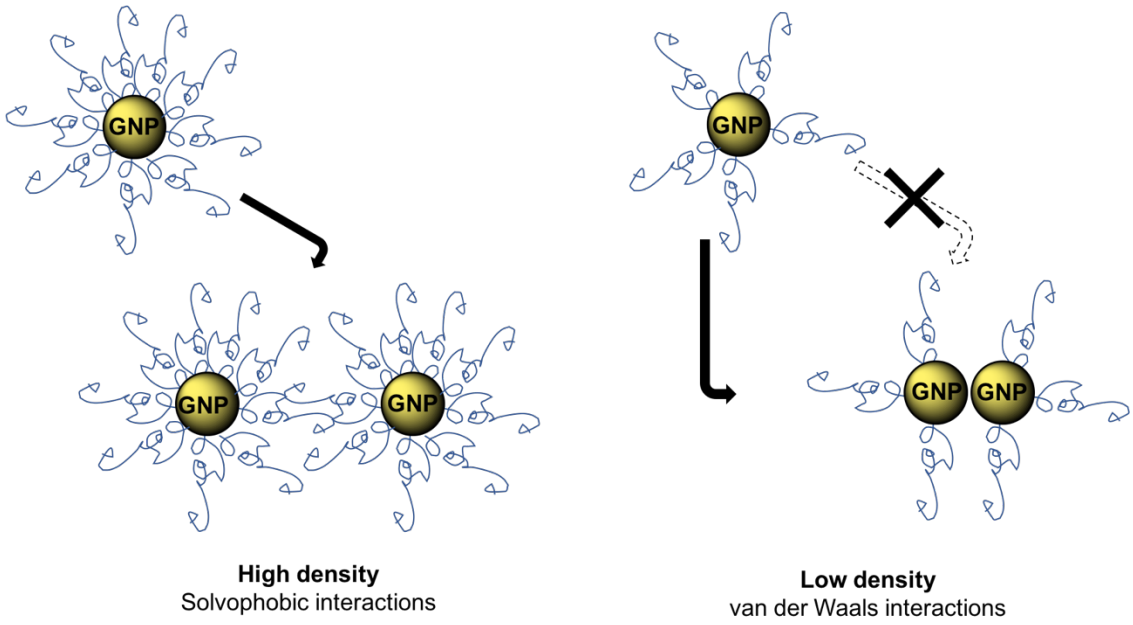

Figure 1.3. AuNPs with high grafting density interact primarily through solvophobic interactions between polymer coatings, favouring the formation of planar assemblies (2D arrays). AuNPs with low grafting interact primarily through van der Waals interactions between particle cores, favouring the formation of particle chains (1D strings). [Adapted from reference [18]].

Self-assembly can therefore be applied to the construction of nanosized materials by the spontaneous assembly of small molecular building blocks that can ultimately result in 3D macroscopic products with a vast range of applications.[19–24]

1.1.3. Supramolecular Gels

Back in 1926, Dorothy Jordon Lloyd stated that 'the colloidal condition, the gel, is easier to recognise than to define' and that it should be 'built up from two components, one which is a liquid (…) and the other (…) often spoken as the gelator, is a solid'.[25] Indeed, gels are well known three-dimensional (3D) soft materials with solid-like rheology, mainly constituted by a liquid phase (usually, 99%) against a very small amount of gelator (usually, 1%).[26] Gels can be categorised into chemical and physical gels (Figure 1.4). In chemical gels, the 3D network is formed through permanent and non-reversible covalent crosslinking of the components. Physical gels are based on reversible non-covalent interactions between the network components, that can consist for instance of polymers, proteins or small organic molecules as gelators, in a liquid phase.[27]

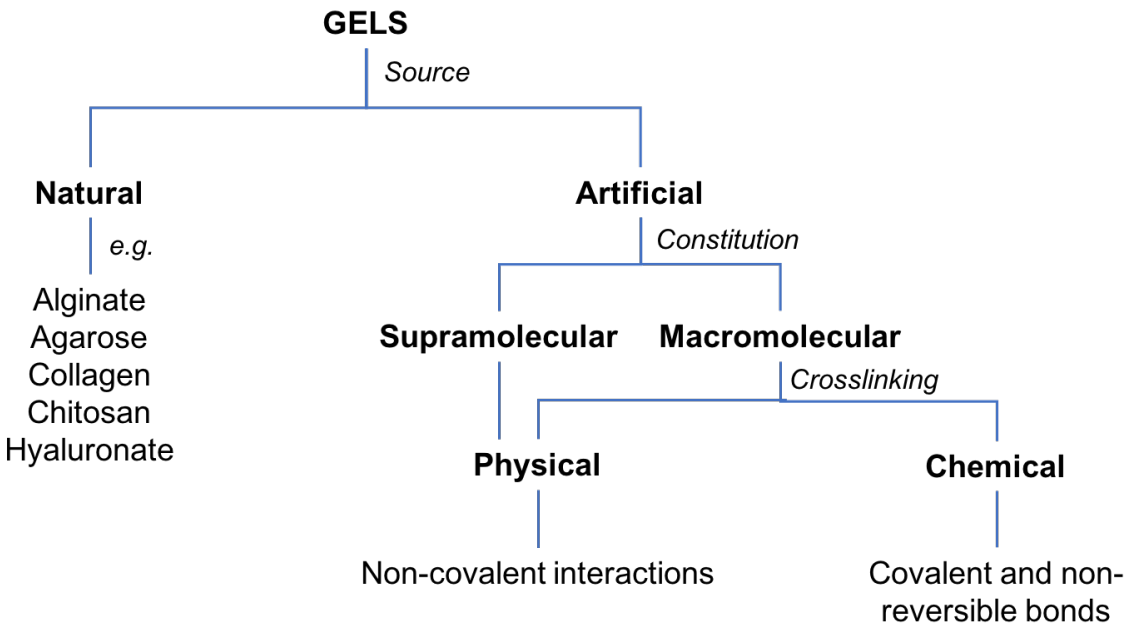

Figure 1.4. Gel classification. [Adapted from reference [28]]

Supramolecular gels are a type of physical gel consisting of small organic molecules able to self-assemble, that combined with the existence of directionality in the interactions, can give rise to nanomaterials capable of immobilizing an impressive amount of solvent. These small molecules are usually called low-molecular-weight gelators (LMWGs), which self-assemble into 1D fibers by noncovalent interactions, such as hydrogen bonds, van der Waals forces, π-π stacking interactions and solvophobic interactions, into a 3D entangled network, preventing the flow of bulk solvent (Figure 1.5).[20,29–32] According to the composition of the liquid phase, supramolecular gels are organogels (if the gelator self-assembles in an organic solvent) or hydrogels (if the gelator self-assembles in water). In the present work hydrogels are of great interest as they are usually biocompatible, non-cytotoxic and biodegradable. These characteristics make hydrogels suitable for diverse biomedical applications, such as drug delivery and tissue engineering.[33–36]

Differently from the covalent crosslinked polymer gels which present 1D structures as the most basic elements, supramolecular gels are composed by 'zero-dimensional' (0D) building blocks which undergo nucleation to form a stable nucleus, prior to self-assembly to form 1D nanofibers and subsequent noncovalent cross-linking to form the 3D network.[37,38] Supramolecular gels are characterised by unique properties such as critical gelation temperatures (T_{gel}), referring to the temperature at which gel-sol transition occurs, and the critical gelation concentration (CGC) which refers to the minimum amount of gelator required to form a gel in a certain solvent. Almost all supramolecular gels present sol-to-gel thermal reversibility, with good solubility when heated and with gelation occurring at low concentrations of gelator (typically < 50 $g.l^{-1}$).[27,38,39]

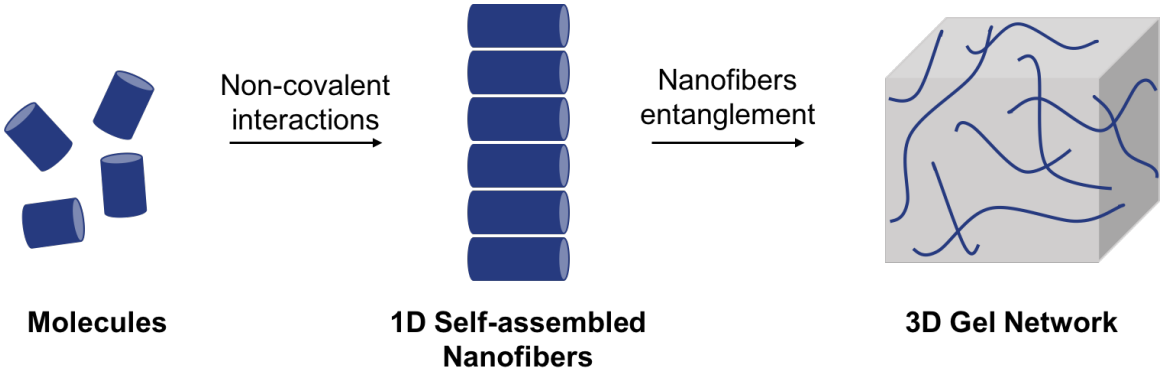

Figure 1.5. Representation of the hierarchical self-assembly of a supramolecular gel. [Adapted from reference [29]]

Apart from thermal responsiveness, supramolecular gels can respond to other external stimuli such as mechanical stress, light irradiation and pH, giving rise to smart soft materials that can be used for a diversity of applications.

As an example, Kiyonaka et al.[40] introduced a hydrogelator based on glycosylated amino acid with a unique thermoresponsive property (Figure 1.6 – Gelator 1.1). The hydrogel undergoes shrinking or swelling as a response to thermal changes instead of exhibiting the conventional gel-sol transition. This hydrogel can be used to successfully release water-soluble drugs trapped within the gel matrix, as upon shrinking, water is expelled, releasing the drugs in a thermally-controlled manner. On the other hand, hydrophobic water pollutants became entrapped in the hydrophobic cavity of the gel and precipitated when the temperature increased and the gel shrunk.

Self-healing supramolecular gels are a class of smart materials that are thixotropic, which means that after applying a mechanical stress, the gel is able to spontaneously repair the damage and be restored after the stress being removed. This property makes gels highly useful for applications that require injectability and therefore, highly desirable in the biomedical field.[41,42] A thixotropic cholesterol-based organogel has been reported by Xue et al.[43] (Figure 1.6 – Gelator 1.2) where it was demonstrated that the LMWG formed stable gels in different organic solvents and after the application of a stress destroyed the gel network, its elastic gel properties spontaneously recovered after 20 seconds. Currently, it is possible to synthesise new gelators based on the structure of known thixotropic LMWGs,

however a general explanation for this phenomenon is still needed as generally these LMWGs (as many other gelators) are discovered serendipitously.[38]

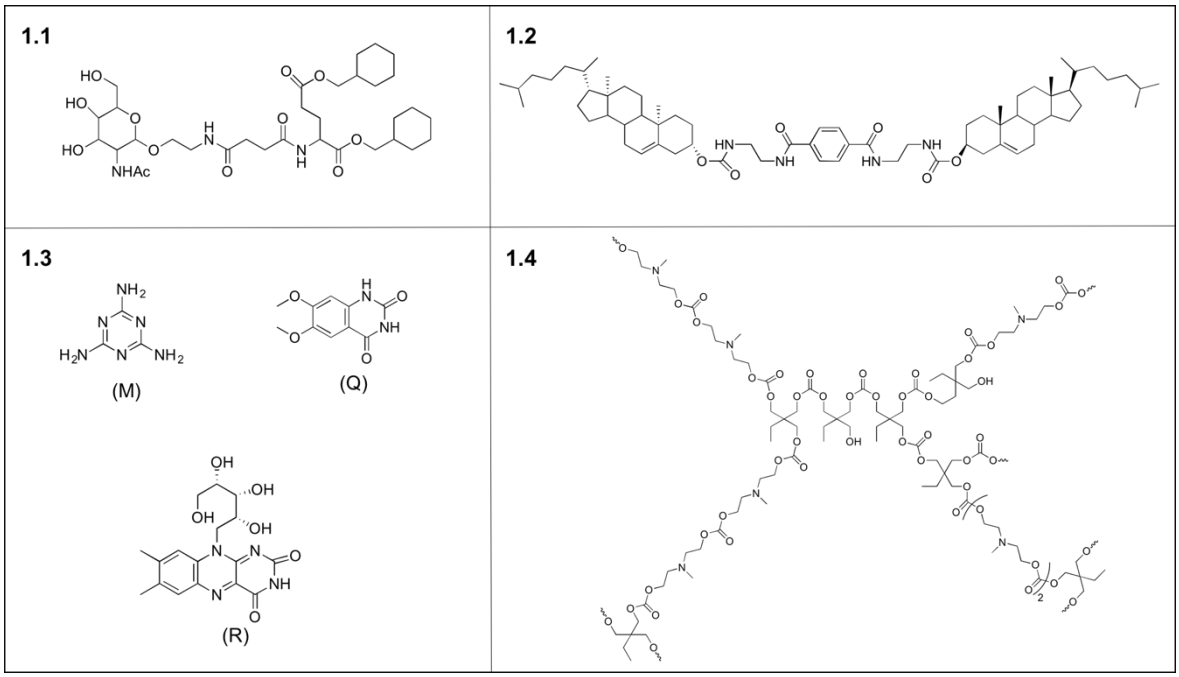

Figure 1.6. Molecular structures of stimuli responsive LMWGs: 1.1) N-acetyl-galactosamine-appended amino acid (GalNAc-aa) derivative; 1.2) Dimeric cholesterol-based $A(LS)_2$ derivative (A - aromatic component, S - steroid moiety, L - linker connecting the two units); 1.3) Melamine (M), 6,7-dimethoxy-2,4[1H,3H]- quinazolinedione (Q), Riboflavin (R) and 1.4) Cationic hyperbranched polycarbonate.

Photoresponsive supramolecular gels have great potential for electroluminescent devices and sensors. Therefore, the incorporation of donor-acceptor chromophores within the gel matrix has been widely investigated.[44] For example, Nandi and coworkers described the energy transfer from a blue-emitting gel consisting of a hydrogen bonding bi-complex of melamine and a quinazolinedione derivative to a green emitting gel when in the presence of the acceptor riboflavin (Figure 1.6 – Gelators 1.3). The properties of this co-assembled supramolecular gel can be useful for stimuli-responsive optoelectronic devices.[45]

Another interesting property that some supramolecular gels can present is pH-sensitivity, which is highly attractive for drug delivery and biomedical applications. Jia et al.[46] has

reported a pH-sensitive supramolecular hydrogel based on the hydrogen bonding of a cationic hyperbranched polycarbonate (Figure 1.6 – Gelator 1.4). While the hydrogel was stable at neutral pH with the possibility to load drugs, it showed a fast response when the pH was decreased from 7.4 to 6.6 due to charge repulsion. This resulted in significant gel volume expansion, favouring local drug release in acidic microenvironments.

The examples described above are among a vast variety of LMWGs that form stimuli-responsive supramolecular gels, involving also different types of stimuli such as redox reactions,[47] enzymes,[48] metals and anions[49]. Stimuli responsive supramolecular gels are very attractive due to their potential applications in a different range of fields. In the present work, we are particularly interest in LMWGs that are able to form supramolecular gels in water, therefore we will focus the next section on the different types of hydrogelators.

1.2. Typical Hydrogelators

Hydrogels can be found in a variety of objects, such as contact lenses, vitamin capsules and baby diapers. As hydrogels consist of a 3D supramolecular network in which the main constituent is water, the attention they have received is not surprising, particularly in life sciences as the only solvent that maintains life forms is water.

Back in 1921, Hoffman reported a molecule named dibenzoyl-l-cystine, which is believed to be the first small molecule hydrogelator (Figure 1.7).[50] The molecule was able to form a gel with only a 0.1% concentration, that was 'rigid enough to hold its shape for a minute or more when the beaker (…) was inverted'.[50] Although hydrogels were already common, they were mainly constituted by large molecules, such as proteins and polymers with complex intermolecular interactions and with molecular structures that were hard to define. It was not until the 1990s with the rise of supramolecular chemistry that small molecules able to form gels started to be studied in more detail in academic labs and only in 2000, did Menger et al.[51] investigate the molecular details of dibenzoyl-l-cystine. The study revealed the importance of aromatic moieties in the design of hydrogelators, as the aromatic-aromatic

interactions proved to be effective in enhancing hydrogen bonds and other interactions in water, promoting molecular self-assembly.

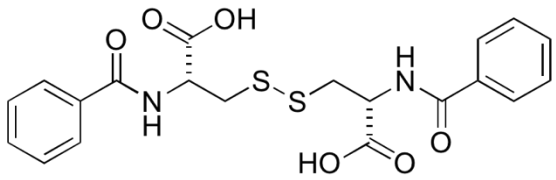

1.5

Figure 1.7. Molecular structure of dibenzoyl-l-cystine (1.5), first small molecule hydrogelator reported.

The fact that supramolecular hydrogels are mainly discovered by serendipity makes it complicated to predict which molecules will self-assemble in water only based on molecular structure. However, they share some properties such as self-assembly by noncovalent interactions, as already described and the presence of amphiphilicity that allows an effective bottom-up fabrication of the 3D gel network and provides the balanced solubility required for both gelator aggregation and compatibility with solvent. Therefore, we will be focusing on the most classical examples of supramolecular hydrogelators, namely hydrogelators based on peptides and small organic molecules.

Peptides are valuable supramolecular building blocks due to their ability to mimic natural architectures such as β-sheets and α-helices in solution and to form gels under physiological conditions, while being biocompatible and biodegradable. Peptide amphiphiles (PAs) consist of a hydrophobic region, usually an alkyl chain, and a hydrophilic peptide sequence, with features of amphiphilic surfactants and functions of bioactive peptides. PAs can self-assemble in water into gels allowing the encapsulation of small hydrophobic drugs and by displaying at their surfaces charged amino acids, PAs can also interact electrostatically with a variety of biomolecules.[52,53] Feng and coworkers[54] reported a cyclopeptide combining lysine and tyrosine able to gelate in water at a CGC of 0.6% wt/vol (Figure 1.8). The stabilisation of the gels was originated by intermolecular hydrogen bonding between the amide groups of the diketopiperazine ring - a type of hydrogen bond interaction similar to that found in nanofibers of cyclic dipeptides. Despite being able to gel

a number of organic solvents, the gelator was only able to form gels in water when ultrasound was applied during cooling, yielding a hydrogel with relatively low mechanical strength. In an attempt to enhance the mechanical properties of the hydrogel, a series of n-alkyl chains (C2-C18) were introduced in the lysine residue. The outcome revealed that hydrogelation ability was dependent on the chain length and only short alkyl tails yielded hydrogels. Moreover, the addition of an alkyl chain with one carbon atom resulted in formation of a robust and thermoreversible hydrogel at 2.5% wt/vol. This modification is believed to tune the solubility and hence the gelation potential.

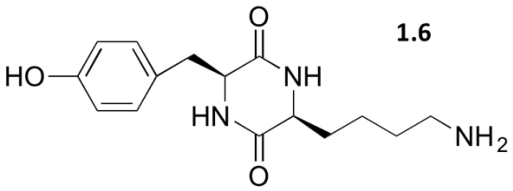

Figure 1.8. Molecular structure of tyrosine-lysine based cyclodipeptide 1.6.

Stupp and coworkers have introduced a family of cationic PAs able to gelate water, consisting of a hydrophobic alkyl chain contributing to the strongly amphiphilic nature of the molecule, followed by a short peptide sequence capable of forming intermolecular hydrogen bonding, typically composed by hydrophobic amino acids, that leads to 1D self-assembly. Additionally, charged amino acids are incorporated into the PA design, enhancing the solubility in water and the pH-response of the 3D network. Finally, the incorporation of different peptide epitopes introduces bioactivity by their ability to interact with cells or proteins.[53,55] The chemical structure of a representative PA synthesised by Stupp and coworkers is shown in Figure 1.9.

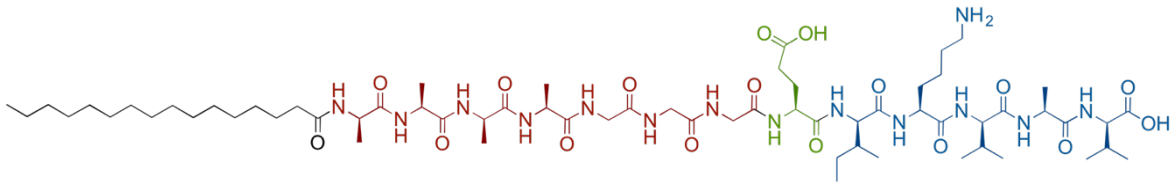

1.7

Figure 1.9. Molecular structure of a representative PA designed by Stupp's research group.

A popular class of hydrogelators based on peptides are the aromatic PAs. Aromatic PAs have gained special attention due to their structural simplicity while maintaining peptidic versatility. This class of self-assembling materials relies on aromatic groups to provide the amphiphilicity required to promote self-assembly. The aromatic PA structure (Figure 1.10) is based on a short peptide sequence (usually, dipeptide or single amino acid) stabilised *via* hydrogen bonding linked to an aromatic moiety (typically a 9-fluorenylmethoxycarbonyl (Fmoc) group[56,57]) that self-assembles through π-π interactions. The linker between these two segments can control their structural orientation and hence also plays an important role in the overall structure. Additionally, the C-terminus can be funtionalised or contribute to the balance between protonated and ionised forms.[58]

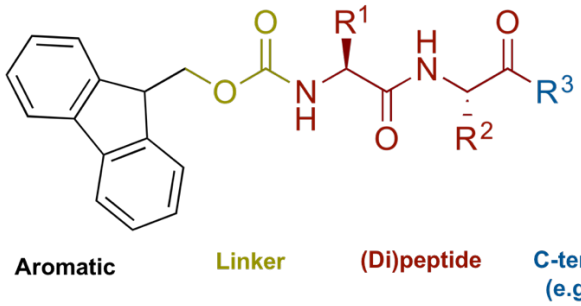

1.8

Figure 1.10. Generic molecular structure of aromatic PAs.

A very well investigated aromatic PA is Fmoc-diphenylalanine (Fmoc-FF), shown on Figure 1.11 – Gelator 1.9.[59–63] Xu and coworkers[64] were the first to report Fmoc-protected amino acids and dipepetides that spontaneously formed fibrous scaffolds. Ulijn and coworkers[65,66] then reported the Fmoc-FF PA as a hydrogelator able to self-assemble into a 3D fibrilar

network under physiological conditions by adjusting the pH of the aqueous solution. Later Adams et al.[67] concluded that the final pH of the Fmoc-FF hydrogels dictated the mechanical properties of the hydrogel, due to the presence of the C-terminal carboxylic group. Adams and coworkers[68] also studied the contribution of different parts of naphthalene-conjugated dipeptide to the overall structural architecture, by testing different dipeptide sequences conjugated to naphthalene with different substituents (Figure 1.11 – Gelator 1.10). Adams and co-workers achieved gelation by the hydrolysis of glucono-δ-lactone (GdL) to adjust the pH. The hydrolysis of GdL in water forms gluconic acid and results in a slow decrease in pH. This controls the kinetics of protonation to make sure that it is not faster than the kinetics of self-assembly – which leads to inhomogeneous materials. The hydrophobicity of the dipeptide influenced the pKa of this class of hydrogelators and consequently the final pH of the gels.[68] Additionally, it was found that the chirality of the naphthalene assemblies was governed by the dipeptide sequence and the molecular packing governed by the nature of the naphthalene conjugate.

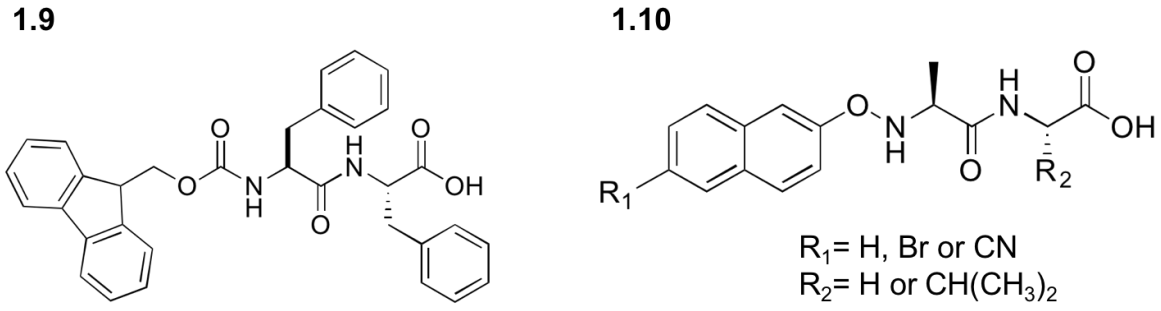

Figure 1.11. Molecular structure of 1.9) Fmoc-FF and 1.10) naphthalene-conjugated dipeptide.

In respect to hydrogels based on small organic molecules there is currently a diverse number of building blocks in this category that can promote gelation in water. Therefore, some examples of effective hydrogelator families based on small organic molecules will be described.

Urea is well-known to form self-assembled nano-architetures and to have a gelation ability dependent on the hydrogen bond interactions, having self-complementary hydrogen bond

donors and acceptors. For that reason several hydrogelators based on urea have been developed.[69–71] The Dastidar group[72,73] has demonstrated that composites of pyridyl-urea (Figure 1.12 – Gelator 1.11) in conjunction with carboxylic acids can produce a range of materials that can either form gels or are crystalline. They demonstrated that when the urea group is at the *para* position of the pyridine it hydrogelates, whereas at the *meta* position is does not. This is thought to be due to the intramolecular CH-O interactions coupled to the good hydrogen bond acceptor of the pyridinyl nitrogen atom when the urea group is in the *meta* position making it a poor gelator as it cannot form the typical urea tape motif responsible for one-dimensional fibre growth.[74] Different urea-based hydrogelators have also been developed by Steed and coworkers.[75–77] Specifically, an imidazole-urea based hydrogelator was developed (Figure 1.12 – Gelator 1.12) in which the imidazole nitrogen atom has the potential to hydrogen bond with the imidazole NH group, leaving the urea moiety free to form the typical hydrogen bonded tape motif and hence act as and effective gelator.[77] van Esch et al introduced a new class of effective hydrogelators based on the modification of the substituents of cyclohexane bis-urea organogelators with hydrophilic hydroxy or amino functionalities (Figure 1.12 – Gelator 1.13). The hydrogels consist of a network of fibers, where the urea groups were involved in intermolecular hydrogen bonding and the gelation was driven by hydrophobic interactions of the methylene groups, while urea hydrogen bonding provided the anisotropic self-assembly and high thermal stability of the gels.[78]

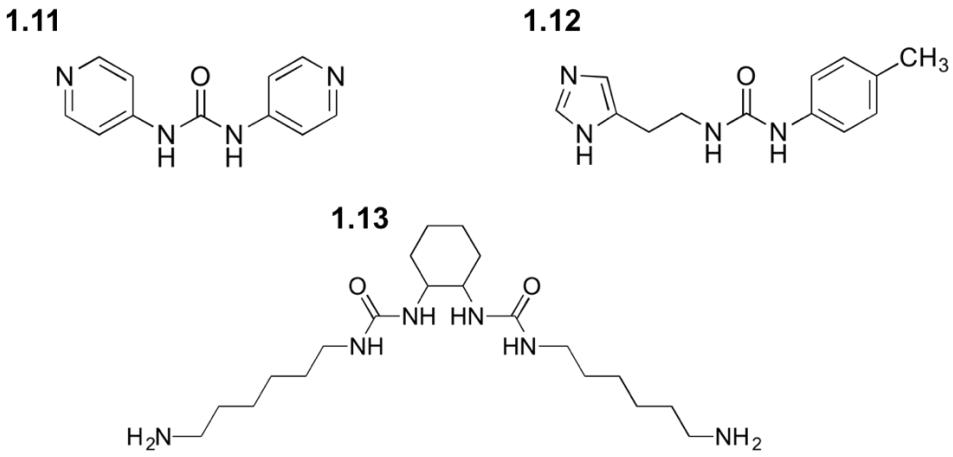

Figure 1.12. Molecular structures of selected urea-based LMWGs 1.11 -1.13.

An alternative type of hydrogelator uses saccharide groups instead of urea to provide hydrogen interactions, as the multiple hydroxyl groups contribute to the presence of both hydrogen bond donors and acceptors for intermolecular interactions, essential for the molecular self-assembly in water, while the hydrophilic saccharide moieties also contribute to the solubility of the gelator in water.[79] Chen et al.[80] reported a cysteine and pH-sensitive saccharide-derived hydrogelator bearing an aldehyde group (Figure 1.13 – Gelator 1.14). The selective response to cysteine was tested by comparing with other eight different amino acid solutions placed on top of the hydrogels. Only when in contact with cysteine was the hydrogel completely transformed into solution indicating that this hydrogelator responds selectively to cysteine, probably due to the specific reaction of the aldehyde with cysteine to form the thiazolidine derivative, while not being able to react with any of the other amino acids. The hydrogelator also proved to be pH-sensitive and could be converted to solution after exposure to acidic medium due to the sensitivity of the acetal moiety to acidic environments. In another approach, Mishra and coworkers[81] demonstrated a glucose-based gelator able to effectively form thermoreversible hydrogels at a CGC of 0.03% wt/vol in a mixture of water and methanol (50:50). The amphiphilic gelator design was based on a hydrophilic glucose head connected through a triazole incorporated linker to the benzene ring with a hydrophobic hydrocarbon tail (Figure 1.13 – Gelator 1.15). Intermicellar aggregation led to the formation of larger micellar structures and the interaction of larger aggregates to form sheet-like spongy gel networks which entrap the solvent molecules by a surface tension effect. It should be noted that mixed aqueous solvents are often used to tune the solubility of a system to achieve effective gelation.

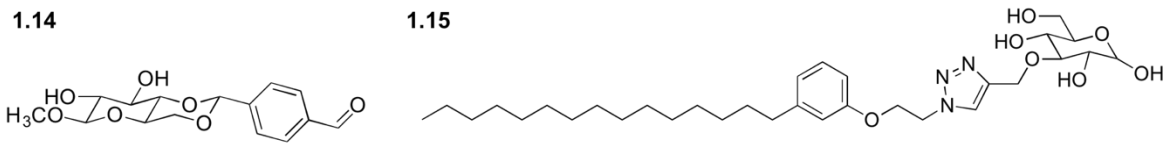

Figure 1.13. Molecular structures of saccharide-based hydrogelators 1.14 and 1.15.

The use of sorbitol as a supramolecular building block has also resulted in the development of effective hydrogelators. An effective amphiphilic hydrogelator based on sorbitol has been reported by Li et al.[82], and the effect of salt on the gelation process of the LMWG

2,4(3,4-dichlorobenzylidene)-D-sorbitol (Figure 1.14 – Gelator 1.16) was studied. It was demonstrated that the addition of NaCl affected the morphology of the gels changing from globular aggregates to entangled long fibers. The presence of salt also contributed to slightly weaker hydrogen bonding interactions, probably due to the fact that the self-assembly of the hydrogelator was not only governed by intermolecular hydrogen bonds but also by π-π interactions and van der Waals interactions, which interfere with the hydrogen-bonding interactions because of steric mismatching. A related example reported a sorbitol-based LMWG (Figure 1.14 – Gelator 1.17) that self-assembles in water and can be used as a gel electrolyte. The hydrogel is formed in the presence of 6 M KOH and has a CGC of 0.3% wt/vol. The hydrogel electrolyte proved to be thermoreversible, with a very good thermal and electrochemical stability that make it suitable for applications in alkaline battery systems.[83]

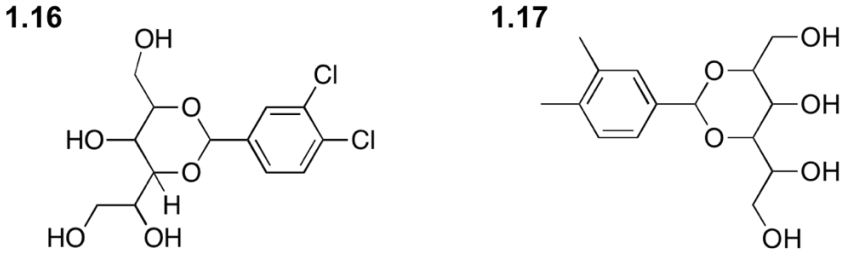

Figure 1.14. Molecular structures of sorbitol-based LMWGs 1.16 and 1.17.

In the present work, hydrogels are formed based on the well-known organogelator 1,3: 2,4-dibenzylidene-D-sorbitol (DBS) (Figure 1.15).[84] This chiral LMWG amphipile is capable of self-assembling into 1D fibers which leads to an intertwined network in the presence of a liquid phase. DBS is a derivative of the sugar alcohol D-sorbitol and presents a butterfly-like shape, having the sorbitol as the body and the benzylidene groups as the wings. The ability of DBS to self-assemble is endowed by the aromatic rings through the solvophobic effect and π-π stacking supported by hydrogen bonding between the acetal oxygens and hydroxyl groups. It is believed that the more internal 5-hydroxy group forms intramolecular interactions with the nearest acetal oxygen, while the most external 6-hydroxy group forms intermolecular hydrogen bonds with the acetal oxygens of DBS "neighbours", hence being crucial for the self-assembly event.[85] Furthermore, Lan et al.[86] disclosed how solvents can alter or influence the gelation of DBS. It was stated that opaque DBS gels tended to be

constituted by bundles of fibers and to be weaker than the transparent gels, which are more likely to form in higher-polarity solvents. Besides the importance of the polarity of the solvent, their ability to accept or donate a hydrogen bond appeared to be very important to determine whether the addition of DBS will result in a solution, clear gel, or opaque gel, with the latter being obtained when the DBS could not accept a hydrogen bond. Therefore, when the solvent presented stronger hydrogen bonding than DBS, clear gels were formed whereas the opposite situation led to the formation of opaque gels. This reflects the fact that gelation is a balance between solubility and aggregation.

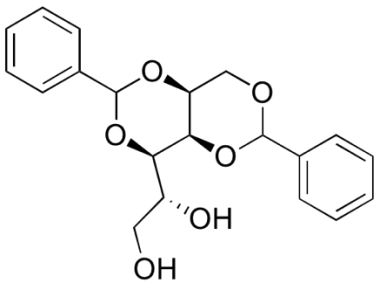

Figure 1.15. Molecular structure of DBS.

The presence of aromatic rings introduces hydrophobicity into the molecule which is a drawback in terms of the formation of hydrogels. In order to overcome this problem, our research group developed DBS derivatives in which the aromatic rings are *para* substituted. When substituted by carboxylic acid groups (Figure 1.16– a), the hydrophilicity of the molecule is increased and allows the formation of efficient pH-controlled hydrogels.[87] Additionally, if functionalised by hydrazide groups (Figure 1.16 – b), which also provides hydrophilicity to support hydrogelation, the system effectively self-assembles in water by application of a heat-cool cycle and forms pH-tolerant hydrogels.[88]

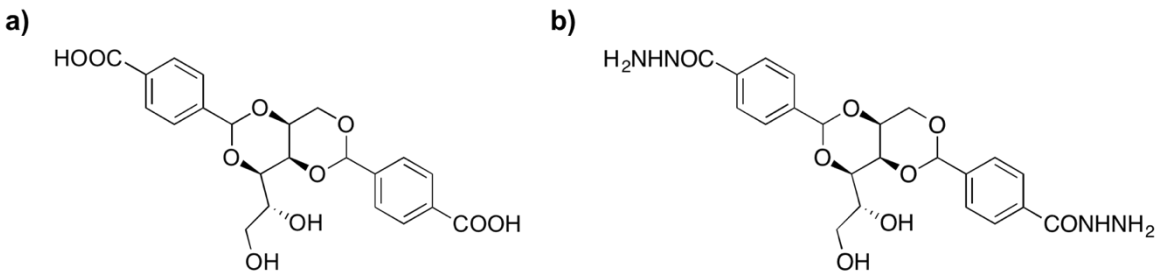

Figure 1.16. Molecular structures of DBS-based LMWGs: a) DBS-COOH and b) DBS-$CONHNH_2$.

1.3. Multicomponent Gels

Most supramolecular gels consist of a solvent and a gelator. However, the individual self-assembly of multi-component supramolecular structures with LMWGs can give rise to new materials with complexity, containing independent functionalities, potentially able to mimic multi-component natural systems.[89–91] Multi-component LMWGs can be achieved using different approaches such as through mixing of different LMWGs,[92–96] or the combination of LMWGs with polymers,[87,97–99] where both molecules can form gels; mixing two or more components that do not gel independently but form gels when combined;[100,101] or the orthogonal self-assembly of LMWGs with non-gelating components such as surfactants.[102–104]

Mixtures of two different LMWGs can originate different behaviours, resulting in different structures, as shown in Figure 1.17. The LMWGs can associate with each other, so the fibers are formed with an exact order of gelators (ordered co-assembly); the LMWGs can mix in a random way (random co-assembly); or the LMWGs can self-assemble individually, so the fibers are formed with only one molecule or the other (self-sorting).[90]

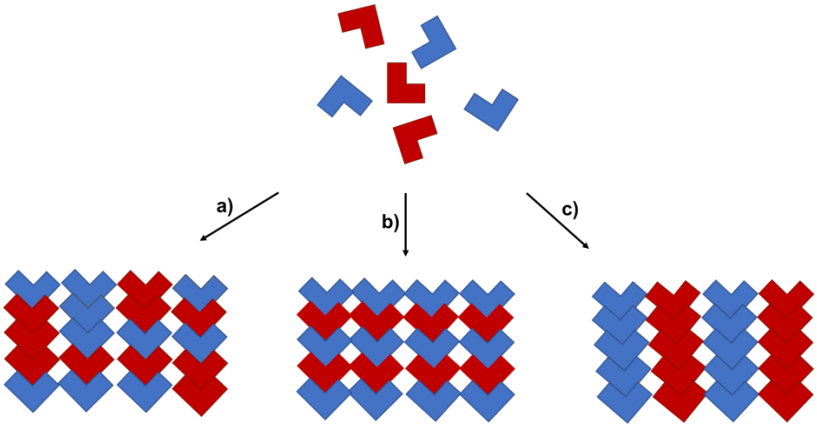

Figure 1.17. Schematic representation of the self-assembling of two LMWGs: a) randomly; b) co-assembly; c) self-sorting. [Adapted from reference [90]]

Recently, Adams and co-workers studied a pH-triggered mixture of two naphthalene-based dipeptide LMWGs and explored whether co-assembly or self-sorting was occurring and the effect of pH on gel network formation (Figure 1.18). As described previously, they lowered pH in a controlled manner using the hydrolysis of GdL to gluconic acid. At high pH both LMWGs remained independent and colloidal structures were formed (LMWG 1.18 forms wormlike micelles, whereas LMWG 1.19 does not). When the pH was decreased there were two main stages in the assembly process of the mixture of LMWG 1.18 and 1.19. The first stage was above the expected pka of LMWG 1.19, with LMWG 1.18 starting to assemble into fibers first. At this stage, there was co-assembly of both LMWGs. As the pH continued to decrease, there was a different rate of assembly and as LMWG 1.19 was not fully incorporated it formed an independent network, thus self-sorting. It was believed that the type of micelle formed at high pH may dictate whether the multicomponent system is driven by self-sorting or co-assembling.[105]

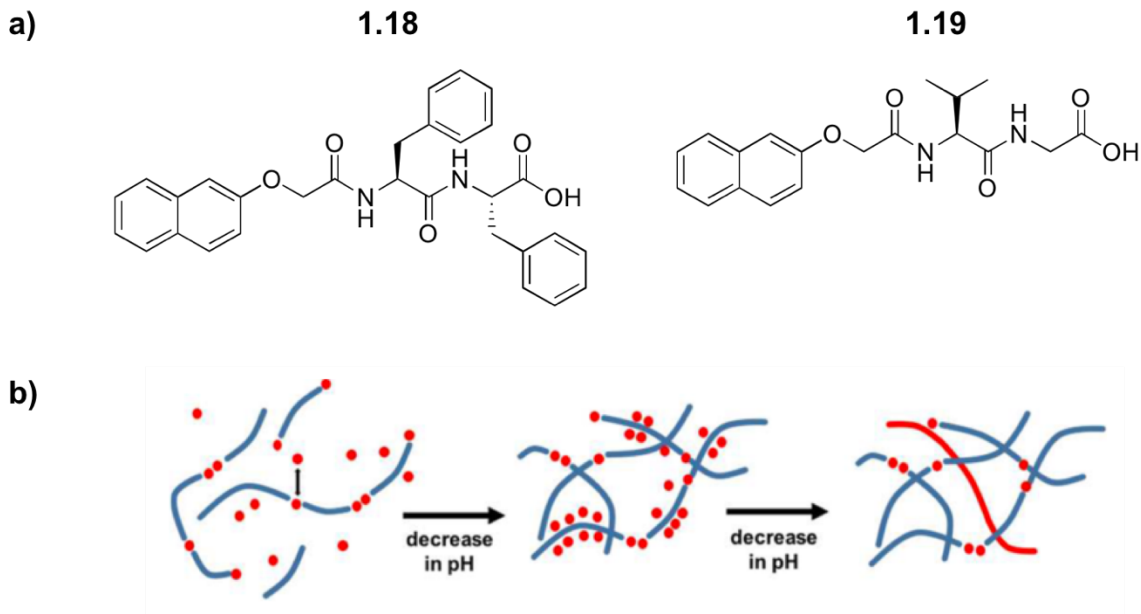

Figure 1.18. a) Molecular structures of naphthalene-based LMWGs 1.18 and 1.19. b) Schematic representation of partial co-assembly of a mixture of the LMWG 1.18 (blue) and LMWG 1.19 (red) with the decrease of pH. LMWG 1.19 is not fully incorporated and assembles alone as the pH decreases.[105]

Despite the responsiveness and tunability of LMWGs, they usually form weak networks, which can make them less applicable than covalently cross-linked gels.[106] Therefore, their combination with polymer gels is of increasing recent interest due to the enhanced mechanical properties which become possible. This combination can be achieved by polymerizing the LMWG fibers; capturing the LMWG in the polymer matrix; adding a non-gelling polymer; adding a polymer that will drive the self-assembly of the LMWG, or mixing a polymer with a LMWG, where both are able to form gels.[97] As an example of the latter approach, our group previously demonstrated the combination of DBS-COOH LMWG with agarose as a polymer gelator (PG) (Figure 1.19) that resulted in independent and non-interacting networks, with the LMWG providing the network with pH responsiveness while the polymer gel ensured the robustness, integrity and porosity of the overall material.[87] The same LMWG has been used to form a hybrid hydrogel with a photo-inducible synthetic polymer (poly(ethylene glycol) dimethacrylate - PEGDM) (Figure 1.19). The hybrid material proved to be a self-sorting multicomponent gel where different regions can be spatially patterned by photo-irradiation and with the LMWG being able to assemble and

disassemble within the PG network by pH variation. Both gelator networks can control diffusion rates with suggested applications in drug delivery with the potential for different kinetics of drug release from different parts of the gel.[98]

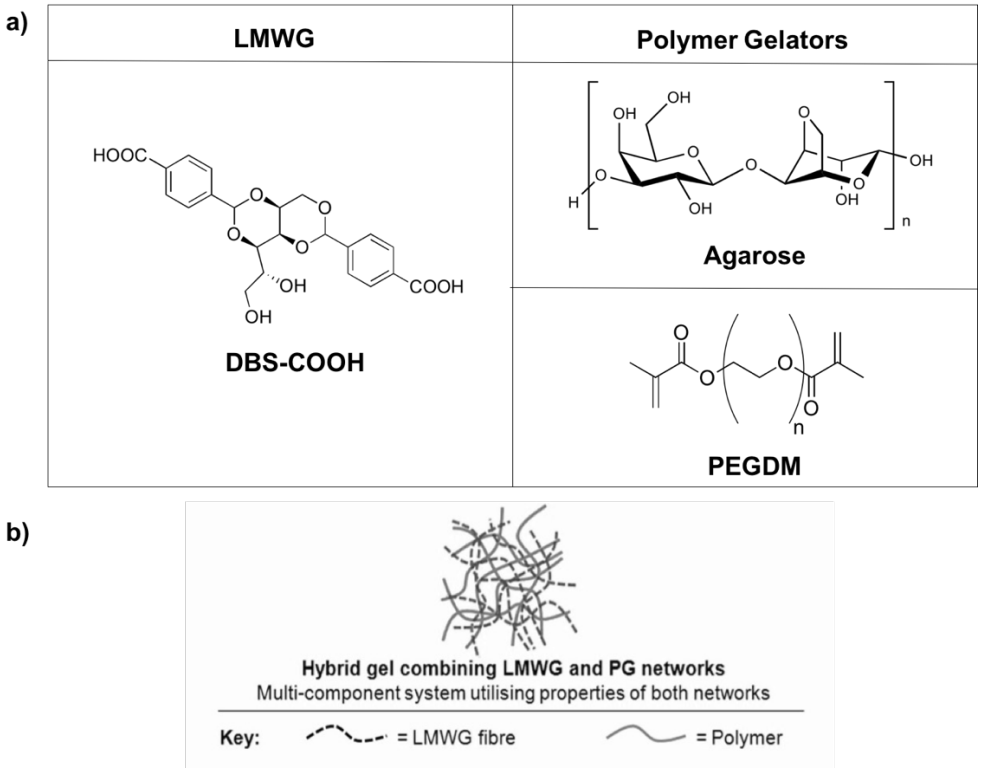

Figure 1.19. a) Molecular structures of LMWG and PGs used to obtain responsive hybrid gels b) Schematic representation of a LMWG-polymer hybrid gel.[97]

Multi-component supramolecular gels can also be obtained from small molecules which individually are not able to form gels. Ding and coworkers[101] reported a peptide that by itself forms nanofibers but not hydrogels due to the weak inter-fiber interactions. In an attempt to use the nanofibers as a vehicle for delivering anticancer drug doxorubicin, they discovered that the drug could not be encapsulated as it formed nanospheres that were located at the surface of the peptide nanofibers. The nanospheres acted as cross-linkers to increase the inter-fiber interactions due to the electrostatic interactions between the negatively charged nanofibers and the positively charged doxorubicin, contributing to the formation of a stable 3D hydrogel network. Additionally, the resulting hydrogel was able to release the drug in a sustained manner while showing a cytotoxicity comparable to the free

doxorubicin. Therefore, the use of nanospheres as cross-linkers to form supramolecular hydrogels with potential for controlled delivery of anticancer drugs was demonstrated.

In a different approach, van Esch and co-workers[102] reported an orthogonal self-assembled architecture involving a 1,3,5-cyclohexyltricarboxamide based hydrogelator (OG2) and surfactants that form compartmentalised structures. The thermoreversilibity of the hydrogels allowed them to be dissolved in solutions of surfactants at a temperature above the T_{gel}, followed by cooling to obtain the hydrogels with the surfactants incorporated. The surfactant vesicles were stable in the presence of the gel nanofibers, with the vesicles being accommodated within the confined space of the gel network pores (Figure 1.20).

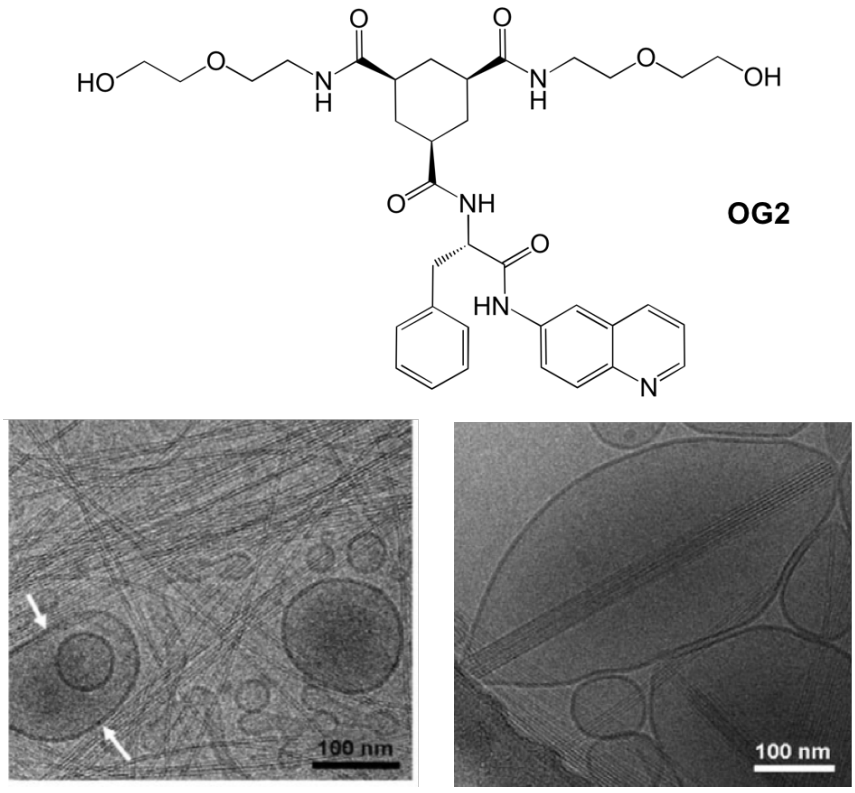

Figure 1.20. Molecular structure of a cyclohexane-based LMWG functionalised with an l-phenylalalanyl-amidoquinoline moiety (OG2) (top) and cryo-transmission electron microscopy (cryo-TEM) images of stable dioleoylphosphocholine (DOPC) vesicles coexisting with OG2 gel network (bottom left) – vesicles shape influenced by confined gel network and DOPC vesicles deformed by the growth of the OG2 gel nanofibers directly in their aqueous compartment (bottom right).[102]

Additionally, as the OG2 hydrogelator can also form reversible hydrogels by adjusting the pH value, the encapsulation of free OG2 monomers in unilamellar liposomes could be achieved at pH 2. The self-assembly of OG2 into nanofibers was then induced by increasing the pH to neutral. As a result, OG2 nanofibers were observed within the aqueous compartment of the unilamellar vesicles, with the growth of the fibers restricted by the membrane wall, and its anisotropic growth and rigidity deforming the spherical shape of the vesicles (Figure 1.20). The orthogonal self-assembly of vesicles with encapsulated hydrogels, usually called 'gellosomes' is very attractive as a mimic of natural systems, such as the cytoskeleton and for drug delivery.[104]

Stupp et al[107] reported aldehyde functionalised PAs, based on the amphiphile structure shown in Figure 1.9, that form supramolecular assemblies capable of reducing silver ions and nucleating uniformly sized silver metal nanoparticles in water. The PA was modified in order to display aldehyde moieties on its surface, which are known to reduce two silver ions to Ag_2 clusters. The fusion of silver clusters into larger nanoparticles was then promoted by rearrangement of PA molecules within the supramolecular structure, generating monodispersed silver particles at regular distances along the length of the PA nanofibers. The metallic supramolecular hydrogels exhibited antimicrobial activity which can be useful for applications in medicine. Our research group has also reported a hybrid hydrogel based on the pH-stable hydrogelator DBS-$CONHNH_2$ which extracts precious metal ions, such as gold and silver, and originates conductive hybrid materials. In this example, gold and silver ions were spontaneously reduced in the gel to form gold and silver nanoparticles (AuNPs and AgNPs, respectively) (Figure 1.21). The diffusion of Au^{3+} and Ag^{+} into the gel leads to its change in colour to ruby or yellow, respectively, indicating that the gel fibers reduce and cap the nanoparticles in situ within the network. These conductive hybrid materials may be useful in nanoelectronics, with modified electrode surfaces and enhanced electrocatalysis, being demonstrated.[108]

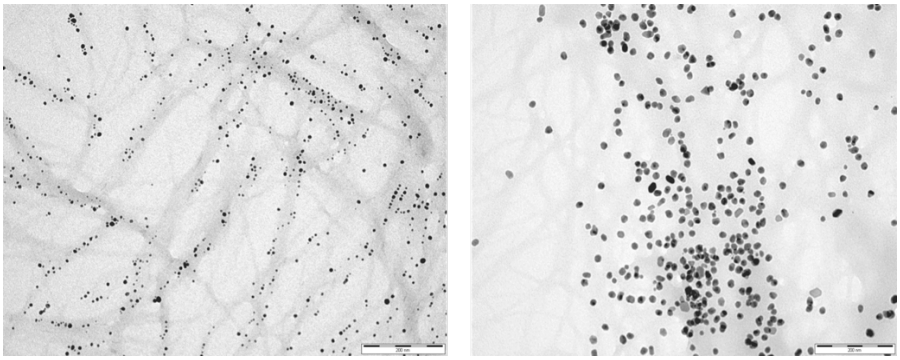

Figure 1.21. Transmission electron microscopy (TEM) images of DBS-$CONHNH_2$-AuNPs (right) and DBS-$CONHNH_2$-AgNPs (left) hydrogels. Scale bars: 200 nm.[108]

1.4. Controlled Release from Gels

The controlled release of pharmaceutical drugs requires the development of optimized systems that will ensure biodegradability; the absence of side effects; drug loading capacity; control on drug release kinetics; and maintenance of the physical-chemical properties of the drug.[109,110] Biomaterials with nanoscale organisation have been successfully used as controlled release vehicles for drug delivery. Promising nanoscale drug delivery systems include nanoparticles, nanocapsules, nanotubes, nanogels and dendrimers, which can be used to deliver small-molecule drugs and biomacromolecules (e.g. peptides, proteins).[111]

Soft materials such as hydrogels, can serve as carriers of encapsulated drugs or can be covalently conjugated with therapeutics, and for that reason have been widely studied to act as drug delivery vehicles.[28,109,110,112–118]For the release of drugs from a polymer hydrogel, the molecular weight of the drug and the network density can affect the release profile of the drugs.[119,120] For example, Menzel et *al.*[120] studied the influence of the network properties of polymer hydrogel cylinders and microspheres on the release rate of proteins. They observed that the degradation of the network leads to the release of the entrapped substances, but the encapsulation of small substances in hydrogels with low polymeric gelator concentrations (10 wt%) resulted in an initial burst release. By increasing the density of the network (30 wt% of gelator) and the drug size, the initial burst disappeared and a continuous release occurred. With the increase of network density and associated decrease in pore size of the network, the substances were entrapped more evenly, which

contributed to a more constant release. So, the network properties, the drug hydrodynamic diameter and degradation proved to be essential factors for the efficiency of controlled release by polymer hydrogels.

In hydrogels formed from LMWGs, the self-assembly process, the gelator concentration, pH, temperature, etc. can be used to obtain a controlled release profile of bioactive molecules. In one example, Hamachi et al. have reported a multi-stimulus responsive phosphate-based hydrogelator which responds to four different stimuli (temperature, pH, Ca^{2+} and light) (Figure 1.22). By using the multi-stimulus responsiveness, they formed supramolecular hydrogels in the presence of various combinations of the stimuli and found that they were able to hold and release bioactive substances (vitamin B_2 and protein Rh-Con [rhodamine-labelled concanavalin A]) in response to various input triggers. For example, when using Ca^{2+} complexed supramolecular hydrogel at pH 2, vitamin B_2 was held in the network in the absence of triggers, even when exposed to aqueous solution or a single additional input (i.e., EDTA or NH_3). When both triggers were applied simultaneously a gel-sol transition occurred and a gradual release of vitamin B_2 was observed. Additionally, by combining this hydrogel with a photoresponsive supramolecular gel, the application of UV light prior or after to the other 2 inputs resulted in different behaviours, with the former leading to the rapid release of vitamin B_2 and the later temporarily modulating its release. Therefore, this supramolecular system presents powerful responses to various stimuli that mean it has potential as a smart material for the controlled release of biological substances.[121]

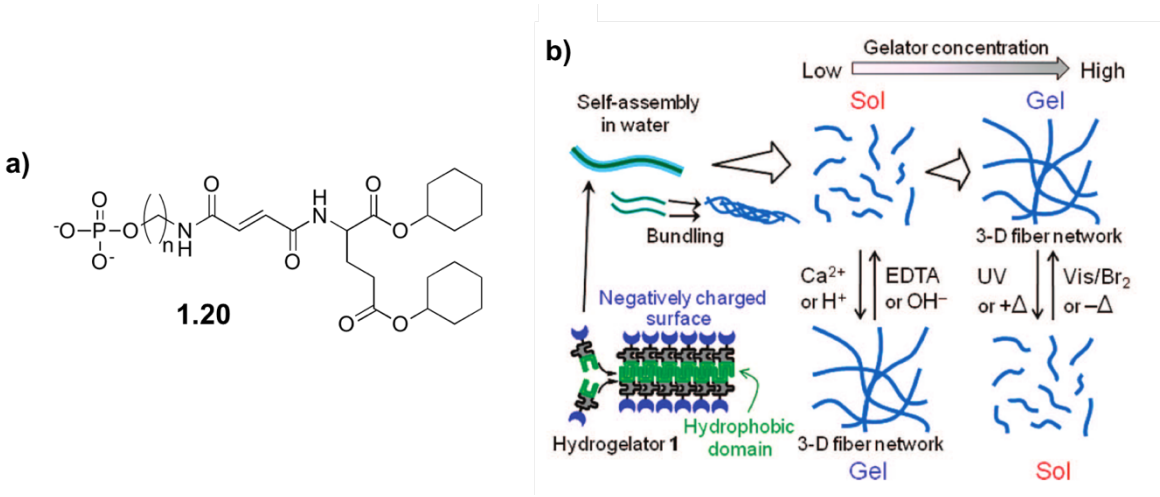

Figure 1.22. a) Molecular structure of multi-stimuli responsive phosphate-based hydrogelator 1.20. b) Schematic representation of hierarchical self-assembly of phosphate-based hydrogelator and gel-sol transition triggered by different stimuli (temperature, pH, Ca^{2+} and light).[121]

Adams et al.[122] showed two Fmoc-aminoacid based hydrogels (Figure 1.23) formed by adjusting pH, that were able to entrap and release model dyes and may be suitable as controlled release systems. The release profiles showed typical sustained release behaviour and when plotting the released amount against the square root of time it indicated that the release of dyes from the hydrogels was under the control of Fickian diffusion.[123] Additionally, while the Fmoc-phenylalanine hydrogels presented similar diffusion times for different dyes and could not retain even the larger dyes (5 nm), Fmoc-tyrosine hydrogels restricted the diffusion of larger dyes, which was expected as the later proved to have a stronger gel network and therefore there is a greater influence on the diffusion of larger molecules. This indicated that network properties control release kinetics in self-assembled systems.

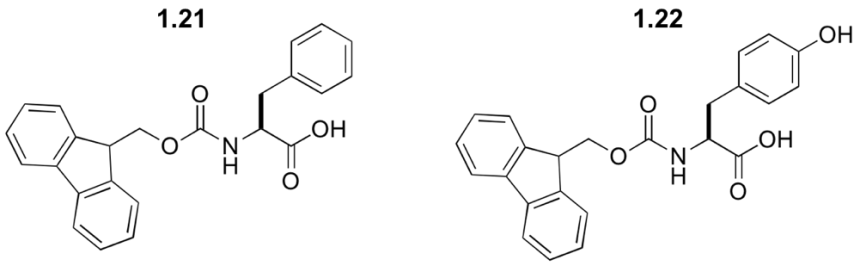

Figure 1.23. Molecular structures of Fmoc-phenylalanine (1.21) and Fmoc-tyrosine (1.22) hydrogelators.

Escuder and coworkers reported an L-proline-based hydrogelator, which provides a nucleophilic reactive site that reacts with aliphatic aldehydes causing the disassembly of the hydrogel network (Figure 1.24). They reasoned that the secondary amine group of the hydrogelator reacts with the electrophilic carbonyl group of the aldehyde yielding a soluble aminal. This feature led the group to further investigate the potential of these hydrogels for the release of drugs. Firstly, it was shown that the disassembly of the hydrogels depends on the aldehyde structure and the rate of response increased with the hydrophobicity of the aldehyde. Additionally, the hydrogels proved to effectively entrap dyes and non-steroidal anti-inflammatory drugs, followed by their controlled release in response to the presence of specific aldehydes. It was reasoned that because the hydrogelator is highly biocompatible it may, via this mechanism, present a protective effect against toxic aldehydes.[124,125]

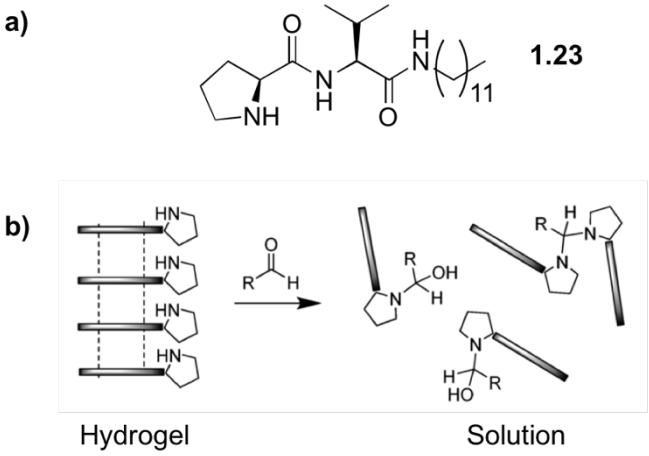

Figure 1.24. a) Molecular structure of l-proline based hydrogelator 1.23. b) Hydrogel disassembly after reacting with aldehydes.[125]

Stupp et al.[126,127] have reported the use of one of their PA nanofiber hydrogels (Figure 1.25) to effectively deliver sonic hedgehog (SHH) protein to the cavernous nerve (CN) to promote regeneration and prevent erectile dysfunction (majority of causes due to injury of the CN). SHH proteins are essential to maintain CN integrity and therefore the group developed a PA hydrogel composed by highly aligned monodomain nanofiber bundles with SHH protein entrapped within the gel network during cation-based assembly and crosslinking. The hydrogels were mechanically strong enough to be manipulated and placed on top of CN at the time of surgery. CN preservation and regeneration were enhanced as the SHH protein was gradually released from the gel. The PA hydrogel acted as a scaffold for the regeneration of axons (nerve fibers) and allowed the direct delivery of SHH proteins to the crush site in the CN. This PA hydrogel allowed customised, controlled protein delivery with a biodegradable vehicle.

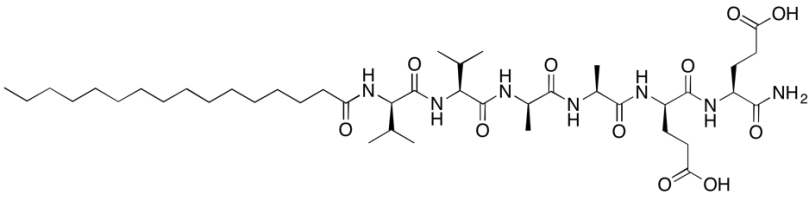

1.24

Figure 1.25. Molecular structure of (C16)-VVAAEE-(NH_2) (V: valine, A: alanine, E: glutamic acid) PA used to form highly aligned, monodomain hydrogels.

Fatouros et al. reported the design of amphiphilic self-assembling lipid-like peptides consisting of six hydrophobic alanines (A) and an aspartic acid (D) or lysine (K) hydrophilic head group (such as, Acetyl-A_6K-$CONH_2$ or Acetyl-A_6D-COOH). These lipid-based systems formed turbid suspensions when added to water as a result of the self-assembly of the peptide monomers to minimise the interaction between hydrophobic domains and the polar environment. By altering the amino acid sequence and the charge distribution, the group was able to obtain different loading capacities and drug release kinetics. Of the tested nanovesicle systems, Acetyl-A_6D-COOH proved to be more suitable for drug delivery. Negatively charged drug carriers are preferable for intravenous administration as they present longer circulation in the bloodstream due to electrostatic repulsions with charged blood cells and vessel walls.[128] Kim and coworkers[129] designed and characterised hydrogelators consisting of cationic lipids coupled with B vitamins (B_2-B_7) (Figure 1.26 - a),

which are overexpressed on the surfaces of cancer cells and thus, their specific receptor can be involved in the biological mechanism for the delivery of therapeutic siRNA into cells. Therefore, they used these nanoassembled LMWGs to effectively deliver siRNA into cancer cells, to silence gene expression. The group suggested that the hydrogels self-assemble into lamellar-type structures which can help in the efficient complexation and delivery of siRNA (Figure 1.26 - b).[130] Specifically, when coupling the cationic polar head groups and hydrophobic chains with vitamin B_7, the resulting transparent biocompatible hydrogels delivered siRNA to tumor tissue and not to other major organs and therefore, may be used to silence gene expression specifically in cancer cells (Figure 1.26 - c).

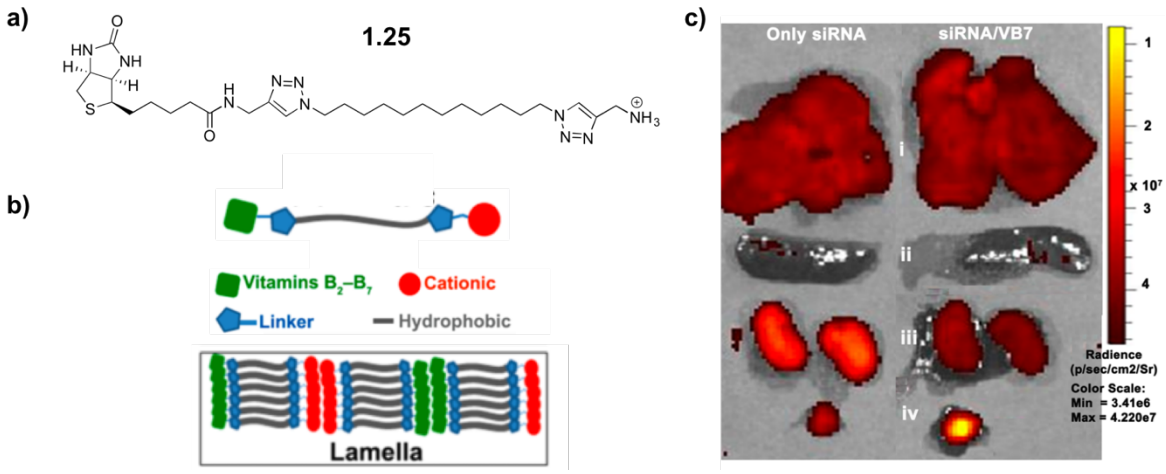

Figure 1.26. a) Molecular structure of cationic lipidic LMWG coupled with Vitamin B_7. b) Schematic representation of LMWG coupled with B vitamins self-assembly in lamellar-type structures. c) Fluorescence images of (i) liver, (ii) spleen, (iii) kidney and (iv) tumor from a rat treated with only siRNA (right) and siRNA incorporated in the hydrogel of lipidic LMWG with Vitamin B_7 (left).[129]

1.5. Tissue Engineering in Gels

Tissue engineering is an interdisciplinary field that uses engineering and natural sciences to attempt the successful repair and replacement of damaged tissues and organs.[131] For the formation of functional tissue, cells ideally need to be seeded in 3D scaffolds before transplantation (Figure 1.27). These 3D biomaterials should be able to retain cells, direct cell proliferation and differentiation, while allowing the appropriate transport of nutrients and metabolites into the cell. The fact that cells need a microenvironment that mimics the

in vivo properties of the tissue and accurately replicates the ECM to undergo the morphogenic process,[i] makes tissue engineering a very challenging field.[132–137]

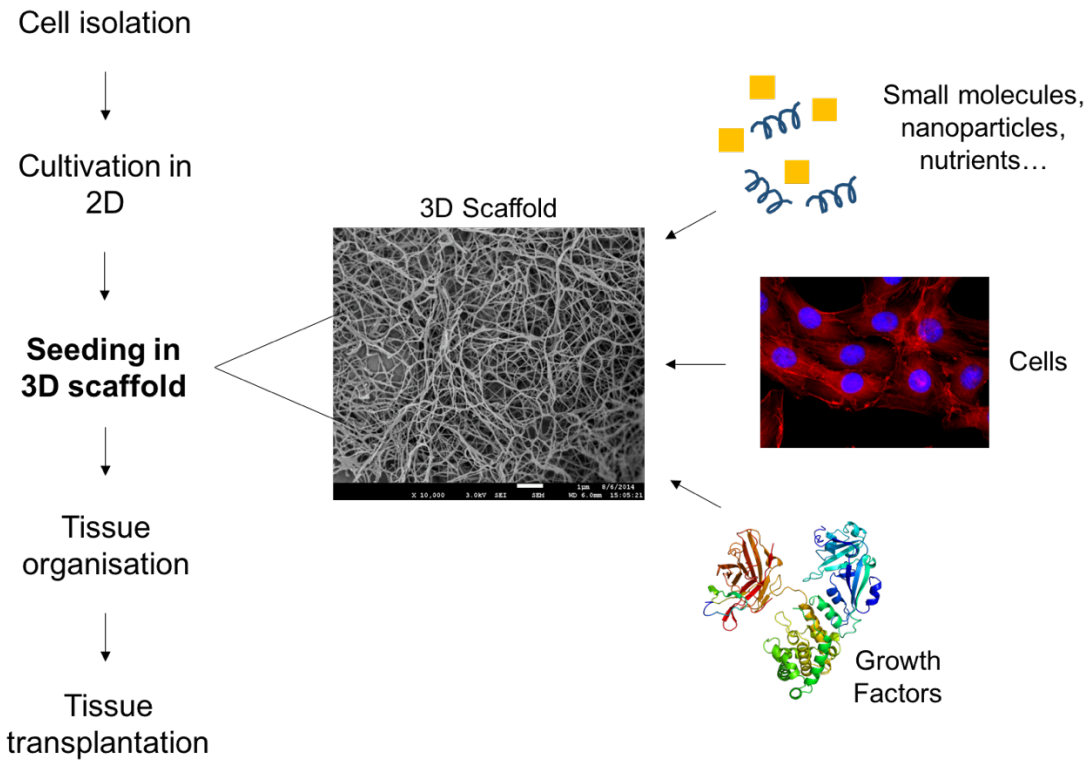

Figure 1.27. Tissue engineering concept involving cell seeding. [Adapted from reference [132]]

Hydrogels have been described as suitable mimics of the ECM due to key characteristics such as high water content, porosity, high loading capacity, degradability, responsiveness to certain stimuli and varied rigidity, being widely exploited to develop efficient 3D scaffolds for cell-culture applications.[138–151] Polymer hydrogels are very widely exploited in this regard but supramolecular gels have been less extensively investigated. In one example, Pradas et *al.*[139] incorporated a self-assembling peptide (SAP) into a porous elastomer scaffold, creating a hydrogel with similar properties to those of ECM and observed that the presence of the SAP in the pores of the scaffold improved the colonization of cells with a more uniform distribution compared with the same system without the SAP. Proliferation also proved to be greater in the pores with SAP gel. Thus,

[i] *Morphogenesis* describes the evolution and development of form.

the existence of a self-assembled hydrogel able to mimic the ECM contributed to creating an effective medium for cell growth. In another example, Suga et al[152] synthesised a lysine amphiphilic compound (Figure 1.28) that forms viscous hydrogels able to attach onto the 96-well plates leading to 10-fold enhanced cell attachment when compared to the control experiment with no gel coating. This hydrogel interacts with cells through electrostatic interactions between NH_3^+ positive charge and the negative charged cell membrane. In addition, this LMWG attached more cells than conventional materials (e.g. sodium alginate, collagen, poly-L-lysine hydrochloride), most probably due to the high viscosity of the material that allowed the hydrogel to strongly stick to the wells enabling better adhesion. The strong adhesive features of this hydrogel may be useful in tissue engineering and biomedicine.

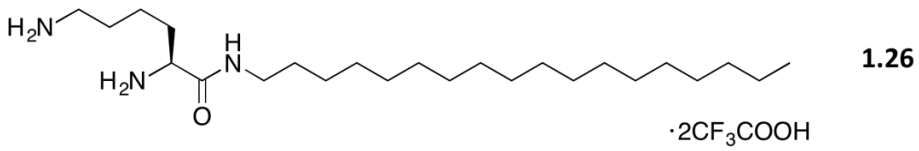

Figure 1.28. Chemical structure of lysine-based hydrogelator 1.26.

Ziane et *al.*[153] also reported a promising LMWG for bone tissue engineering, consisting of a thermosensitive hydrogel based on a glycosyl-nucleosyl-fluorinated (GNF) compound, with a hydrophobic fluorinated carbon chain, a central thymidine group and a glucose moiety (Figure 1.29), that self-assembles into organised supramolecular structures at room temperature. This study revealed a slow degradation *in vitro* and *in vivo*, that is desired for bone tissue engineering, with the degradation of the hydrogel being replaced with newly formed tissue. Furthermore, the differentiation and growth of adipose tissue derived stem cells (ASC) was achieved when ASC aggregates were incorporated in the GNF-based hydrogels.

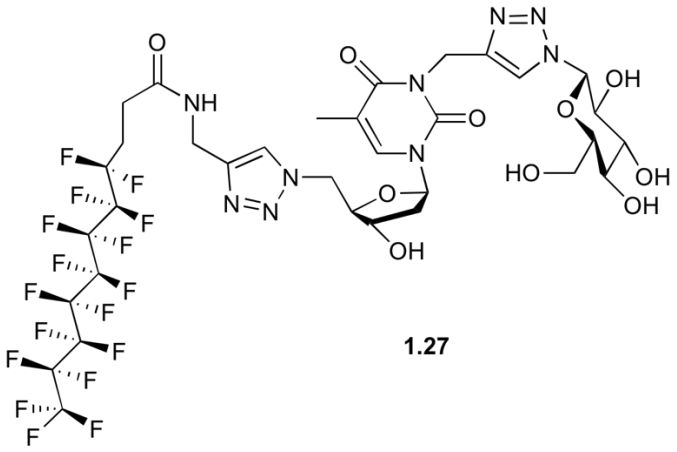

Figure 1.29. Chemical structure of glycosyl-nucleosyl-fluorinated hydrogelator 1.27.

In a different example, Bai et al.[154] introduced a self-reinforcing injectable hydrogel used for bone repair. To enhance the mechanical strength of the hydrogel without compromising its water content, the group developed a hydrogel based on noncovalent and Diels-Alder chemical dual crosslinking. The noncovalent crosslinking was obtained by the supramolecular interaction of β-cyclodextrin and adamantane, which allowed the hydrogel to be formed *in situ* after injection. The covalent crosslinking then occurred following the injection of chondroitin sulfate (ChS-F) and maleimide-terminated poly(ethylene glycol) (PEG-AMI) via Diels-Alder reaction to reinforce the network. The resulting hydrogel showed high mechanical strength (≈25 MPa) and high water content (98%). Additionally, the hydrogel induced bone repair without using cells or growth factors (GFs) indicating that the dual crosslinking hydrogel may be useful as an injectable skeleton to encourage bone repair.

These examples demonstrate how promising LMWGs can be as artificial 3D scaffolds, and provide the physical support and environment needed to promote cells growth and tissue regeneration.

Hydrogels for tissue engineering can also include adhesion sites and the incorporation of GFs.[134] GFs are soluble signalling polypeptides which induce cellular responses through their interactions with specific transmembrane receptors on target cells.[155] Due to their short biological half-lives and slow diffusion, GFs act differently to hormones and rather

than acting in an endocrine fashion they are sequestered in the ECM until required. ECM stabilises GFs, enabling precise temporal and spatial control over their actions. Cell degradation of the ECM releases the GFs allowing them to diffuse locally and induce a specific response in nearby cells (Figure 1.30).[156] The integral role played by GFs in directing cellular behaviour makes them a highly desirable tool for tissue engineering, and a vast amount of research has been conducted into a better understanding of how to use GFs to direct the growth and regeneration of various tissue types, such as nerve, cartilage, bone and blood vessels.[157,158]

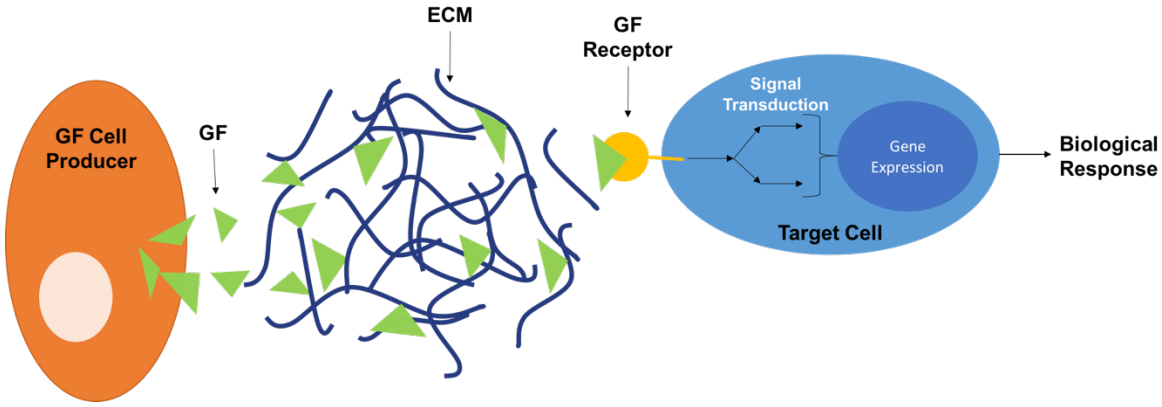

Figure 1.30. Schematic representation of interactions between GFs with the ECM and cells. The producer cell secretes GFs into the ECM, where they are bound, held and stabilised until required. Partial cell degradation of the ECM allows the local release of GFs, which bind to GF receptors on the surface of the cell, initiating the signalling which will be translated into a specific biological response. [Adapted from reference [156]]

GFs can be incorporated into hydrogels via two main methods: physical entrapment, where electrostatic forces or pore size prevents the GF from leaving the hydrogel; or chemical immobilisation, where the GF is typically covalently linked to the hydrogel network.[159] GF release from hydrogels can occur by diffusion[160–164] or external stimuli such as pH,[165,166] light[167] or enzymes.[168,169]

Once again many of these studies have been performed using polymer hydrogels. Nguyen et al.[170] developed a 3D synthetic hydrogel cell culture by testing different concentrations of poly(ethylene glycol) (PEG) including different concentrations of adhesion peptides, in

order to mimic the 3D extracellular environment that exists *in vivo* and incorporated vascular endothelial growth factor (VEGF) in the presence of human umbilical vein endothelial cells (HUVEC). Variations of the composition of the hydrogel surrounding the HUVECs influenced their viability and proliferation, and modulated the signalling of the VEGF. This proved that the combination of different parameters of hydrogel composition led to different cell behaviours due to the existence of different cell-matrix interactions.

In the field of supramolecular materials, Stupp and coworkers[171] investigated how different degrees of intermolecular hydrogen bonding from PA nanofibers affect GF signalling for osteogenesis. They developed two supramolecular PA assemblies formed by primary amino acid sequences with strong β-sheets and weak β-sheets. It was observed that weaker β-sheet hydrogen bonding promoted cell differentiation by enhancing bone morphogenic protein-2 (BMP-2) signalling. Differently, the presence of stronger hydrogen bonding in the supramolecular assemblies reduced BMP-2 signalling. They believed that the intercalation of weak, positively charged PA nanostructures into the cell membrane increases the lipid raft mobility, which results in the enhancement of cell signalling. Therefore, by simply altering the nature of the supramolecular PA hydrogen-bond interactions it was possible to potentiate cell signalling by GFs.

Hartgerink and coworkers[172] reported the orthogonal self-assembly of multidomain peptide nanofibers (MDP) and GFs encapsulated in liposomes, as a supramolecular hydrogel that can act as a delivery vehicle. Hydrogels were incorporated with placental growth factor-1 (PlGF-1), which plays a key role in the formation of blood vessels, and their potential as scaffolds for cellular infiltration and vascularisation was tested (Figure 1.31). The method of incorporation of PlGF-1 within the gel network resulted in different *in vivo* responses after being injected subcutaneously in rats. When PlGF-1 was incorporated directly in the hydrogel network it contributed to an early and fast release of the GFs which led to an immature signalling and low vessel development in the short term. On the other hand, when incorporated in the liposomes, PlGF-1 release was delayed up to 3 days, allowing high levels of cellular infiltration, followed by the formation of blood vessels when PlGF-1 is released. The study revealed that the orthogonal self-assembly of the MDP hydrogels with liposomes loaded with PlGF-1 contributed to a higher order structure, able

to drive controlled release and promote high vessel density while mimicking the ECM environment.

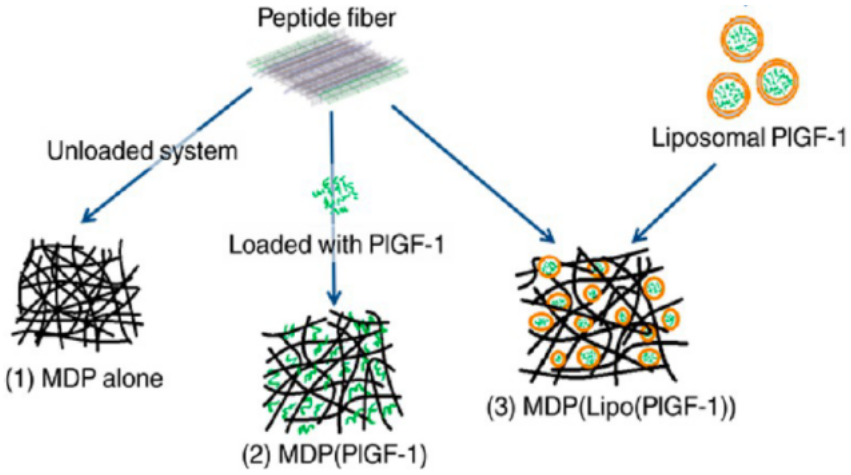

Figure 1.31. Schematic representation of 1) supramolecular MDP hydrogel and supramolecular orthogonal self-assembly of 2) MDP hydrogel incorporated with PlGF-1 and 3) MDP hydrogel loaded with liposomes encapsulating PlGF-1.[172]

1.6. Heparin and its Applications

The formation of new blood vessels is crucial in tissue engineering to avoid rejection and due to the need for nutrients and oxygen for the growth of tissue and cell survival.[173] Therefore different approaches have been investigated such as dispersing signalling molecules and/or GFs within 3D scaffolds as previously described or alternatively by using heparin as a delivery agent of GFs to promote neo-tissue formation.[174–178]

Heparin is a biological macromolecule with high negative charge density that belongs to the family of glycosaminoglycans (GAG) and has a molecular weight range between 2500 – 25000 Da. This polyanionic polysaccharide is polydisperse but is typically formed by repeated units of uronic acid and glucosamine residues and owes its high negative charge to the presence of sulfate and carboxylic acid groups in its structure (Figure 1.32). The understanding of heparin structure has allowed the development of low-molecular-weight heparins (LMWH) which consists of polysaccharides with molecular weights typically between 4000 – 6000 Da, contributing to better definition of its chemical and biological properties.[179–182]

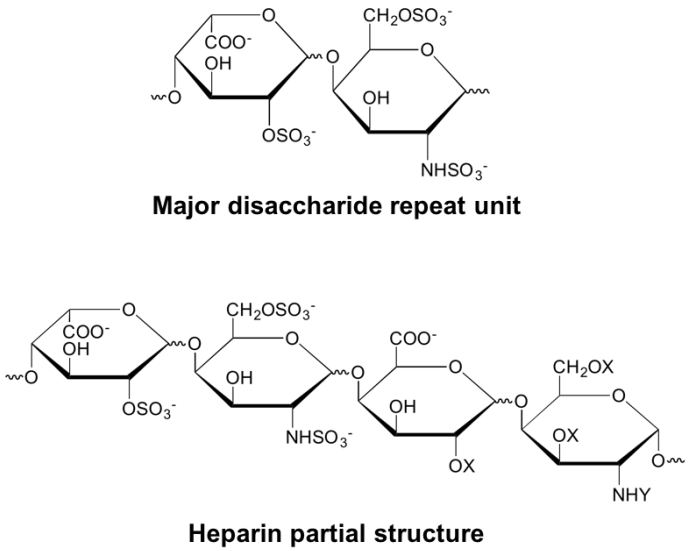

Figure 1.32. Heparin predominant disaccharide repeat unit (top) and heparin partial structure (X = H or SO_3^-; Y = Ac, SO_3^- or H) (bottom).

Heparin interacts with a vast number of proteins, such as proteases, GFs, chemokines, lipoproteins and adhesion proteins, at the cell surface and in the ECM. Being widely known for its anticoagulant effect,[183] heparin has also generated special attention due to its interactions with GFs which are known to form stable complexes that regulate the proliferation, migration and angiogenesis of cells.[184–188] Angiogenesis is related to the formation of new blood vessels from existing ones. Heparin is known to bind to several angiogenic growth factors such as fibroblast growth factor (FGF), VEGF and transforming growth factor beta (TGFβ). These growth factors are heparin-binding proteins in which the most obvious and common interaction between them is electrostatic, where positively charged amino acids from the protein growth factors will interact with the sulfate and carboxylate groups in heparin.[180,189] Figure 1.33 represents the 2:2:1 fibroblast growth factor receptor (FGFR)-FGF-heparin complex. To initiate signal transduction, the three compounds FGF, FGFR and heparin need to interact simultaneously. In this particular example, the complex assembles around a heparin chain that is bound to two FGF. The FGF-heparin complex then acts as a bridge between the two FGFR. Heparin plays an important role here due to the existence of very few protein-protein contacts.[180,189] Furthermore, heparin-binding epidermal growth factors (EGFs) mediate the earliest cellular

response to proliferate a rapid and efficient protection to tissue damage contributing to wound healing and regeneration.[176,190]

Figure 1.33. Structure of 2:2:1 FGF-FGFR-heparin complex. FGFR is represented as gold ribbons and FGF as green ribbons. Heparin is shown as space-filling models: sulfur (yellow), oxygen (red) and nitrogen (blue).[180]

Several studies have reported the use of heparin bound to growth factors in diverse systems, for controlled delivery into cell cultures and subsequent controlled release of the growth factors, to promote cell growth.[191–195] For instance, d'Angelo et *al.*[196] described the influence of heparin on VEGF stability and bioactivity, and its ability to modulate the interaction between growth factors and ECM. The fact that the heparin-binding domain is localised close to the VEGF receptor-binding, allows heparin to form a complex with VEGF, stabilizing it and extending its half-life. The stability of VEGF is shown to be crucial to effective angeogenic activity, promoting cell proliferation and growth. In addition, Johnson at *al.*[197] reported the importance of heparin-binding EGF in wound healing. The controlled release of heparin-EGF enhanced bioactivity and promoted human keratinocyte migration with wound closure within 17 days, while free growth factors showed no influence on the closure rate when compared to controls. Zhao et *al.*[191] developed a polyion complex in which a cationic polymer bound electrostatically to heparin in order to enable the controlled release of heparin into cell cultures in the presence of growth factors. It was found that the size of the cationic block copolymer and the heparin/polymer ratio influenced the biological activity of heparin as well as the cell uptake, demonstrating that the properties of the block copolymers can be tuned for different applications including GF

delivery and heparin-binding drug uptake into cells. Niu et al.[198] disclosed the use of a heparin-modified gelatin scaffold for transplantation of human corneal endothelial cells (HCECs) into the anterior chamber of the eye, as an alternative for cadaveric cornea transplantation. The work aimed to develop a transparent and flexible scaffold based on gelatin, due to its high cell compatibility and biodegradability *in vivo*, making it a suitable medium to seed the HCECs. In order to improve the binding of growth factors that supported HCEC growth, the scaffolds were functionalized with heparin. The presence of heparin provided a greater capacity of the scaffolds to absorb FGF and a better release kinetics, with the FGF being continuously released for up to 20 days, while for the non-modified scaffolds the release only lasted for 3 days. The presence of heparin in the studied gelatin scaffold contributed to improved HCECs survival, viability, and growth and reduced cellular loss. Additionally, the use of heparin to immobilize VEGF into fibroblast-derived extracellular matrix (FDM) as a novel platform for angiogenic growth factor delivery has been reported.[199] VEGF bound effectively to heparin-modified FDM in 2D and 3D environments and was released in a sustained manner. The bioactivity of VEGF was retained by heparin which also contributed to the immobilization of VEGF in the FDM resulting in an increased migration of the human umbilical vein endothelial cells toward the FDM. Furthermore, VEGF delivery with this system was more competitive in promoting neovascularization when compared to other groups. The presence of heparin in the FDM contributed to the development of an efficient delivery system of angiogenic GFs.

Other approaches have been exploited in which heparin is incorporated into hydrogels in order to create a biocompatible 3D scaffold that mimics the ECM and carries the heparin, which in turn binds to cell growth factors for controlled release, leading to the perfect environment and conditions for cell adhesion and proliferation with the formation of blood vessels that are crucial for the cell survival and to avoid rejection.[200–204] Figure 1.34[200] shows a schematic representation of a PEG-heparin hydrogel with the immobilization of TGF-β to promote wound healing. The design was thought to be a way of obtaining cell responsiveness and adhesion independent of the gel network features, through incorporation of cleavable linkers and peptides; with the degradability of the hydrogel contributing to the effective administration of GFs. On the other hand, the strong interactions between the negatively charged heparin and the basic amino acids of TGF-β

allowed the stabilization, protection and retention of the GFs in the hydrogel for subsequent controlled release.

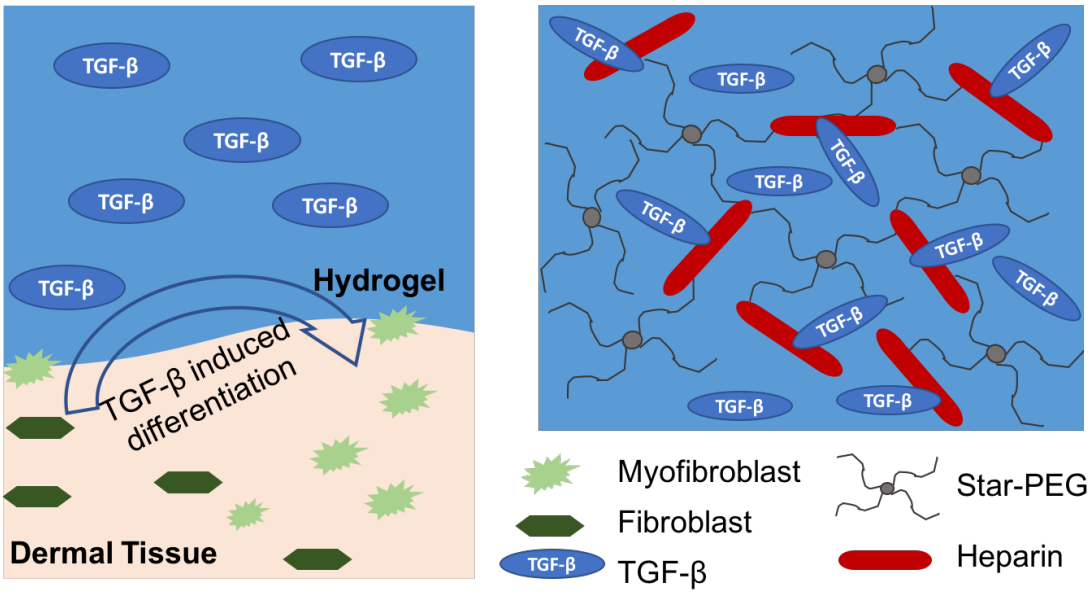

Figure 1.34. Schematic representation of PEG-heparin hydrogel. Left: TGF-β are immobilised within the hydrogel scaffold and released over time to induce cell differentiation. Right: Network structure of PEG-heparin hydrogel. Electrostatic interactions between heparin and TGF-β allows the protection and controlled release of TGF-β. [Adapted from reference [200]]

In supramolecular materials, Stupp et al.[195,205] described the use of heparin to nucleate the self-assembly of a PA into 1D nanofibers and trigger gel formation. Through electrostatic interactions heparin is adsorbed into the large surface area of the nanofibers and is available to interact with angiogenic GFs and GF receptors (Figure 1.35). The self-assembled system forms a rigid scaffold allowing local retention of GFs, their protection from enzymatic activity and orientation of the GF domains for an adequate binding with heparin.

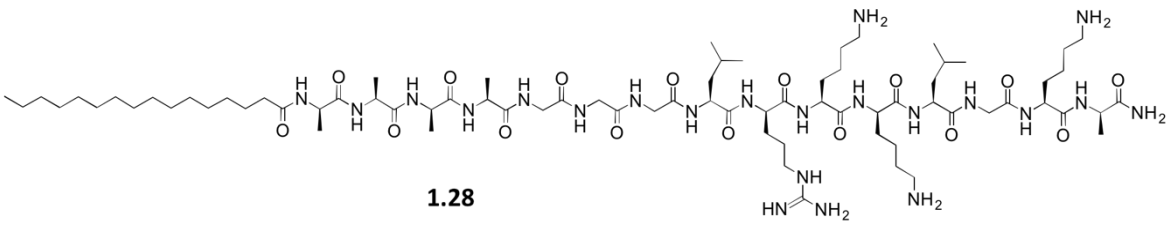

1.28

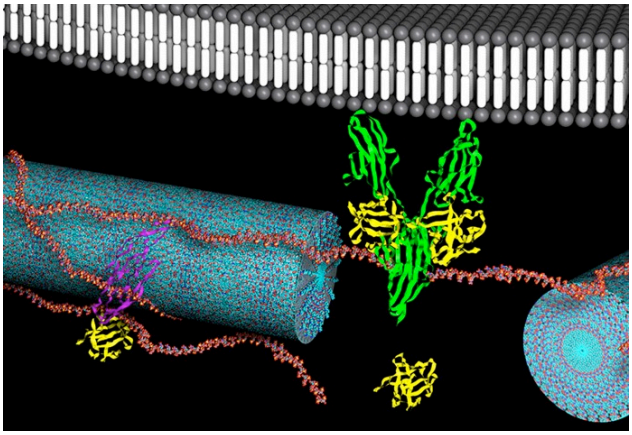

Figure 1.35. Molecular structure of the PA 1.28 designed to bind heparin chains by the Stupp research group (top). Schematic representation of nanofibers (blue) with adsorbed heparin (red) which is binding to growth factors (VEGF (purple); FGF (yellow) and FGF receptors (green)) (bottom).[195]

Although these systems revealed successful results and efficiency in the promotion of cell growth and angiogenesis, the incorporation of heparin into hydrogels could lead to an initial burst release of heparin, being difficult to control in a constant way. In this sense, the incorporation of a heparin/ heparin binding molecule complex into a biocompatible and biodegradable hydrogel may overcome these issues. Our group has developed some heparin ligands for purposes related to the anticoagulation properties of heparin, which have been revealed to be very efficient. These ligands are amphiphilic systems that self-assemble into micelles, having a cationic hydrophilic head which efficiently binds to heparin through multivalent electrostatic interactions.[206,207]

1.6.1. Multivalency

Multivalency is often used in biological and chemical systems to achieve high affinity binding and is related with the simultaneous interaction of multiple binding groups on one

molecule with the complementary receptors on another. Therefore, multivalent interactions (Figure 1.36 - b) can be stronger than corresponding monovalent interactions (Figure 1.36 - a) and while rigid multivalent systems form highly organised structures with lower binding entropic cost, flexible multivalent systems can benefit from the possibility of optimisation of individual interactions and screening from the surrounding competitive medium.[208]

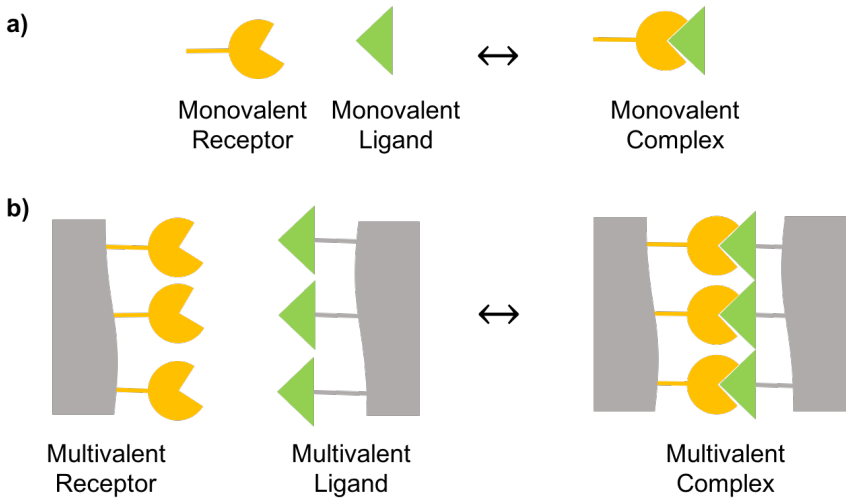

Figure 1.36. Schematic representation of a) monovalent interactions and b) multivalent interactions. [Adapted from reference [208]]

In order to quantify the degree of cooperativity of a multivalent interaction, Whitesides et al compared the binding of a multivalent ligand with equivalent monovalent counterparts and calculated the 'enhancement factor', α (Equation 1.1). A successful multivalent system should have an overall binding constant for a multivalent interaction (K^{multi}) superior to the binding constant of the monovalent system (K^{mono}), indicating that the individual interactions of the multivalent system bind collectively to the receptor in a more effective manner than multiple copies of a monovalent ligand. This equation allows to define three types of multivalent interactions: positively cooperative, if $\alpha > 1$ (where the second binding is more favourable than the first); non-cooperative, if $\alpha = 1$ (where the second binding has the same affinity as the first); and negatively cooperative, if $\alpha < 1$ (where the second binding to the receptor is inhibited by the first ligand). Despite truly positively cooperative

multivalent interactions being rare, for a successful multivalent system, it is only required to have a higher affinity for the receptor than the monovalent counterpart.[208–210]

$$\alpha = \frac{K^{multi}}{K^{mono}}$$

Equation 1.1. Calculation of the binding enhancement factor α to obtain the degree of cooperativity of multivalent systems.

1.6.2. Self-Assembling Multivalency (SAMul)

It is perhaps not surprising that numerous examples of supramolecular systems with biological functions have arisen making use of self-assembly to organise molecules to generate multivalent recognition, this is, through self-assembling multivalency (SAMul).[211,212] Typically, synthetic SAMul systems are achieved by using amphiphilic molecules able to self-assemble in aqueous solutions. These building blocks present a number of advantages over covalent structures as they are usually simple to synthesise, the design of the individual binding ligands can be tuned for different receptors and by changing the hydrophobic tail, different aggregate morphologies can be obtained. Another fundamental advantage is the reversibility of the SAMul systems that can lead to multivalent binding being switched off by triggering disassembly, which can reduce the toxicity of bioactive SAMul nanostructures and improve specificity. As an example, Smith and co-workers compared the binding affinity of different amphiphilic molecules containing a hydrophilic arginine-glycine-aspartic acid (RGD) ligand group. RGD tripeptides were chosen to provide the system with integrin[ii] binding ability and a comparison was performed between a large covalent RGD multivalent binder, the equivalent self-assembled monomer and an analogous non-assembled monomer (Figure 1.37). It was concluded that the self-assembling system demonstrated similar integrin binding to the covalent RGD dendrimer, revealing higher affinity than the non-assembling monomer, due to the multivalency of the binding.[213] Other SAMul systems have been developed by Smith's research group for DNA[214] and heparin binding.[207]

[ii] *Integrins* are transmembrane proteins which play an important role in cell signalling and adhesion.

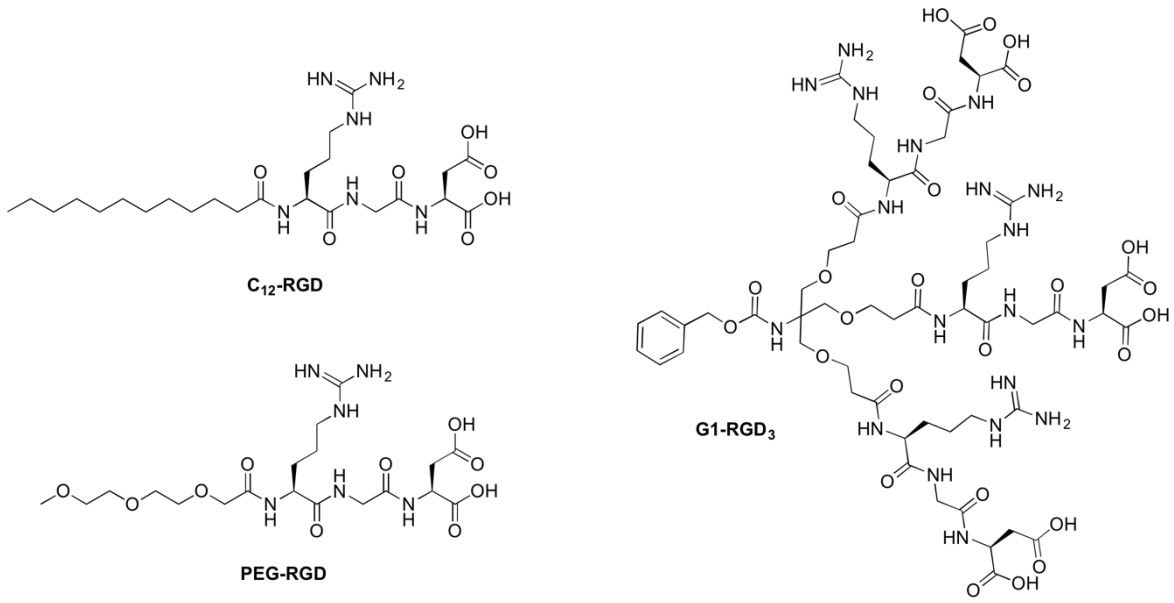

Figure 1.37. Molecular structures of self-assembling multivalent C12-RGD, non-assembling dendritic G1-RGD_3 and non-assembling PEG-RGD monomer, from Smith and coworkers work.

1.7. Project Aims

Despite the importance of developing structures as similar as possible to the complex and natural systems used to successfully form tissue, advances in tissue engineering did not yet allow a full understanding and development of orthogonal self-assembled biocompatible architectures (specially using LMWGs as 3D scaffolds) that mimic the complexity of natural structures and allow the effective proliferation and growth of cells.

The aim of this project was to study the orthogonal self-assembly of multi-component hybrid materials using LMWGs as 3D scaffolds, which incorporate bioactive heparin (Figure 1.38), gain a detailed understanding of their activity, and explore their potential high-tech applications. Understanding these multi-component materials assembled from the bottom-up is highly challenging and will require the development of innovative characterisation techniques to probe the extent of orthogonal self-sorting. It is proposed that this family of gels may be useful for tissue engineering given the key role of heparin in angiogenesis, and that the breakdown of the nanospheres within the gel matrix may allow release of the bound heparin in a triggered manner. This may allow the gel to release

heparin in response to changes induced by cellular proliferation, endowing these soft materials with the possibility to be smart matrices for multi-step cell growth, which may encourage controlled differentiation of stem cells.

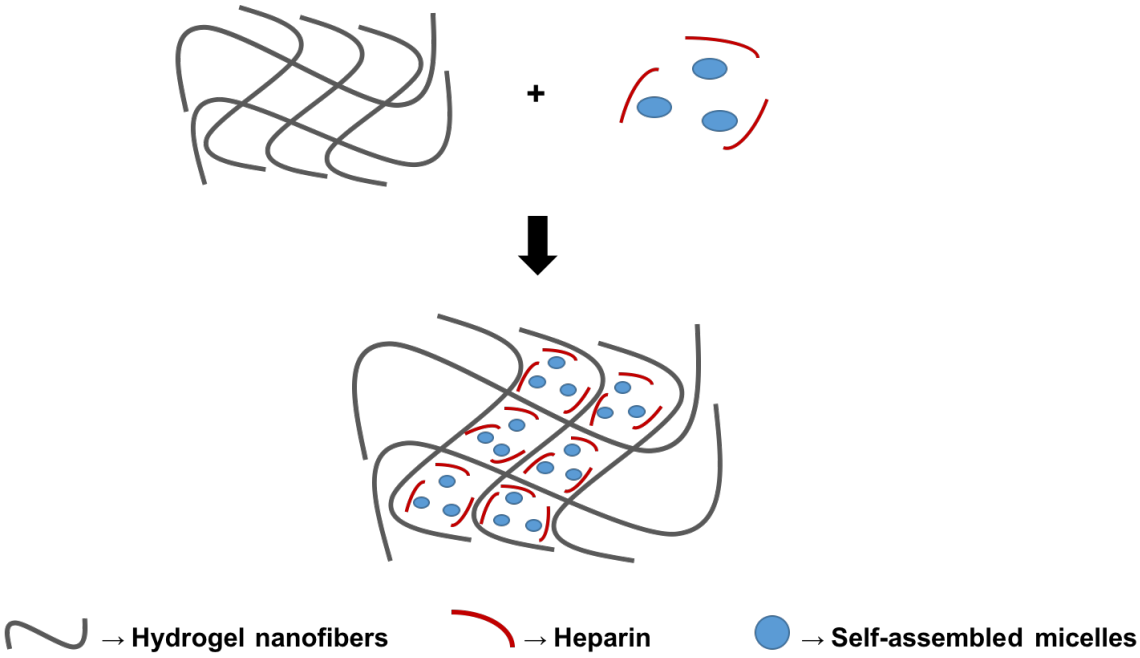

Figure 1.38. Representation of the orthogonal self-assembled bioactive hydrogel.

2. DAPMA-based Self-Assembling Multivalent Ligands for Heparin Binding

Results from this chapter have been published in *J. Mater. Chem. B*, 2017, **5**, 341-347.

2.1. Introduction

The development of amphiphilic molecules that self-assemble into micelles in aqueous media has been widely exploited as suitable SAMul systems to bind to biomolecules such as integrins[213] and DNA.[215,216] These building blocks have a general structure that contains a hydrophobic unit that will be directed towards the interior of the nanostructure and a hydrophilic ligand unit that will be displayed at the surface towards the solvent. Given the efficiency of these SAMul structures in interacting with biomolecules it became of great interest to explore them as mimics of the large covalent structures which are known to bind to heparin, such as protamine and dendrimers.[206,217,218]

A good example of a self-assembling system with high affinity to bind to heparin was developed by Smith's group with a design inspired by the Fréchet dendron scaffold.[219] The ligand is shown in Figure 2.1 and contains peripheral amines that protonate at physiological pH and hence can interact electrostatically with polyanionic heparin. It also has a degradable ester linkage and a hydrophobic unit that drives the self-assembly in aqueous media due to the hydrophobic effect. This molecular building block self-assembles into a positively charged spherical micelle nanostructure and is capable of efficient multivalent heparin binding. This SAMul system can therefore be introduced as an alternative to covalent proteins, such as protamine and macromolecules such as dendrimers, with equal or improved affinity to bind to heparin.[207]

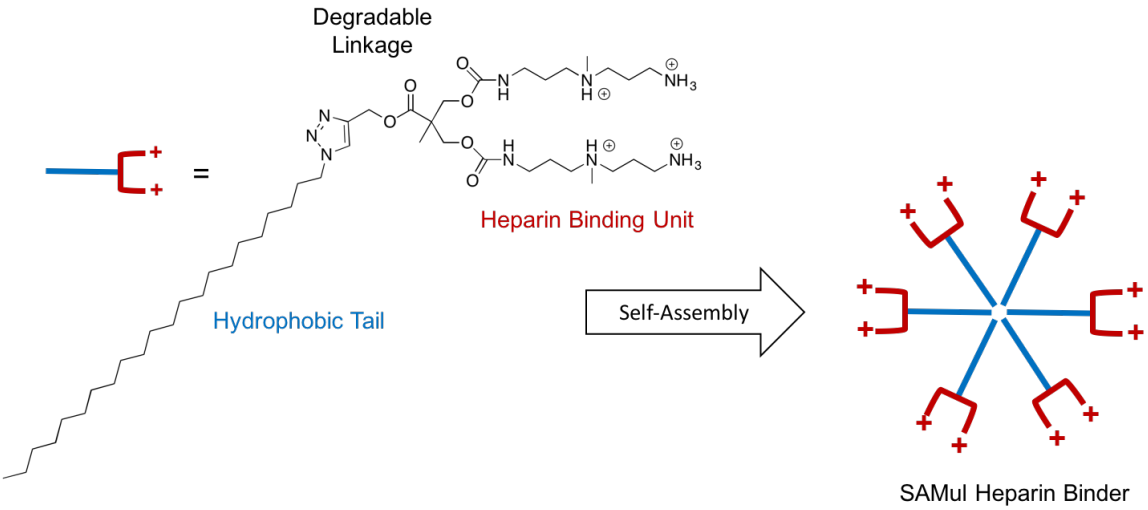

Figure 2.1. Structure of the self-assembling heparin binder C_{22}G1DAPMA and schematic representation its self-assembly.[207]

Considering the clinical importance of heparin binding,[220] and with the goal of incorporating such structures in controlled release gels, we were interested in better understanding the potential of this type of SAMul nanostructure. To this purpose, this chapter will focus on the study of simple cationic SAMul heparin binders in order to achieve a detailed characterisation in terms of structure, hydrophobic region influence in self-assembly and heparin binding and hierarchical assembly processes. In particular, we aimed to go beyond our previous research by synthesising simple binders, which can be easily made at scale and incorporated into gels. Ultimately, the most efficient system will be selected as heparin binder to proceed with further investigations of orthogonal self-assembled soft materials.

2.2. Synthesis of Amphiphilic Heparin Binders

Three amphiphilic heparin binders were synthesised with a polar head group constituted by amine groups and an apolar tail constituted by saturated fatty acids. The fatty acids used were myristic acid with 14 carbon atoms, palmitic acid with a 16 carbon atoms and stearic acid with 18 carbon atoms.

In the first step, and in order to have selective coupling of only one amine group from *N*,*N*-di-(3-aminopropyl)-*N*-methylamine (DAPMA) and the carboxylic group of the fatty acids, *tert*-butyl dicarbonate (Boc) was used as protecting group (Scheme 2.1). Mono- protection was achieved by using an excess of DAPMA and purification was achieved by simple washing protocols.

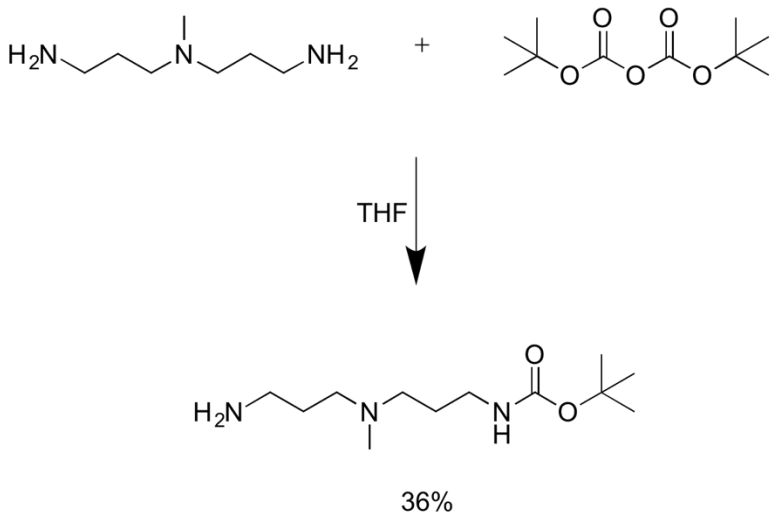

Scheme 2.1. Boc protection of N,N-di-(3-aminopropyl)-N-methylamine.

The coupling between tert-butyl 3-((3-aminopropyl)(methyl)amino)propyl carbamate (protected DAPMA) and the fatty acids was performed using a highly efficient coupling agent 2-[(1H-Benzotriazole-1-yl)-1,1,3,3- tetramethyluroniumtetrafluoroborate] (TBTU). TBTU is an uronium salt frequently used as coupling agent in peptide chemistry, being stable and soluble in the most common organic solvents and water and producing easily-removed by-products with low toxicity.[221] TBTU coupling was performed for the three fatty acids, followed by acid-mediated Boc group removal (Scheme 2.2), achieved by bubbling HCl gas through a methanolic solution. This yielded the desired products as their hydrochloride salts.

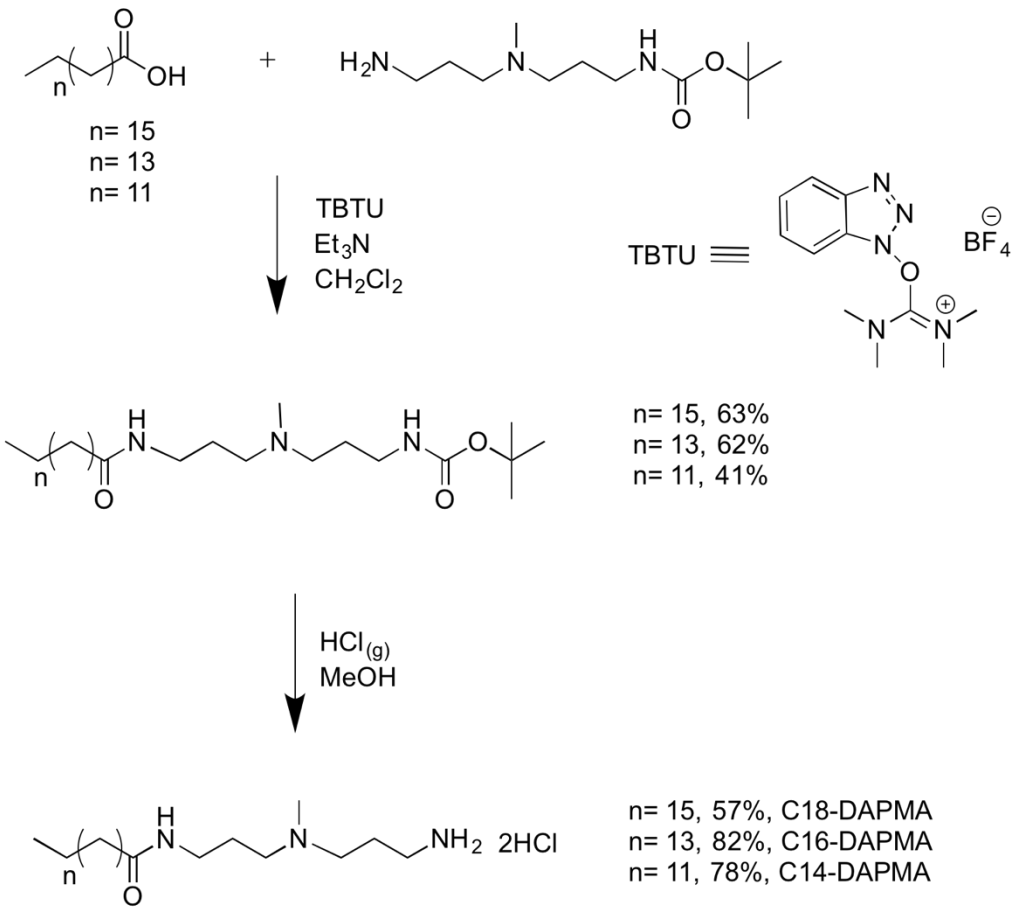

Scheme 2.2. TBTU coupling of DAPMA with saturated fatty acids followed by Boc group removal.

From here, the coupled molecule with myristic acid as apolar chain will be referred as C14-DAPMA, the coupled molecule with palmitic acid will be referred to as C16-DAPMA and the coupled molecule with stearic acid will be referred as C18-DAPMA. These molecules were synthesised in very good overall yields and had characterisation data fully in agreement with their structures (see Experimental Section).

2.3. Nile Red Assay

Nile Red was used to determine the critical micelle concentration (CMC) of the synthesised amphiphilic molecules. Nile Red is a hydrophobic dye highly dependent on the environmental conditions. Its excitation and emission maxima can vary by ca. 60 nm, depending on the hydrophobicity of the solvent, whereas no emission is detected when

the solvent is water due to its poor solubility.[222] This makes it possible to use Nile Red as a fluorescent hydrophobic probe to identify the aggregation of amphiphilic molecules. In micelles or other amphiphilic aggregates in the presence of water, Nile Red tends to interact with the hydrophobic domains of the self-assembled structures, and is hence able to emit intense fluorescence. If no aggregation occurs, no emission is detected, making it possible to determine the CMC of the amphiphile.[223] This approach was used to obtain the CMC values of the synthesised amphiphiles by measuring the fluorescence of solutions with constant concentration of Nile Red and different concentrations of binder in 10 mM of phosphate buffered saline (PBS, pH 7.4).

The CMC values were obtained from the graphs in Figure 2.2-2.4, for C14-DAPMA, C16-DAPMA and C18-DAPMA, respectively. To determine these values, the points were separated into two groups, each of which were fitted linearly. These were associated with non-aggregating and aggregating Nile Red, and the intercept between the two linear fits was considered to represent the CMC.

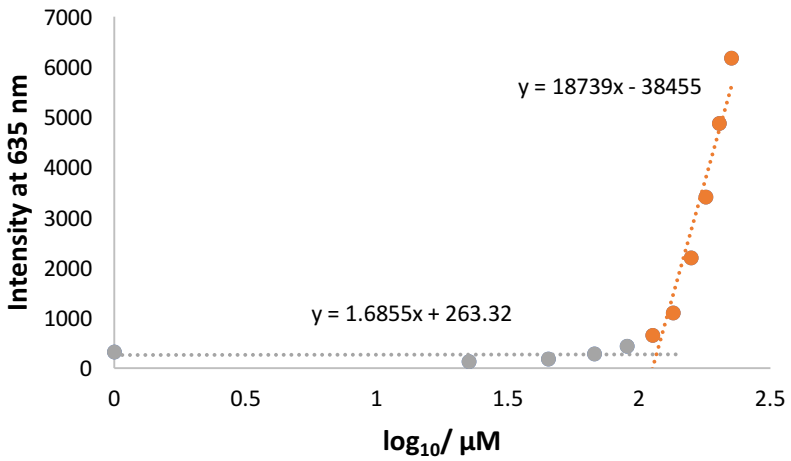

Figure 2.2. Fluorescence intensity of Nile Red (2.5 mM in PBS, pH 7.4) at 635 nm with increasing concentration of C14-DAPMA.

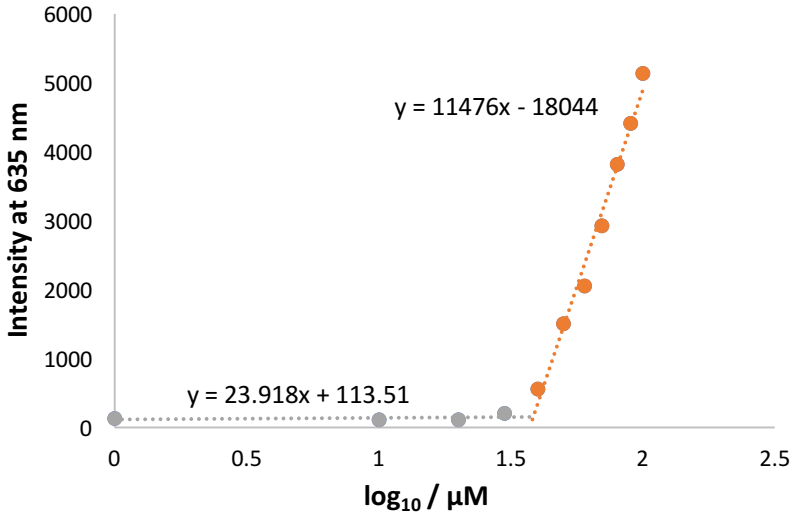

Figure 2.3. Fluorescence intensity of Nile Red (2.5 mM in PBS, pH 7.4) at 635 nm with increasing concentration of C16-DAPMA.

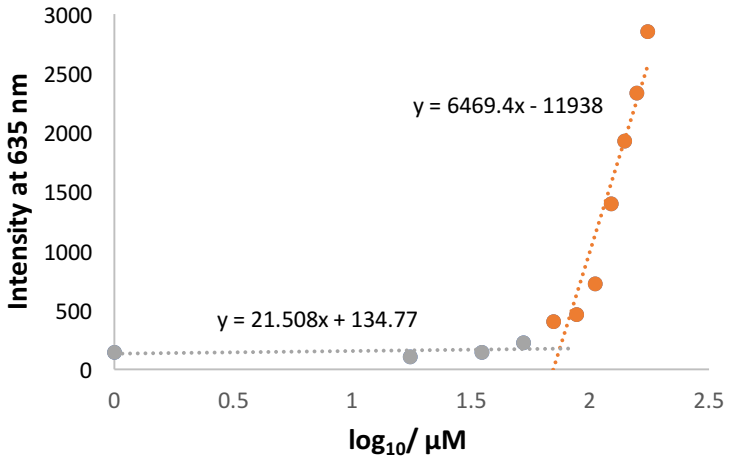

Figure 2.4. Fluorescence intensity of Nile Red (2.5 mM in PBS, pH 7.4) at 635 nm with increasing concentration of C18-DAPMA.

The calculated CMC values are shown in Table 2.1. As expected, C14-DAPMA has the highest CMC value because it has the smallest hydrophobic chain and therefore the lowest driving force for self-assembly. The CMC of C16-DAPMA was significantly lower as the longer chain assists self-assembly. Perhaps surprisingly, however, the CMC value for C18-

DAPMA was higher than for C16-DAPMA. We suggest this is a result of the relatively low solubility of C18-DAPMA in PBS buffer caused by the larger hydrophobic block – we have noted for related compounds that the balance between hydrophobic and hydrophilic block size is important in controlling solubility,[218] as is indeed well-known in surfactant chemistry.[224] As such, C16-DAPMA appears optimised in this family in terms of its ability to self-assemble.

Table 2.1.CMC values of C14-DAPMA, C16-DAPMA and C18-DAPMA.

Binder	CMC (μM)
C14-DAPMA	116.5 ± 1.4
C16-DAPMA	38.5 ± 0.4
C18-DAPMA	73.0 ± 5.9

2.4. Mallard Blue Assay

Mallard Blue (MalB) assays were then performed in order to test the heparin binding effectiveness of each system. Mallard Blue is a cationic dye developed by the Smith group which has high affinity for heparin.[225] The success of MalB in detecting heparin led to development of a dye displacement competition assay to probe the efficiency of synthetic molecules to bind heparin.[225,226] When free in solution, MalB presents a characteristic UV-Vis band with a maximum absorbance at 615 nm. When interacting with heparin, this UV-Vis band decreases substantially in intensity. Therefore, if MalB is being displaced from its complex with heparin by the interaction of heparin with another molecule, this can be easily verified by an increase in the MalB absorbance. An assay is then performed by increasing the concentration of binder and monitoring MalB by UV-Vis.

Figures 2.5, 2.6 and 2.7 confirm the gradual displacement of MalB with the increasing concentration of C14-DAPMA, C16-DAPMA and C18-DAPMA, respectively, proving the efficiency of the binders towards heparin.

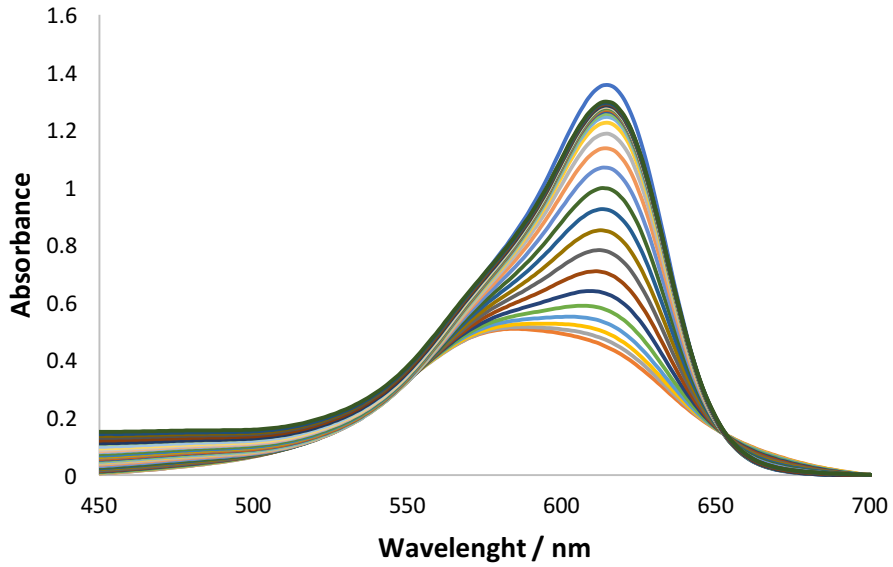

Figure 2.5. Uv-vis spectra of C14-DAPMA replacing MalB.

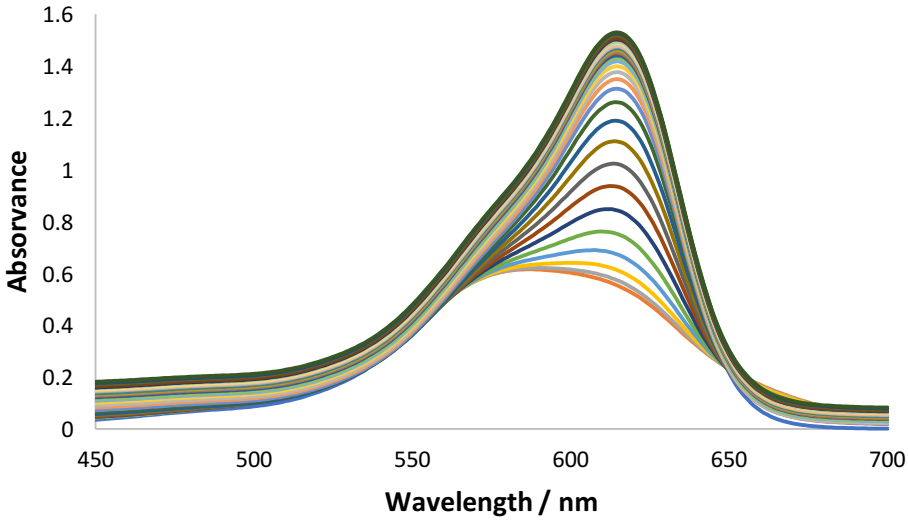

Figure 2.6. Uv-vis spectra of C16-DAPMA replacing MalB.

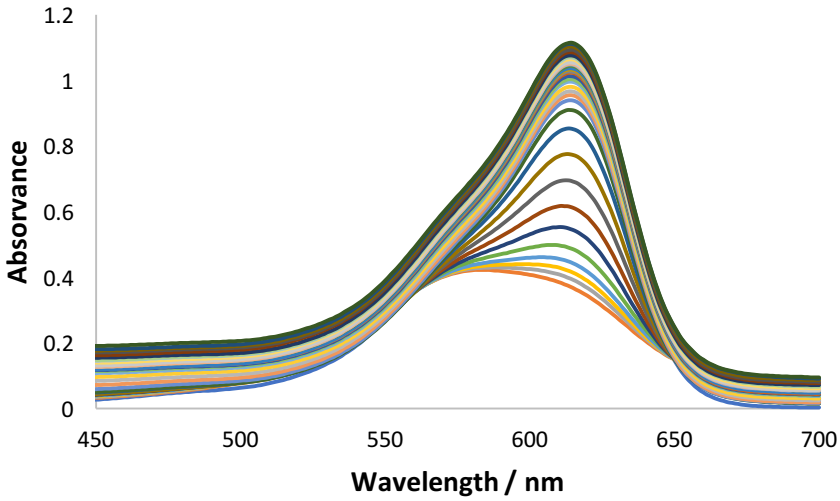

Figure 2.7. Uv-vis spectra of C18-DAPMA replacing MalB.

The charge ratio was then calculated after each addition of C14-DAPMA, C16-DAPMA or C18-DAPMA, and plotted against the normalized absorbance at 615 nm as shown in Figure 2.8 – 2.10.

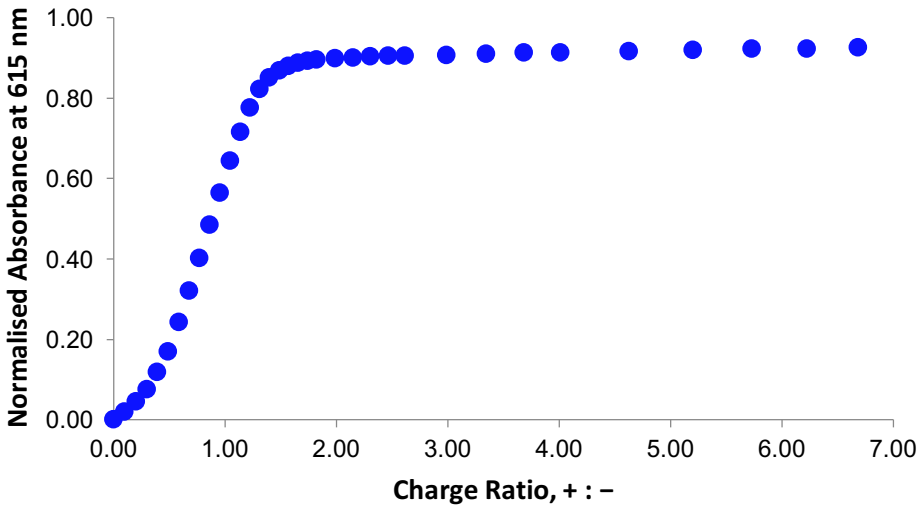

Figure 2.8. Charge ratio versus normalised absorbance at 615 nm from the MalB displacement assay for C14-DAPMA.

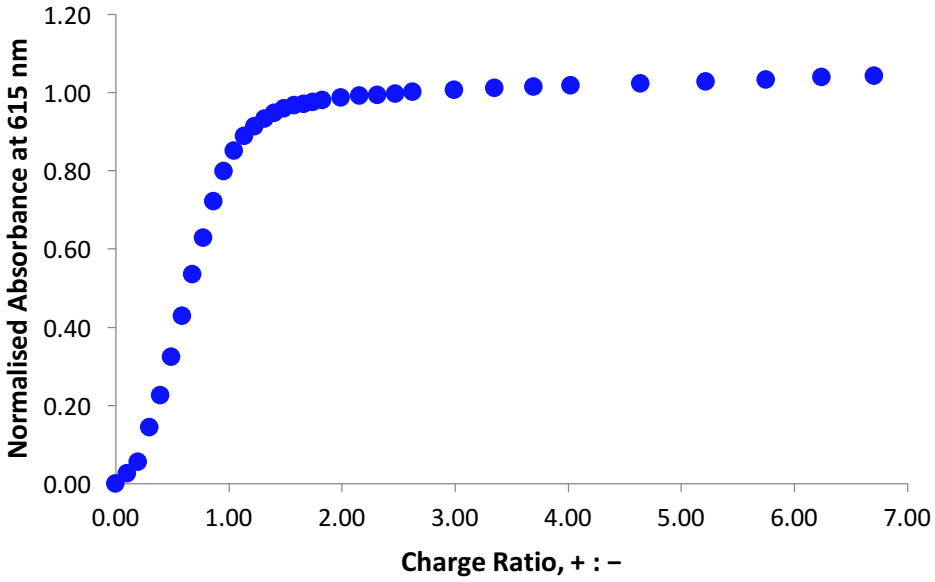

Figure 2.9. Charge ratio versus normalised absorbance at 615 nm from the MalB displacement assay for C16-DAPMA.

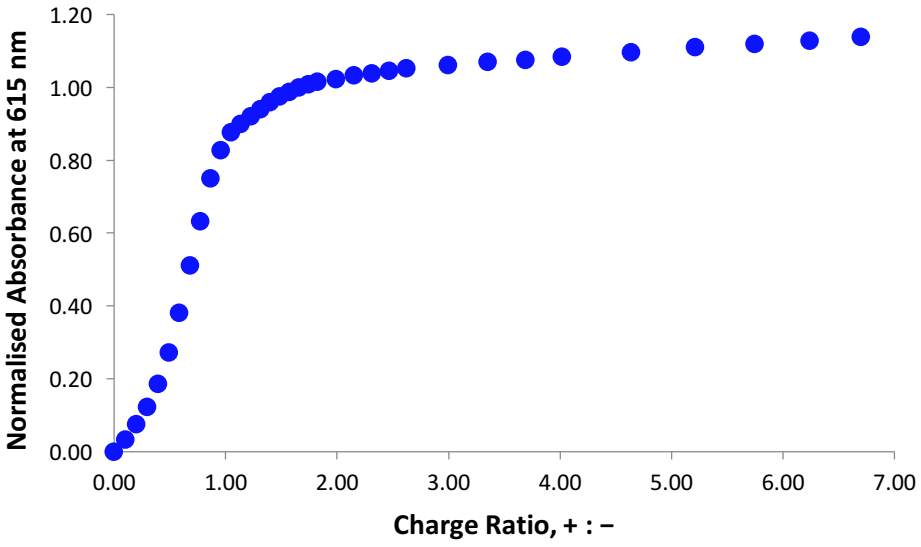

Figure 2.10. Charge ratio versus normalised absorbance at 615 nm from the MalB displacement assay for C18-DAPMA.

Therefore, this assay enables the calculation of the charge excess (CE_{50}) that corresponds to the number of positive charges needed per heparin negative charge to obtain 50%

displacement of MalB, the effective concentration (EC_{50}) that is the concentration of binder needed to displace 50% of MalB and the dose, which clinically relevant quantity is the mass of binder required to bind 100 IU of heparin.

All three binders bind heparin and displace MalB at micromolar concentrations, indicative of highly effective SAMul binding (Table 2.2). Among the three binders C16-DAPMA had the highest efficiency in terms of MalB displacement and hence heparin binding. This would suggest that in the same way that self-assembly was optimised for this molecular structure as a result of it possessing the optimal hydrophobic/hydrophilic balance, these self-assembly properties are translated into its heparin binding capability. Nonetheless, all three compounds were effective heparin binders and furthermore, differences between them in this assay were relatively small. It should be noted that heparin binding occurs at concentrations below the CMC – this is not surprising as it is well-known that the presence of polyanions can encourage the self-assembly of oppositely-charged polycations, and lower the effective CMC.[227,228] Furthermore, this provides a mechanism by which optimised self-assembly, as observed for C16-DAPMA, can be matched with heparin binding, as these two processes act to reinforce one another.

Table 2.2. CE_{50}, EC_{50} and dose values obtained for C14-DAPMA, C16-DAPMA and C18-DAPMA using MalB assay (25 μM MalB, 27 μM Heparin in 10 mM Tris-HCl, 150 mM NaCl, pH 7.0).

Sample	CE_{50}	EC_{50} / μM	Dose / mg 100 IU^{-1}
C14-DAPMA	0.88 ± 0.05	48 ± 3	0.59 ± 0.03
C16-DAPMA	0.64 ± 0.02	34 ± 1	0.46 ± 0.01
C18-DAPMA	0.68 ± 0.09	37 ± 5	0.52 ± 0.07

2.5. Dynamic Light Scattering (DLS) and Zeta Potential

The size and surface charges of the three binders in the presence and absence of heparin in 10 mM Tris-HCl/ 150 mM NaCl buffer were then characterised using DLS and zeta potential measurements.

DLS is a technique that measures the time-dependent fluctuations in the intensity of scattered light that occur because particles undergo Brownian motion.[229] The analysis of these intensity fluctuations can determine the diffusion coefficients, which can be converted into a size distribution using the Stokes-Einstein equation:

$$R_H = \frac{KT}{6\pi\eta D}$$

where R_H is the hydrodynamic radius, D the diffusion coefficient, K is the Boltzmann's constant, T is the temperature and η is the viscosity.[229,230] This approach makes the assumption that the species under investigation are spherical in morphology.

The size distribution obtained from a DLS measurement is based on intensity distribution, which relates with the intensity of light scattered. However, intensity distribution can be misleading, as larger particles scatter significantly more light than smaller particles, and can incorrectly indicate a higher contribution of larger species and that they will be present as the majority in solution. For example, Figure 2.11 shows the size distribution by intensity obtained for C16-DAPMA, where it is clear the presence of two different size particle species. The larger particle size appears to dominate the distribution. However, this may not correspond to the most realistic view, as mentioned above larger particles scatter more light. In this case, intensity size distribution can be converted to volume distribution (based on the mass or volume of the particles instead of scattered light) to have a better understanding of the contribution of the larger aggregates. Figure 2.12 shows the size distribution by volume for C16-DAPMA, with the presence of only one size particle species. The larger species in solution observed in the intensity distribution completely disappear when converted to volume distribution. This proves that the larger species observed are present in insignificant amounts and that the smaller species are dominant in solution. As such, larger aggregates are often not observed in the volume distribution and all peaks are shifted to smaller diameters as the larger components have their larger contributions re-weighted. We therefore use volume distribution to characterise and report the size of the dominant species in solution. The results are shown in Table 2.3.

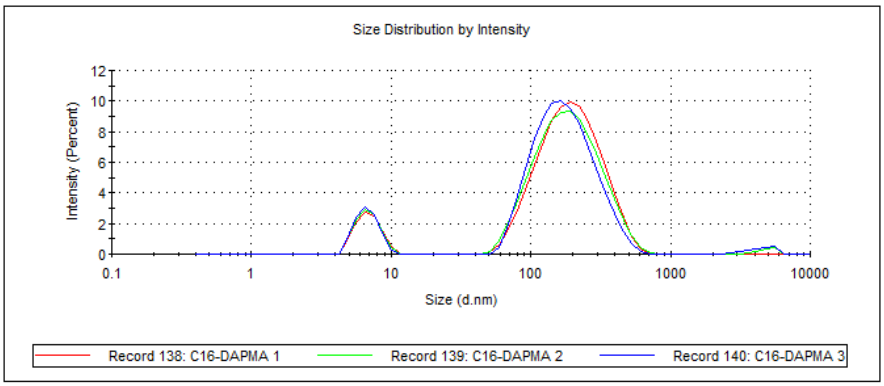

Figure 2.11. Size distribution by intensity from DLS of C16-DAPMA in 10 mM Tris-HCl/ 150 mM NaCl buffer.

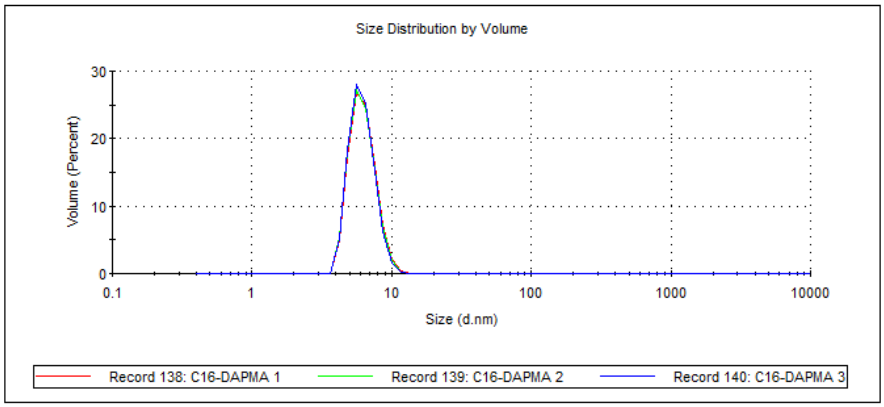

Figure 2.12. Size distribution by volume from DLS of C16-DAPMA in 10 mM Tris-HCl/ 150 mM NaCl buffer.

C14-DAPMA and C16-DAPMA assembled into micelles with diameters of ca. 5.8 nm and 6.2 nm respectively. The aggregates formed by C16-DAPMA were slightly bigger than those formed by C14-DAPMA, as would be expected, due to the difference in length of the hydrocarbon chain. C16-DAPMA has 2 additional carbon-carbon bonds which results in 4 additional bonds when the micelles are formed. This means that it should be approximately 6 Å, 0.6 nm, bigger than C14-DAPMA. Taking into account experimental error it is possible to confirm that this is the size difference observed. On the other hand, C18-DAPMA revealed the presence of significantly large aggregates (ca. 100 nm). As the self-assembled micelles were expected to have smaller sizes and C18-DAPMA has poor solubility, it is possible that the large population corresponds to relatively uncontrolled aggregation

associated with poor solubility, as DLS is carried out at relatively high concentrations, which can encourage aggregation into larger structures.

Additionally, high zeta potentials were obtained for each of the three binders, indicating the existence of highly-charged cationic nanoscale surfaces as a result of protonation of DAPMA at physiological pH values. The zeta potential becomes larger as the hydrophobic block becomes bigger, presumably because there is a greater driving force for the assembly of positively charged molecular building blocks into close proximity, enabling the formation of micelles with higher surface charge density. Furthermore, the larger size of nanostructures formed by C18-DAPMA may incorporate a greater total charge and support a greater charge density.

Table 2.3. Average hydrodynamic diameter (volume distribution) and zeta potential of C14-DAPMA, C16-DAPMA and C18-DAPMA in the presence and absence of heparin.

Sample	Z-Average (nm)	ζ Potential (mV)
C14-DAPMA	5.8 ± 1.6	41.3 ± 1.6
C16-DAPMA	6.2 ± 1.3	51.7 ± 2.2
C18-DAPMA	93 ± 26	54.1 ± 4.2
C14-DAPMA+Heparin	1321 ± 249	-8.0 ± 0.5
C16-DAPMA+Heparin	1185 ± 151	26.6 ± 0.8
C18-DAPMA+Heparin	480 ± 59	4.8 ± 0.7

When the binders were in the presence of heparin a significant increase of the size distribution was observed (at 2:1 binder:heparin charge ratio). The presence of a very broad and large population when the binders are in the presence of heparin suggests the formation of agglomerates between them, providing evidence of the existence of hierarchical interactions between the binders and heparin (see TEM images in the following section). Additionally, it is noticeable that when heparin is interacting with C18-DAPMA smaller aggregates were formed when compared with C14-DAPMA and C16-DAPMA, which

may correspond to decreased levels of hierarchical aggregation of the C18-DAPMA micelles (in fact this will later be confirmed by TEM images). However, it should be stated that the aggregate dimensions are not particularly accurate, as clearly the hierarchical aggregates are not spherical (see TEM images in the following section) and, as mentioned above, this approach makes the assumption that the species under investigation are spherical in morphology.

Furthermore, on binding to heparin, the zeta potential decreased, as a result of charge neutralisation induced by heparin binding – the charge neutralisation was greatest for the least effective binder C14-DAPMA, while the most effective binder C16-DAPMA, showed the lowest extent of charge neutralisation – in line with the view that C16-DAPMA is actually very efficient in using its positive charge to bind to the fixed amount of heparin present. DLS therefore suggests a degree of nanoscale aggregation between the polycationic self-assembled micelles and heparin polyanions. The evolution of hierarchical structures in micelle- polyelectrolyte systems is a known phenomenon, but has not previously been explored in detail for heparin binding.[231,232]

2.6. Transmission Electron Microscopy (TEM)

To further characterise the morphologies of the nanostructures, and the impact of heparin binding on them, TEM images were obtained for the three binders before and after binding to heparin.

TEM images of C14-DAPMA (Figure 2.13, left) and C16-DAPMA (Figure 2.14, left) showed the presence of spherical self-assembled nanostructures, in agreement with DLS. When in the presence of heparin it was possible to verify a different behaviour, with the formation of highly-organised semi-crystalline nanostructured arrays (Figure 2.13 and 2.14, right). It was believed that a hierarchical nanoscale self-assembly process is taking place between the spherical cationic micelles, and the 'linear' heparin polyanions (see below). These TEM observations clearly suggest that the self-assembled micelles formed by C14-DAPMA and C16-DAPMA have excellent stability, and appear to remain intact without disruption or

reorganisation, even in the presence of heparin, with which they can form very strong electrostatic interactions, and an effective 2D 'ionic lattice' on the TEM grid.

C18-DAPMA (Figure 2.15, left) showed less obvious spherical-shaped self-assembled micelles, and although when in the presence of heparin (Figure 2.15, right) the formation of aggregates was also noticeable, they appear to be somewhat less ordered in terms of hierarchical structuring. This is in-line with the DLS observations which suggested that the self-assembly of this compound is less well-defined, presumably as a consequence of its lower solubility and a greater tendency to aggregate in an uncontrolled way – especially at elevated concentrations.

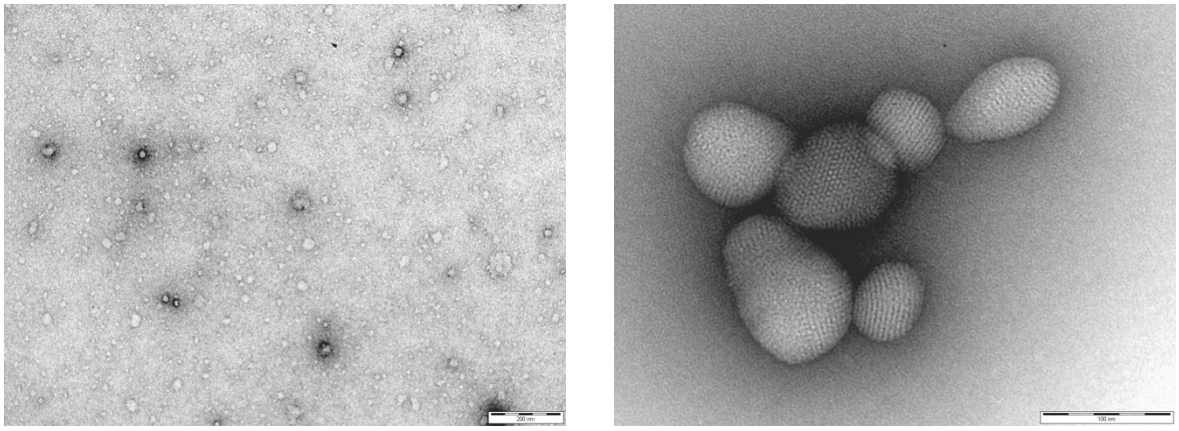

Figure 2.13. TEM images of C14-DAPMA (left, scale bar: 200 nm) and C14-DAPMA with heparin (right, scale bar: 100 nm) in aqueous solution.

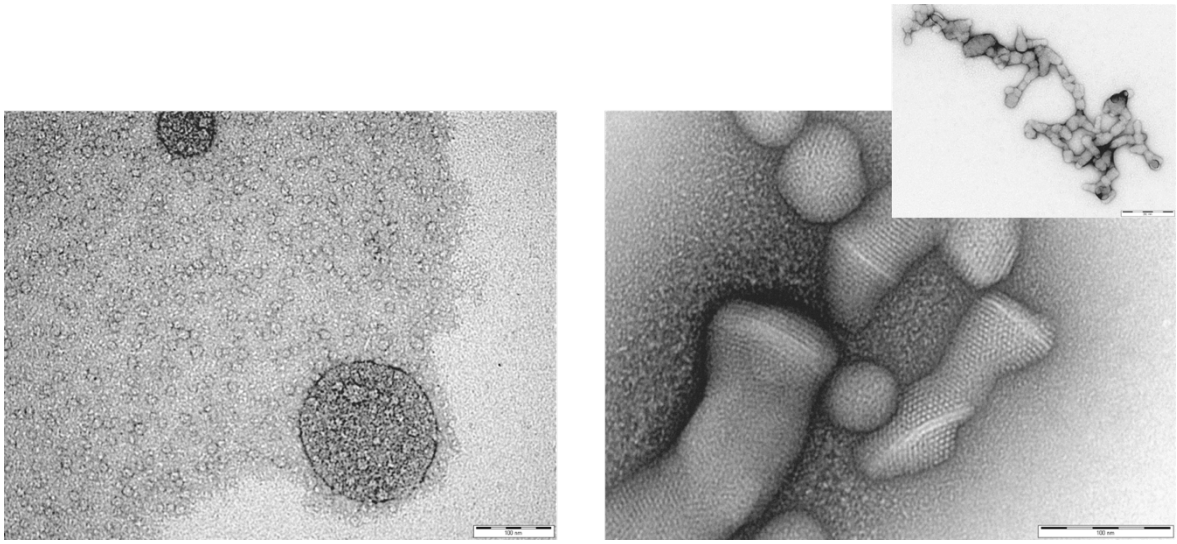

Figure 2.14. TEM images of C16-DAPMA (left, scale bar: 100 nm) and C16-DAPMA with heparin (right, scale bar: 100 nm - inset: 200 nm) in aqueous solution.

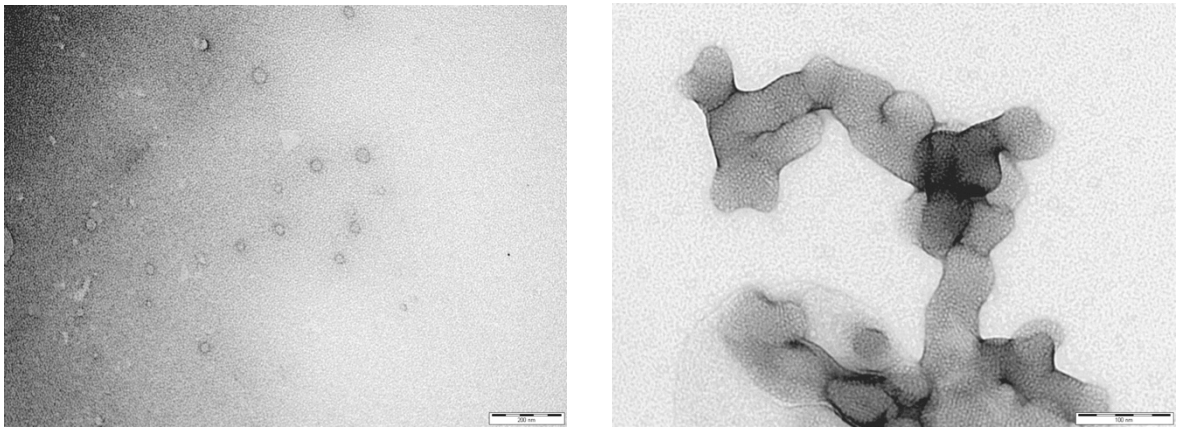

Figure 2.15. TEM images of C18-DAPMA (left, scale bar: 200 nm) and C18-DAPMA with heparin (right, scale bar: 100 nm) in aqueous solution.

According to the previous results, research proceeded with C16-DAPMA and C14-DAPMA, as C18-DAPMA revealed significant solubility problems in the physiological buffers of interest.

2.7. Modelling Heparin Binding

Given the potential clinical relevance of self-assembled nanostructures for heparin binding and reversal,[220] it is of great interest to verify whether the highly ordered hierarchical

nanoscale aggregates revealed by TEM for C14-DAPMA and C16-DAPMA are preserved in solution. Therefore, our collaborators at University of Trieste, Italy, led by Professor Sabrina Pricl performed Dissipative Particle Dynamics (DPD) simulations[206,207,217,218,225,226,233] to predict the self-assembly and spatial organization of these two amphiphiles in solution in presence of heparin (Figure 2.16).

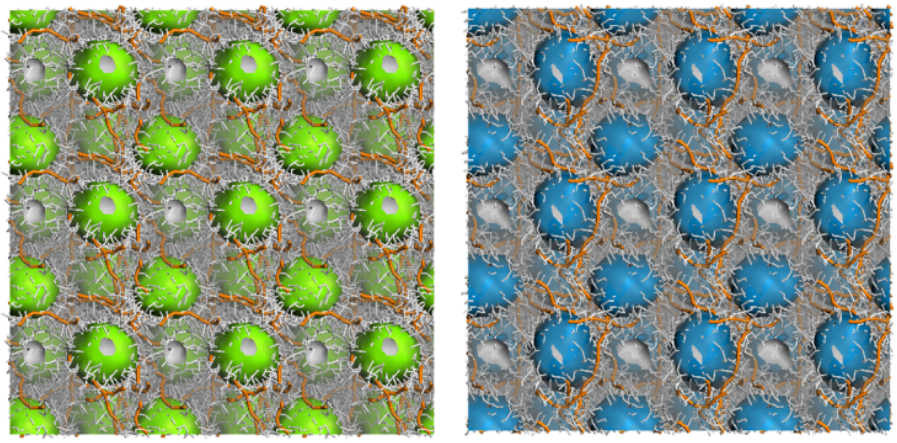

Figure 2.16. DPD snapshots of C14-DAPMA (left) and C16-DAPMA (right) self-assembly in presence of heparin (2:1 binder:heparin ratio). The hydrophobic micellar core is highlighted as green and blue isosurfaces, respectively. Hydrophilic moieties of each aggregate are shown as white sticks, while heparin molecules are shown as orange rods. A continuous light grey field portrays the aqueous medium.

In agreement with TEM analysis, mesoscale computational models reveal that both binders self-assemble into highly ordered spherical nanostructures in the presence of the polyanion. The nanoscale organization is characterised by face-centred (fcc) packing of the hierarchical assemblies, as evidenced by the relevant isodensity surfaces of the micellar hydrophobic cores. The predicted lattice structures of the C14-DAPMA and C16-DAPMA micelles are characterised by lattice constants, a, of 8.1 nm and 8.6 nm, respectively. Thus, the unit cell size of the fcc structure of C16-DAPMA is predicted to be slightly bigger than that of C14-DAPMA. The corresponding centre-to-centre distance ($a/\sqrt{2}$) is 5.7 nm for C14-DAPMA and 6.1 nm for C16-DAPMA. It is worth reflecting that this is in agreement with measurements of micelle diameters achieved by DLS (Table 2.3).

2.8. Small Angle X-Ray Scattering (SAXS)

The nanostructure of the aqueous binder-heparin complex was then investigated experimentally by small angle X-ray scattering for C14-DAPMA and C16-DAPMA, in collaboration with Professor Mauri Kostiainen's group at Aalto University, Finland. A Debye ring with a diffuse symmetric halo without intensity differences was obtained from the 2D diffraction patterns for both binder-heparin complexes (Figure 2.17a inset), which is typical for polycrystalline samples with isotropic orientation of multiple crystals.[234] For the assembly formed between C14-DAPMA and heparin the positions of the diffraction peaks were at q = 0.129 and 0.259 $Å^{-1}$ which in terms of crystal plane reflections with Miller indices corresponds to (*hkl*) = (111) and (222), assuming a face-centred cubic (fcc) structure. For the assemblies comprising C16-DAPMA and heparin, SAXS measurements (Figure 2.17) showed diffraction peaks at q = 0.122, 0.138 and 0.246 $Å^{-1}$ which in terms of crystal plane reflections with Miller indices corresponds to (*hkl*) = (111), (200) and (222), assuming a fcc structure. The additional observation of the (200) peak for the C16-DAPMA complexes, not observed for those formed by C14-DAPMA, may be suggestive of a greater degree of nanocrystalline order for the C16-DAPMA system or a different form factor for the micelles. This would be in agreement with the lower CMC and greater heparin binding ability observed for this compound, as well as the very highly ordered repetitive structures observed by TEM (Figure 2.14 - right).

It has been noted that in the same way atomic structure controls crystallisation events, molecular structures can play a directing role in the formation of nanocrystalline assemblies via electrostatic interactions between polyionic species.[235–237] In this case, the modification of lattice parameters based on the size of the molecular scale surfactant building block is a clear example of the way in which molecular parameters can be translated into the packing of hierarchical nanocrystalline structures.

The quadratic Miller indices were plotted against the measured $q_{(hkl)}$ values for C14-DAPMA-heparin and C16-DAPMA-heparin complexes, as shown in Figure 2.17b and c, respectively. The lattice constant a, was then estimated by linear regression. For cubic phases $a = 2\pi\sqrt{(h^2+k^2+l^2)}/q_{(hkl)}$, which was determined to be 8.5 nm for C14-DAPMA and 8.9 nm for C16-DAPMA, in good agreement with the corresponding values obtained from the

theoretical calculations. The centre-to-centre distance ($a/\sqrt{2}$) of the particles was 6.0 nm for the C14-DAPMA and 6.3 nm for the C16-DAPMA, again in line with mesoscale predictions.

The centre-to-centre distances are also in agreement with the micellar diameters determined by DLS methods. It should be remembered that as a solution-phase method, DLS also includes the solvent and counterions at the micellar periphery, which will be replaced by polyanion once heparin has bound. As such, and supported by the binder:heparin complex organization predicted by simulation, these SAXS data would fit with a view in which self-assembled cationic micelles are packed into a polycrystalline array by polyanionic heparin in analogy to the ionic model only using electrostatically-charged nanoscale building blocks instead of simple inorganic ions. Most importantly, these SAXS results once again confirm that the self-assembled micelles retain their structural integrity on binding to heparin, and are not disrupted, even on formation of high-affinity electrostatic interactions with their binding partner.

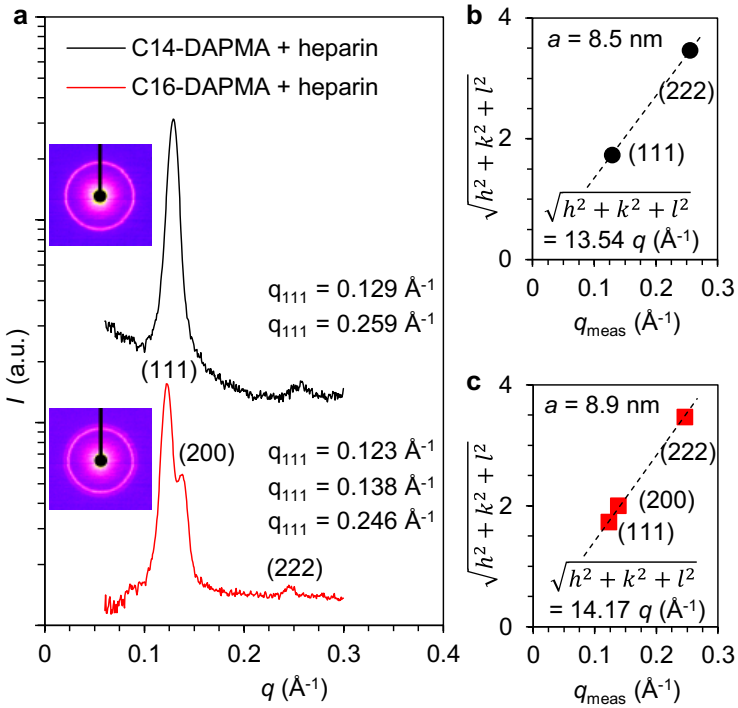

Figure 2.17. SAXS characterisation of C14-DAPMA and C16-DAPMA in the presence of heparin. a) Integrated SAXS curve measured from self-assembled C14-DAPMA and C16-DAPMA in the presence of heparin. Inset: 2D-scattering pattern of C14-DAPMA and C16-DAPMA with heparin. b, c) Quadractic Miller indices of assigned reflections for fcc structure versus measured q-vector positions for indexed peaks, related with (b) C14-DAPMA and (c) C16-DAPMA, both binding heparin.

Finally, the data obtained from simulations and SAXS were compared with the TEM images. Figure 2.18a and 2.19a show the TEM images of C14-DAPMA and C16-DAPMA, respectively, binding to heparin, where it is possible to distinguish the crystal projection viewed along the [110] zone axis (Figures 18b and 19b, left). Analysing the line profile over the crystal projection (marked in red) yields an average period (ap) of 4.5 ± 0.3 nm, which corresponds to a fcc lattice constant (a = 3ap/$\sqrt{3}$) of 7.8 nm for C14-DAPMA. As expected, the corresponding values for C16-DAPMA are slightly higher (ap = 4.6 ± 0.3 nm and a = 8.0 nm, Figure 2.19). These values are in good agreement with the a values obtained by DPD and SAXS and the slight reduction in unit cell size could be attributed to a drying effect on the TEM grid or grid-lattice interactions causing minor reorganisation. Calculating a fast Fourier transform (Figures 18b and 19b inset) from the crystalline area (Figures 18b and 19b) and filtering the inverse Fourier transform from selected Fourier components, yields an image

that represents the unit cell of the crystal viewed along the [110] zone axis (Figures 18c and 19c, left). This can be also confirmed by overlaying the image and a model of the unit cell (Figures 18c and 19c, middle) shown in Figures 18c and 19c, right. Taken together, our data indicates that the proposed hierarchical nanoscale assembly model is valid, and confirms the viewpoint that the micellar objects have excellent structural integrity and can be considered as intact nanoscale building blocks throughout the heparin binding and hierarchical assembly process.

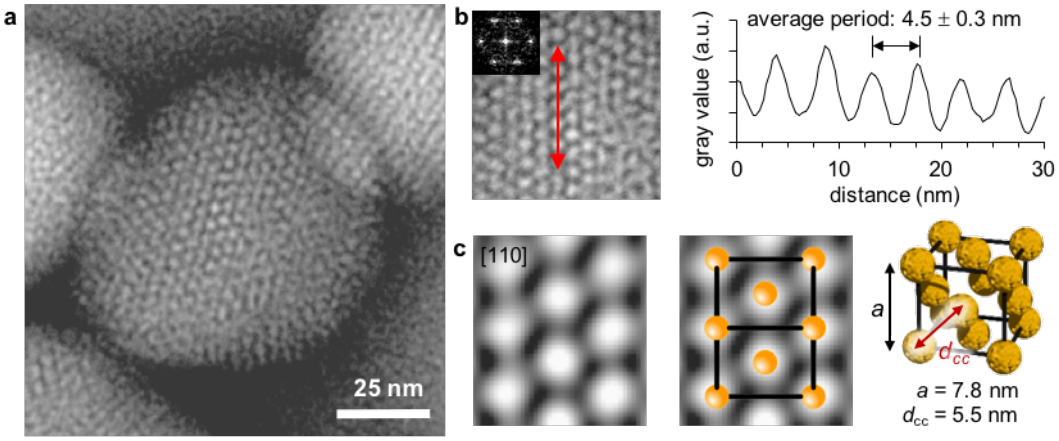

Figure 2.18. a) TEM image of C14-DAPMA heparin complex. b) A crystalline area (left, inset: fast Fourier transform) and a line profile analysis (right) along the red line. c) Filtered inverse Fourier transform from selected Fourier components (left), overlay of the image and fcc unit cell (middle) and model of the fcc unit cell with key dimension (right). Micelles shown in yellow, diameter reduced for clarity.

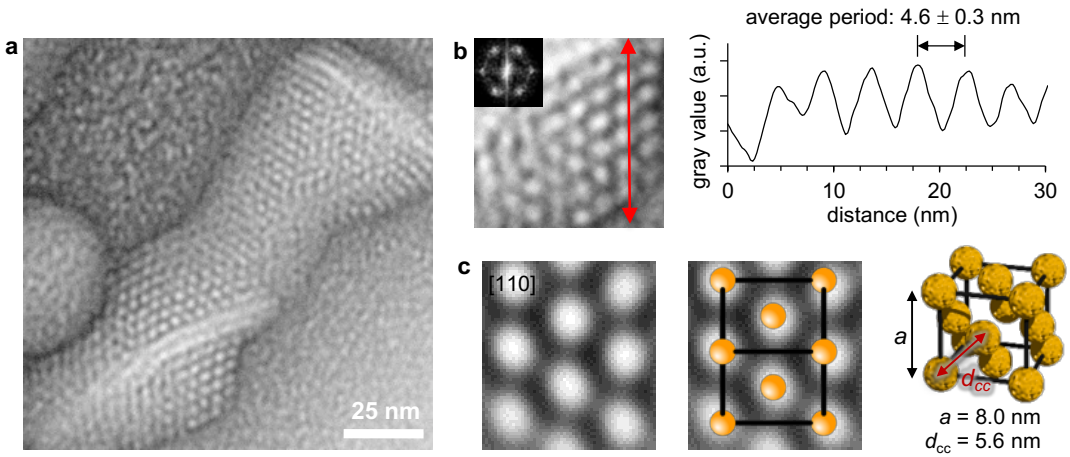

Figure 2.19. a) TEM image of C16-DAPMA heparin complex. b) A crystalline area (left, inset: fast Fourier transform) and a line profile analysis (right) along the red line. c) Filtered inverse Fourier transform from selected Fourier components (left), overlay of the image and fcc unit cell (middle) and model of the fcc unit cell with key dimension (right). Micelles shown in yellow, diameter reduced for clarity.

This is the first such study of a hierarchical nanoscale recognition process in any heparin binding event and we suggest that such structures may be of clinical relevance.

2.9. Degradation Studies

To gain a better understanding of how these heparin binders behave over time, degradation studies were performed using two different approaches to study both the molecular degradation as well as the disassembly process of C14-DAPMA and C16-DAPMA. In order to determine the molecular degradation of C14-DAPMA and C16-DAPMA, a mass spectrometry study was performed over time. Each binder was dissolved in buffered solution at pH 7.5 and incubated at 37 °C. Gly-Ala dipeptide was added as internal standard to the binder solutions prior to measurement and mass spectra of both binders were obtained at 0 and 24 hours.[215] The mass spectra for C14-DAPMA and C16-DAPMA are shown in Figure 2.20 and Figure 2.21, respectively.

From the obtained spectra it is possible to observe that the molecular ions of both binders remain fully intact after 24 hours, indicating that no molecular degradation of both binders

occurs over this period of time. Previous work from Smith[207,215] group has shown the design of degradable binders with ester linkages that are easily cleaved under physiological conditions. By replacing the ester with an amide linkage in the C14-DAPMA and C16-DAPMA it was expected to have a more stable bond and consequently non-degradable compounds under these conditions. Furthermore, the use of these compounds as heparin binders was intended to facilitate the study of multicomponent systems with simple stable structures that at the same time are effective heparin binders.

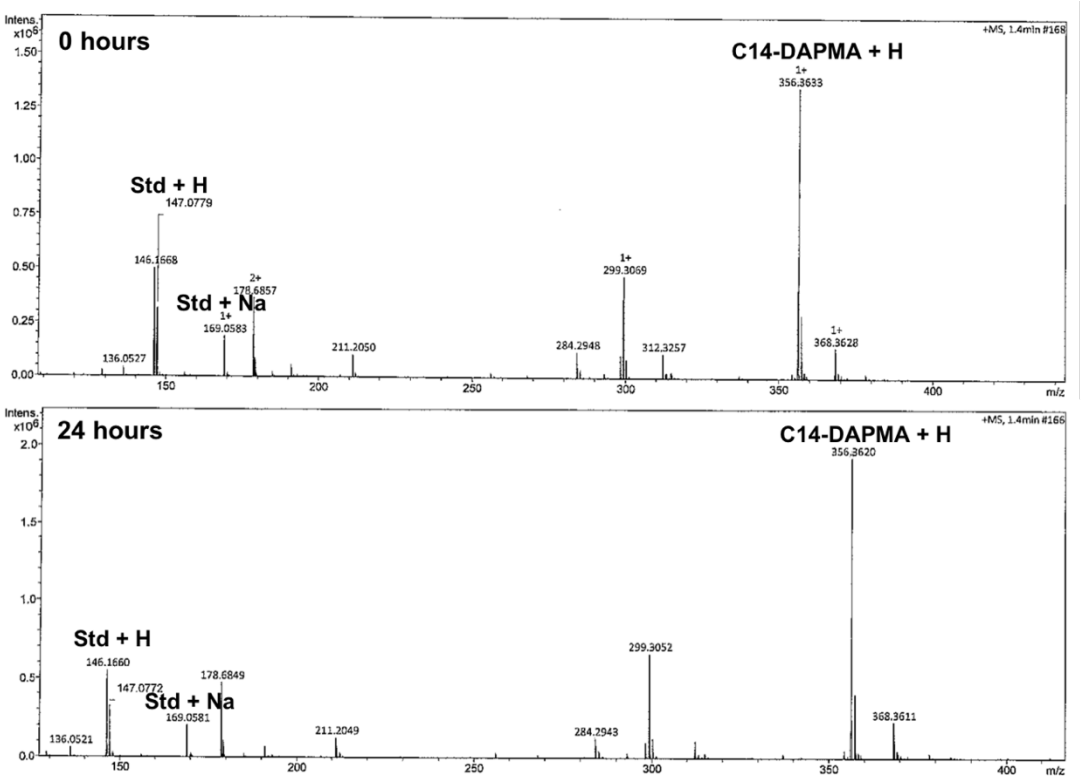

Figure 2.20. Mass spectra of C14-DAPMA at 0 (top) and 24 hours (bottom) in the presence of Gly-Ala and incubated at 37 °C.

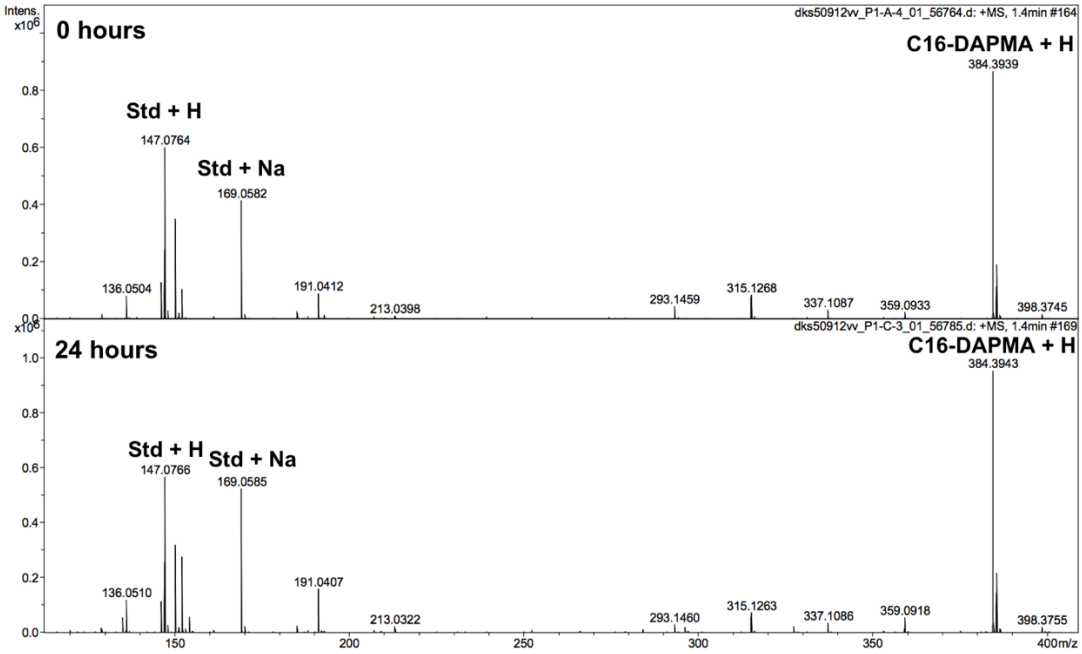

Figure 2.21. Mass spectra of C16-DAPMA at 0 (top) and 24 hours (bottom) in the presence of Gly-Ala and incubated at 37 °C.

After concluding that no molecular degradation occurs after 24 h for C14-DAPMA and C16-DAPMA the disassembly of both binders was also tested using Nile Red encapsulated in C14-DAPMA and C16-DAPMA micelles. The fluorescence intensity of Nile Red was recorded at 635 nm over time. This fluorescence should be maintained as long as the hydrophobic environment of the micellar core remains existing in the buffer solution.[206] The obtained data is shown in Figure 2.22 and Figure 2.23.

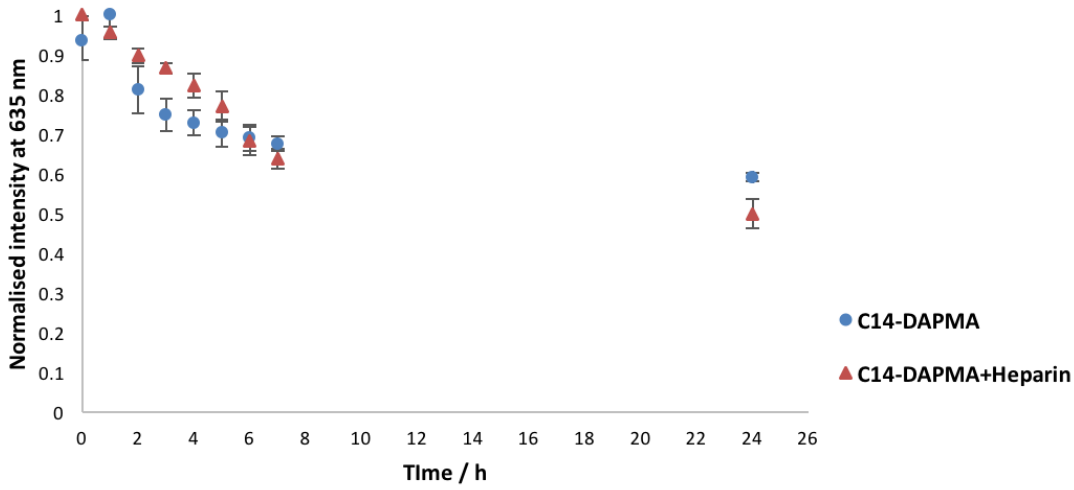

Figure 2.22. Normalised fluorescence intensity of Nile Red at 635 nm in the presence of C14-DAPMA (circles) and C14-DAPMA with heparin (triangles), over time.

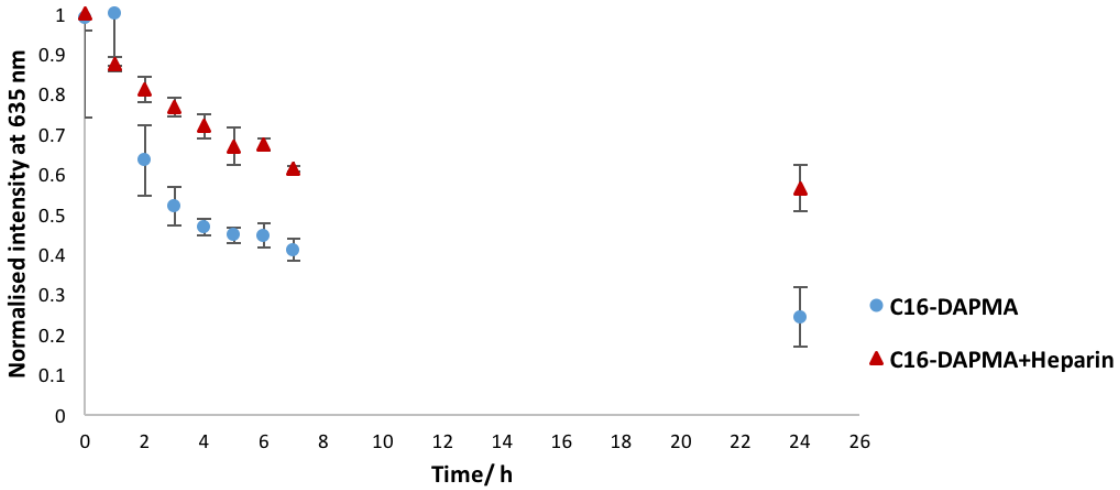

Figure 2.23. Normalised fluorescence intensity of Nile Red at 635 nm in the presence of C16-DAPMA (circles) and C16-DAPMA with heparin (triangles), over time.

A gradual release of Nile Red from C14-DAPMA micelles was obtained (Figure 2.22) with a half-life of approximately 24 hours in 10 mM Tris-HCl/ 150 mM NaCl buffer. The presence of heparin resulted in a similar release profile indicating that approximately 50% of the Nile Red was released after 24 hours in the absence and the presence of heparin. Given there is no molecular scale degradation it seems strange that the micelles should apparently disassemble over time. We suggest that slow reorganisations of the micellar structures in the presence of the Nile Red probe may give rise to its exclusion from the hydrophobic domain and release into solution.

Interestingly, with the increase of the hydrocarbon chain length (Figure 2.23) the release of Nile Red was faster, with a half-life of approximately 4 hours. However, the faster disassembly of C16-DAPMA was retarded with the presence of heparin leading to the half-life increasing to approximately 24 hours. This result suggests once more that the formation of stable self-assembled nanostructures when heparin is present, corroborating with the highly ordered crystalline nanostructures observed by SAXS for these two binders in the presence of heparin.

2.10. Conclusions

In conclusion, three self-assembling amphiphilic molecules have been successfully synthesised, based on a fatty acid tail and an amine ligand to bind electrostatically to heparin. CMC values for the three molecules were obtained, with C18-DAPMA presenting a higher value than expected due to its low solubility in buffer and C14-DAPMA showing a higher CMC value than C16-DAPMA, since the shorter apolar chain contributes to a smaller hydrophobic effect, hence requiring a higher concentration for aggregation to occur. Therefore, C16-DAPMA proved to be the optimal system in terms of self-assembly. MalB assays were performed in order to investigate the binding of the synthesised molecules to heparin. C16-DAPMA revealed the lowest EC_{50}, CE_{50} and dose, proving that it corresponds to the most effective heparin binder, of this simple family of compounds. DLS measurements for the three binders proved the existence of larger aggregates when heparin was present in solution, indicating once more the effective interaction between the binder and heparin. Furthermore, TEM images showed highly organised nanocrystalline hierarchical assemblies when C14-DAPMA and C16-DAPMA were in the presence of heparin. In addition, characterisation by mesoscale simulations and SAXS of C14-DAPMA and C16-DAPMA with heparin gave new insights on the nanoscale to reveal isotropic orientation of the crystals with a fcc structure, confirming that the micelles remained intact during hierarchical assembly. This analysis was in good agreement with the TEM images. Finally, a Nile Red release assay proved that the presence of heparin stabilizes the self-assembled binders, most effectively for C16-DAPMA, which has a half-life of *ca.* 24 hours.

3. Orthogonal Self-Assembly of DBS-COOH Hydrogels with C16-DAPMA and Heparin

Part of the work presented in this chapter was carried out in conjunction with MChem student Laura Hay and published in *Chem. Sci.*, 2017, DOI: 10.1039/C7SC03301J. Cytocompatibility studies were performed on a placement at Nano-FM in Groningen, Netherlands, as part of the SmartNet network.

3.1. Introduction

Supramolecular hydrogels are desirable tissue engineering scaffolds and drug delivery vehicles due to their ability to respond to a variety of external stimuli, undergoing sol-gel transitions in response to temperature or pH.[87,238] Additionally, hydrogels are of particular interest as a consequence of their ability to encapsulate and deliver bioactive molecules for drug delivery and to promote cell adhesion, migration, differentiation and proliferation.[239–244] Therefore, the self-assembly of LMWGs with the incorporation of bioactive factors that can be released in a controlled manner, can originate a single system with the independent formation of supramolecular materials that will have its individual biological functions. Multicomponent hydrogels therefore have a higher potential to mimic the ECM as they can mimic the orthogonal chemistries existing in natural systems.[245–247] This way, multicomponent hydrogels are very promising nanostructures for tissue engineering. Their complexity, and potential for independent roles of the different networks can give rise to highly responsive and stable scaffolds able to be employed as multi-functional cell microenvironments.

However, despite the intrinsic responsiveness of LMWGs, their inherent weak mechanical strength can limit their applications, and therefore a method of improving this without losing the responsive nature of such gels can be achieved by integration of LMWGs with PGs creating a hybrid hydrogel, where the mechanical strength of the gel is greatly enhanced.[87,98,248–251] The responsive nature of hybrid hydrogels was proven when the pH responsive ability of a LMWG, 1,3:2,4-dibenzylidene-D-sorbitol–*p,p'*-dicarboxylic acid (DBS–COOH), to assemble and dissemble into a hydrogel in the presence of the PG agarose was demonstrated (Figure 3.1).[87] Importantly this highlights that there is potential to

harness the pH-responsive nature of DBS-COOH to release bioactive molecules, while utilising the robustness of agarose to maintain structural integrity.

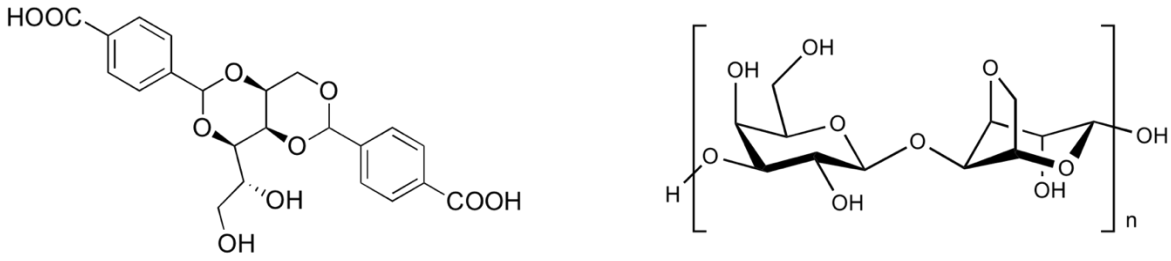

Figure 3.1. Chemical structures of LMWG DBS-COOH and PG agarose, used in the formation of a hybrid hydrogel.

Additionally, there is an interest in applying heparin, which has clinical use as an anticoagulant,[182,252] for transdermal or subcutaneous low-dose delivery for long term use in hospital settings.[194,253] Heparin has also been included in gels with potential applications in tissue engineering, to control growth factor release and/or encourage tissue growth.[161,162] However, supramolecular gels which incorporate heparin remain very rare, and are restricted to gels based on relatively complex self-assembling peptides.[202,205,254,255]

In this chapter, pH responsive DBS-COOH hydrogelator is presented and the orthogonal self-assembly of the hydrogel with self-assembled C16-DAPMA for heparin binding is investigated. Additionally, the incorporation of heparin within a two-component hybrid hydrogel combining a polymer gelator (agarose) and a LMWG (DBS-COOH) is studied. Heparin release from the multi-component systems will be quantified and the cytocompatibility of these systems tested.

3.2. Synthesis of DBS-COOH Gelator and pH-induced Hydrogelation

DBS-COOH was synthesised according to previously reported methodology from the Smith group.[87] Firstly, D-sorbitol was condensed with two equivalents of methyl 4-formylbenzoate in the presence of a catalytic acid, specifically *p*-toluenesulfonic acid (p-TsOH). The reaction was carried at 70 °C in a mixture of cyclohexane and methanol to yield

DBS-$COOCH_3$ (Scheme 3.1). Methanol was used to solubilize the reagents for the reaction to take place, while cyclohexane allowed the product to precipitate.

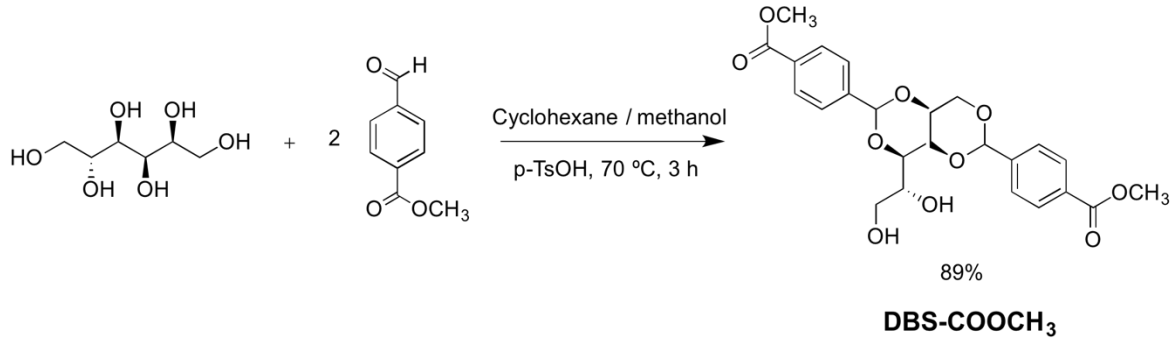

Scheme 3.1. Synthesis of DBS-$COOCH_3$.

Following the formation of DBS-$COOCH_3$, saponification of the methyl ester groups with sodium hydroxide (NaOH) was carried out to obtain the DBS-COOH derivative, as shown in Scheme 3.2.

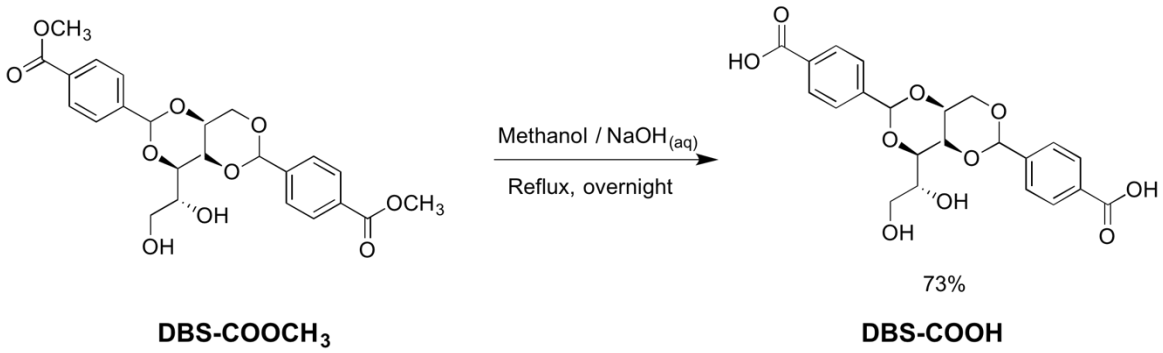

Scheme 3.2. Synthesis of DBS-COOH.

The ability of DBS-COOH to form gels in 10 mM Tris-HCl/150 mM NaCl (pH 7.4) was then tested using different concentrations of LMWG (0.2% w/v, 0.15% w/v and 0.1% w/v). In order to form supramolecular hydrogels with carboxylic acid gelators, the pH values should be below the pK_a of the carboxylic acid (4-5). For this reason, hydrogels were formed using slow acidification of a basic solution. Initially, NaOH was added in order to basify the solution and subsequently, the addition of glucono-δ-lactone (GdL), which undergoes

alkaline hydrolysis forming gluconic acid (Scheme 3.3) slowly lowers the pH, enabling the formation of uniform homogeneous gels.

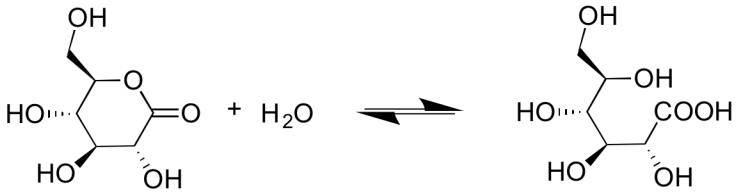

Scheme 3.3. Hydrolysis of GdL.

The three different concentrations of DBS-COOH tested, resulted in the formation of homogeneous gels, as shown in Figure 3.2. However, for concentrations of 0.1% w/v a very weak gel was formed, easily collapsing when gently moving the vial. Therefore, studies proceeded using a DBS-COOH concentration of 0.2% w/v, in order to ensure the formation of stable gels.

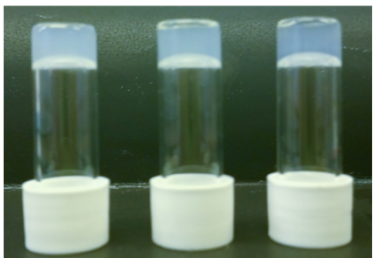

Figure 3.2. DBS-COOH gel formation using different concentration of gelator: 0.2% w/v; 0.15% w/v and 0.1% w/v (from left to right) in 10 mM Tris- HCl/ 150 mM NaCl.

3.3. Study of Orthogonal Self-Assembly of DBS-COOH with C16-DAPMA and Heparin

The main aim of this project consists in studying the self-assembly of multi-component hydrogels with the incorporation of a bioactive factor - heparin. To gain initial insight into multi-component systems, simple visual experiments of gelation were performed. Therefore, the assembly of DBS-COOH hydrogel with C16-DAPMA micelles bound to heparin was firstly investigated by testing different orders of addition of heparin-C16-DAPMA aggregates to verify their influence in gel formation. The concentration of heparin-

C16-DAPMA used was the same as for the TEM images in Chapter 2. In a first attempt, a solution of 150 µM C16-DAPMA/ 38 µM heparin was added into a solution of DBS-COOH (0.2% w/v) with GdL in 10 mM Tris-HCl/ 150 mM NaCl (pH 7.4) approximately 20 minutes after the addition of GdL. It was noticed when adding the C16-DAPMA/heparin solution that the gel was already forming, and on the addition of the binder/heparin solution and further agitation the conditions to form the gel were disrupted (Figure 3.3).

Figure 3.3. 0.2% w/v DBS-COOH gel formation with addition of 150 µM C16-DAPMA /38 µM Heparin solution 20 minutes after the addition of GdL, in 10 mM Tris-HCl/ 150 mM NaCl (pH 7.4).

The same test was repeated, but adding the heparin-C16-DAPMA solution immediately after GdL or before the GdL addition. The formation of stable gels in both cases was verified, with a final pH of 5. Therefore, in a first analysis it is possible to conclude that the orthogonal self-assembly of DBS-COOH hydrogels in the presence of heparin/heparin binder complexes is achievable.

The following studies were performed with the addition of the heparin - C16-DAPMA solution immediately after the GdL using 10 mM Tris-HCl/ 150 mM NaCl buffer (pH 7.4) as medium.

Gel Formation with Different Concentrations of Heparin

To test the influence of heparin alone on the gel formation, different concentrations of heparin (38 µM; 50 µM; 100 µM; 150 µM; 300 µM; 400 µM; 500 µM) were added to DBS-COOH. From all the different concentrations used homogeneous and stable gel formation

occurred (Figure 3.4), meaning that the presence of heparin does not stop gelator self-assembly.

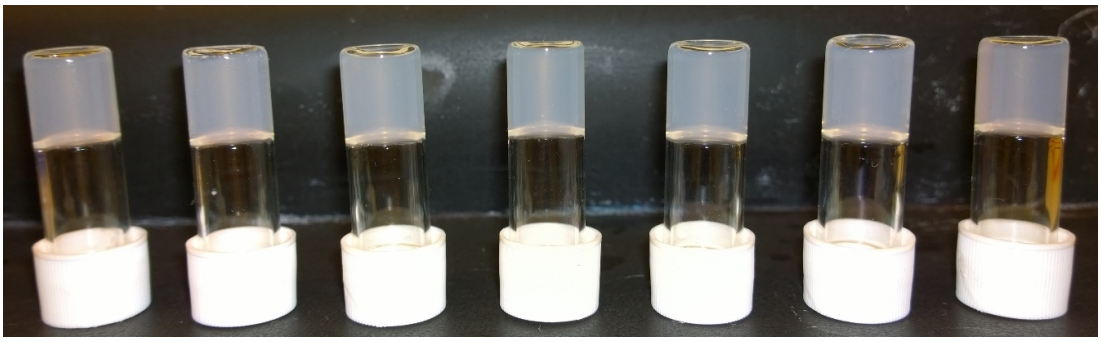

Figure 3.4. 0.2% w/v DBS-COOH gel formation with 38 µM; 50 µM; 100 µM; 150 µM; 300 µM; 400 µM; 500 µM (from left to right) of heparin.

Gel Formation with Different Concentrations of C16-DAPMA

The influence of C16-DAPMA alone on DBS-COOH gel formation was also tested: 150 µM; 300 µM; 400 µM; 500 µM; 600 µM; 700µM; 800 µM; 900 µM and 1000 µM of C16-DAPMA were added to DBS-COOH and unlike the addition of heparin, none of these concentrations of C16-DAPMA led to the formation of gel (Figure 3.5). This clearly indicates that C16-DAPMA has a direct negative influence on the self-assembly of DBS-COOH, even though an acidic pH was achieved (pH ≅ 5). We suggest that the amine groups of C16-DAPMA may interact with DBS-COOH carboxylic acid groups and thus, effective self-assembly does not take place and consequently no gel is formed.

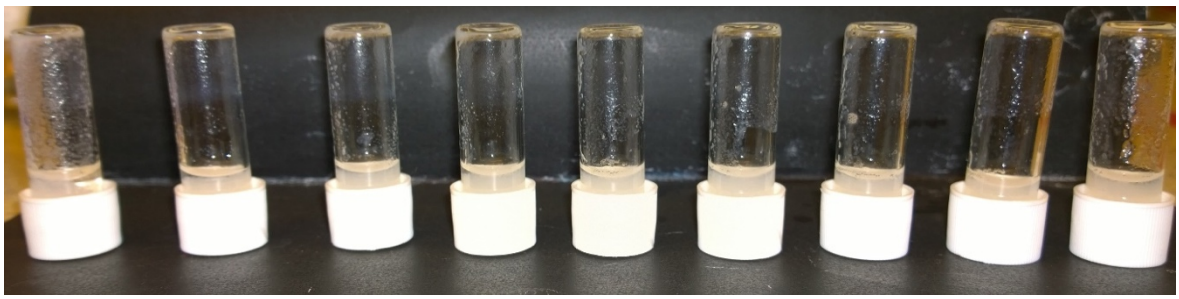

Figure 3.5. 0.2% w/v DBS-COOH gel formation with 150 µM; 300 µM; 400 µM; 500 µM; 600 µM; 700µM; 800 µM; 900 µM; 1000 µM (from left to right) of C16-DAPMA.

Gel Formation with Constant Concentrations of Heparin and Different Concentrations of C16-DAPMA

Following the obtained results, gel formation was next tested at constant concentrations of heparin but with increasing concentration of C16-DAPMA in order to verify the optimum charge ratio of these two molecules for formation of stable gels. As the concentration of 150 μM C16-DAPMA/ 38 μM heparin has been already tested, higher concentrations of heparin were studied: 150 μM, 300 μM, 400 μM and 600 μM (Table 3.1). At 150 μM heparin the threshold concentration, for formation of a stable gel, of C16-DAPMA was 450 μM – above this, gel formation was disturbed. For 300 μM heparin the threshold concentration of C16-DAPMA was 800 μM, for 400 μM heparin it was 900 μM and for 600 μM heparin it was 1400 μM. In each case, excess C16-DAPMA led to disruption of the gel – for example partial gel formation, or at higher concentration, no gelation.

Table 3.1. Test of different heparin/binder ratio in gel formation.

[Heparin] (μM)	[C16-DAPMA] (μM)	Gel Formation
150	600	No gel formation
	500	Unstable gel
	Below 450	Stable gel
300	Above 1000	No gel formation
	900	Gel without incorporation of all solvent
	Below 800	Stable gel
400	Above 1500	No gel formation
	1400 -1000	Gel with aggregates
	900	Stable gel
600	Above 2100	No gel formation
	2000-1800	Unstable gel
	1700-1500	Gel with aggregates
	1400	Stable gel

We note that no gel forms in the presence of excess C16-DAPMA, and suggest that this is because the excess C16-DAPMA is not binding to heparin and thus disrupts gelation as observed for C16-DAPMA alone. We note that as the concentration of heparin/binder in the network increases the gel becomes more sensitive to the excess of binder which in

molar terms becomes more significant (Table 3.2). Overall, these results suggest that the DBS-COOH gel is tolerant of heparin and can also tolerate C16-DAPMA – as long as the surfactant is bound to the heparin within the multi-component system.

Table 3.2. Binder/Heparin molar ratio and charge ratio +/- with increasing heparin concentration.

[Heparin] (μM)	Binder/Heparin Molar Ratio	Charge ratio +/-
38	4:1	2.0
150	3:1	1.5
300	2.7:1	1.3
400	2.2:1	1.1
600	2.3:1	1.2

3.3.1. Thermal Stability and T_{gel} Determination

The thermal stability of the gels formed in the previous section was then tested by simple reproducible tube inversion methodology. The T_{gel} was considered as the temperature when the gel starts to deform and starts to slip down the vial walls when it is inverted.

For the DBS-COOH hydrogel (0.2% w/v) formed in 10 mM Tris-HCl/ 150 mM NaCl buffer (pH 7.4) it was possible to verify that the T_{gel} value was over 100 °C, the boiling point of the solvent, which indicate a high thermal stability. For all different concentrations of heparin in DBS-COOH tested, the T_{gel} obtained was over 100 °C, proving that the presence of heparin does not adversely impact on the thermal stability of the gel. For the different concentrations of C16-DAPMA with heparin that resulted in gel formation, the T_{gel} values again all appeared to be above 100 °C, indicating that the presence of heparin bound to C16-DAPMA does not significantly affect the thermal stability of the gel, which remains above the boiling point of the solvent.

3.3.2. Infrared Characterisation (IR)

Detailed IR characterisation was performed for the gel formed with DBS-COOH (0.2% w/v) alone, in the presence of 300 μM of heparin and in the presence of 300 μM of heparin and 800 μM of C16-DAPMA (Figure 3.6). By comparing the spectra it is possible to notice that

the expected peaks are present in the analysed xerogels and that the spectra broadly correspond to the simple overlap of the three compounds. A broad band appears at 3272 cm^{-1} which is characteristic of the O-H stretching vibration but probably it has such high intensity due to some remaining solvent in the sample. C-H stretches at 2924 and 2845 cm^{-1} are present, as well as a C=O stretch at 1775 cm^{-1}. At 1596 cm^{-1}, a C=C stretch from the aromatic rings of DBS is observed and at 1598 cm^{-1} the presented peak overlaps with the carboxylate peak of heparin. Between 1400 and 1294 cm^{-1} several peaks from the DBS sugar are noticeable. At 1018 cm^{-1} a strong peak is verified, probably corresponding to the overlap of S=O stretch and C-O stretch. Due to the fact that several IR frequencies are common in the three compounds that formed the gel an overlap of the characteristic peaks of each molecule occurred. This suggests that the gel is self-sorted and each component can behave independently in the bottom-up assembled material.

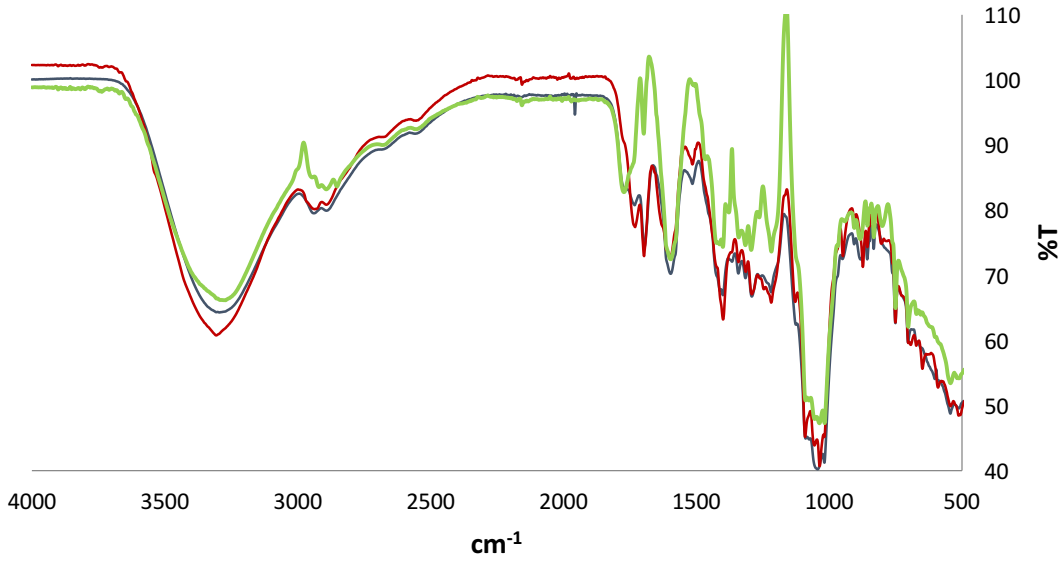

Figure 3.6. IR spectra of xerogels formed by DBS-COOH gel (blue line); DBS-COOH gel with 300 µM of heparin (red line) and DBS-COOH gel with 800 µM of C16-DAPMA and 300 µM of heparin (green line).

3.3.3. Study of Gel Formation Kinetics

The incorporation of different components within the gel network raised our interest in understanding how the presence of heparin and heparin-C16-DAPMA aggregates could affect the self-assembly of DBS-COOH into gel nanofibers. Knowing that DBS-COOH gelation

is a slow process (at least 4h, depending on GdL-gelator ratio) it was possible to monitor the kinetics of self-assembly of DBS-COOH over time using two complementary approaches as described below.

Nuclear Magnetic Resonance (NMR)

An interesting characteristic of the formation of gels in NMR is that before starting to self-assemble, the molecules of the gelator are mobile on the NMR timescale and hence present a NMR spectrum with characteristic resonances. As the gelator assembles, however, the molecules become immobile and hence disappear from the spectrum. This methodology is a powerful way of obtaining detailed information on the kinetics of gelation by quantifying the peaks in spectrum over time by determining the relative integration of the resonances, using a mobile standard as internal reference. This test was performed by recording NMR spectra every 60 minutes for 10 hours, for samples in D_2O containing only 0.2% w/v of DBS-COOH; with 0.2% w/v of DBS-COOH and 300 µM of heparin and 0.2% w/v of DBS-COOH, 300 µM of heparin and 800 µM of C16-DAPMA as shown in Figure 3.7. The internal standard was 28 mM.

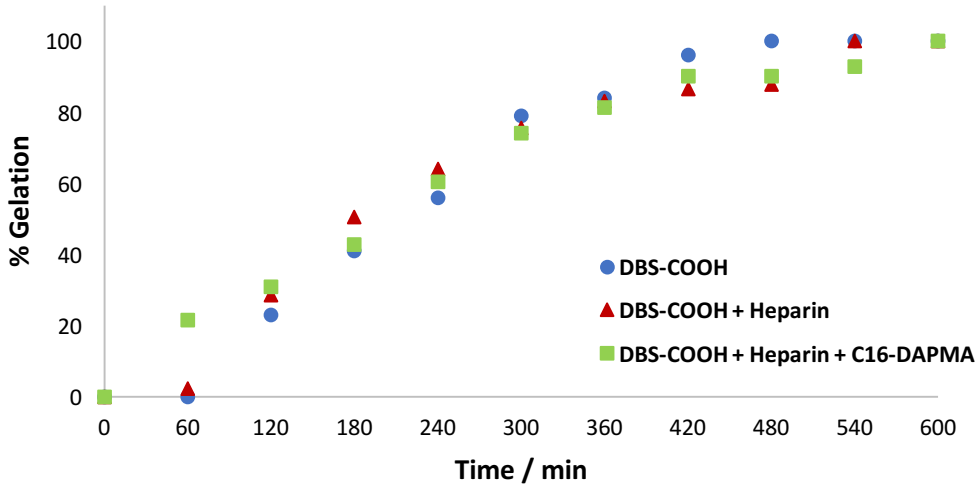

Figure 3.7. % Gelation over time for DBS-COOH (0.2% w/v) (blue circles); DBS-COOH (0.2% w/v) with heparin (300 µM) (red triangles) and DBS-COOH (0.2% w/v) in the presence of heparin (300 µM) and C16-DAPMA (800 µM) (green squares), as monitored by NMR spectroscopy.

For the DBS-COOH sample, no gel formation occurred for the first hour and a gradual increase in the % gelation takes place over the next seven hours, until all the molecules are immobilised, meaning that 100% of the molecules formed a gel after approximately 8 hours. DBS-COOH with 300 μM of heparin presented a similar kinetic profile, with a gradual increase in % of immobilised gelator over time, achieving 100% gelation after approximately 9 hours. The sample of DBS-COOH, 300 μM of heparin and 800 μM of C16-DAPMA revealed equivalent behaviour, achieving 100% of gel in the sample after approximately 10 hours. Therefore, the presence of heparin and heparin with C16-DAPMA appear to have little impact on the kinetics of DBS-COOH assembly into supramolecular gel fibers. Once again this is supportive of self-sorting within this multi-component system.

Circular Dichroism (CD)

CD studies were then performed to follow the nanoscale organisation and assembly of the nanoscale network of the DBS-COOH hydrogel, DBS-COOH hydrogel in the presence of heparin and DBS-COOH hydrogel in the presence of both heparin and C16-DAPMA. It is noteworthy that this experiment was performed below the gelation concentration of DBS-COOH (0.02% w/v), hence we observe the assembly of organised nanofibers within the sample but not the complete formation of the gel-phase material.

From the obtained data (Figure 3.8), in each case the presence of a CD band at approximately 260 nm was observed, with increasing intensity over time. This indicates that π-π stacking of the aromatic rings of the gelator occurs even in the presence of heparin, and C16-DAPMA with heparin. However, it is possible to observe subtle differences in the CD intensities of the different samples.

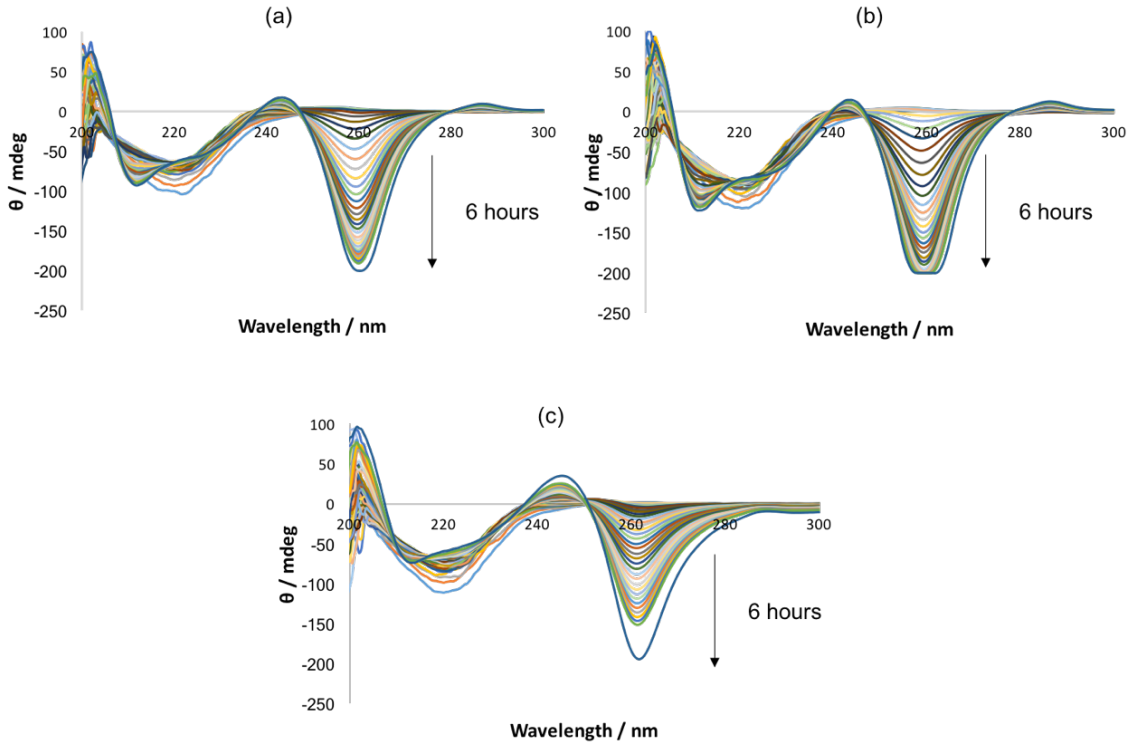

Figure 3.8. Kinetic studies of the growth of DBS-COOH fibrillar network over time, using CD spectroscopy. (a) DBS-COOH (0.02% w/v); (b) DBS-COOH (0.02% w/v) in the presence of heparin (38 µM) and (c) DBS-COOH (0.02% w/v) in the presence of C16-DAPMA (150 µM) and heparin (38 µM).

The intensity of the polarized light at 260 nm was plotted against time for the three tested gels (Figure 3.9) and it became clear that in the presence of heparin, the assembly of the gelator fibers appears to be faster, reaching a maximum intensity after 4 h while, DBS-COOH alone needed more than 5 h. On the other hand, the presence of both heparin and C16-DAPMA revealed a slower change in band intensity, although after 6 hours a similar intensity was obtained for all three different samples. It can therefore be suggested that the presence of heparin promotes the growth of the DBS-COOH nanofibers while the presence of C16-DAPMA-heparin complex appears to somewhat slow the rate of growth of the nanofibers but does not prevent their formation. We might therefore suggest that there are some direct interactions between self-assembled DBS nanofibers and the heparin biopolymer or that heparin helps the fibre nucleation process. Furthermore, the presence of binder may somewhat inhibit gel fibre assembly; indeed we know from the experiments described above that an excess of binder can completely supress gelation.

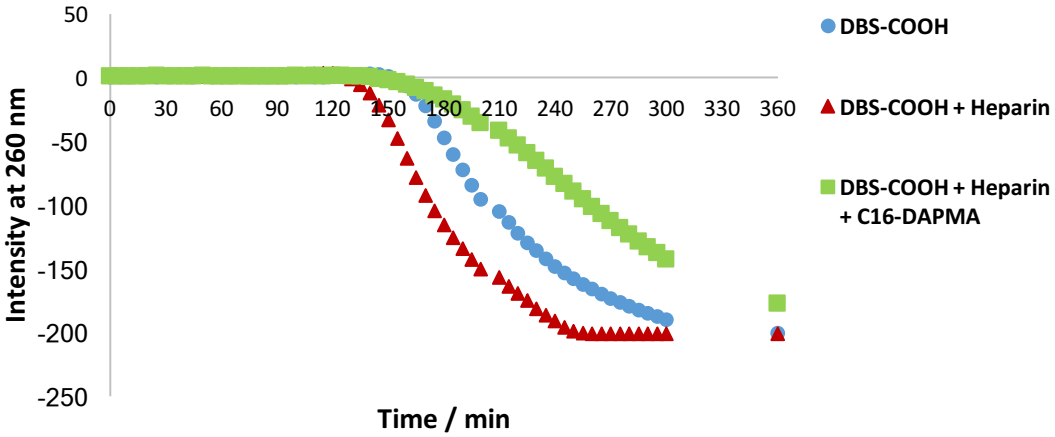

Figure 3.9. Absorbed polarized light at 260 nm of DBS-COOH (blue circles), DBS-COOH in the presence of heparin (red triangles) and DBS-COOH in the presence of heparin and C16-DAPMA (green squares), over 6 hours.

3.3.4. Mallard Blue Diffusion Assay

After studying the influence of incorporating C16-DAPMA and heparin within the DBS-COOH gel network, we were interested to obtain a better understanding of the existing interactions between C16-DAPMA and heparin when incorporated within the DBS-COOH gel. For that purpose, MalB (25 µM) solution (3 mL) was placed on top of gels (3 mL) (Figure 3.10) containing only DBS-COOH (0.2% w/v), DBS-COOH (0.2% w/v) with 38 µM heparin and DBS-COOH (0.2% w/v) with 150 µM C16-DAPMA and 38 µM heparin. The variations in intensity of MalB in the solution on top of the three different gels were then studied over one week by UV-Vis. As described in Chapter 2, MalB changes significantly its UV absorbance when interacting with heparin and therefore, when in contact with the gel can indicate the existence of free heparin.

Figure 3.10. DBS-COOH gel with MalB solution on top.

The obtained results are plotted in Figure 3.11. It is evident that the decrease of the MalB concentration over time for the three different gels, due to natural dilution phenomena as the MalB is distributed between the supernatant and the solvent within the gel. Figure 3.12 shows a DBS-COOH gel sample after one week of experiment where it is possible to verify the presence of blue colour in the gel, the diffusion of MalB into the gel results in the decrease of concentration of MalB present in the solution on top of the gel. The predicted dilution factor in the absence of MalB binding to heparin, is 50%.

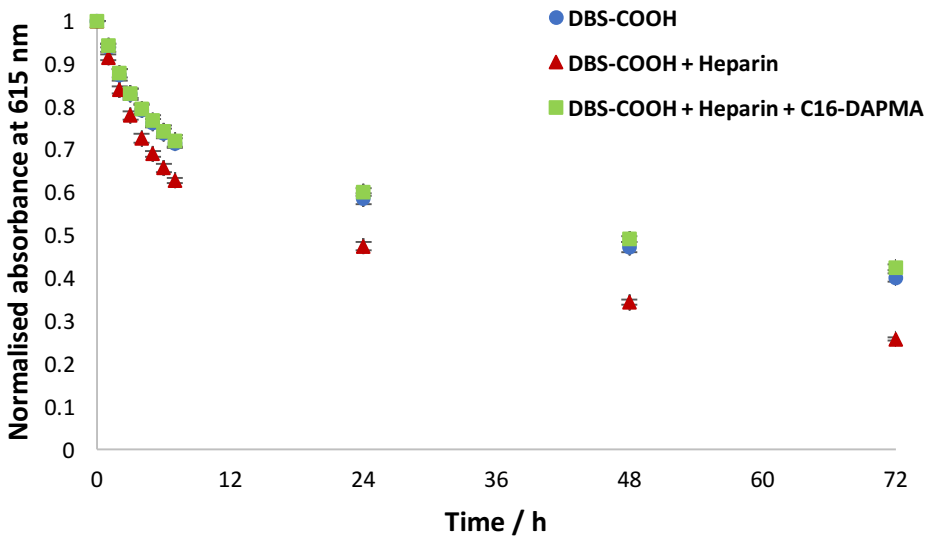

Figure 3.11. Normalised absorbance of MalB at 615 nm over time when placed on top of DBS-COOH; DBS-COOH with heparin and DBS-COOH with heparin and C16-DAPMA.

Figure 3.12. DBS-COOH gel with MalB solution on top after 1 week.

Using the sample containing only DBS-COOH gel as a control experiment, it is possible to verify that the sample of DBS-COOH containing C16-DAPMA and heparin resulted in a decrease of MalB absorbance similar to the control. On the other hand, when the DBS-COOH gel contains heparin a higher decrease of the MalB absorbance over time is

noticeable, when compared with the other two tested gels. This indicates that MalB is interacting with the free heparin present in the gel, and binding to heparin released from the gel, resulting in a lower absorbance of MalB. When C16-DAPMA is present, MalB is no longer able to interact with heparin and thus its intensity over time has a similar behaviour to the control experiment. This provides clear evidence that the interactions between C16-DAPMA and heparin are maintained when incorporated into the gels, indicating that in this multi-component system, each individual component keeps its own unique behaviour.

3.3.5. Electron Microscopy

TEM images of DBS-COOH gel, DBS-COOH gel in the presence of heparin, and in the presence of heparin and C16-DAPMA were obtained, in order to better understand the morphology and behaviour of these three different systems.

TEM images of DBS-COOH gel (Figure 3.13) showed the presence of intertwined long and twisted nanofibers, proving the self-assembly into 1D fibers of this gelator in water. When heparin was added into the gel (Figure 3.14) long nanofibers were once again observed, and at a heparin concentration of 38 μM it was possible to distinguish the existence of some differentiated structures, particularly, but not exclusively on the tips of the nanofibers. This may be related to the fact that heparin can induce the growth of the nanofibers, as already observed in the CD studies. It is known that in organogels, polymers can adsorb onto the tips of growing gel fibers and modify their growth kinetics and morphology; we suggest heparin plays a similar role here.[98]

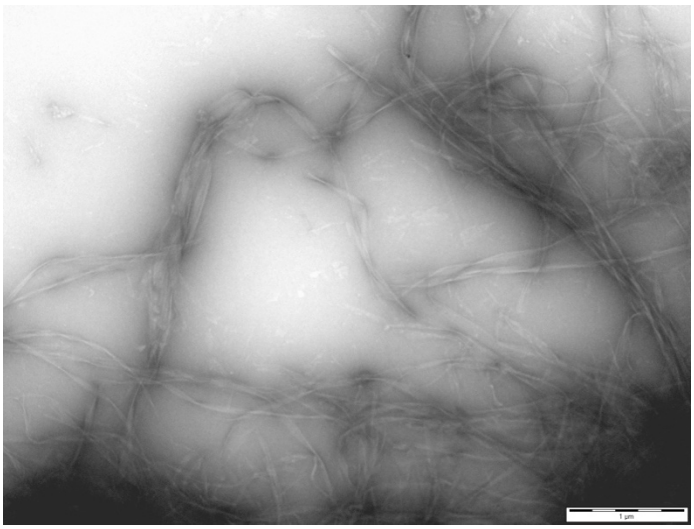

Figure 3.13. TEM image of DBS-COOH gel (0.2% w/v). Scale bar: 1 μM.

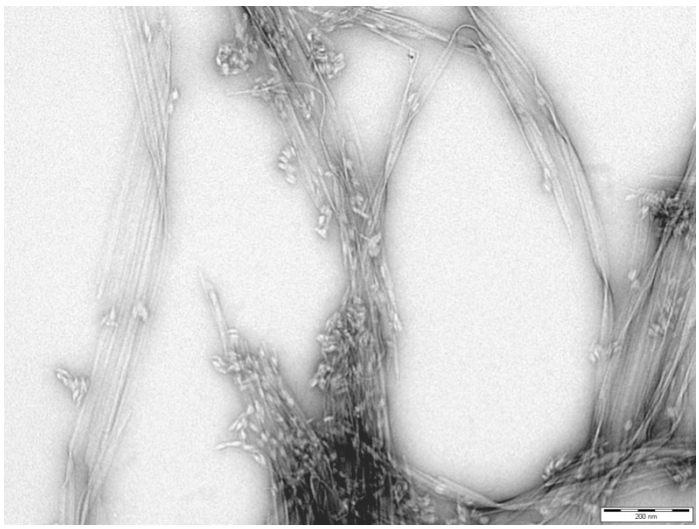

Figure 3.14. TEM image of DBS-COOH gel (0.2% w/v) in the presence of heparin (38 μM). Scale bar: 200 nm.

Figure 3.15 shows TEM images of DBS-COOH gel formed in the presence of both heparin and C16-DAPMA, where the presence of aggregates along with the nanofibers of DBS-COOH is evident. The observed hierarchical aggregates should correspond to the binding between C16-DAPMA and heparin (as discussed in Chapter 2). Therefore, the obtained images indicate that interactions between binder and heparin are maintained within the gel nanostructure, which is in agreement with the obtained results for the MalB assay. This provides evidence that orthogonal assembly and binding are maintained within the multi-component gel.

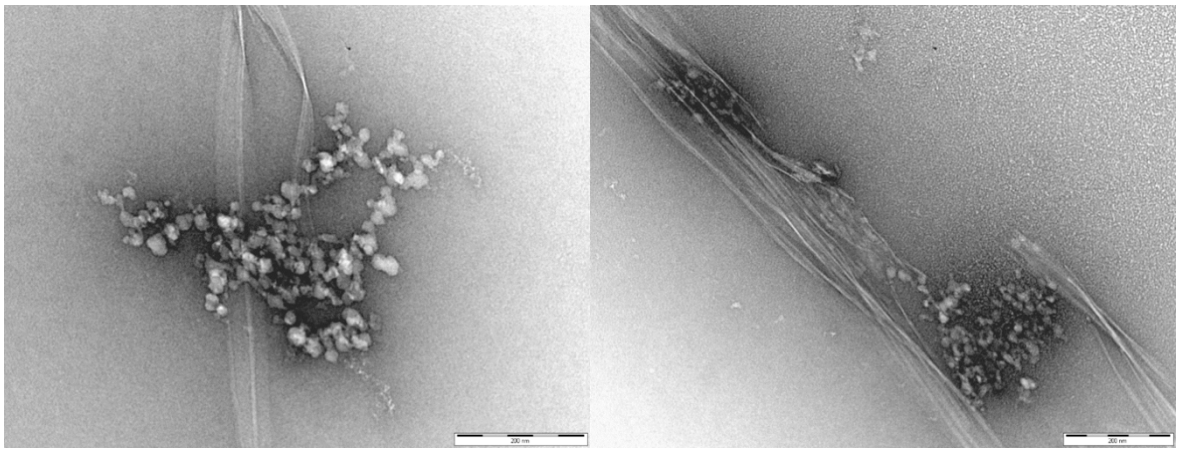

Figure 3.15. TEM images of DBS-COOH gel (0.2% w/v) in the presence of heparin (38 µM) and C16-DAPMA (150 µM). Scale bar: 200 nm.

Scanning electron microscopy (SEM) was then performed. SEM images of the DBS-COOH gel (Figure 3.16) showed a network structure comprising nanofibers, in agreement with the TEM imaging. In the presence of heparin (Figure 3.17) it was possible to verify once more the formation of nanofibers, with a 'spaghetti' like structure and some twisted regions. It is worth noting that these heparin-modified nanostructures are narrower (DBS-COOH with heparin: 49 ± 2 nm; DBS-COOH: 82 ± 1 nm) and this again agrees with the view that the heparin polymer interacts with the growing self-assembled fibres and modifies their morphology and kinetics of growth.[98]

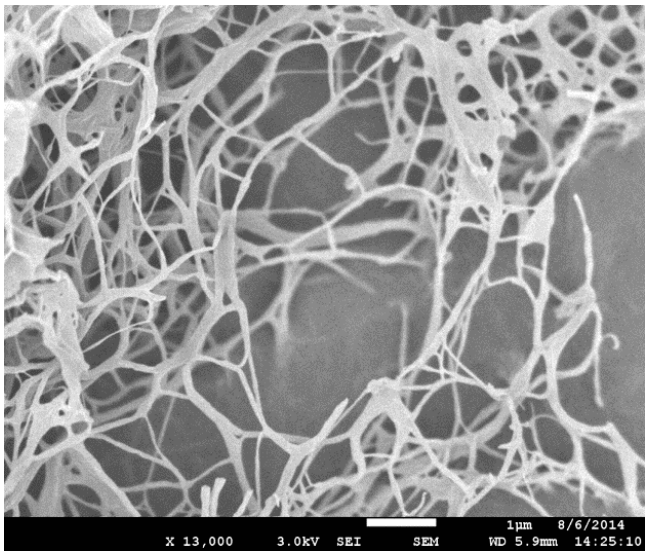

Figure 3.16. SEM images of DBS-COOH gel (0.2% w/v).

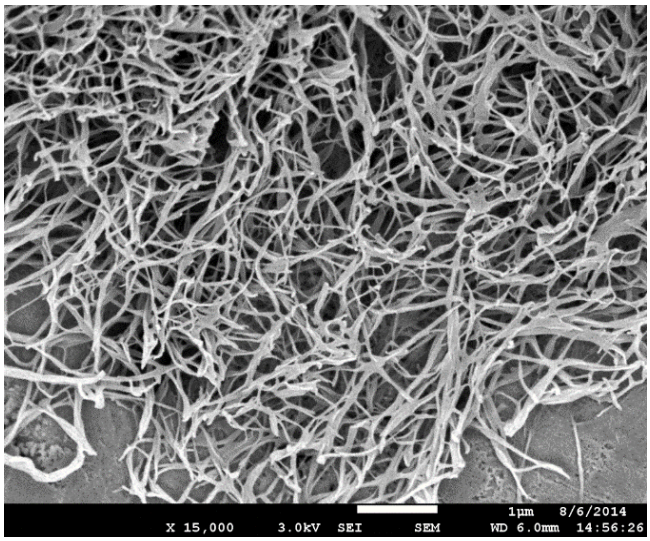

Figure 3.17. SEM images of DBS-COOH gel (0.2% w/v) in the presence of heparin (38 µM).

SEM images obtained for DBS-COOH gel incorporating both C16-DAPMA and heparin (Figure 3.18), only revealed the presence of nanofibers from the DBS-COOH self-assembly; it was not possible to distinguish the presence of C16-DAPMA interacting with heparin. Interestingly, however, the fibers were equivalent to those formed in the absence of heparin which would suggest that C16-DAPMA binds heparin and prevents its interaction with the growing DBS-COOH nanofibers. The fact that the concentration of gelator (4.5 mM) used was much higher to the concentration of binder (150 µM) and heparin (38 µM) may be the reason why it was only possible to identify nanofibers. Additionally, it is well known that relatively soft self-assembled micelles are difficult to image using this technique as they suffer from damage under the electron beam.

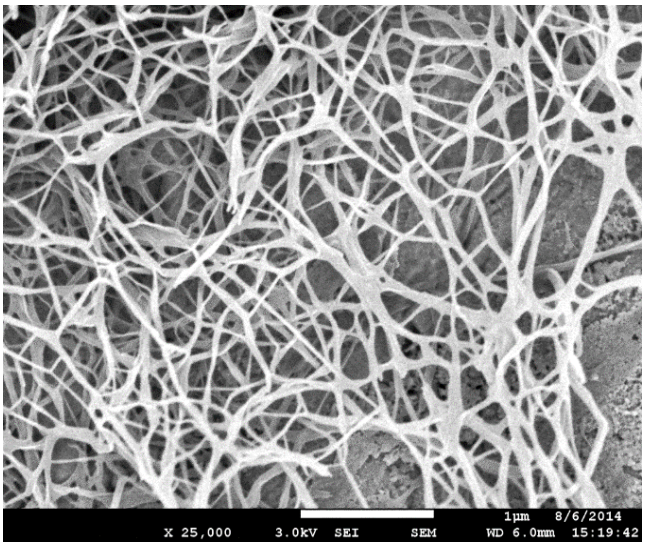

Figure 3.18. SEM images of DBS-COOH gel (0.2% w/v) in the presence of heparin (38 µM) and C16-DAPMA (150 µM).

3.3.6. Rheology

The viscoelastic properties of DBS-COOH gel alone, in the presence of 1 mM of heparin and 1 mM of heparin bound to 2 mM of C16-DAPMA, were then studied by rheology. This technique allows us to obtain the storage or elastic modulus (G') and the loss or viscous modulus (G'') for a soft material, through the application of oscillating strains. A gel is a solid-like material and thus it must exhibit a G' which is an order of magnitude higher than G'' and low frequency dependence.[256,257]

The application of a range of strains gives an indication of how stable a material is, with the linear viscoelastic region (LVR) corresponding to the region where the storage modulus is constant and thus the sample is stable and 'solid-like', with its decrease indicating the loss of the elastic properties and thus the breakdown of the structure into a 'liquid-like' phase. Figure 3.19 shows the strain amplitude dependence of G' and G'' for a 0.2% w/v DBS-COOH gel; it is possible to observe a LVR up to approximately 3% strain for DBS-COOH alone or in the presence of heparin, decreasing significantly to approximately 1% strain when heparin-C16-DAPMA aggregates are present. This suggests that when heparin and C16-DAPMA are incorporated within the hydrogel, the overall material is less stable macroscopically as the gel network breaks down at lower strains than for the other two tested conditions. We suggest that the presence of C16-DAPMA-heparin hierarchical aggregates may impact on

the overall stability of the network perhaps somewhat limiting nanoscale chain entanglement which contributes to macroscopic behaviour and network formation. Additionally, the incorporation of heparin and heparin-C16-DAPMA aggregates within the gel network resulted in a decrease of G' value from approximately 2600 Pa to approximately 700 Pa, indicating that the addition of these components reduced the stiffness of DBS-COOH gel.

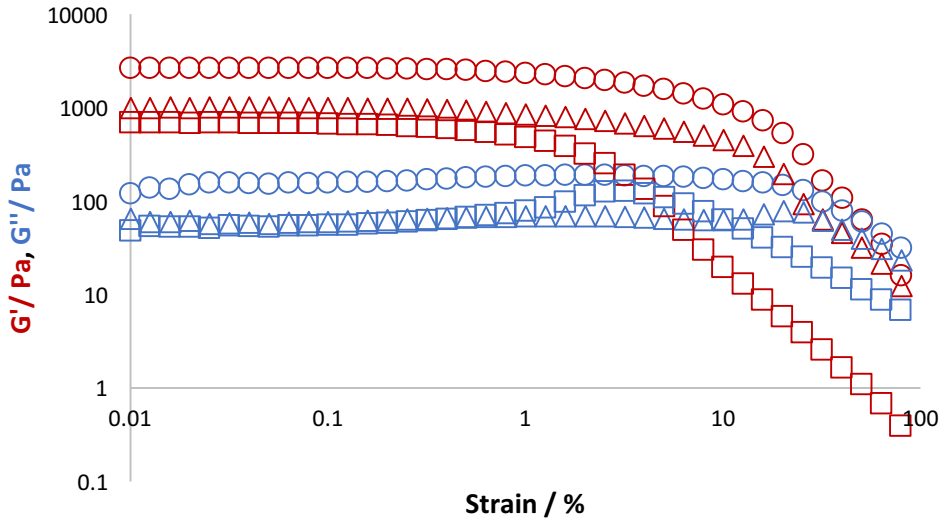

Figure 3.19. Strain amplitude dependence of the storage modulus (G') and loss modulus (G'') for DBS-COOH gel (○), DBS-COOH gel with heparin (△) and DBS-COOH gel with heparin and C16-DAPMA (□). Frequency = 1 Hz.

In an attempt to obtain a stronger and stiffer gel network, agarose (1% w/v) was mixed with the DBS-COOH hydrogelator (0.2% w/v) and the mechanical properties of the hydrid hydrogels tested in the presence and absence of heparin (1 mM), as shown in Figure 3.20. DBS-COOH-agarose hybrid gels were formed by applying a heat-cool cycle to a solution of dissolved DBS-COOH and agarose followed by addition of GdL to induce pH change. The addition of 1% w/v of agarose to DBS-COOH (0.2% w/v) resulted in a significant increase of G' value from approximately 2600 Pa to approximately 7900 Pa, meaning that agarose contributes to the formation of a stiffer gel network, while presenting a stability similar to the DBS-COOH hydrogel (LVR approximately 3%). The addition of heparin to the hybrid hydrogel gave rise to an identical G' value and LVR. Once again, this indicates that the

presence of agarose gives rise to a more robust stiffer gel, with G' increasing from approximately 700 Pa to 7900 Pa.

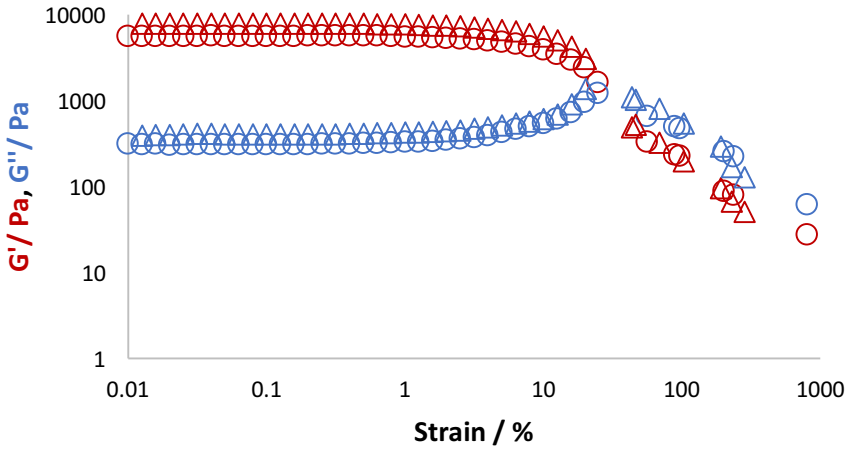

Figure 3.20. Strain amplitude dependence of the storage modulus (G') and loss modulus (G'') for DBS-COOH gel with agarose (○) and DBS-COOH gel with agarose and heparin (△). Frequency = 1 Hz.

The frequency dependencies (Figure 3.21) indicated that all gels were stable up to ca. 10 Hz. The G' and G'' values were as described in the variable strain experiments. The addition of agarose (Figure 3.22) significantly increased the stability to frequency up to ca. 50 Hz. Once again the G' and G'' values were as described in the variable strain experiments. It should be noted that in these experiments, frequencies were increased to unusually large values, in order to probe the response. As the frequency increases, the timescale over which properties are being measured becomes much shorter, and the gel eventually begins to harden, leading to an increase in G' and G". Similar effects have been discussed in the literature.[258,259]

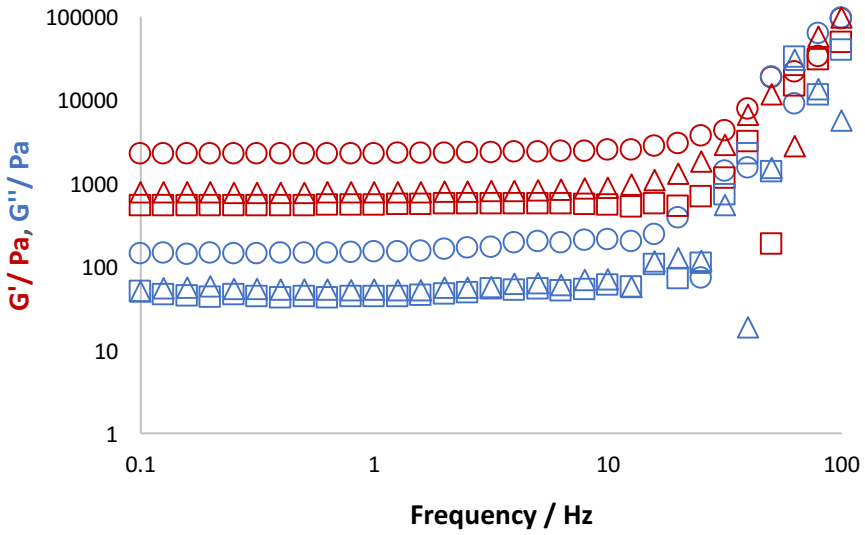

Figure 3.21. Frequency dependence of the storage modulus (G') and loss modulus (G'') for DBS-COOH gel (○), DBS-COOH gel with heparin (△) and DBS-COOH gel with heparin and C16-DAPMA (□). Amplitude strain = 0.1%.

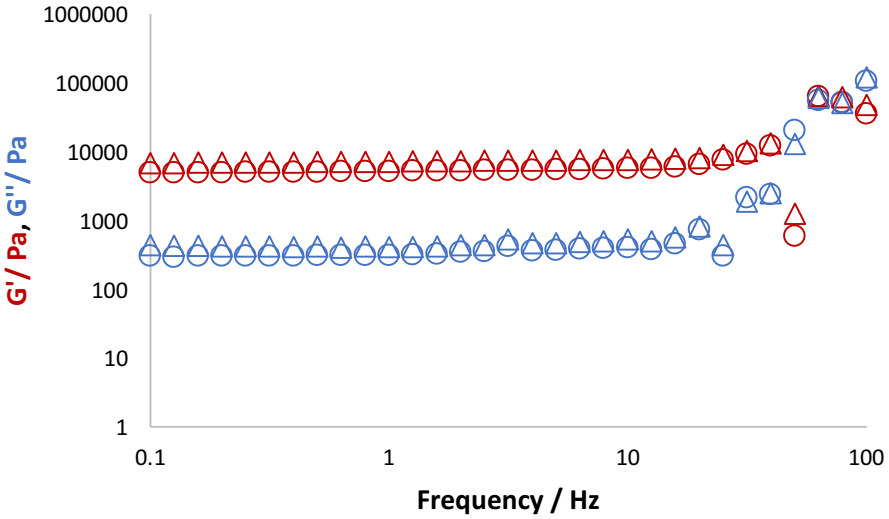

Figure 3.22. Frequency dependence of the storage modulus (G') and loss modulus (G'') for DBS-COOH gel with agarose (○) and DBS-COOH gel with agarose and heparin (△). Amplitude strain = 0.1%.

3.4. Release Studies

Heparin release: Buffer on top of the gel

One of the key aims of this project is to release heparin from hydrogels that may therefore act as a vehicle for heparin delivery in a controlled manner for clinical purposes and alternatively, to understand whether heparin angiogenic properties can promote cell growth. Therefore, the release of heparin from DBS-COOH hydrogels was investigated.

Heparin release from the hydrogels was studied by placing 1 mL of 10 mM Tris-HCl/ 150 mM NaCl buffer on top of 3 mL of hydrogel incorporating 1 mM of heparin, as shown in Figure 3.23. DBS-COOH hydrogels were prepared as described in Section 3.2. in 10 mM Tris-HCl/ 150 mM NaCl buffer. Aliquots (65 μL) of the supernatant buffer were removed over time, added into MalB solution (25.84 μM, 1935 μL) and the absorbance measured. As already discussed, MalB acts as a heparin sensor,[225] and in the presence of heparin, the MalB absorbance band changes significantly, so if heparin is being released into the buffer solution, it is possible to quantify this by means of a calibration plot using known heparin concentrations added into MalB solution.

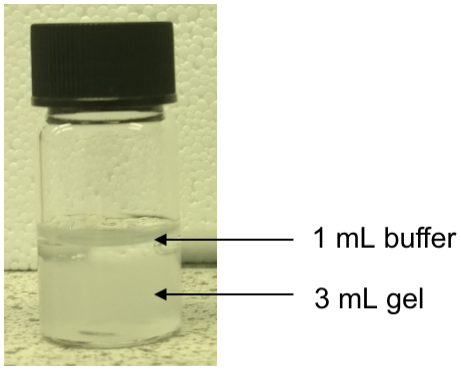

Figure 3.23. DBS-COOH hydrogel containing 1 mM of heparin with buffer on top for monitoring the release of heparin.

Results from Figure 3.24 show the release of heparin from DBS-COOH hydrogel (0.2% w/v) in the presence and absence of C16-DAPMA. Gradual release of heparin from DBS-COOH hydrogels was observed over time, reaching 86% of heparin being released after 72 h. Pleasingly, when C16-DAPMA was present it was possible to observe that no heparin was

released over 72 h, proving that it is indeed effectively binding to heparin and completely preventing release. A triggered release could therefore eventually be achieved, potentially by degradation of the binder.

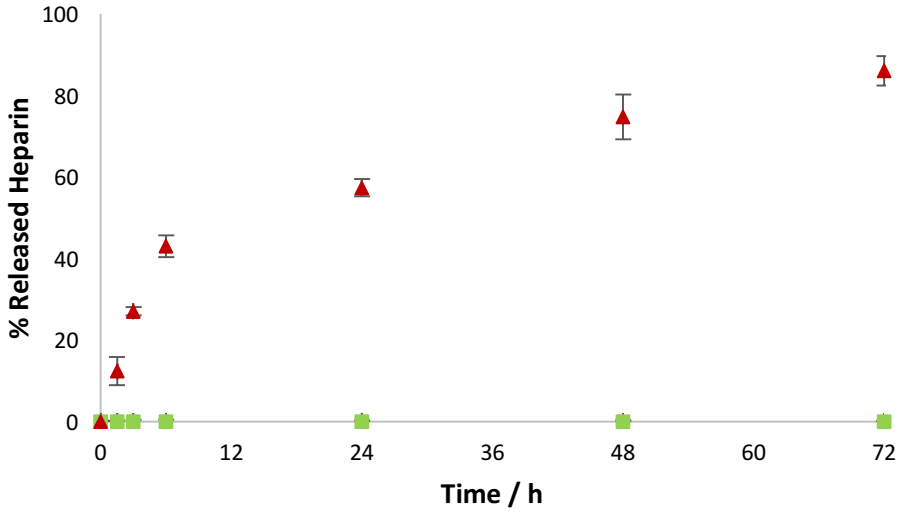

Figure 3.24. Heparin release from DBS-COOH hydrogel (0.2% w/v) with 1 mM of heparin (▲) and DBS-COOH hydrogel (0.2% w/v) with 1 mM of heparin interacting with 2 mM of C16-DAPMA(■).

Furthermore, the use of DBS-COOH hydrogelator alone as a heparin carrier may allow its controlled release due to the responsiveness of DBS-COOH to changes in (e.g.) pH or by controlling network density.[87] The DBS-COOH concentration was increased to 2% w/v with the aim of limiting diffusion of heparin out of the gel, so that release would only be achieved on breakdown of the DBS-COOH network. The same procedure as described above was followed. Comparing release from the 0.2% w/v and 2% w/v DBS-COOH gels (Figure 3.25) shows that increasing the DBS-COOH concentration significantly slows heparin release, stabilising at 35% release after 6 hours rather than continuing to increase up to 86% of released heparin. Increasing the concentration of gelator contributed to the decrease of the pore size of the gel, thus increasing the chance of the heparin becoming trapped in the network.[162] We suggest that the heparin that is initially rapidly released is that which is close to the surface of the gel and hence able to access the supernatant solvent. Once this surface-located heparin has been released, the remainder is entrapped within the dense gel network.

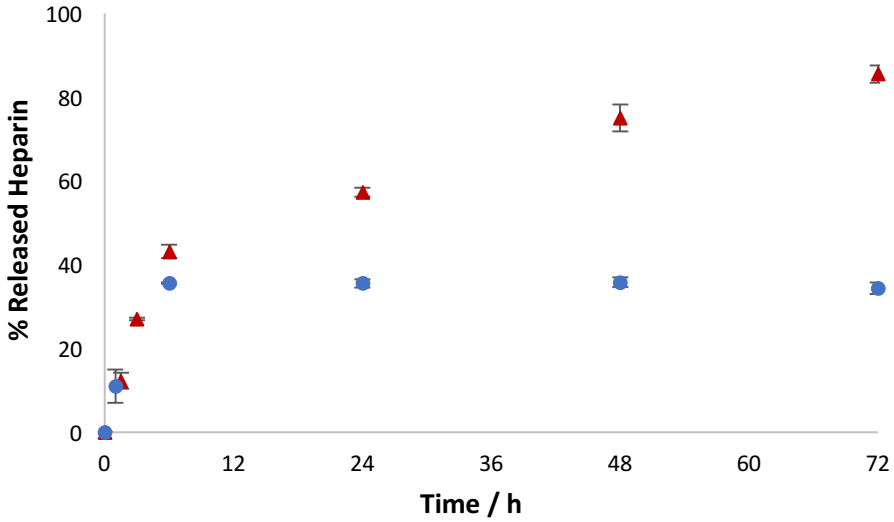

Figure 3.25. Heparin release from 0.2% w/v (▲) and 2% w/v (●) of DBS-COOH hydrogels with 1 mM of heparin.

We then studied further the impact of network density on heparin release. The DBS-COOH concentration was increased further to 5% w/v and 10% w/v. As this requires a large amount of DBS-COOH, for the initial study only 2 replicates of the 5% w/v and 1 replicate of the 10% w/v gels were produced. Figure 3.26 shows the obtained results, where it is possible to observe that the use of 5% w/v and 10% w/v DBS-COOH resulted in identical release profiles as for 2% w/v, with all reaching between 35%-40% maximum release of heparin. Since 5% w/v and 10% w/v of DBS-COOH did not contribute to any further reduction in release of heparin or significant changes in initial release kinetics when compared to 2% w/v, a concentration of 2% w/v DBS-COOH was chosen for all further release studies.

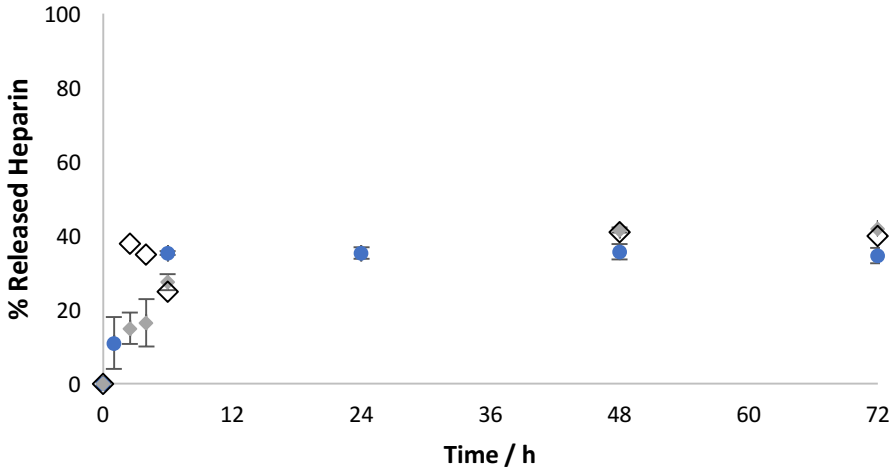

Figure 3.26. Heparin release from 2% w/v (●), 5% w/v (◆) and 10% w/v (◇) DBS-COOH hydrogels containing 1 mM of heparin.

To improve the strength of the DBS-COOH hydrogels, agarose was added to form a hydrid hydrogel with enhanced mechanical strength as described above, while keeping the properties of the LMWG, such as reversibility and response to external stimuli.

The effect of agarose concentration on heparin release was firstly studied by preparing gels with 1, 2.5, 5, 7.5 and 10% w/v agarose concentrations having 1 mM of heparin in 10 mM Tris-HCl/ 150 mM NaCl buffer, using the same method as described above. Figure 3.27 shows that as agarose concentration increases, heparin release is inhibited. With the increase in agarose concentration, a gel network will be formed with smaller pore sizes that will contribute to the entrapment of heparin and consequently to a lower release. Moreover, it is possible to verify that 1% w/v of agarose allows to the release of 93% of the heparin indicating that at this concentration it only has a small influence on heparin release, and hence only contributes to a higher gel strength as intended.

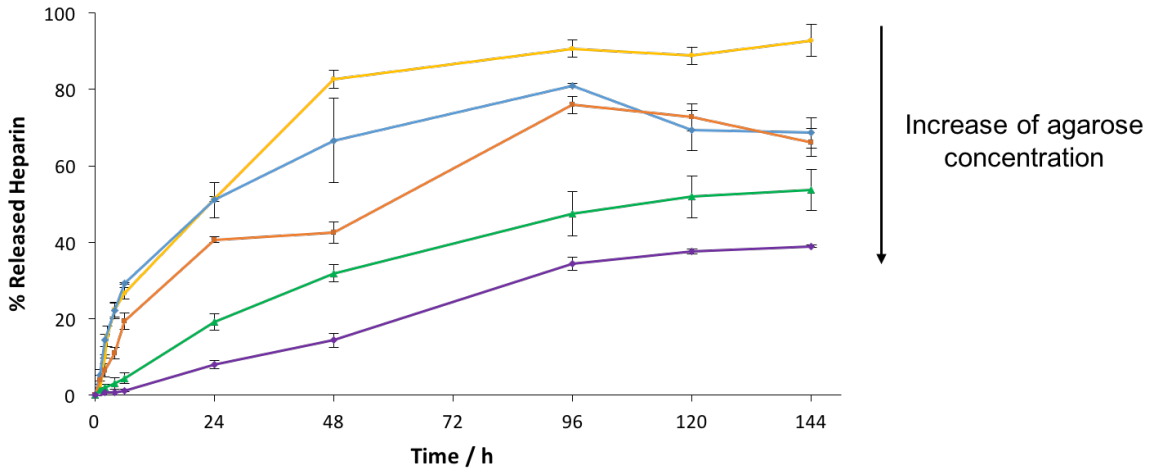

Figure 3.27. Heparin release from 1.0% w/v (yellow), 2.5% w/v (blue), 5.0% w/v (orange), 7.5% w/v (green) and 10% w/v (purple) of agarose gels with 1 mM of heparin.

Hybrid hydrogels were then prepared using 2% w/v DBS-COOH and 0.5% w/v and 1% w/v of agarose in order to test the influence of these hybrid gels on heparin release when compared with DBS-COOH hydrogels (2% w/v). As shown in Figure 3.28, the presence of 0.5 or 1% w/v of agarose together with DBS-COOH hydrogelator resulted in the same heparin release profile as when only DBS-COOH is used. In addition, of the two agarose concentrations, 1% w/v of agarose with 2% w/v DBS-COOH proved to form stronger hydrogels, being easier to handle without breaking. This indicates that the presence of 1% w/v of agarose allows the formation of a more robust gel while not affecting the release of heparin that can then be controlled by disruption of the DBS-COOH nanofibers.

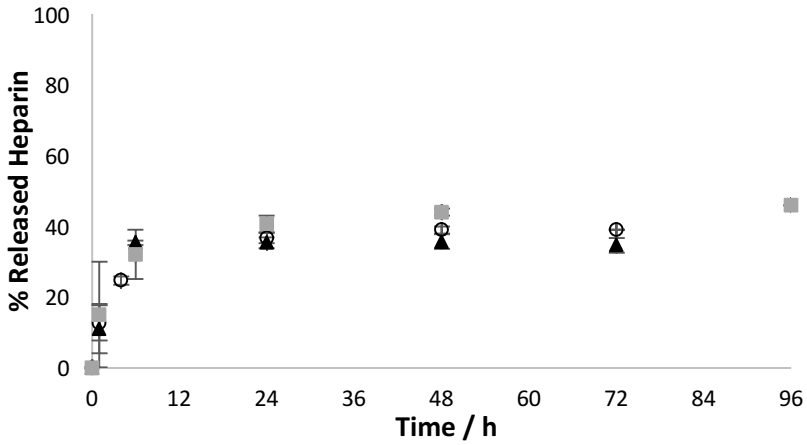

Figure 3.28. Heparin release from DBS-COOH hydrogel (2% w/v) with 1 mM of heparin in the absence of agarose (▲), with 0.5% of agarose (○) and 1% w/v of agarose (■).

Heparin Release: Gel cylinders

In vivo, heparin release would occur from the entire gel surface rather than just the top face; thus in an attempt to mimic these conditions, release was studied from gel cylinders containing 2.0% w/v DBS-COOH, 1.0% w/v agarose, and 17 mM heparin (Figure 3.29). It is important to note that the addition of agarose was essential to make these gels robust enough to handle in this way. The cylinders were each placed in 35 mL buffer giving a heparin concentration at full release of ca. 0.5 mM, within the range quantifiable by MalB.

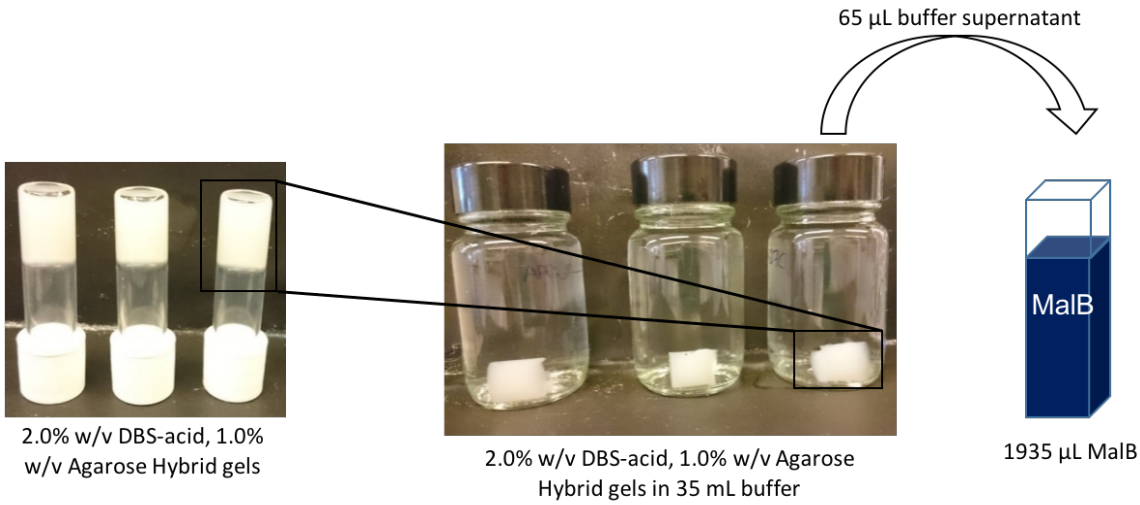

Figure 3.29. Assay design for heparin release from hybrid gel cylinders containing 2.0% w/v DBS-COOH, 1.0% w/v agarose and 17 mM heparin. 1 mL gels were prepared in small sample vials. The gel cylinders were then transferred to large glass jars and 35 mL buffer was added. 65 µL of buffer was removed over time, added to 1935 µL MalB and a UV-Visible spectrum recorded.

Figure 3.30 compares the release of heparin from the two different methods: gel-in-vial and gel cylinder. As expected the hybrid gel cylinders allow greater heparin release than the gels in vials, with 80% of release after 144 h instead of 40%. The higher release percentage obtained is due to the greater surface area to volume ratio of the gel cylinders in contact with the buffer. When the buffer is placed only on top of the gel this reduces significantly the surface area from which heparin release can occur.

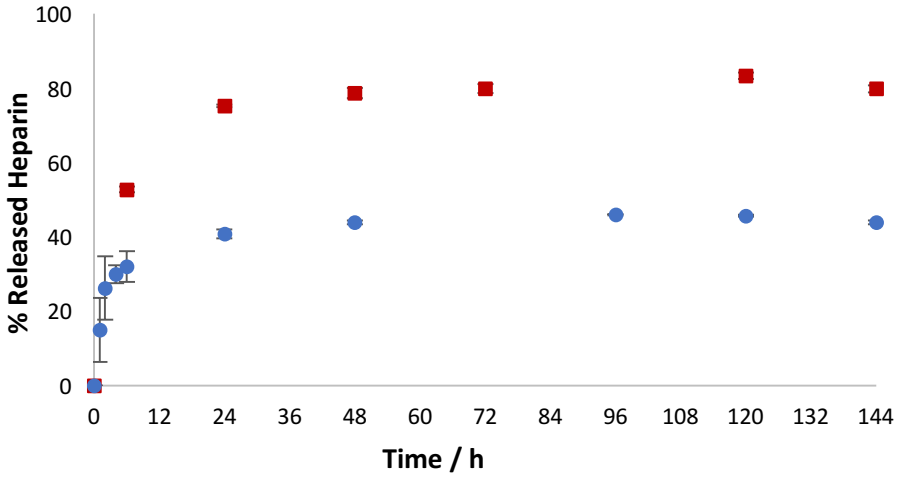

Figure 3.30. Different methods of heparin release from DBS-COOH hydrogel (2% w/v) and agarose (1% w/v). (●): Buffer on top of the gel. (■): Gel cylinder.

Heparin Release: pH triggered

The pH responsive assembly and disassembly of DBS-COOH in the presence of agarose has previously been reported.[87] Prior to using pH to achieve release of heparin, an NMR study was carried out to check that DBS-COOH is still able to disassemble with heparin present. Two hybrid gels (0.2% w/v DBS-COOH, 0.5% w/v agarose) were prepared, in the presence and absence of heparin. Their NMR spectra were recorded before and after gelation. $NaOH_{(aq)}$ was then added to the top of each gel and NMR spectra recorded periodically to observe the breakdown of the DBS-COOH (Figure 3.31).

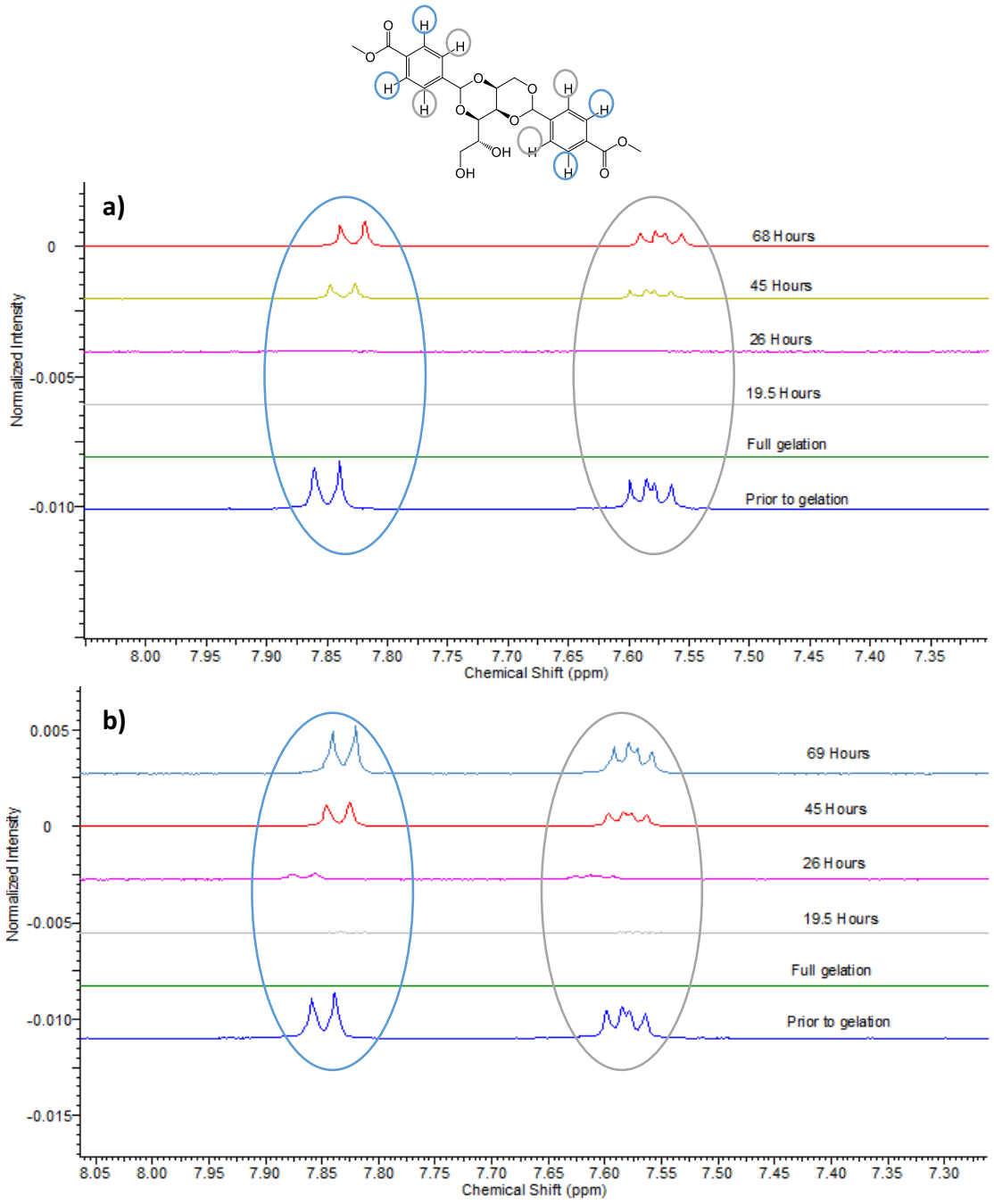

Figure 3.31. NMR spectra of aromatic protons of DBS-COOH prior to gelation, after full gelation, and after 19.5, 26, 45, and 68/69 hours exposure to NaOH a) in presence of agarose and absence of heparin, and b) in presence of agarose and heparin.

Prior to gelation the resonances corresponding to the aromatic protons of DBS-COOH appear as a duplet at 7.86-7.83 ppm and as a quartet at 7.59-7.56. As the DBS-COOH molecules self-assemble into gel fibres they become immobile on the NMR timescale, hence the peaks disappear from the spectrum. In both gels, these resonances then reappear after treatment with NaOH, indicating that the DBS-COOH fibres are being broken

down into mobile DBS-COO^- molecules, thus heparin does not inhibit the pH responsive disassembly of DBS-COOH nanofibers.

Subsequently, attempts were made to study pH-triggered release of heparin from the hybrid gels. 1 mL $NaOH_{(aq)}$ was added to the top of three hybrid gels (2.0% w/v DBS-COOH, 1.0% w/v agarose, 1mM heparin), and after 1 hour 65 µL supernatant was removed and neutralised with $HCl_{(aq)}$. However, neutralisation caused gelation of the supernatant, due to the presence of DBS-COO^-. This prevented its analysis by addition to MalB. Due to the pH sensitivity of MalB, neutralisation is necessary to quantify heparin release. Nonetheless, we are reasonably confident that heparin will be released from the gel along with DBS-COO^-.

A milder base, pH 9 buffer ($Na_2B_4O_7$/HCl), was then trialled as this could be added directly to MalB without affecting its absorbance. However, after 4 weeks the DBS-COOH gel (pK_a *ca* 4-5) remained intact, and so it appears that this base is unable to deprotonate DBS-COOH on a suitable timescale. A pH 10 buffer (borax/NaOH) was trialled but this was also unable to break down the DBS-COOH, thus future experiments should seek to find a base able to disassemble DBS-COOH on an appropriate timescale, while still allowing facile quantification of heparin release using MalB.

3.5. Cytocompatibility of DBS-COOH Hydrogels

The cytocompatibility of DBS-COOH hydrogels was then studied using mouse embryonic fibroblasts (3T3 cells). Both 2D and 3D cellular microenvironments were tested. For the 2D cell culture, the hydrogels were tested in 96-well plates, with cells added on top after the gelation process occurred (Figure 3.32). In addition, the gels were also prepared in inserts (transwells), with cells seeded in the well plate (Figure 3.33).

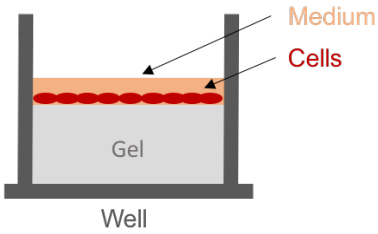

Figure 3.32. Schematic representation of 2D cell culture performed in 96 well plates.

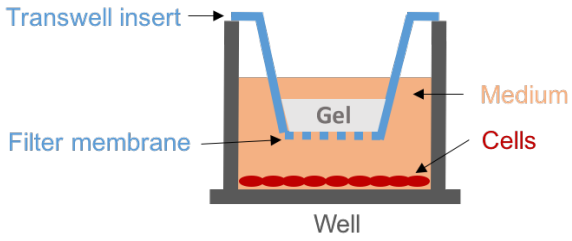

Figure 3.33. Schematic representation of 2D cell culture performed in transwells.

For both experiments, cell morphology was observed by optical microscopy and using phalloidin/ 4',6-diamidino-2-phenylindole (DAPI) staining. The distinction between live and dead cells was achieved by Calcein acetomethoxy (AM)/Propidium iodide (PI) staining. The labelling of cell mitochondria was obtained using MitoTraker green dye and the metabolic activity of the cells studied using the cells proliferation reagent: water soluble tetrazolium salt (WST-1).

3.5.1. 2D Cell Culture with Cells on Top

2D cell culture was tested using DBS-COOH hydrogels, however, it was observed that the addition of culture medium (Table 3.3 - a) dissolved the gel. The use of very small volumes of gel in the wells can contribute to a less stable network, which together with the fact that DBS-COOH only forms stable gels at acidic pH, may explain why it becomes liquid when in contact with cell culture media (pH 7-7.4).

A number of different media were tested (Table 3.3– b-e) in order to verify if only the DMEM, 10% FBS, 1% P/S medium was disrupting the gel. However, the use of different media also resulted in the dissolution of the DBS-COOH gels.

Table 3.3. Media tested in DBS-COOH gels.

	Medium/ Buffer	**Description**
a.	DMEM, 10% FBS, 1% P/S	Dulbecco's Modified Eagle's Medium (89% DMEM – high glucose in 3.7 g/L $NaHCO_3$), 10% fetal bovine serum (FBS) and 1% Penicillin/Streptomycin (P/S)
b.	$NaHCO_3$	3.7 g/L, pH=8.39
c.	EBM-2	Endothelial basal medium
d.	Mesencult ACF	Animal component free medium for human mesenchymal stem cells
e.	DPBS	Dulbecco's phosphate-buffered saline

Nonetheless, 2D cell culture assays with DBS-COOH gels were performed. Although on the addition of cell culture medium the gels became liquid. Therefore, instead of having cells growing on top of the gels, they were growing attached to the bottom of the wells. Subsequently, this assay only allows us to understand how the acidic properties of DBS-COOH can affect the cells, and as such it acts as an effective toxicity assay. 2D experiments were performed using a cell density of 50000 cells/mL and DBS-COOH in the absence of heparin, with 1 mM – 667 μg/mL and 2 mM – 1330 μg/mL of heparin.

Cell Morphology

Cell morphology was followed by optical microscopy and phalloidin/DAPI staining. Optical microscopy of DBS-COOH hydrogels allowed us to identify on day 1 the presence of slightly oval cells and the confluence of cells by day 5 (Figure 3.34). Images from day 7 were similar to the ones from day 5, with cells starting to detach due to the high confluency. Identical results were observed for samples containing 667 μg/mL, 1330 μg/mL of heparin and for the control experiments (cells with medium).

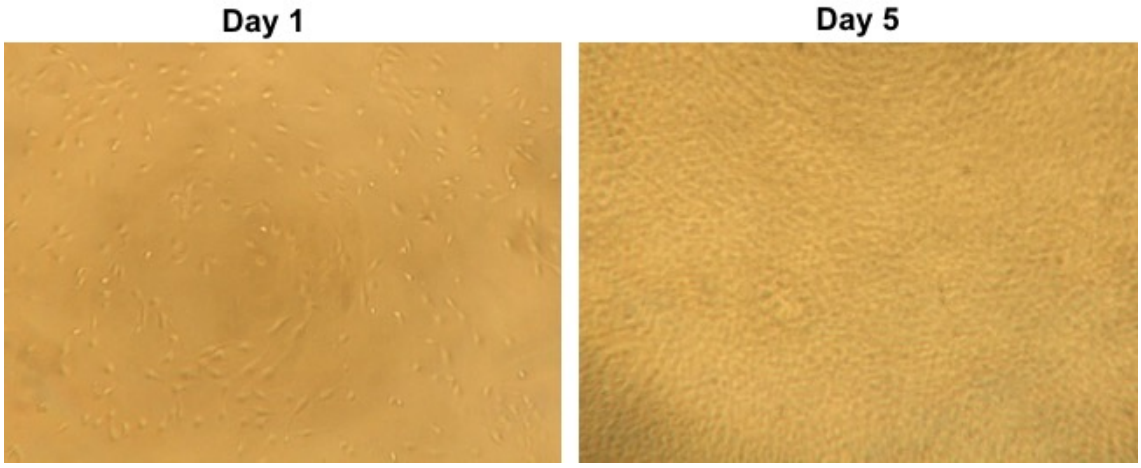

Figure 3.34. Optical microscopy images of DBS-COOH hydrogels with cells on top, at day 1 and 5. Magnification: 10x.

Fluorescence microscopy images of phalloidin/DAPI staining cells in DBS-COOH hydrogels are shown in Figure 3.35. Phalloidin is a peptide stain that binds to actin filaments, whereas DAPI is a blue fluorescent nucleic acid stain that specifically labels nuclei, allowing more detailed imaging of cell morphology.

On day 1 it is possible to verify that the cells are more spherical than on day 5, but the presence of some cell extensions are also visible, indicating adhesion onto the bottom of the wells. On day 5 the existence of stretched filaments is clearly noticeable, indicating a good adhesion of cells to the bottom of the wells. Similar images were obtained for samples containing 667 μg/mL, 1330 μg/mL of heparin and for the control experiments.

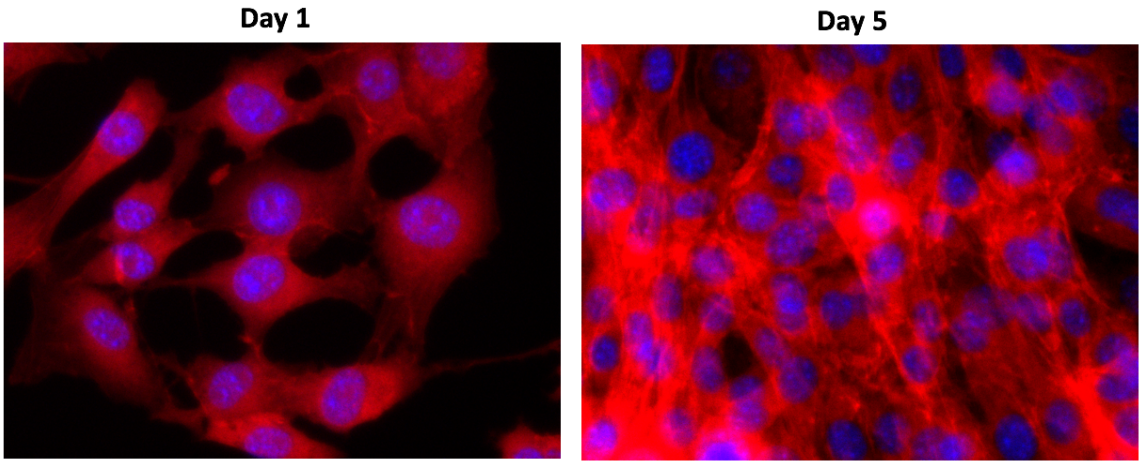

Figure 3.35. Fluorescence microscopy images of phalloidin/DAPI staining of cells on top of DBS-COOH hydrogels, at day 1 and 5. Magnification: 40x.

Live/Dead Staining

Calcein-(AM) was used to label live cells and PI was used to label dead cells. The former can enter viable cells and will undergo esterase cleavage of AM groups only if the cells are alive, as esterase activity does not exist in dead cells. Fluorescent calcein will then be trapped inside the cells, allowing the labelling of live cells. On the other hand, PI can only penetrate damaged cell membranes and thus only labels dead cells.

Figure 3.36 shows the fluorescence microscopy images obtained for DBS-COOH hydrogels in the absence and presence of heparin at day 1 and 7. On day 5, cells were fixed in order to try to have more time to obtain fluorescence microscopy images of all the samples. However, this did not allow clear images to be obtained; it was therefore not possible to identify the cells under the fluorescence microscope.

From the images it is possible to observe that on day 1 cells were alive (green fluorescence) and in the presence of 1330 μg/mL of heparin it appeared that cells were more stretched in comparison with the samples with no heparin and 667 μg/mL of heparin. Dead cells (red fluorescence) were not present on day 1, however it is believed that they may have been washed off due to the fact that dead cells are not attached and the samples were washed twice with DPBS. On day 7, cells were already confluent as expected, as optical microscopy showed that on day 5 confluency was achieved. Thus, an optimization of the initial number

of cells is needed. Importantly, however the cells were able to live for the 7 days of assay and proliferate in the presence of the DBS-COOH disrupted hydrogels. This suggests that DBS-COOH has low cellular toxicity which is promising for this class of material even though DBS-COOH could not maintain its gel structure under cell-growth medium.

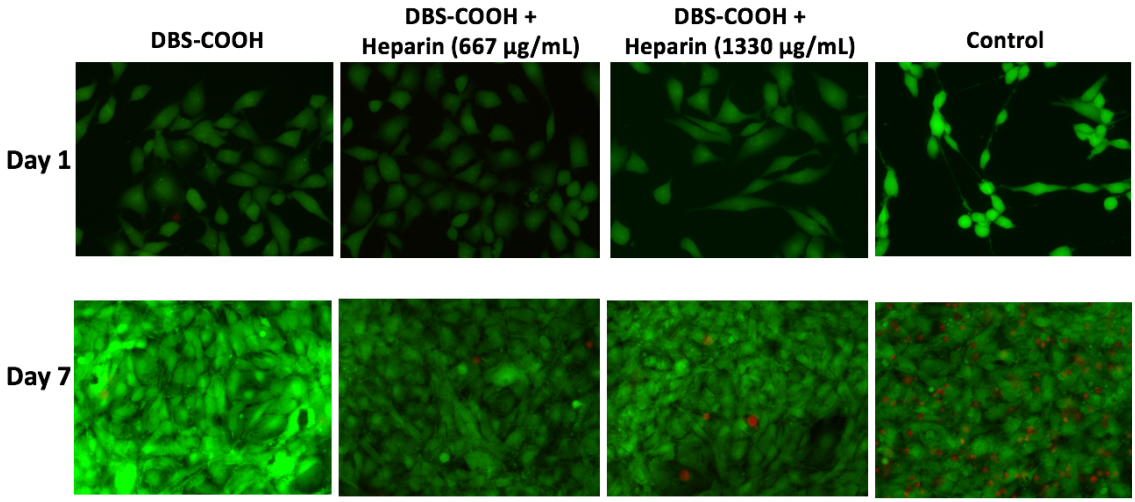

Figure 3.36. Fluorescence microscopy images of calcein-AM/PI staining of DBS-COOH hydrogels, DBS-COOH hydrogels in the presence of heparin (667 μg/mL and 1330 μg/mL) and controls (medium with cells), with cells on top, at day 1 and 7. Magnifcation: 20x.

MitoTracker Staining

MitoTracker green was used to label cell mitochondria and Hoechst stain was used to stain cells nuclei. MitoTracker green is a cell permeant dye that binds to the thiol groups in the mitochondria, while Hoechst dye is a cell permeable nucleic acid stain.

From Figure 3.37 it is possible to observe that on day 1, no significant differences are present between the cell mitochondria of DBS-COOH hydrogels with no heparin and with 667 μg/mL of heparin, which are similar to the control cells. However, when 1330 μg/mL of heparin is present, slightly more stretched cells appear to be present. These differences between cells under different conditions are more evident on day 5. Despite some cell confluency and the fact that for all the samples the cells became more elongated, when 1330 μg/mL of heparin is present, the cell elongation appear to be more obvious, as shown

in more detail on Figure 3.38. This suggests the presence of this concentration of heparin does impact on cell growth and importantly morphology.

On day 7, it was difficult to achieve clear images due to high confluency of the cells. Thus, it was not possible to obtain any more information related with this staining in specific, only the fact that cells appeared to continue to grow from day 5 to 7.

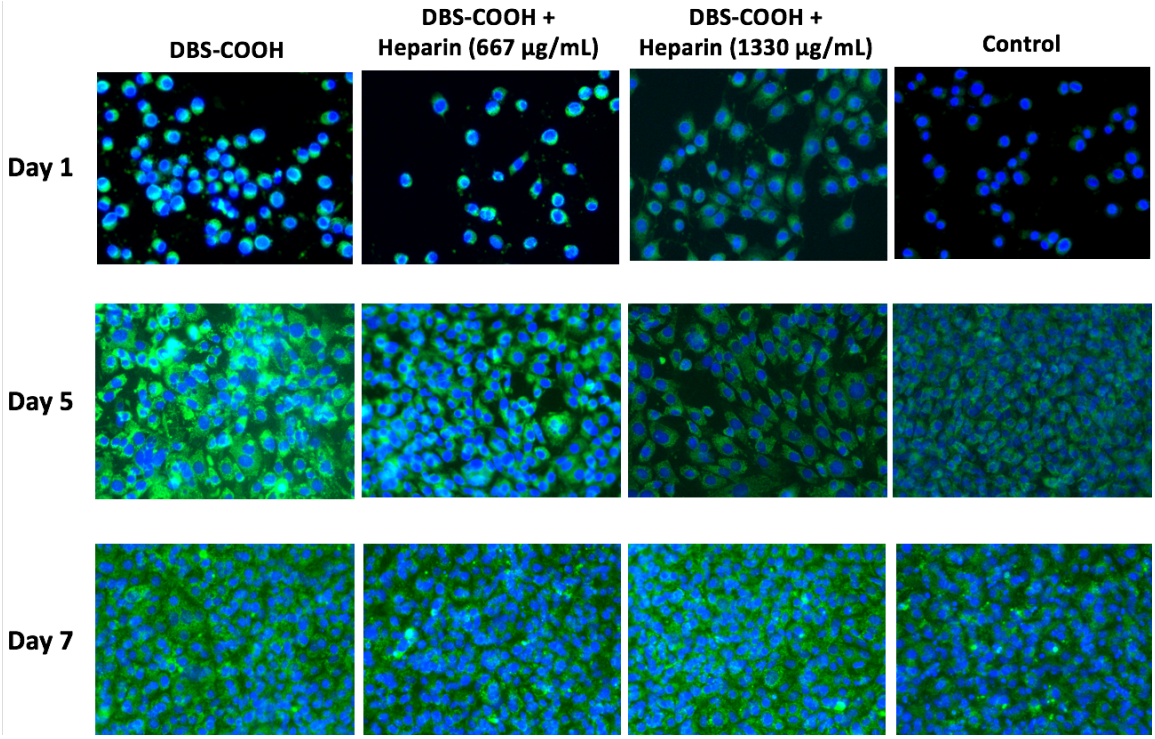

Figure 3.37. Fluorescence microscopy images of mitotraker/hoechst staining of DBS-COOH hydrogels, DBS-COOH hydrogels in the presence of heparin (667 µg/mL and 1330 µg/mL) and controls (medium with cells), with cells on top, at day 1, 5 and 7. Magnifcation: 20x.

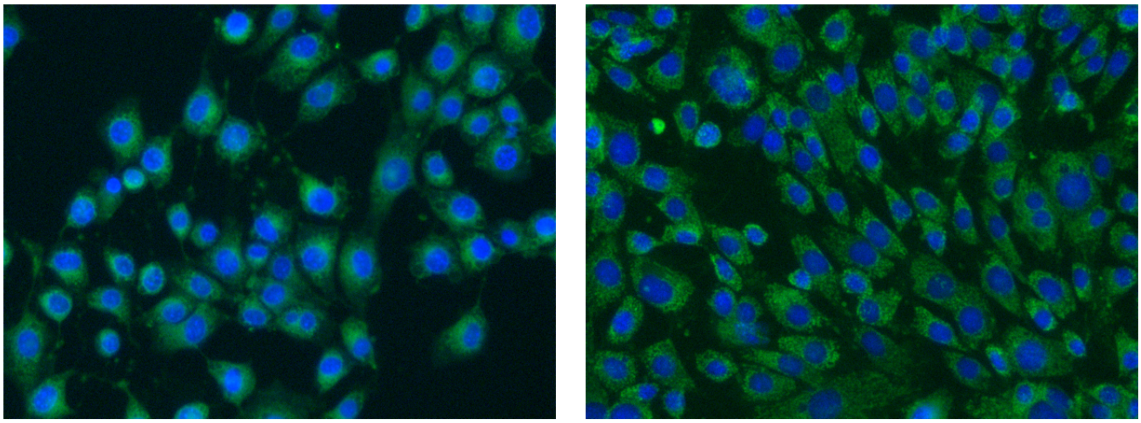

Figure 3.38. Fluorescence microscopy images of cell in DBS-COOH hydrogels with 1330 μg/mL heparin at day 1 (left) and 5 (right). Magnifcation: 20x.

Metabolic Activity

Cell proliferation reagent WST-1 was used to determine the metabolic activity of the cells. Cellular enzymes cleave tetrazolium salt WST-1 to formazan dye. This way, when measuring the dye absorbance it is possible to correlate it with the number of metabolically active cells - the higher the number of viable cells, the higher the concentration of formazan dye. Figure 3.39 shows the absorbance at 440 nm of formazan in DBS-COOH with no heparin, 667 μg/mL of heparin and 1330 μg/mL of heparin. When compared to the control absorbance values, it is noticeable that at days 1 and 5 for all conditions, there is a potential effect of DBS-COOH on the proliferation of the cells, with a higher metabolic activity being obtained in the control assay. However, by day 7 the cells have recovered and a similar metabolic activity to control was obtained.

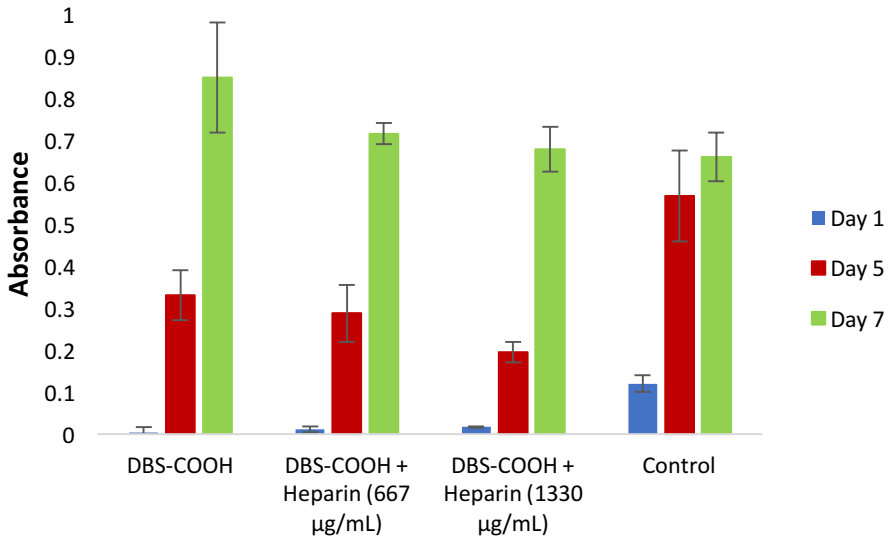

Figure 3.39. Absorbance of formazan at 440 nm with DBS-COOH hydrogels, DBS-COOH hydrogels in the presence of heparin (667 µg/mL and 1330 µg/mL) and control (medium with cells), with cells on top, at day 1, 5 and 7.

3.5.2. 2D Cell Culture in Transwells

DBS-COOH hydrogels were tested in transwells, with gels prepared in inserts, which were placed on top of medium, containing cells that were growing attached to the well plates (cell density: 40000 cells/mL). Once again, after the gels were in contact with cell culture medium they broke down.

Cell Morphology

Figure 3.40 shows the optical microscopy images obtained for the DBS-COOH hydrogels where it is possible to observe the presence of round and slightly oval cells on day 1. On day 5, the number of cells on the plates showed a reasonable increase, and presented more elongated shapes. On day 7, cells were confluent and thus it was difficult to obtain clear images. Similar results were obtained for samples containing 667 µg/mL, 1330 µg/mL of heparin and for the control experiments.

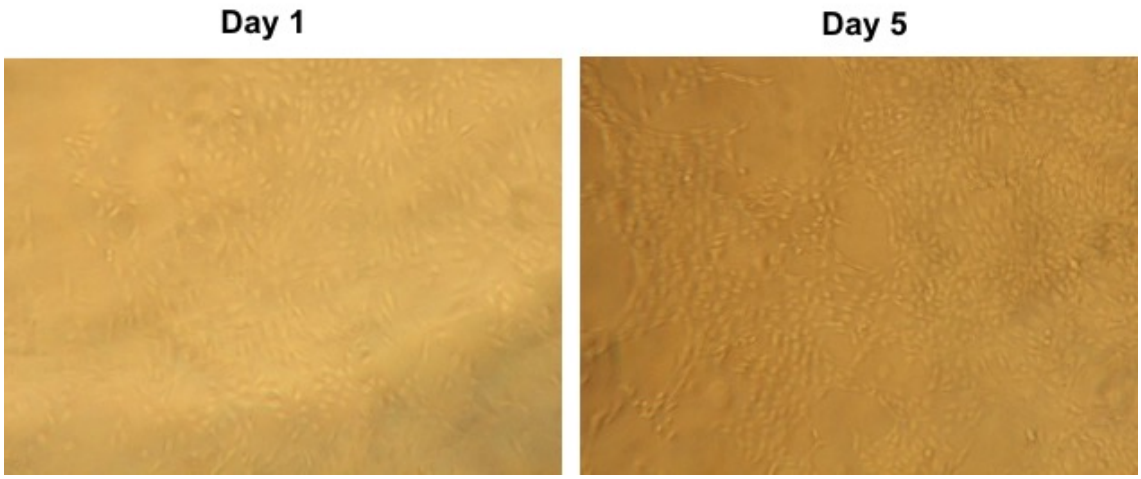

Figure 3.40. Optical microscopy images of DBS-COOH hydrogels in transwells, at day 1 and 5. Magnification: 10x.

Phalloidin/DAPI staining of cells with DBS-COOH hydrogels in transwells is shown on Figure 3.41. The obtained results were similar to the already described 2D cell culture with cells on top (see section 3.5.1.). Comparable images were also obtained for samples containing 667 μg/mL, 1330 μg/mL of heparin and for the control assays.

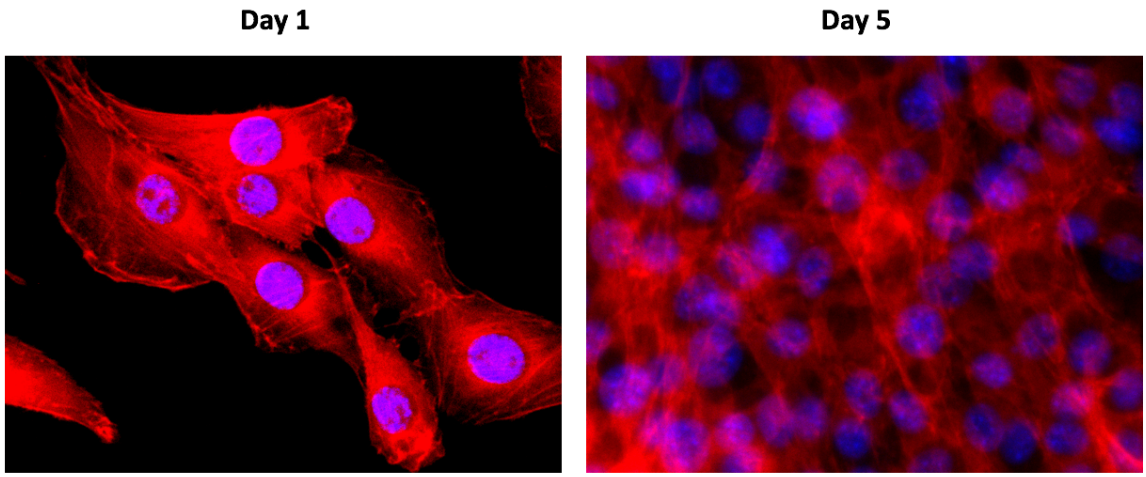

Figure 3.41. Fluorescence microscopy images of phalloidin/DAPI staining of DBS-COOH hydrogels in transwells, at day 1 and 5. Magnification: 40x.

Live/Dead Staining

Live/dead cells of DBS-COOH hydrogels in transwells can be identified on Figure 3.42. On day 1 live cells are easily detected and when 667 μg/mL and 1330 μg/mL of heparin is within the gels, it appears that cells are slightly more elongated than when no heparin is present. On day 5, cells from samples with 667 μg/mL and 1330 μg/mL of heparin were alive and proliferating. Cells from DBS-COOH hydrogels with no heparin and the control assay were fixated on day 5, thus clear images were not possible to obtain. On day 7, we can observe cells in high confluency once more. However, cells adhere and proliferate over 7 days indicating that the DBS-COOH is non-cytotoxic.

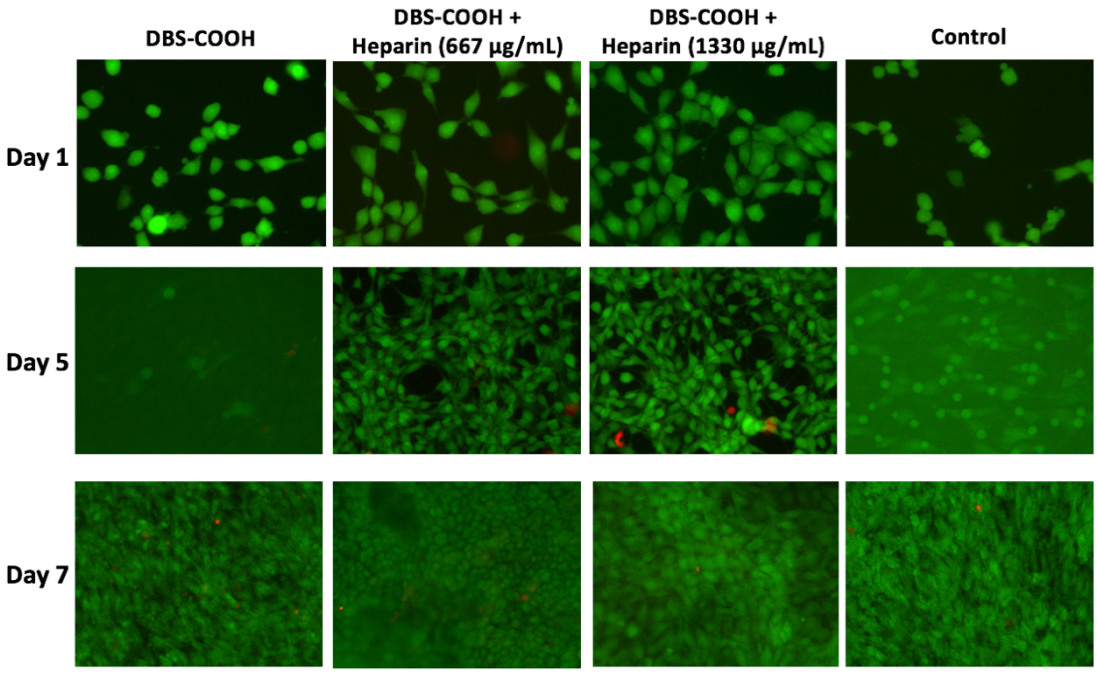

Figure 3.42. Fluorescence microscopy images of calcein-AM/PI staining of DBS-COOH hydrogels, DBS-COOH hydrogels in the presence of heparin (667 μg/mL and 667 μg/mL) and controls (medium with cells), in transwells, at day 1, 5 and 7. Magnifcation: 20x.

MitoTracker Staining

MitoTracker staining of cells with DBS-COOH hydrogels in transwells was obtained and is shown on Figure 3.43. On day 1 it is possible to observe that when 1330 μg/mL of heparin is within the gel network, the mitochondria appear to be slightly more stretched (Figure 3.44 for a more detailed image) than in the samples without heparin or with 667 μg/mL of

heparin. On day 5 and 7, cells high confluency makes it difficult to see clearly the mitochondria, and as on section 3.5.1. it is only possible to verify that cells appeared to continue to grow from day 5 to 7.

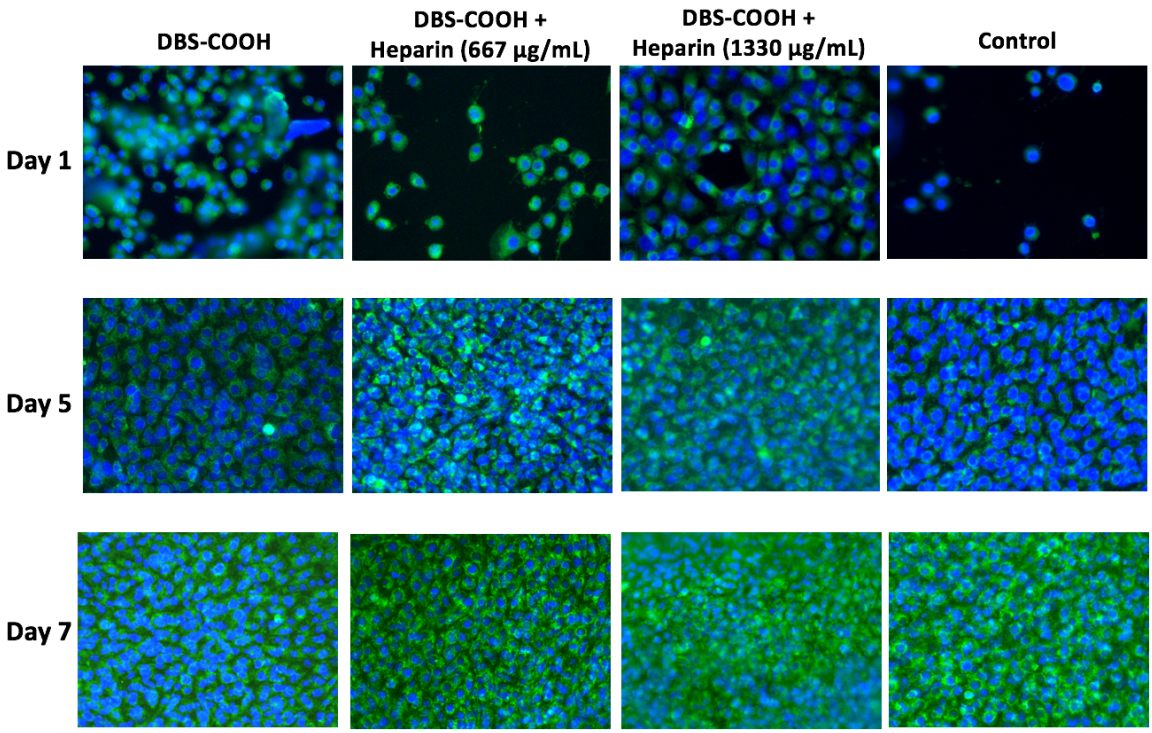

Figure 3.43. Fluorescence microscopy images of mitotraker/hoechst staining of DBS-COOH hydrogels, DBS-COOH hydrogels in the presence of heparin (667 µg/mL and 1330 µg/mL) and controls (medium with cells), in transwells, at day 1, 5 and 7. Magnifcation: 20x.

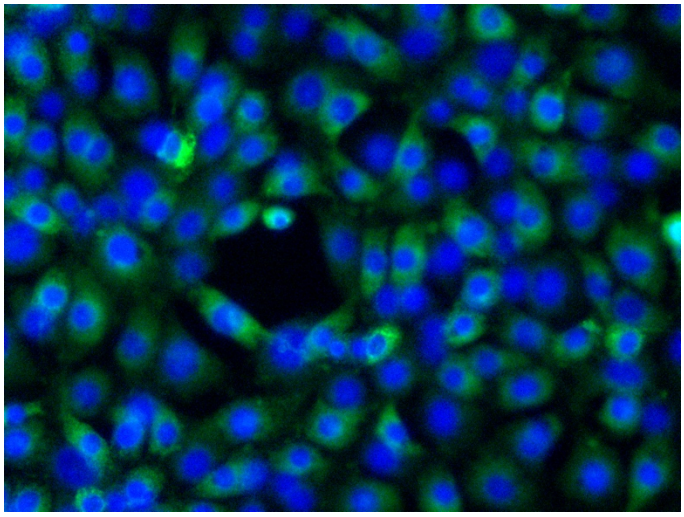

Figure 3.44. Fluorescence microscopy images of cell in DBS-COOH hydrogels with 1330 μg/mL heparin at day 1. Magnifcation: 20x.

Metabolic Activity

Figure 3.45 shows the obtained absorbance of formazan for DBS-COOH hydrogels in transwells assay. On day 1, the metabolic activity of cells from DBS-COOH hydrogels without heparin is slightly lower than the control, while when heparin is present the metabolic activity is similar to the control. Moreover, it is possible to verify on day 5, that when cells are in contact with DBS-COOH hydrogels without heparin and with 667 μg/mL of heparin, their metabolic activity is affected and is not as high as the control. However, when 1330 μg/mL of heparin is present the metabolic activity is higher and almost identical to the control, indicating a potential positive influence of heparin, at this concentration, on cell viability.

Despite the first 5 days showing a lower cell proliferation for DBS-COOH hydrogels with no heparin and 667 μg/mL of heparin, on day 7 the metabolic activity of cells increased. On the other hand, when 1330 μg/mL of heparin is incorporated, the metabolic activity of the cells remains practically the same. This may indicate that the presence of a certain concentration of heparin may have a positive influence on cell proliferation for the first 5 days and as the cells became confluent in the well they were then not able to proliferate further from day 5 to 7. To have a better understanding the cell number should be reduced, so the confluency of the cells does not interfere with the results. It should be noted that this result is significantly different from the metabolic activity obtained for the 'cells on top

of the gel', where in the absence or presence of heparin similar metabolic activity was obtained. This may be due to the fact that when gels were in transwells there was not an immediate contact of the cell medium with the gels and therefore the acidic conditions of the disrupted gels did not affect the cells in the same extent, and the influence of heparin was more evident in the transwells experiment.

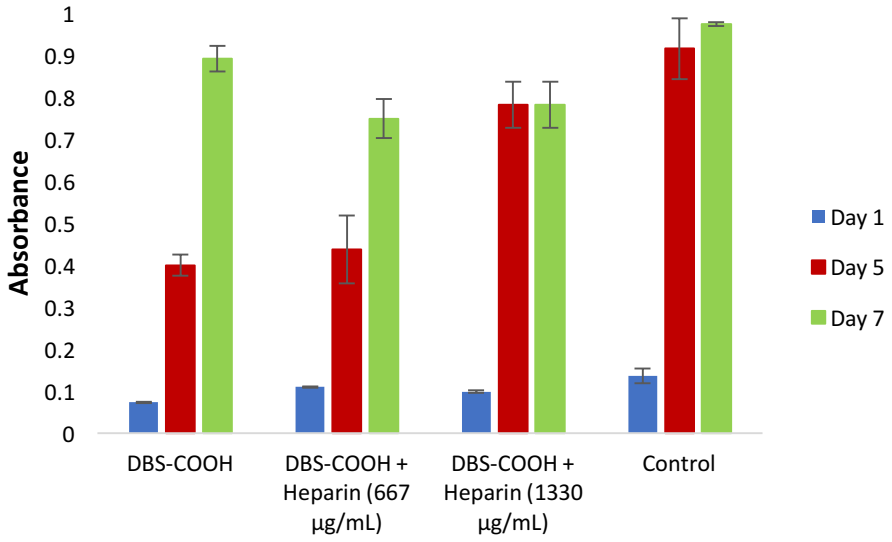

Figure 3.45. Absorbance of formazan at 440 nm with DBS-COOH hydrogels, DBS-COOH hydrogels in the presence of heparin (667 µg/mL and 1330 µg/mL) and control (medium with cells), in transwells, at day 1, 5 and 7.

3.5.3. 3D Cell Culture

The incorporation of cells within the DBS-COOH network could not be achieved, as the addition of culture medium dissolved the gel. Therefore, 3D cell culture assays were not performed.

3.6. Summary, Conclusions and Future Work

LMWG DBS-COOH was successfully synthesised and its orthogonal self-assembly with heparin and C16-DAPMA investigated. With the addition of different concentrations of binder and heparin to DBS-COOH separately, it was possible to verify that heparin did not prevent the formation of DBS-COOH gels, in contrast with the binder, which significantly affected the self-assembly of DBS-COOH, with no gels being formed at any tested concentration of binder, indicating the interaction of the amine heads of C16-DAPMA with

DBS-COOH. The orthogonal self-assembly of DBS-COOH with both binder and heparin revealed that when the binder is bound to heparin, gel formation does still occur. The presence of heparin and binder-heparin in DBS-COOH gels did not altered the apparent thermal stability, which was above 100 °C. IR spectra of the gel in the presence of binder and heparin showed the overlap of the characteristic vibrations of C16-DAPMA, heparin and DBS-COOH suggesting orthogonal assembly. The study of gel formation by NMR, revealed slight differences in the formation of gel with time, between DBS-COOH, DBS-COOH in the presence of heparin and DBS-COOH in the presence of heparin and binder, however the three different samples presented a gradual increase in the % of gel over time with 100% of gel being formed in the samples after 7 hours. The growth of the DBS-COOH nanofibers was also studied using CD and it was observed that heparin appeared to promote the growth of the fibers – suggesting that the nanofibers formed by DBS-COOH nucleate more quickly in the presence of heparin; while the presence of heparin with binder contributed to slower self-assembly of DBS-COOH gelator nanofibers – which can reflect greater difficulty in assembling nanofibers as a result of steric hindrance provided by the relative large hierarchical C16-DAPMA-heparin aggregates. The use of MalB solution on top of the gel allowed to prove that binder - heparin interactions are maintained within the gel. TEM and SEM images of DBS-COOH in the presence of heparin demonstrated that heparin alone has same impact on the assembly and morphology of the gel. In the presence of both, C16-DAPMA and heparin TEM showed the clear presence of hierarchical aggregates along with the fibers, proving once more that the binder-heparin interactions are still present when incorporated in the hydrogel. This clearly indicates that within this highly complex multi-component material, orthogonal interactions can occur in order to generate highly structured potentially functional nano-composites. The mechanical properties of DBS-COOH confirmed its gel-like characteristics, that were not significantly affected with the incorporation of heparin and heparin-C16-DAPMA aggregates, while the addition of agarose contributed to the formation of a stronger gel, which could be handled. Therefore, it is possible to conclude that DBS-COOH and heparin are largely orthogonal while DBS-COOH and C16-DAPMA are clearly not orthogonal. Additionally, mixing both heparin and C16-DAPMA into DBS-COOH leads to a largely orthogonal system in which both DBS-COOH and C16-DAPMA self-assemble into their own respective nanostructures, with heparin preventing the disruptive effect of C16-DAPMA by binding strongly to the micelles.

Furthermore, the release of heparin from DBS-COOH hydrogels was achieved with the presence of C16-DAPMA completely inhibiting the release of heparin. The incorporation and release of heparin from a hybrid gel combining the PG agarose with the LMWG DBS-COOH was successfully demonstrated. Initial heparin release studies indicate that release can be controlled either by changing the surface area for release, or by altering the concentration of agarose and/or DBS-COOH, resulting in a change of pore size of the gel. In conclusion, there is a threshold DBS-COOH network density that prevents heparin diffusion, limiting total release, while agarose has a progressive effect on diffusion and release of heparin with higher agarose loadings decreasing heparin release kinetics. NMR studies indicate that DBS-COOH in the presence of heparin and agarose is still able to assemble and disassemble in response to pH changes, releasing heparin whilst still maintaining gel integrity. However, problems were faced quantifying this release due to the pH sensitivity of the MalB dye.

The present study also allowed to conclude that 3D cell culture assays are not possible to perform using DBS-COOH gels as they dissolve in cell culture medium. In respect to the 2D cell culture it is possible to conclude that DBS-COOH hydrogels are not good candidates, once more because they dissolve in cell culture medium and thus no gel is present. On the other hand, from the obtained results it seems that DBS-COOH is not cytotoxic - the cells were able to adhere onto the bottom of the wells and proliferate, and thus other biological applications may be explored. However, we should take into account that the medium was replaced over the week and, as the gels dissolved, they could had been washed off, specially for the 2D cell culture with cells on top. Moreover, the cells used are very resistant and the use of more sensitive cells may give more conclusive results about DBS-COOH cytotoxicity. The cytotoxicity should therefore be investigated by optimizing the number of cells used and by using different type of cells.

Further studies could seek to optimise pH-responsive heparin release by finding a base able to deprotonate DBS-COOH on a suitable timescale, while still allowing facile heparin quantification using MalB. Additionally, the fact that C16-DAPMA is a very stable binder may make it difficult to achieve the controlled release of heparin from the multi-

component hydrogel network. It can easily be replaced by a heparin binder with a degradable linkage.[207]

4. Orthogonal Self-Assembly of DBS-CONHNH$_2$ Hydrogels with C16-DAPMA and Heparin

Cytocompatibility studies were performed on a placement at Nano-FM in Groningen, Netherlands, as part of the SmartNet network.

4.1. Introduction

Following the results obtained in Chapter 3 and the limitations observed for our pH responsive LMWG for mammalian cell culture in terms of gel instability, the replacement of DBS-COOH with a different DBS derivative was of great interest. DBS hydrazide (DBS-CONHNH$_2$ - Figure 4.1) has previously been reported by the Smith group as a LMWG capable of gelating water as solvent, and forming stable hydrogels across a wide range of pH (2-11.5) by applying a simple heat-cool cycle.[88] Therefore, DBS-CONHNH$_2$ hydrogels ideally can provide a more stable microenvironment to which cells can adhere and proliferate. For this purpose, this chapter will focus on the properties of DBS-CONHNH$_2$ as a potential scaffold for cell growth and the orthogonal self-assembly of the hydrogel with heparin and self-assembled C16-DAPMA. As in the previous Chapter, the incorporation of heparin into a hybrid hydrogel containing agarose as PG and DBS-CONHNH$_2$ as LMWG will also be studied and the release of heparin from different multi-component hydrogels investigated. Additionally, the cytocompatibility of these systems will be tested.

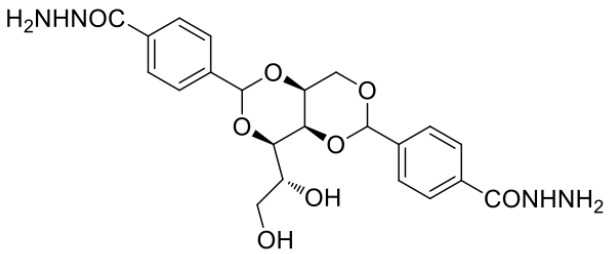

Figure 4.1. Chemical structure of LMWG DBS-CONHNH$_2$.

4.2. Synthesis of DBS-CONHNH$_2$ Gelator and Temperature Induced Hydrogelation

DBS-CONHNH$_2$ was obtained from the DBS-COOCH$_3$ derivative using a hydrazination[260] reaction as previously reported the by Smith group.[88] DBS-COOCH$_3$ was synthesised as previously described in Chapter 3. The reaction between DBS-COOCH$_3$ and excess hydrazine monohydrate resulted in a white precipitate that after filtration and washing yielded DBS-CONHNH$_2$, as shown in Scheme 4.1. All characterisation data for DBS-CONHNH$_2$ were in agreement with previous reports.

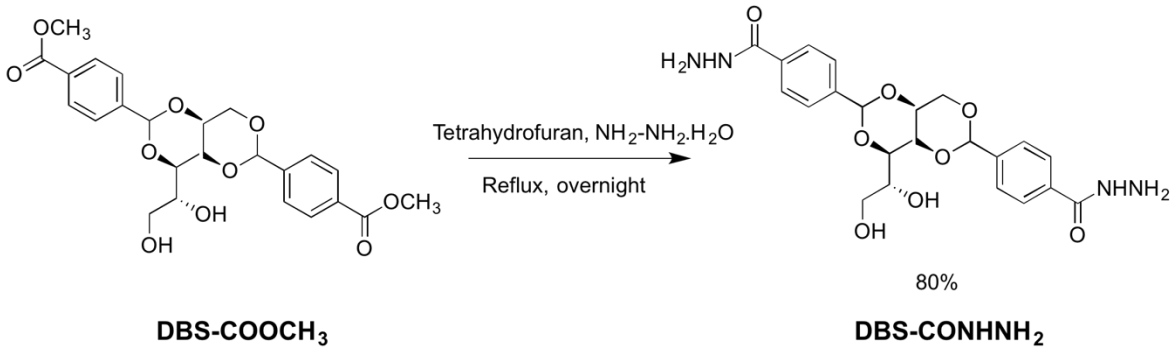

Scheme 4.1. Synthesis of DBS-CONHNH$_2$.

The gelation of the hydrazide gelator in 10 mM Tris-HCl/ 150 mM NaCl buffer was achieved using a heat-cool cycle. The formation of hydrogels was obtained after heating the DBS-CONHNH$_2$ solution until the gelator was completely dissolved and a clear solution was observed, following by cooling to room temperature. In order to obtain stable and uniform gels, a concentration of 0.4% w/v of DBS-CONHNH$_2$ was used. This concentration of DBS-CONHNH$_2$ was found to be the maximum concentration of gelator that resulted in the formation of stable and uniform hydrogels. When using higher concentrations of DBS-CONHNH$_2$ not all of the gelator was dissolved upon heating, resulting in a weak and unstable hydrogel. Heating the samples for longer periods of time was not possible as the solutions started to boil.

4.3. Study of Orthogonal Self-Assembly of DBS-CONHNH$_2$ with C16-DAPMA and Heparin

The self-assembly of DBS-CONHNH$_2$ hydrogels incorporating heparin, and heparin interacting with C16-DAPMA micelles were each studied to understand how the properties of the individual nanoarchitectures are affected when incorporated into a single system.

C16-DAPMA Stability at High Temperatures

DBS-CONHNH$_2$ hydrogels are formed immediately after heating, thus the only way to incorporate heparin and heparin-C16-DAPMA aggregates within the gel network was by adding them to the solution before heating. Therefore, the stability of the C16-DAPMA micelles at high temperatures was tested, to understand how temperature affects C16-DAPMA self-assembly and interactions with heparin.

DLS studies of C16-DAPMA were performed at 25 °C and 70 °C (Table 4.1). From the obtained results, it is possible to observe that the hydrodynamic diameter of the micelles is similar after heating, indicating that micellar size does not appear to be influenced by high temperatures. High zeta potential values, in the same range, were also obtained for the two different temperatures, indicating that heating does not affect the repulsion between the particles and the micelles are highly charged at 70 °C. Moreover, it was observed that the increase in temperature contributed to a decrease of the polydispersity index, indicating that at high temperatures the micelle population has a better monodispersity. This is in line with expectation – micellar assembly occurs through the entropically driven hydrophobic effect, which will be favoured at elevated temperatures.

Table 4.1. Average hydrodynamic diameter, zeta potential and polydispersity index (PdI) of C16-DAPMA micelles at 25 °C and 70 °C.

	Micelles at 25 °C	**Micelles at 70 °C**
Z-Ave (nm)	6.2 ± 1.3	5.6 ± 0.2
PdI	0.63 ± 0.02	0.13 ± 0.04
ζ Potential (mV)	51.7 ± 2.2	49.7 ± 6.9

The interactions between C16-DAPMA and heparin were then studied at 85 °C using a MalB assay. As described in Chapter 2, when free in solution, MalB presents a characteristic UV-Vis band with a maximum absorbance at 615 nm. When interacting with heparin, this UV-Vis band decreases substantially in intensity. Therefore, if MalB is displaced from its complex with heparin by the interaction of heparin with another molecule, this can be easily verified by an increase in the absorbance. As discussed in Chapter 2, C16-DAPMA is an effective heparin binder at room temperature, and in order to understand the influence of high temperature on heparin-C16-DAPMA interactions, a solution of C16-DAPMA was heated to 85 °C in an oil bath and added into a MalB solution with heparin. In addition, a solution containing C16-DAPMA micelles interacting with heparin was also heated at 85 °C for 10 min and added into a solution of free MalB. The absorbance spectra were recorded and compared with the spectra obtained for the same conditions at 25 °C (Figure 4.2).

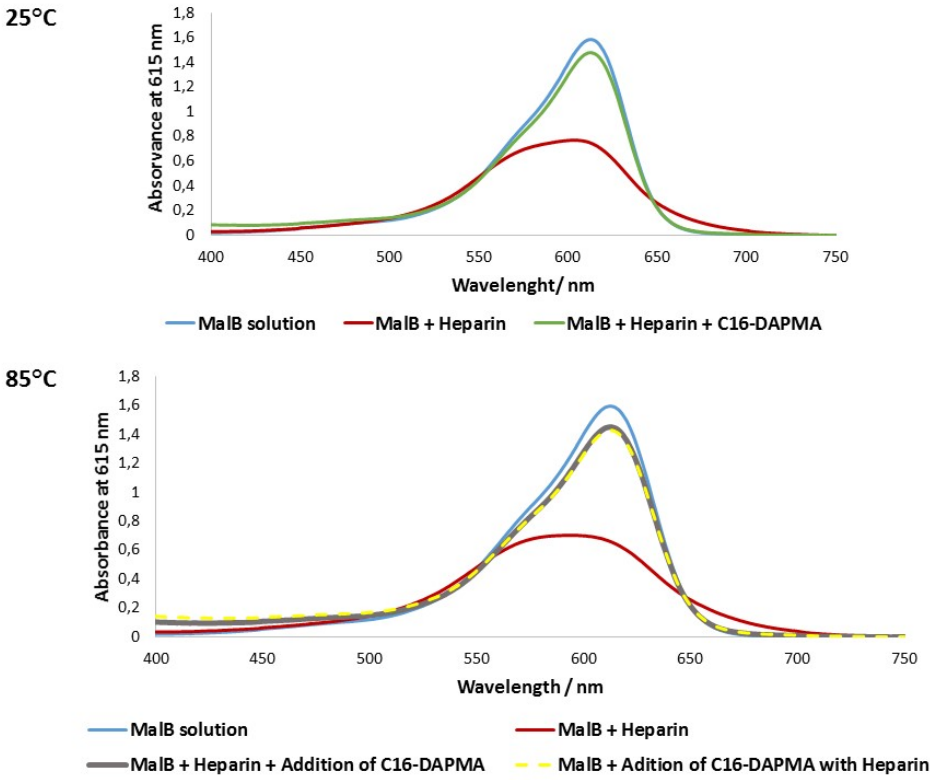

Figure 4.2.UV-Vis spectra of MalB free in solution, with heparin and in the presence of C16-DAPMA, at 25 °C and 85 °C.

From the obtained results it is evident that for both situations tested at high temperature, the MalB band absorbance increased in intensity when the C16-DAPMA was present, indicating that the MalB is displaced from its complex and thus C16-DAPMA is interacting with heparin at 85 °C.

In conclusion, the characteristics of C16-DAPMA and its interactions with heparin do not appear to be affected with high temperatures. Therefore, studies proceeded with the incorporation of heparin and C16-DAPMA into the DBS-$CONHNH_2$ hydrogels via a heat-cool cycle.

Gel Formation with different Concentrations of Heparin

In order to initially and quickly test the influence of heparin on the formation of the hydrazide gel, different concentrations of heparin (38 µM; 150 µM; 300 µM; 400 µM; 600 µM) were added to DBS-$CONHNH_2$. From all concentrations tested, stable and

homogeneous gels were obtained, indicating that the presence of heparin does not prevent self-assembly of the gelator.

Gel Formation with Different Concentrations of C16-DAPMA

Different concentrations of C16-DAPMA (150 μM; 300 μM; 600 μM; 800 μM; 1000 μM; 1200 μM) were also added to DBS-$CONHNH_2$ gels in order to observe their influence on gel formation. Once more, for all the concentrations used, the formation of stable and homogeneous gels was observed. This indicates that the presence of C16-DAPMA micelles does not interfere in the self-assembly of the DBS-$CONHNH_2$ gelator. This is contrary to what was observed with DBS-COOH LMWG and highlights our previous suggestion in Chapter 3 that acid-amine interactions were the reason C16-DAPMA inhibited the gelation of DBS-COOH.

Gel Formation with Constant Concentrations of Heparin and Different Concentrations of C16-DAPMA

Gel formation was also tested by keeping the heparin concentration constant and increasing C16-DAPMA concentration in order to verify the optimal charge ratio of these two molecules for formation of stable gels. For heparin concentrations of 150 μM, 300 μM, 400 μM and 600 μM a maximum of 600 μM, 1200 μM, 1600 μM and 2400 μM of C16-DAPMA was used, respectively, and concentrations below these values were also tested (Table 4.2). These maximum values correspond to charge ratios +/- of 2.

Table 4.2. Test of different heparin/binder ratio in gel formation.

[Heparin] (μM)	[C16-DAPMA] (μM)	Gel Formation
150	Below 600	Stable gel
300	Below 1200	Stable gel
400	Below 1600	Stable gel
600	Above 1600	Non uniform gel
	Below 1500	Stable gel

It was verified that for heparin concentrations below 400 µM the use of the maximum concentrations of C16-DAPMA calculated still gave rise to the formation of stable gels, as did concentrations below that. For 600 µM of heparin, only concentrations of C16-DAPMA below 1500 µM led to the formation of stable gels, with higher concentrations resulting in gels with the presence of aggregates or unstable gels (Figure 4.3).

Figure 4.3. DBS-$CONHNH_2$ (0.4% w/v) gel in 10 mM Tris-HCl/ 150 mM NaCl buffer: stable and uniform gel (left), non-uniform gel (centre) and unstable gel (right).

Therefore, the incorporation of C16-DAPMA interacting with heparin did not affect gel formation, but at higher heparin/C16-DAPMA concentrations non-uniform or unstable gels resulted. This may relate to the fact that at higher heparin/C16-DAPMA concentrations, more larger aggregates will be present, and the dispersity of these aggregates become greater. We suggest the self-assembly of the DBS-$CONHNH_2$ becomes more sensitive to the excess aggregates. Thus, it is believed that on increasing the heparin concentration a lower molar ratio between C16-DAPMA and heparin is needed (Table 4.3), limiting the formation of aggregates that may affect gel formation.

Table 4.3. Binder/Heparin molar ratio and charge ratio +/- with increasing heparin concentration.

[Heparin] (µM)	Binder/Heparin Molar Ratio	Charge ratio +/-
38	4:1	2.0
150	4:1	2.0
300	4:1	2.0
400	4:1	2.0
600	2.5:1	1.2

4.3.1. Thermal Stability and T_{gel} Determination

The thermal stability of the gels formed in the previous section was tested by simple tube inversion methodology. The T_{gel} was considered to be the temperature when the gel starts to deform and starts to slip in the vial walls when it is turned upside down.

DBS-$CONHNH_2$ (0.4% w/v) gel in 10 mM Tris-HCl/ 150 mM NaCl buffer presented a T_{gel} value of 86 °C. For the different concentrations of heparin tested in DBS-$CONHNH_2$ gel, the T_{gel} values obtained were between 83-86 °C, proving that the incorporation of heparin does not affect significantly the thermal stability of the gel. The same was observed for the different concentrations of C16-DAPMA with T_{gel} values also between 83-86 °C. For the different concentrations of C16-DAPMA with constant heparin concentrations (150 μM; 300 μM; 400 μM; 600 μM) that resulted in uniform and stable gels, the T_{gel} values were approximately 66 °C, below the T_{gel} value of DBS$CONHNH_2$ gel, indicating that the presence of C16-DAPMA and heparin aggregates somewhat affects the thermal stability of the gel, consistent with the view that that hierarchical aggregates may somewhat hinder gel network formation.

4.3.2. Infrared Characterisation

IR characterisation was performed for the gel formed with DBS-$CONHNH_2$ (0.4% w/v) alone, in the presence of 300 μM of heparin, 1200 μM of C16-DAPMA and in the presence of 300 μM of heparin and 1200 μM of C16-DAPMA (Figure 4.4). By comparing the obtained spectra, it is possible to observe that the expected peaks are present in the multi-component gel and that the spectrum corresponds to simple overlap of IR spectra of the three compounds. Additionally, the IR spectra of DBS-$CONHNH_2$ with heparin and DBS-$CONHNH_2$ with C16-DAPMA also correspond to the overlap between the typical IR frequencies of each molecule. In respect to the multi-component gel, a strong peak appears at 3182 cm^{-1} which is characteristic of the N-H stretching. C-H stretches at 2981 and 2943 cm^{-1} are present, as well as C=O stretch at 1629 cm^{-1}. At 1505 and 1406 cm^{-1}, C=C stretches from the aromatic rings of DBS is observed and at 1400 cm^{-1} the presented peak overlaps with the carboxylate peak of heparin. Between 1300 and 1120 cm^{-1} several peaks from DBS sugar are noticeable. At 1095 cm^{-1} a strong peak is verified and probably corresponding to

the overlap of S=O stretch and C-O stretch. Due to the fact that several IR frequencies are common in the three compounds that formed the gel an overlap of the characteristic peaks of each molecule occurred. This indicates that each component can behave independently when the gel is formed and there are no molecular scale interactions between the different components in the multi-component gels.

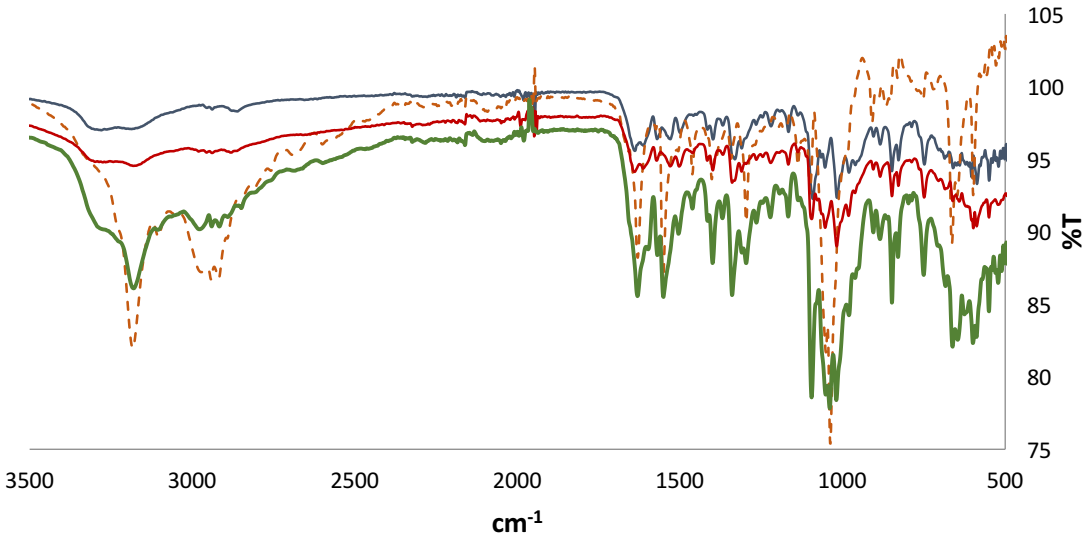

Figure 4.4. IR spectra of xerogels formed by DBS-CONHNH$_2$ gel (blue line); DBS-CONHNH$_2$ gel with 300 µM of heparin (red line); DBS-CONHNH$_2$ gel with 1200 µM C16-DAPMA (dashed orange line) and DBS-CONHNH$_2$ gel with 1200 µM of C16-DAPMA and 300 µM of heparin (green line).

4.3.3. Study of Gel Formation Kinetics

Following the incorporation of heparin and C16-DAPMA within the DBS-CONHNH$_2$ gel network, the influence of the addition of these components, individually and as aggregates, on the self-assembly kinetics of DBS-CONHNH$_2$ nanofibers was investigated.

Circular Dichroism

CD studies were performed to follow the kinetics of growth of the self-assembled fibrillary network of (a) DBS-CONHNH$_2$, DBSCONHNH$_2$ in the presence of (b) heparin, as well as in the presence of (c) C16-DAPMA and in the presence of (d) both heparin and C16-DAPMA.

It is noteworthy that DBS-CONHNH$_2$ undergoes gelation immediately after heating and therefore, the CD cuvette was incubated at 90 °C prior to the transfer of its hydrosol into the cuvette and the beginning of kinetic measurements. From the obtained data (Figure 4.5) the presence of an absorbed left-handed circularly polarized light at approximately 275 nm was observed, with increased intensity over time for all the tested gels. This indicates that π-π stacking of the aromatic rings of the gelator occurs in all cases consistent with the formation of self-assembled nanofibers. However, it is possible to observe differences in the intensities of the gels.

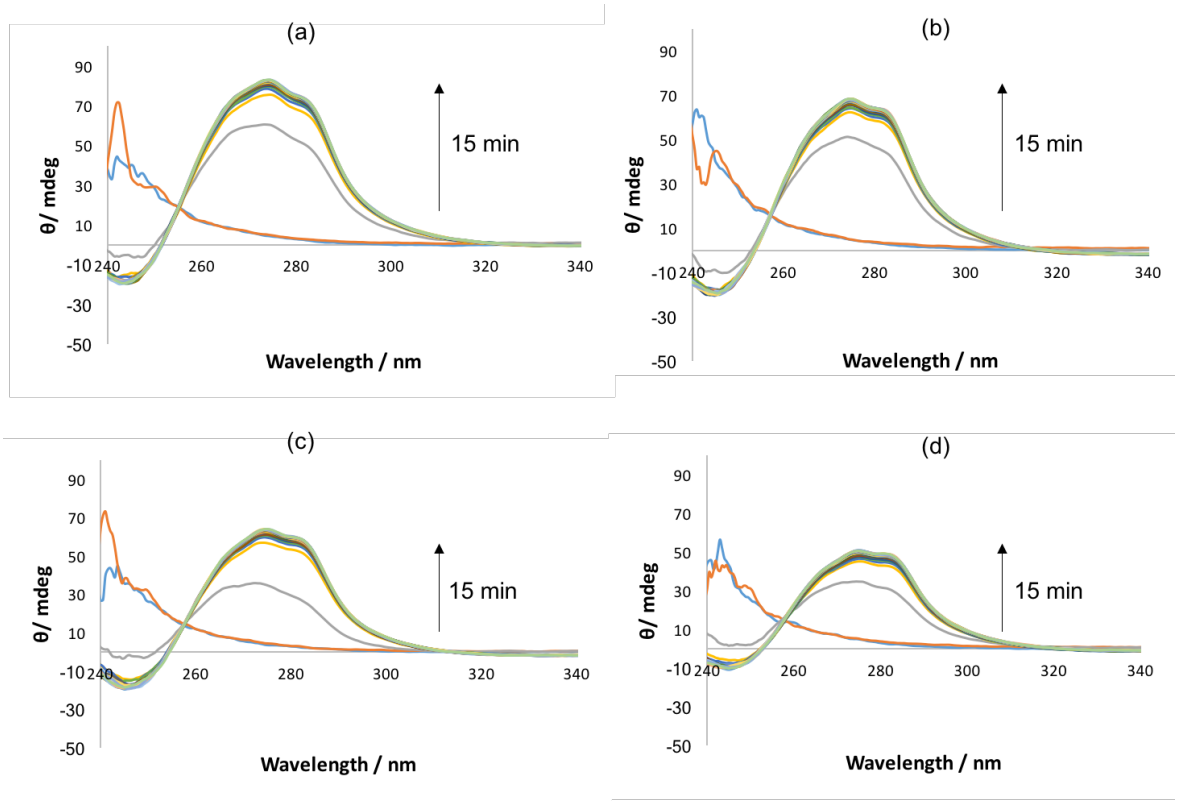

Figure 4.5. Kinetic studies of the growth of DBSCONHNH$_2$ fibrillar network over time, using CD spectroscopy. (a) DBS-CONHNH$_2$; (b) DBS-CONHNH$_2$ in the presence of heparin; (c) DBS-CONHNH$_2$ in the presence of C16-DAPMA and (d) DBS-CONHNH$_2$ in the presence of C16-DAPMA and heparin.

The intensity of the CD band at 275 nm was plotted against time for the gels in the four different conditions (Figure 4.6). For all conditions rapid self-assembly of the gelator fibers was observed, reaching a maximum intensity after approximately 300 seconds. However, the presence of heparin led to a decrease in intensity when compared with the DBS-

$CONHNH_2$ gel, indicating an influence on fiber formation, despite the similar rate of fibers growth. Identical behaviour was observed when C16-DAPMA was present in the gel. The incorporation of both C16-DAPMA and heparin in the gel revealed a significant decrease of the absorbance intensity when compared to the DBS-$CONHNH_2$ gel, suggesting that the presence of the aggregates may inhibit gel fiber assembly, specifically in terms of chirality or helical twist. This corroborates with the lower T_{gel} obtained for this system that indicated same influence of the C16-DAPMA and heparin aggregates on the thermal stability of this gel.

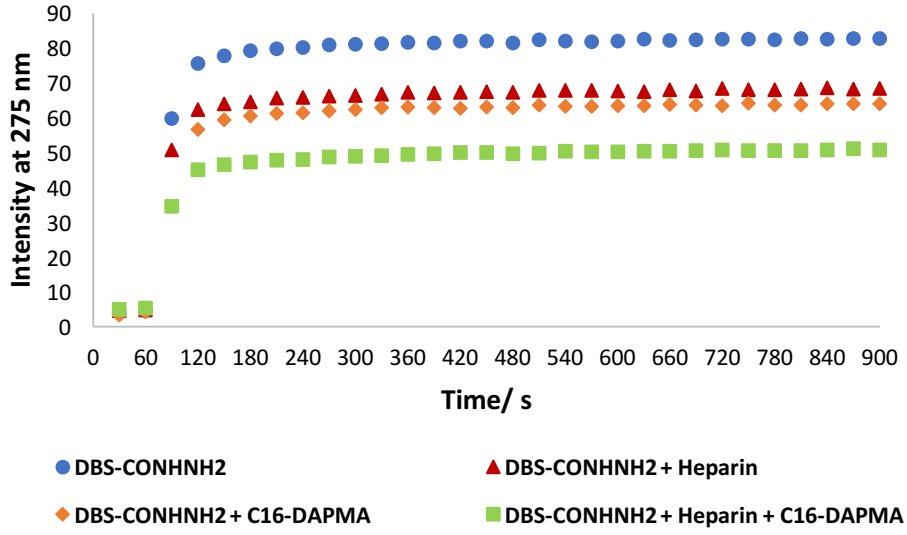

Figure 4.6. CD intensity at 275 nm of DBS-$CONHNH_2$, DBS-$CONHNH_2$ in the presence of heparin, DBS-$CONHNH_2$ in the presence of C16-DAPMA and DBS-$CONHNH_2$ in the presence of C16-DAPMA and heparin, over 15 minutes.

4.3.4. Mallard Blue Diffusion Assay

To obtain a better understanding of the interactions between C16-DAPMA and heparin incorporated within the DBS-$CONHNH_2$ gel, MalB (25 µM) solution was placed on top of gels (Figure 4.7) containing only DBS-$CONHNH_2$ (0.3% w/v), DBS-$CONHNH_2$ (0.3% w/v) with 38 µM heparin, DBS-$CONHNH_2$ (0.3% w/v) with 150 µM C16-DAPMA and DBS-$CONHNH_2$ (0.3% w/v) with 150 µM C16-DAPMA and 38 µM heparin. The variations in intensity of MalB in the solution on top of the four different gels were studied over three days by UV-Vis.

Figure 4.7. DBS-$CONHNH_2$ gel with MalB solution on top.

Figure 4.8 shows the DBS-$CONHNH_2$ gel sample after three days where it is possible to verify the presence of a blue colour in the gel, which is due to natural dilution phenomena that resulted in a decrease of MalB absorbance present in the solution supernatant (Figure 4.10). The predicted dilution factor in the absence of MalB binding to heparin, is 50%. It is noteworthy that of the four tested samples, the only one presenting a greater decrease in MalB absorbance was the gel with only heparin incorporated (Figure 4.9). It was observed that instead of a uniform dispersion of MalB over the gel, a deep blue ring on the surface of the gel was formed, providing evidence that the MalB is interacting with heparin and thus does not diffuse into the gel in the same way as for the other samples.

Figure 4.8. DBS-$CONHNH_2$ gel with MalB solution on top after 72 h.

Figure 4.9. DBS-$CONHNH_2$ gel in the presence of heparin with MalB solution on top after 72 h.

From Figure 4.10 and using the sample containing DBS-$CONHNH_2$ gel as a control experiment, it is possible to verify that the samples with C16-DAPMA and C16-DAPMA with heparin resulted in a smaller decrease of MalB absorbance over time when compared with DBS-$CONHNH_2$ gel, that may correspond to the fact that as the gels have more components within the network it becomes more difficult for the MalB to diffuse into the gel, thus resulting in a lower dilution and higher absorbance. On the other hand, when DBS-$CONHNH_2$ gel contains heparin it is noticeable a higher decrease of the MalB absorbance over time, when compared with DBS-$CONHNH_2$ gel. This may indicate that MalB is interacting with the free heparin present in the gel, and binding to heparin released from the gel, resulting in a lower absorbance of MalB. Importantly, when C16-DAPMA is present, MalB no longer interacts with heparin and thus a higher absorbance is observed over time. Therefore, C16-DAPMA and heparin interactions are maintained when incorporated into the multi-component gel.

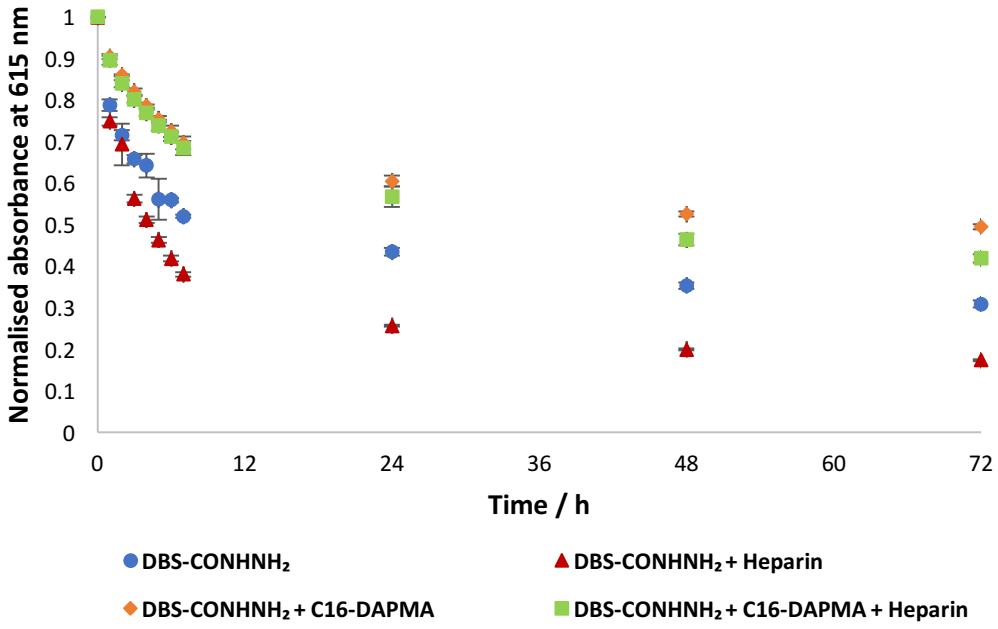

Figure 4.10. Normalised absorbance of MalB at 615 nm over time when placed on top of DBS-$CONHNH_2$; DBS-$CONHNH_2$ with heparin; DBS-$CONHNH_2$ with C16-DAPMA and DBS-$CONHNH_2$ with heparin and C16-DAPMA.

4.3.5. Electron Microscopy

TEM and SEM images of DBS-$CONHNH_2$ gel, DBS-$CONHNH_2$ gel in the presence of heparin, or C16-DAPMA and in the presence of both heparin and C16-DAPMA were obtained, in order to better understand the morphology and behaviour of these four different systems. TEM images of DBS-$CONHNH_2$ gel (Figure 4.11) showed the presence of twisted and branched nanofibers, proving the self-assembly of this gelator into 1D fibers in water. When heparin was present within the gel (Figure 4.12) it was possible to observe the presence of the twisted fibers as well as large unspecific aggregates that correspond to heparin. This appears to indicate that there are no interactions occurring between the gelator and heparin when the former is self-assembling. This is in contrast to what was observed with DBS-COOH in Chapter 3. The incorporation of C16-DAPMA into the DBS-$CONHNH_2$ gel (Figure 4.13) appears to have a similar effect. Once more, it is possible to distinguish the presence of nanofibers along with undefined agglomerates that correspond to self-assembled C16-DAPMA micelles. It is noteworthy that due to the difficulty of imaging these micelles using TEM, it was hard to obtain images with good quality and with

clear micellar morphology. Nevertheless, we can conclude that no significant interactions appear to occur between the two components.

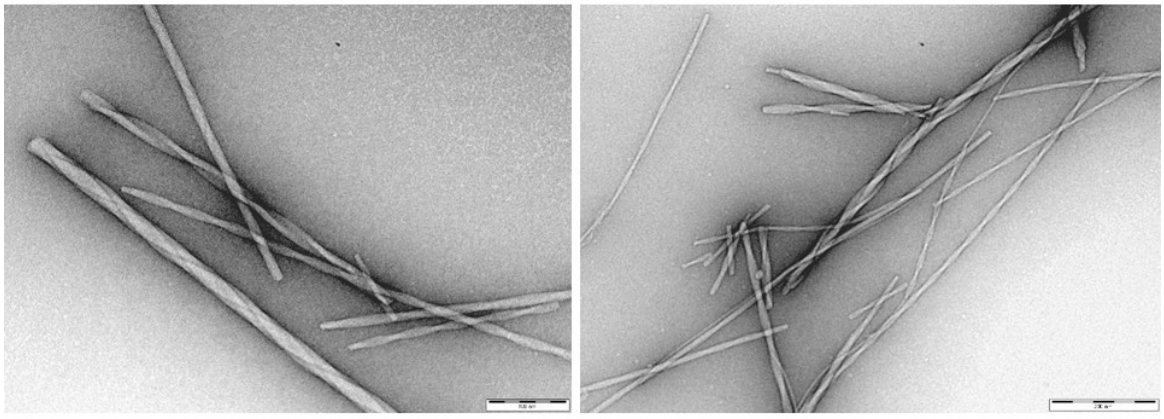

Figure 4.11. TEM images of DBS-$CONHNH_2$ (0.4% w/v) gel. Scale bars: 100 nm (left) and 200 nm (right).

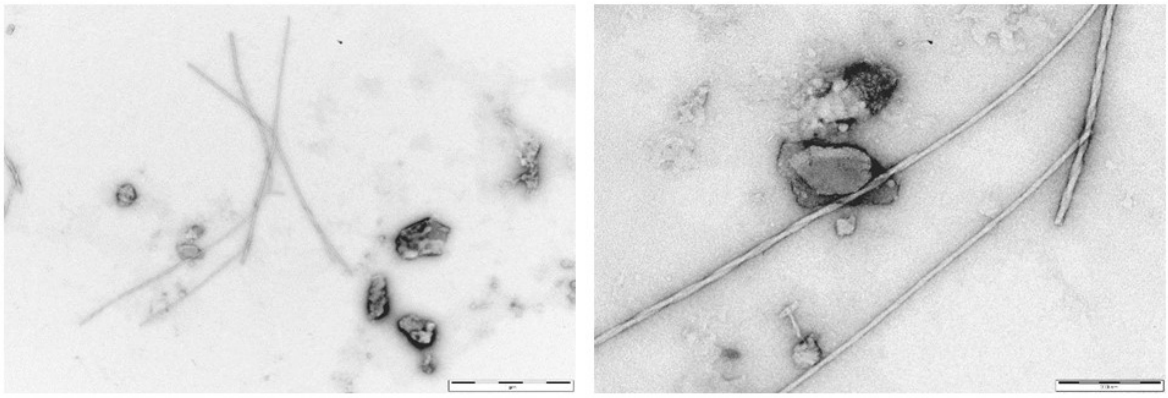

Figure 4.12. TEM images of DBS-$CONHNH_2$ (0.4% w/v) gel in the presence of heparin (38 μM). Scale bars: 1 μM (left) and 200 nm (right).

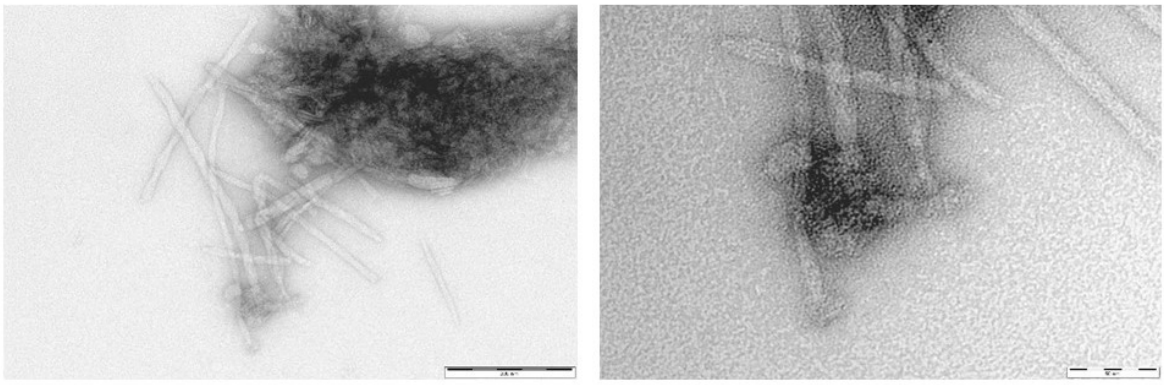

Figure 4.13. TEM images of DBS-$CONHNH_2$ (0.4% w/v) gel in the presence of C16-DAPMA (150 μM). Scale bars = 200 nm (left) and 50 nm (right).

Figure 4.14 presents a TEM image of DBS-$CONHNH_2$ gel formed in the presence of both C16-DAPMA and heparin, where it is possible to identify nanofibers of DBS-$CONHNH_2$ and aggregates. The observed aggregates showed a highly organised semi crystalline nanostructure (Figure 4.15), characteristic of the hierarchical systems formed by C16-DAPMA when binding to heparin (as described in Chapter 2). Therefore, the obtained images proved the maintenance of the interactions between heparin and C16-DAPMA when the gel is formed and also provides evidence of the orthogonal self-assembly of this multi-component gel.

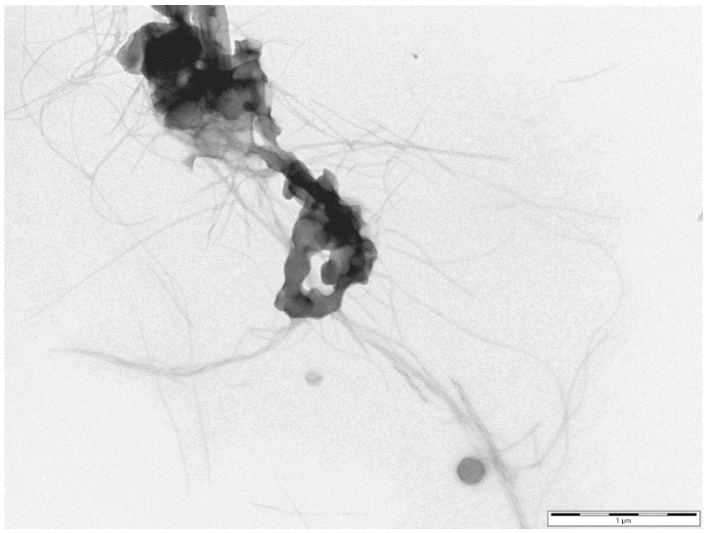

Figure 4.14. TEM image of DBS-$CONHNH_2$ (0.4% w/v) gel in the presence of C16-DAPMA (150 μM) and heparin (38 μM). Scale bar = 1 μM.

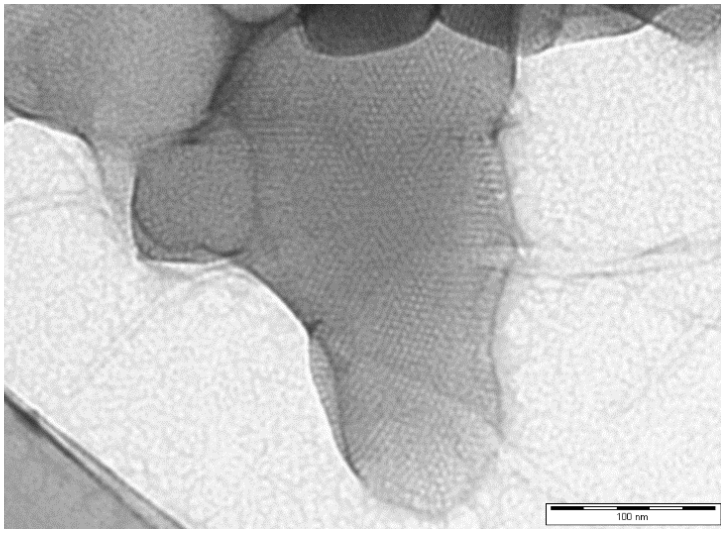

Figure 4.15. TEM image of the aggregates observed in the DBS-$CONHNH_2$ (0.4% w/v) gel in the presence of C16-DAPMA (150 μM) and heparin (38 μM). Scale bar: 100 nm.

However, in addition to the nanofibers and hierarchical aggregates shown in Figure 4.14, it was also possible to identify some large and aligned structures (Figure 4.16) that may correspond to a different organization of the DBS-$CONHNH_2$ fibers. These different morphologies are better explained using the SEM images described below.

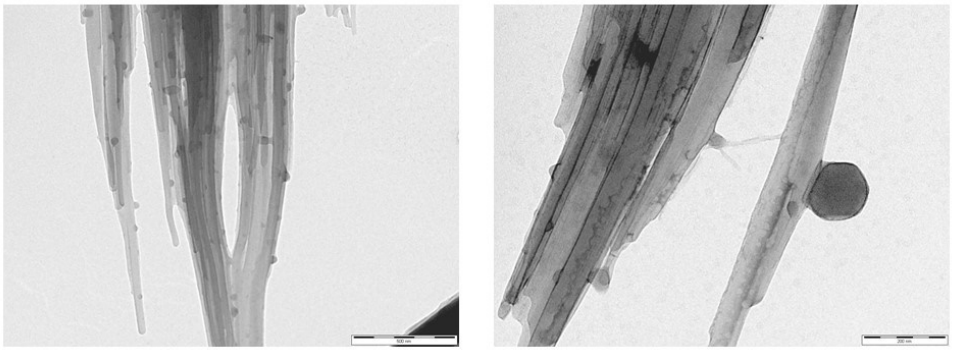

Figure 4.16. TEM images of Scale bars = 500 nm (left) and 200 nm (right).

SEM images of DBS-$CONHNH_2$ gel (Figure 4.17) showed a network structure comprising nanofibers, which supports the corresponding TEM images. In the presence of heparin (Figure 4.18) it was possible to observe once more the formation of fibers but thicker than the nanofibers of DBS-$CONHNH_2$ gel, presenting a width of 66 ± 1 nm with heparin and 38 ± 3 nm for the gel alone. This may be due to the fact that heparin is surrounding the fibers

on drying and in this way they become larger, however no interactions should be occuring between the two components as shown in the TEM images. When C16-DAPMA is present in the gel (Figure 4.19) we observe the existence of nanofibers with a similar width as for the DBS-$CONHNH_2$ gel alone (40 ± 1 nm). The detection of the C16-DAPMA micelles was not possible because they present a very small size average (6 nm). It is known that this micelles are difficult to image using this technique. However, no interactions appear to exist between the C16-DAPMA and the DBS-$CONHNH_2$, as the nanofiber morphology is similar to that obtained for the gel alone, in agreement with the TEM images.

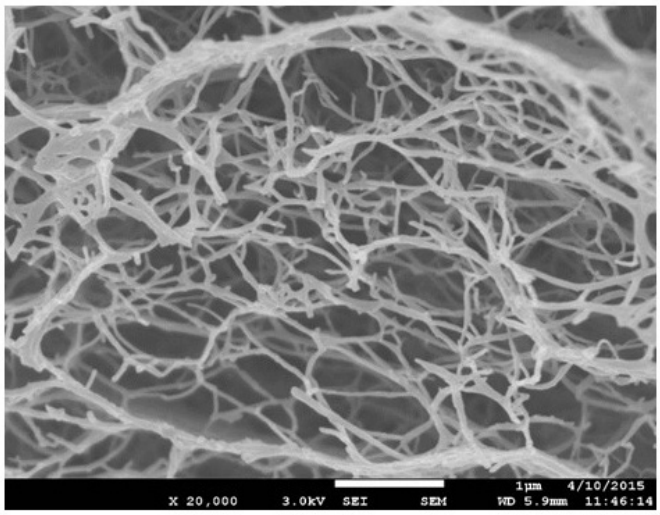

Figure 4.17. SEM image of DBS-$CONHNH_2$ (0.4% w/v) gel.

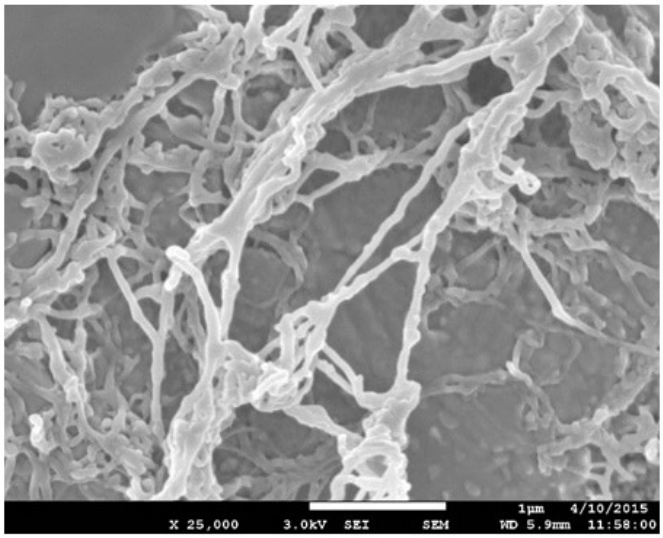

Figure 4.18. SEM image of DBS-$CONHNH_2$ (0.4% w/v) gel in the presence of heparin (38 µM).

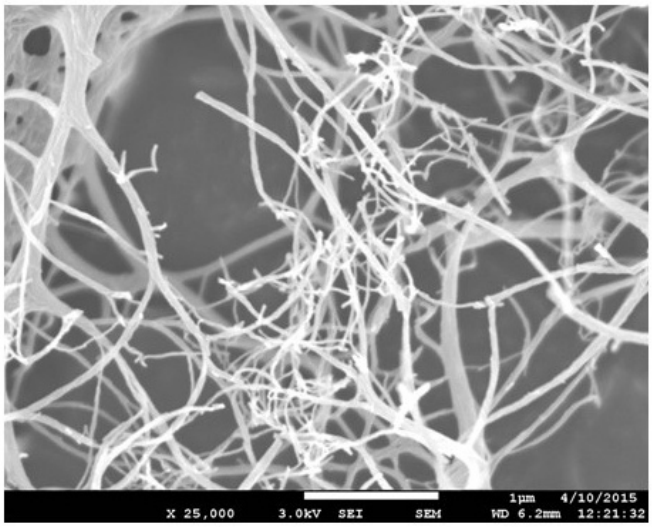

Figure 4.19. SEM image of DBS-CONHNH2 (0.4% w/v) gel in the presence of C16-DAPMA (150 µM).

SEM images of DBS-$CONHNH_2$ with both heparin and C16-DAPMA incorporated (Figure 4.20) revealed the presence of gel nanofibers but also thicker structures (916 ± 213 nm) that resemble needles. A closer look at these structures showed what appears to be a rigid alignment of gel nanofibers. We suggest this alignment may be induced by the highly organised hierarchical nanostructures formed when C16-DAPMA interacts with heparin. With these SEM images we could obtain a better understanding of the different morphologies obtained in the corresponding TEM images. This morphology would support the lower thermal stability and smaller CD signal obtained for this system. We propose that the presence of C16-DAPMA micelles interacting with heparin has some influence on the self-assembly and hierarchical organisation of the DBS-$CONHNH_2$ fibers.

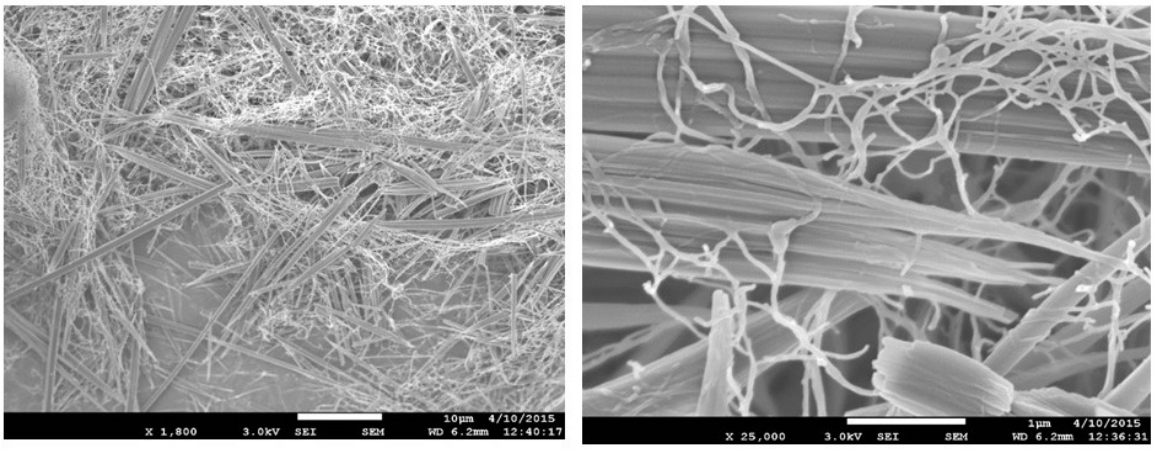

Figure 4.20. SEM images of DBS-$CONHNH_2$ (0.4% w/v) gel in the presence of C16-DAPMA (150 µM) and heparin (38 µM).

4.3.6. Rheology

The viscoelastic properties of DBS-$CONHNH_2$ gel alone, in the presence of 1 mM of heparin, 2 mM of C16-DAPMA and 1 mM of heparin bound to 2 mM of C16-DAPMA, were each studied by rheology. Additionally, the viscoelastic properties of DBS-$CONHNH_2$ and agarose hybrid hydrogels were also studied. The addition of a PG can help to strengthen the gel network of LMWGs, specifically, agarose that is a well-known biocompatible polymer gel.[97,261,262] As described in Chapter 3, this technique allowed us to understand how the mechanical properties of DBS-$CONHNH_2$ hydrogels can be affected by the incorporation of heparin and C16-DAPMA and also by the presence of a strengthening PG. To that purpose, the storage or elastic modulus (G') and the loss or viscous modulus (G'') of the material were obtained, through the application of oscillating strains. If the material presents a higher G' than G'' with low frequency dependency it has mechanical properties characteristic of a gel.[256,257]

Figure 4.21 shows the strain amplitude dependence of G' and G'' for 0.4% w/v DBS-$CONHNH_2$ gels, where it is possible to observe a LVR up to approximately 1% strain when C16-DAPMA is incorporated within the network and approximately 2.5% for all the other conditions. These results indicate that the DBS-$CONHNH_2$ gel with C16-DAPMA is a less stable material on the macroscopic level, with the disruption of its structure occurring at lower strains than for the other tested conditions, despite the presence of C16-DAPMA not

affecting the stiffness of the gel network as the G' value was in fact slightly higher (from 2150 Pa for the gel alone to 2820 Pa for the gel with C16-DAPMA). This may be due to the fact that as C16-DAPMA is a surfactant it forms some foam, which results in the presence of holes in the gel (Figure 4.22) that will contribute to a weaker and therefore, less stable macroscopic gel network. However, when heparin or heparin/C16-DAPMA aggregates were present within DBS-$CONHNH_2$ gels, the LVR of the gel was not affected, meaning that the incorporation of these components did not affect the stability of the gel material. As such if the self-assembling C16-DAPMA is bound to heparin, it no longer limits the LVR of the gel.

Additionally, and contrarily to what was observed with DBS-COOH, the presence of heparin and heparin-C16-DAPMA aggregates resulted in an increase of G' from approximately 2150 Pa to approximately 4100 Pa, indicating that the addition of these components increased the stiffness of DBS-$CONHNH_2$ gel.

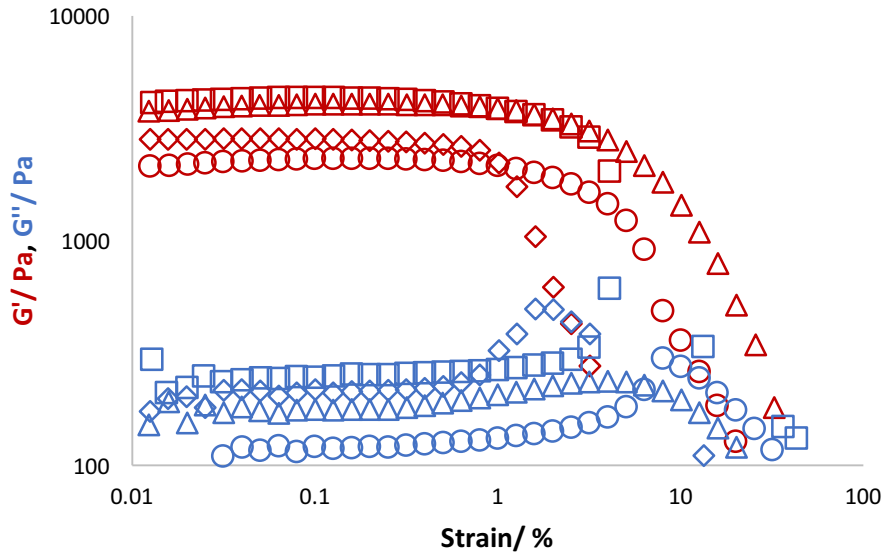

Figure 4.21. Strain amplitude dependence of the storage modulus (G') and loss modulus (G'') for DBSCONHNH$_2$ gel (○), DBSCONHNH$_2$ gel with heparin (△), DBSCONHNH$_2$ gel with C16-DAPMA (◇) and DBSCONHNH$_2$ gel with heparin and C16-DAPMA (□). Frequency = 1 Hz.

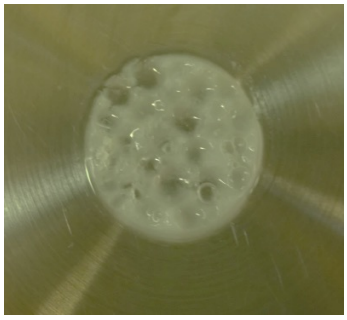

Figure 4.22. DBS-CONHNH$_2$ gel with C16-DAPMA.

When 1% w/v agarose was added into 0.4% w/v DBS-CONHNH$_2$ gels (Figure 4.23), a large increase of G' from approximately 3800 Pa to 15000 Pa was observed, indicating the presence of a much stiffer gel, resulting from the robustness of agarose. However, the LVR only reaches approximately 2% of strain. When heparin was added to DBS-CONHNH$_2$ in agarose, the G' decreases to approximately 3800 Pa again but the stability increases, presenting the highest LVR of all tested materials (stable to approximately 4% of strain).

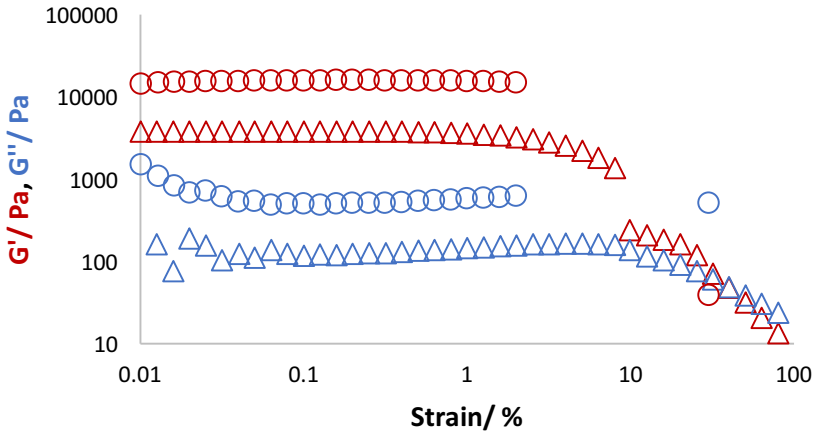

Figure 4.23. Strain amplitude dependence of the storage modulus (G') and loss modulus (G'') for DBSCONHNH$_2$ gel with agarose (○) and DBSCONHNH$_2$ gel with agarose and heparin (△). Frequency = 1 Hz.

The frequency dependence of DBS-CONHNH$_2$ in the same conditions described above was also tested, as shown in Figure 4.24. The incorporation of heparin, C16-DAPMA or both, did not influence the gel mechanical properties when different frequencies were applied to the

samples, exhibiting a storage modulus higher than the loss modulus (G' > G'') and a frequency independence up to ca. 25 Hz. Therefore, DBS-$CONHNH_2$ gel alone and incorporating different components has the characteristics of a typical gel-like material with no changes in the viscoelastic properties from 0.1 to 25 Hz. A similar frequency dependence was observed when 1% of agarose was added to DBS-$CONHNH_2$ gel and DBS-$CONHNH_2$ gel with heparin, as shown in Figure 4.25.

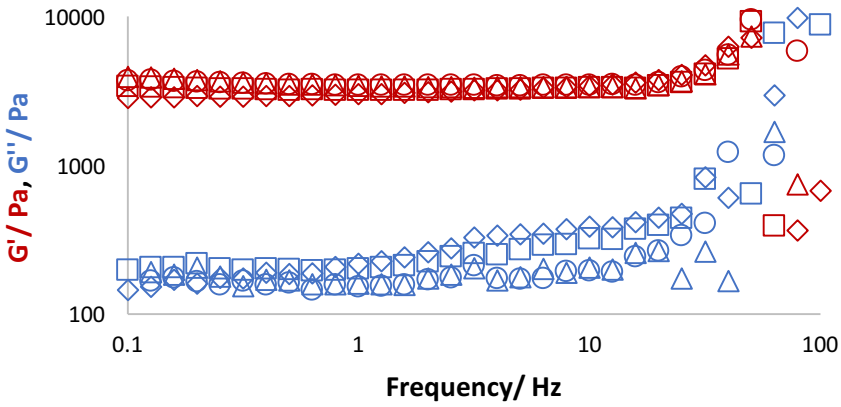

Figure 4.24. Frequency dependence of the storage modulus (G') and loss modulus (G'') for DBS$CONHNH_2$ gel (○), DBS$CONHNH_2$ gel with heparin (△), DBS$CONHNH_2$ gel with C16-DAPMA (◇) and DBS$CONHNH_2$ gel with heparin and C16-DAPMA (□). Amplitude strain = 0.1%.

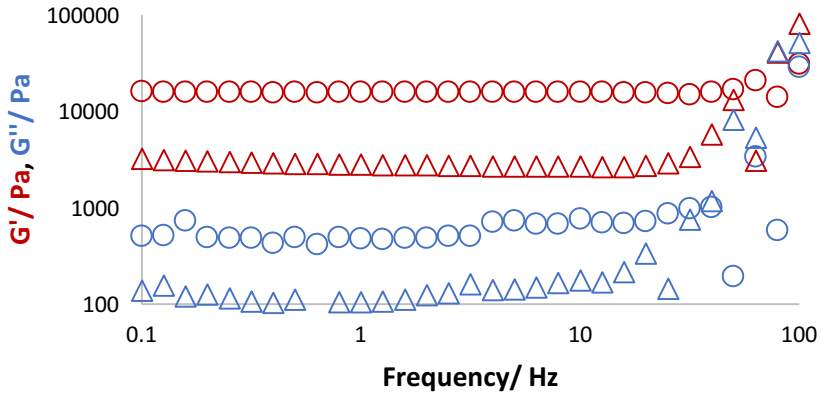

Figure 4.25. Frequency dependence of the storage modulus (G') and loss modulus (G'') for DBSCONHNH$_2$ gel with agarose (◯) and DBSCONHNH$_2$ gel with agarose and heparin (△).

Figure 4.26 shows the temperature dependence of the G' and G'' on heating DBS-CONHNH$_2$ gel alone, with heparin, with C16-DAPMA, and with both heparin and C16-DAPMA. For DBS-CONHNH$_2$ gel it is possible to observe the disruption of the gel network at approximately 60 °C. Strangely, above 65 °C the gel appears to recover its structure, with G' becoming higher than G'' again. The experiment was repeated to verify its reproducibility and a similar result was obtained. This may indicate some thermal reorganisation of the nanofibers and the ability to self-heal. However, further studies would need to be performed to ensure that this unusual feature is a characteristic of this gelator. In addition, an identical temperature dependence behaviour up to 60 °C is observed when heparin is incorporated within the gel, but the gel structure becomes completely lost at approximately 60 °C. For DBS-CONHNH$_2$ gel with C16-DAPMA the storage modulus remains higher than the loss modulus from 25 to 80 °C, indicating a solid-like behaviour of the gel across the whole temperature range tested, however it is possible to observe a steady decrease of G' with the increase of temperature (G'=3.09x10^3 Pa at 25°C and G'=1.72x10^3 Pa at 80°C), indicating changes in the viscoelastic properties of the gel and possibly the breakdown of the gel structure at higher temperatures. When both heparin and C16-DAPMA aggregates are incorporated within the gel network, the gel reveals temperature independent behaviour across the tested range, with G' higher than G'' from 25 to 80 °C. Overall this suggests good stability of these gels in terms of mechanical performance once

both C16-DAPMA and heparin are incorporated. However, it should be noted that these values are not in agreement with the T_{gel} values obtained in section 4.3.1. This may be due to the fact that different concentrations of heparin and C16-DAPMA were used along with different gel volumes for each experiment. For accurate comparison identical experimental conditions would be required.

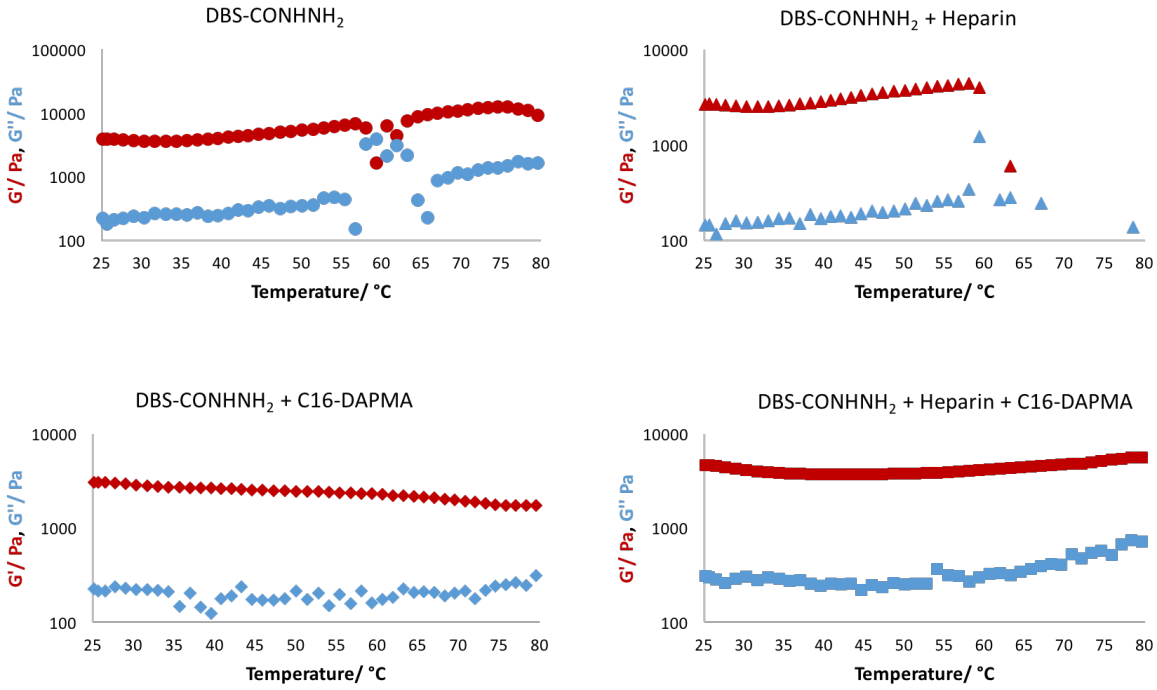

Figure 4.26. Temperature dependence of the storage modulus (G') and loss modulus (G'') for DBSCONHNH$_2$ gel (○), DBSCONHNH$_2$ gel with heparin (△), DBSCONHNH$_2$ gel with C16-DAPMA (◇) and DBSCONHNH$_2$ gel with heparin and C16-DAPMA (□). Amplitude strain = 0.1%, Frequency = 1 Hz.

4.4. Release Studies

To understand whether heparin could be released from DBS-CONHNH$_2$ hydrogels and determine how its release could be controlled, different release assays were performed. The release of heparin from these LMWG hydrogels is of great importance, as it is intended to have heparin contacting cells in a controlled way so its angiogenic properties can promote cell growth.

Heparin release: Buffer on top of the gel

As described on Chapter 3, heparin release from the hydrogels was obtained by placing 1 mL of buffer on top of 3 mL of hydrogel incorporating 1 mM of heparin, as shown in Figure 4.27. Aliquots of buffer were removed over time, added into MalB solution and the absorbance measured.

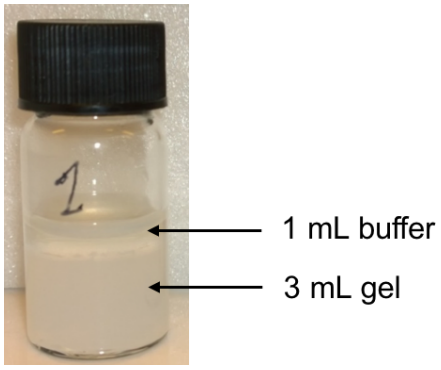

Figure 4.27. DBS-$CONHNH_2$ hydrogel containing 1 mM of heparin, with 10 mM Tris-HCl/ 150 mM NaCl buffer on top for monitoring the release of heparin.

Figure 4.28 shows the release profile of heparin from DBS-$CONHNH_2$ gels containing just heparin and also those in which heparin is interacting with C16-DAPMA. When just heparin is present within the gel network, it is possible to observe a gradual increase of the percentage of heparin being released into the buffer, reaching a maximum of 62% after 72 hours. The incorporation of C16-DAPMA into the gel resulted in significantly lower heparin release over time (only 24% after 72h). Therefore, C16-DAPMA is inhibiting the release of heparin by binding it into hierarchical aggregates. In this way, it should be possible to trigger the release of heparin by degrading the binder or adding a biocompatible competitor that will preferentially interact with the binder, hence releasing the heparin. It is worth noting, however, that for DBS-COOH (Chapter 3) the release was 0% from the hydrogel with heparin-C16-DAPMA aggregates. We suggest that the release observed for DBS-$CONHNH_2$ hydrogel in the presence of heparin and C16-DAPMA is related with the gel preparation method, as when heating larger volumes of sample (3 mL instead of 1 mL) it was possible to observe the formation of foam which is characteristic of C16-DAPMA free in solution. Consequently, this may indicate the presence of some heparin within the gel network that is not interacting with the binder and is released.

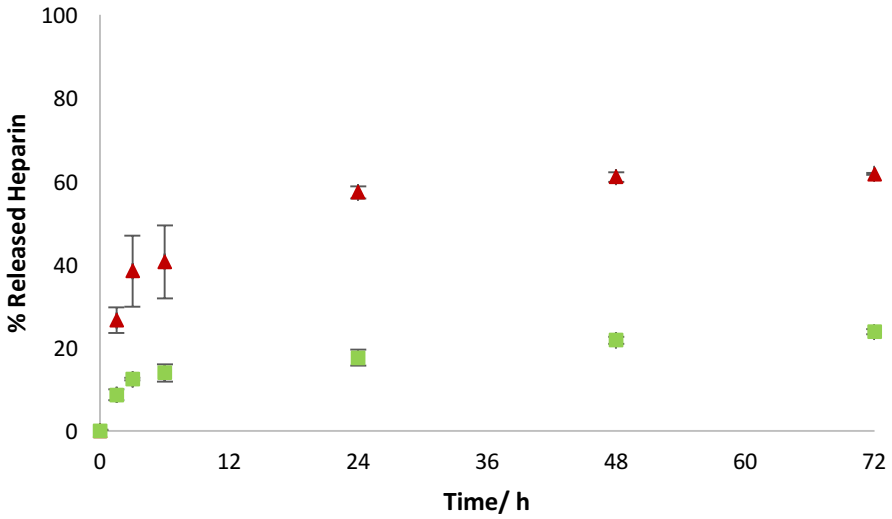

Figure 4.28. Heparin release from DBS-$CONHNH_2$ hydrogel (0.4% w/v) with 1 mM of heparin (▲) and DBS-$CONHNH_2$ hydrogel (0.4% w/v) with 1 mM of heparin interacting with 2 mM C16-DAPMA (■).

In an attempt to trigger the release of heparin from the gel network when bound to C16-DAPMA, negatively charged molecules, such as sodium dodecylsulfonate (SDS) and sodium dodecylbenzenesulfonate (SDBS) (Figure 4.29 and 4.30) were added to the buffer placed on top of the hydrogels containing heparin-C16-DAPMA aggregates, in order to bind electrostatically to C16-DAPMA when diffusing through the hydrogel, hence releasing heparin. However, when different concentrations of SDS and SDBS were added into MalB solution, the same displacement profile as when heparin is added to MalB was obtained. Therefore, it is not possible to distinguish if the displacement observed, would correspond to the release of heparin, or the presence of SDS or SDBS. By using the MalB method to detect heparin release, it is not possible to use negatively charged molecules to compete with heparin and bind to C16-DAPMA.

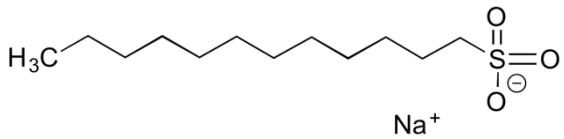

Figure 4.29. Chemical structure of sodium dodecylsulfonate.

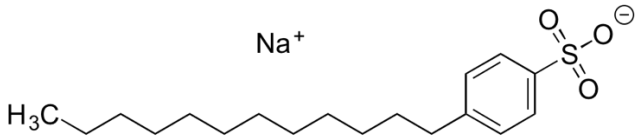

Figure 4.30. Chemical structure of sodium dodecylbenzenesulfonate.

A different approach was tested by replacing the buffer adding on top of the hydrogels from 10 mM Tris-HCl/ 150 mM NaCl buffer (pH 7.4) to borax/NaOH buffer (pH 10). As previously reported, DBS-$CONHNH_2$ hydrogels are stable across a wide pH range, from 2 to 11.5, so the change in pH will not affect the gel network.[88] Additionally, by increasing the pH, the protonated C16-DAPMA should be neutralised and therefore, not be able to interact electrostatically with heparin anymore. Figure 4.31 compares the release of heparin from DBS-$CONHNH_2$ hydrogels in the presence of C16-DAPMA when 10 mM Tris-HCl/ 150 mM NaCl buffer and borax/NaOH buffer are added on top of the hydrogels. After the first 1.5 hours the release of heparin went from 9% with the 7.4 pH buffer to 24% with the pH 10 buffer. After 3 days, almost double the percentage of heparin had been released when in contact with the pH 10 buffer (from 24% to 42%). This result indicates that by increasing the pH of the buffer on top of the hydrogel it is possible to increase the release of heparin, therefore triggering release without damaging the gel network.

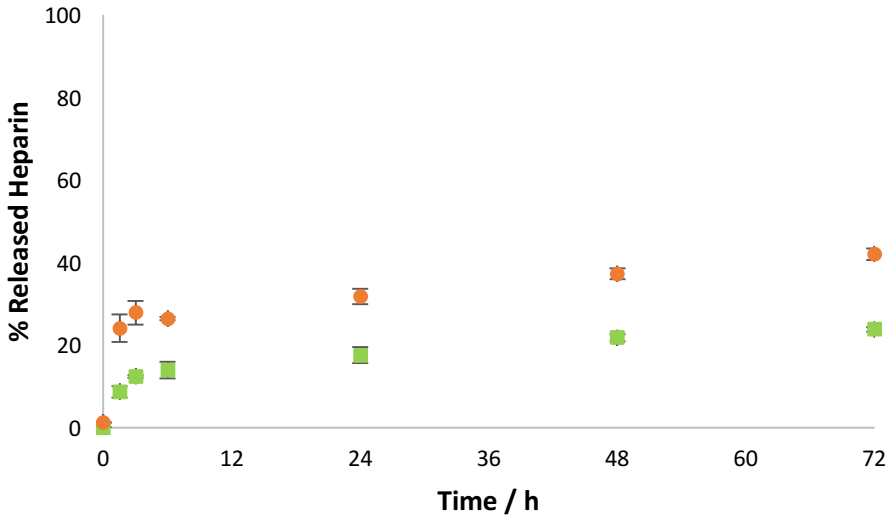

Figure 4.31. Heparin release from DBS-CONHNH$_2$ hydrogel (0.4% w/v) with 1 mM of heparin and 2 mM of C16-DAPMA over time, by adding 10 mM Tris-HCl/ 150 mM NaCl buffer (pH 7.4) (■) and borax/NaOH buffer (pH 10) (●) on top of the hydrogel.

We then tested whether the addition of agarose had an effect on heparin release (Figure 4.32). On increasing the agarose concentration, the release of heparin slows down during the first 6 hours, giving 41% in the absence of agarose, 35% in the presence of 0.5% agarose and only 28% release in the presence of 1% agarose. At longer times, however, the presence of agarose does not show an influence on the release, with approximately 53% of heparin being released after 24 hours for all three different hybrid gels. Thus, the presence of agarose may have an effect on the kinetics of heparin release but does not affect the final equilibrium amount of heparin being released into the buffer.

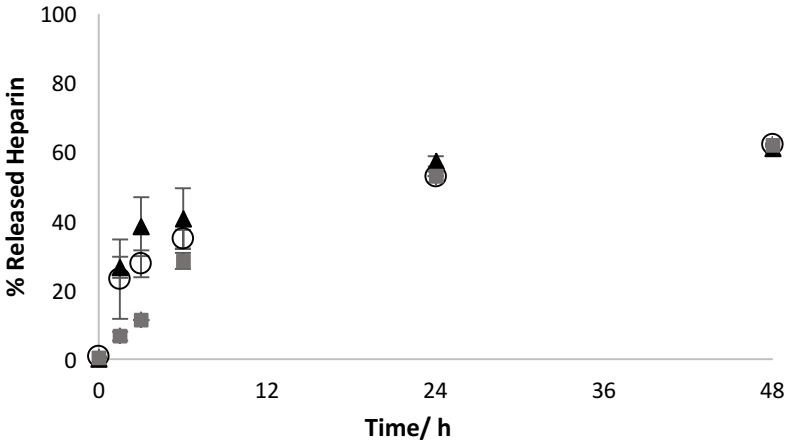

Figure 4.32. Heparin release from DBS-CONHNH$_2$ hydrogel (0.4% w/v) with 1 mM of heparin in the absence of agarose (▲), with 0.5% w/v of agarose (○) and 1% w/v of agarose (■).

Heparin Release: Gel cylinders

A different release assay was performed using hybrid gel cylinders containing 0.4% w/v of DBS-CONHNH$_2$, 1% w/v of agarose and 17 mM of heparin. The presence of agarose contributes to the formation of stiffer gels, making it possible to remove them from the vials and immerse them in buffer (Figure 4.33). By using this method, the entire gel surface is in contact with the buffer rather than just the top surface.

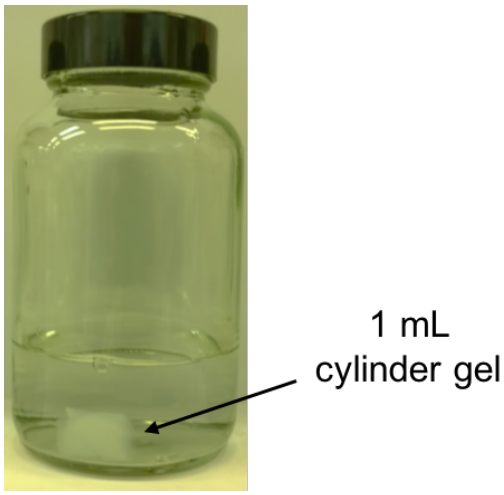

Figure 4.33. Hybrid gel cylinder containing 0.4% w/v of DBS-CONHNH$_2$, 1% w/v of agarose and 17 mM of heparin, immersed in 35 mL of buffer.

Figure 4.34 compares the release of heparin from the two different assays. As expected, the gel cylinders resulted in a greater heparin release than the hydrogels with buffer just on top, with 90% of heparin being released after 72 hours for the former method, instead of 64% of release for the later method. The fact that the gel cylinders have a bigger surface area to volume ratio for the release to occur, when comparing to the hydrogels in a vial with buffer on top, contributes to the greater amount of heparin being released into the buffer. Furthermore, the initial release rate is higher with ca. 60% being released in the first 6 hours compared with ca. 30%. Therefore, by controlling the surface area of DBS-$CONHNH_2$ hydrogels in contact with the release environment it is possible to control the amount of heparin being released.

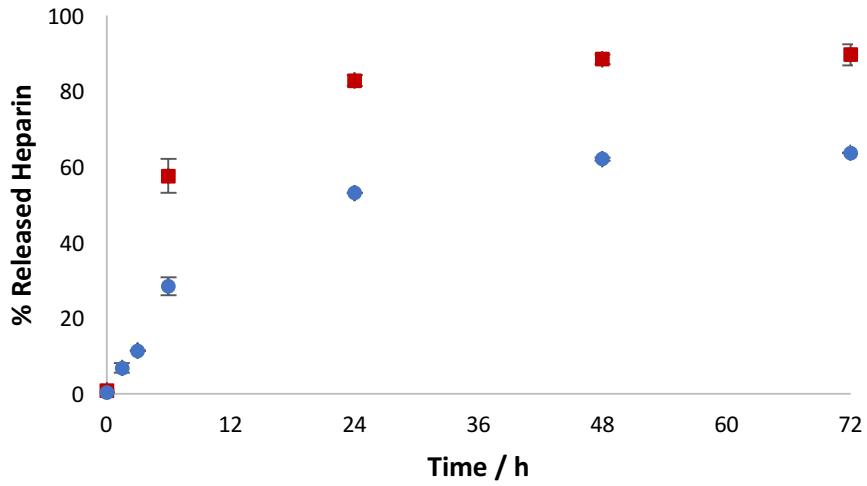

Figure 4.34. Different methods of heparin release from DBS-$CONHNH_2$ hydrogel (0.4% w/v) and agarose (1% w/v). (●): Buffer on top of the gel. (■): Gel cylinder.

4.5. Cytocompatibility of DBS-$CONHNH_2$ Hydrogels

The cytocompatibility of DBS-$CONHNH_2$ hydrogels was studied using mouse embryonic fibroblasts (3T3 cells). As described in Chapter 3, 3D and 2D cell cultures were tested and for the latter, the hydrogels were tested in 96 plates with the cells added on top of the gels and in transwells with the cells seeded on the bottom of the well. The same stainings and techniques used in the study of the cytocompatibility of DBS-COOH hydrogels (Chapter 3) were used for these DBS-$CONHNH_2$ hydrogels.

4.5.1. 2D Cell Culture with Cells on Top

2D cell culture assays were performed for DBS-$CONHNH_2$ hydrogels by seeding cells on top of the gels. Initially the number of cells added per well was based on the standard number used in the laboratory, as there was no time during the placement to optimise the cell number for the first performed assays. Therefore, a cell density of 50000 cells/mL was initially used together with an excess of heparin concentration (1 mM - 667 µg/mL and 2 mM - 1330 µg/mL).

Cell Morphology

The morphology of cells on top of DBS-$CONHNH_2$ gels was followed by optical microscopy. However, it was not possible to identify any cells, once the microscope used was inverted and only gels could be observed. The gels were not transparent enough to allow the visualization of the cells, as shown in Figure 4.35. In addition, from the control images it was possible to observe the existence of cell confluency after 5 days indicating that an optimization of the cells number is needed, with fewer cells in the initial culture.

Phalloidin/DAPI staining was not performed for this cell culture method as it was previously seen that it is not possible to obtain clear images of the cells under the microscope.

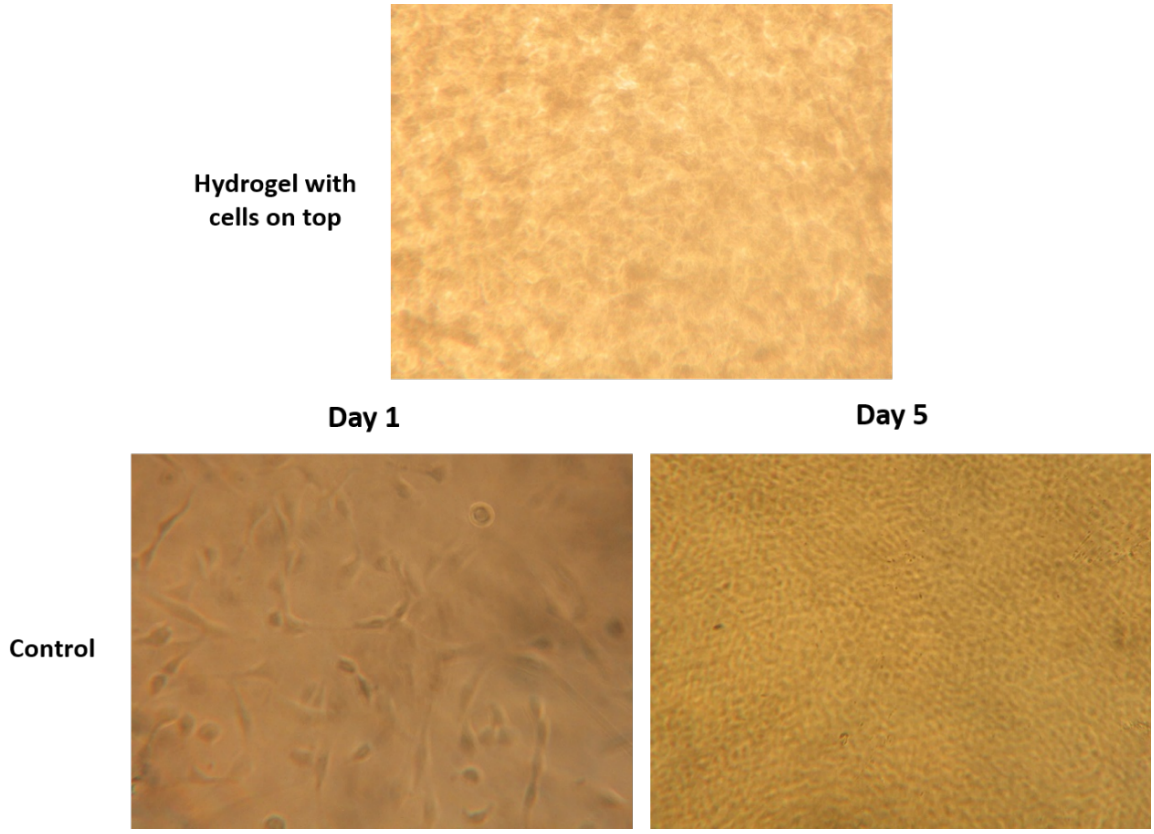

Figure 4.35. Optical microscopy images of DBS-$CONHNH_2$ hydrogels with cells on top (top) and controls (medium with cells) at day 1 and 5 (bottom). Magnification: 10x.

Live/Dead Staining

Live/dead staining was performed for DBS-$CONHNH_2$ hydrogels and DBS-$CONHNH_2$ hydrogels in the presence of heparin, with cells on top. However, as the fluorescence microscope was also inverted it was not possible to obtain clear images of the cells (Figure 4.36). On day 1 it was possible to observe the presence of cells but the images were blurred, on day 5 and 7 it was not possible to identify any cells, probably because of the existing cell confluency causing microscope focus problems, making it difficult to obtain clear images through the dense gels.

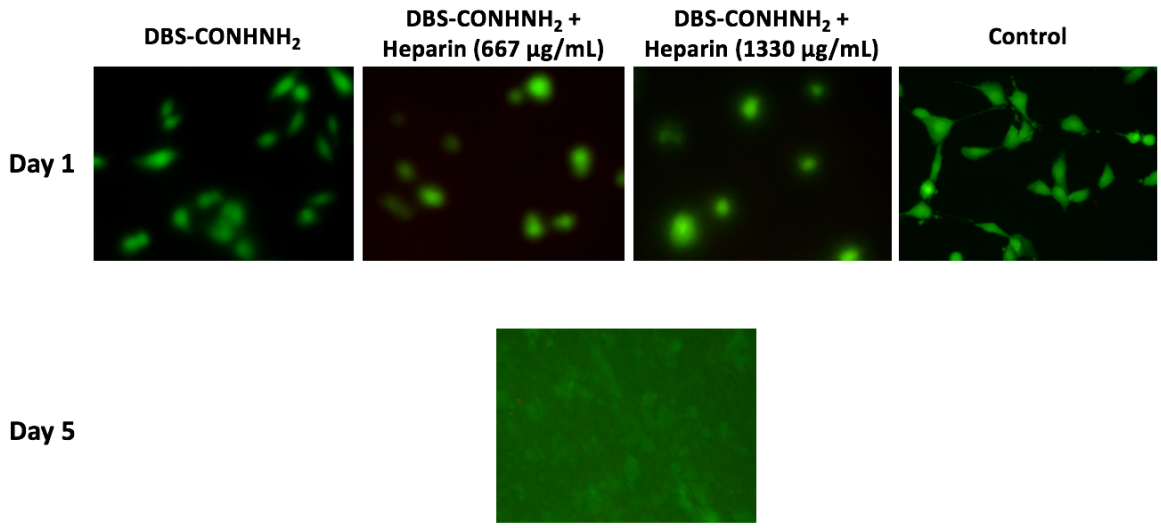

Figure 4.36. Fluorescence microscopy images of calcein-AM/PI staining of DBS-$CONHNH_2$ hydrogels, DBS-$CONHNH_2$ hydrogels in the presence of heparin (667 µg/mL and 1330 µg/mL) and controls (medium with cells), with cells on top, at day 1 and 5. Magnification: 20x.

MitoTracker Staining

In respect to the MitoTraker staining, the same problem was faced as for live/dead staining. Thus, it was not possible to obtain clear images, as can be observed on Figure 4.37.

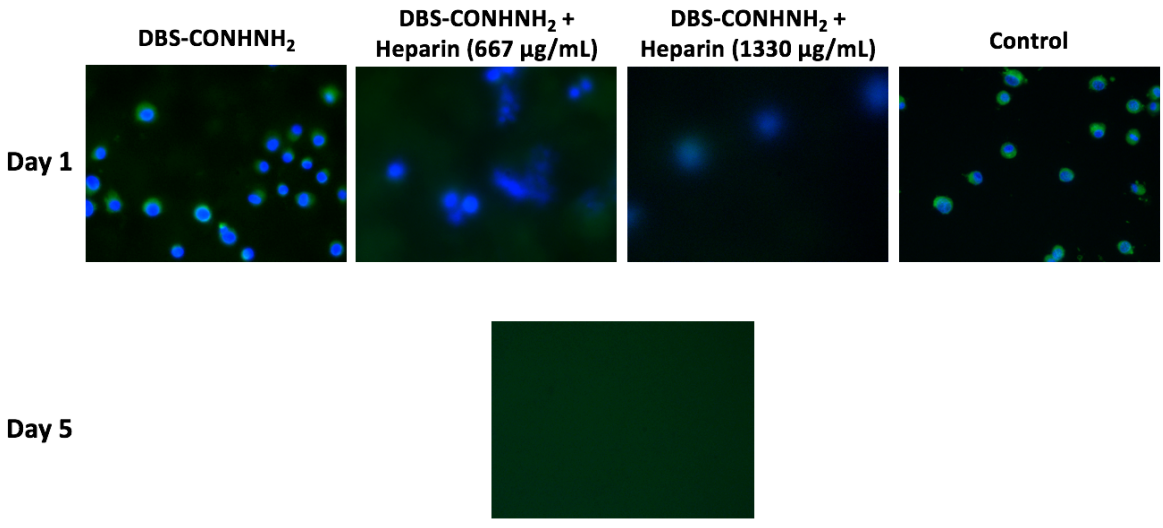

Figure 4.37. Fluorescence microscopy images of mitotraker/hoechst staining of DBS-$CONHNH_2$ hydrogels, DBS-$CONHNH_2$ hydrogels in the presence of heparin (667 µg/mL and 1330 µg/mL) and controls (medium with cells), with cells on top, at day 1 and 5. Magnification: 20x.

Metabolic Activity

The metabolic activity of the cells on top of DBS-CONHNH$_2$ hydrogels was studied using cell proliferation reagent WST-1, as described in Chapter 3. The obtained results (Figure 4.38) indicate that the presence of an excess of heparin within the DBS-CONHNH$_2$ gel network contribute to a lower metabolic activity of the cells over 7 days, when compared with the control assay. This is in agreement with the literature,[263–265] where it is demonstrated that the concentration of heparin is crucial for cell proliferation and that high concentrations of heparin result in the inhibition of cell growth. It is worth noting that the fact that there is a decrease of metabolic activity from day 5 to day 7 for both DBS-CONHNH$_2$ hydrogels and the control is due to the confluency of the cells that resulting in a lack of sites to which cells can adhere and therefore contributing to cell death. Nevertheless, the increase of the metabolic activity from day 1 to day 7 when the cells were in contact with DBS-CONHNH$_2$ indicates that this gel network appears to provide excellent conditions for the cells to adhere onto the gel surface and proliferate.

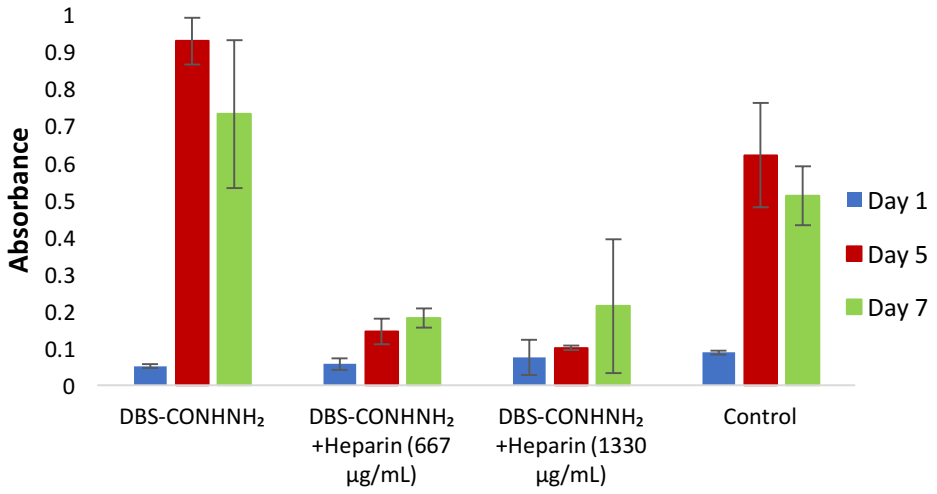

Figure 4.38. Absorbance of WST-1 reagent at 440 nm with (from left to right): DBS-CONHNH$_2$ hydrogels; DBS-CONHNH$_2$ hydrogels in the presence of heparin (667 µg/mL and 1330 µg/mL, respectively) and control (medium with cells), with cells on top, at day 1, 5 and 7.

In a later placement, cytocompatibility studies proceeded with an optimization of the number of cells, to avoid confluency, as well as an optimization of heparin concentration.

Thus, an initial cell density of 25000 cell/mL was used, together with lower heparin concentrations of 50 µg/mL, 25 µg/mL and 10 µg/mL.[263,266] Additionally, the cytocompatibility of DBS-$CONHNH_2$ hydrogels in the presence of heparin-C16-DAPMA aggregates and of hybrid hydrogels with DBS-$CONHNH_2$ and agarose was also studied. DBS-$CONHNH_2$ hydrogels in the presence of C16-DAPMA were not tested in 2D cell culture with cells on top of the gel, due to the fact that the presence of C16-DAPMA alone involves the formation of foam and therefore the hydrogel presents air bubbles and does not have an uniform surface, making it inappropriate to seed cells. Therefore, C16-DAPMA was only tested when interacting with heparin. From the studies described above we knew that it was not possible to obtain clear images from optical and fluorescence microscopy using DBS-$CONHNH_2$ hydrogels, therefore only the metabolic activity was tested for these optimized conditions (Figure 4.39).

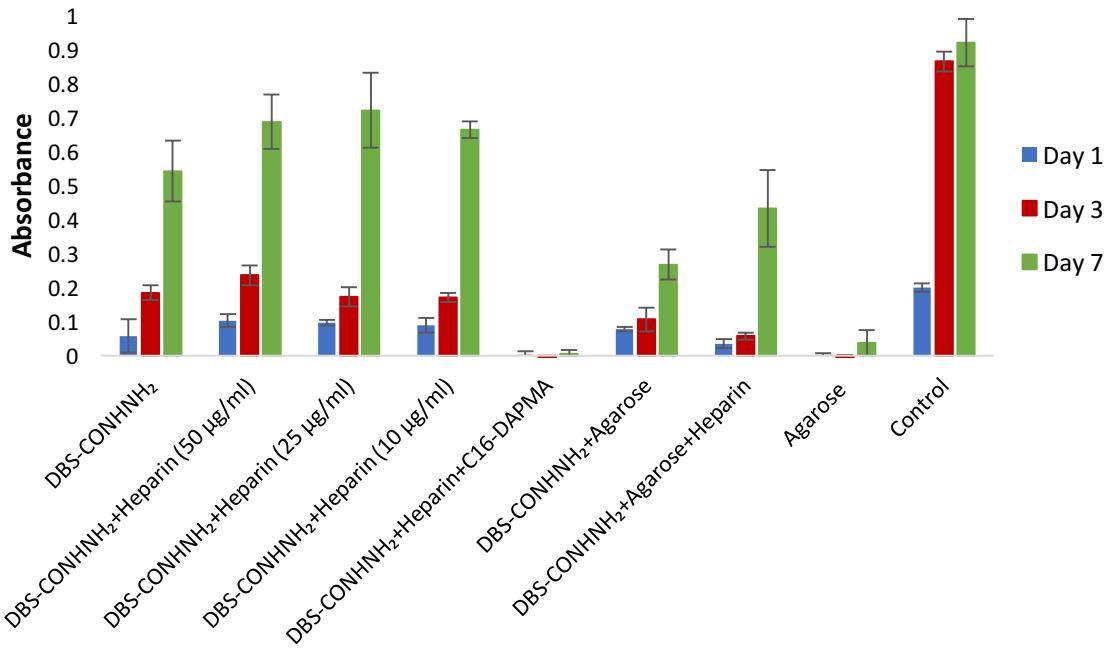

Figure 4.39. Absorbance of WST-1 reagent at 440 nm with (from left to right): DBS-$CONHNH_2$ hydrogels; DBS-$CONHNH_2$ hydrogels in the presence of heparin (50 µg/mL, 25 µg/mL and 10 µg/mL); DBS-$CONHNH_2$ hydrogels in the presence of heparin (50 µg/mL) and C16-DAPMA (140 µg/mL; DBS-$CONHNH_2$ hydrogels with agarose (1% w/v); DBS-$CONHNH_2$ hydrogels with agarose (1% w/v) and heparin (50 µg/mL); agarose (1%) and control (medium with cells), with cells on top of the gels, at day 1, 3 and 7.

From the obtained results, it is possible to verify that the presence of appropriate concentrations of heparin within DBS-$CONHNH_2$ gel network can slightly increase the metabolic activity of the cells over 7 days. The presence of heparin within the gel matrix can therefore, potentiate cell proliferation. Conversely, the presence of heparin-C16-DAPMA impaired cell proliferation, indicating a negative influence of the presence of C16-DAPMA within the gel or of the C16-DAPMA/heparin aggregates. Saturated fatty acids have been reported to induce apoptosis[iii] in different type of cells[267–272] with the carbon chain length having a direct influence on cell growth inhibition and inducing cell loss. In fact, while short to medium chain saturated fatty acids are presumably used by cells as an energy source, thus promoting cell growth, long-chain saturated fatty acids can be involved in the apoptosis of cells through the formation of ceramide,[273] reactive oxygen species[274] or alteration of mitochondrial membrane permeability.[275] Harvey et al[276] have shown the impact that the chain length of saturated fatty acids can have in endothelial cell functions. While medium (C6-C12) and short (C4) chain saturated fatty acids did not significantly affect cell growth, and short chain saturated fatty acids actually enhanced cell proliferation, long chain (C14-C20) fatty acids contributed to an increase of cell apoptosis and necrosis[iv]. Therefore, the use of palmitic acid as a building block for heparin binding may contribute to the inhibition of cell growth when incorporated in DBS-$CONHNH_2$ hydrogels. Alternatively, the adverse impact may be a result of using an amine-modified fatty acid, due to the high affinity of cationic molecules for net negative charge cell membranes (typically bacteria and cancer cells) or even mainly neutral zwitteronic cell membranes (e.g. mammalian cell membrane – only 5-10% of negatively charged phospholipids and 90-95% of zwitteronic phospholipids) which can be disrupted by interactions with high positive charge density molecules.[277–279]

When the cells were on top of agarose their proliferation was completely inhibited. This is most likely due to the absence of adhesion points therefore preventing cell growth. Although agarose is known for being biocompatible and having mechanical properties suitable for cell culture, one of its main limitations relates to the fact that it does not

[iii] *Apoptosis* describes the process of programed cell death.

[iv] *Necrosis* describes the premature death of cells caused by external factors.

contain moieties associated with cellular adhesion resulting in low cell adhesiveness and cell proliferation.[280,281] As agarose gels are transparent it was possible to observe them under the optical microscope, which showed that the cells were all aggregated on top of the gel in a spheroid shape, as shown in Figure 4.40. This proves that agarose does not allow the cells to adhere and subsequently proliferate. This feature probably had a negative influence on the metabolic activity of cells grown on hybrid hydrogels of DBS-$CONHNH_2$ and agarose, which was significantly decreased compared to the DBS-$CONHH_2$ hydrogels used alone. However, it was possible to verify that cells could grow effectively on DBS-$CONHNH_2$ and that the presence of heparin had some beneficial impact on metabolic activity.

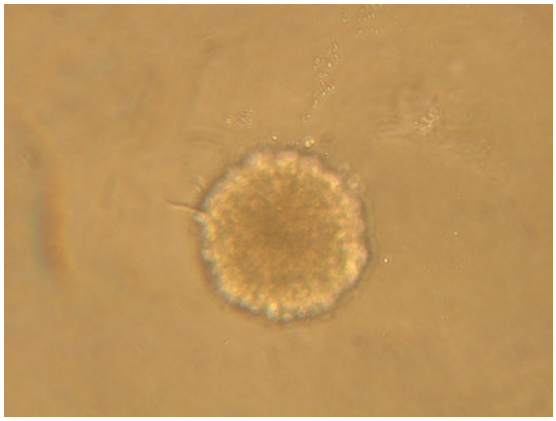

Figure 4.40. Optical microscope image of cells on top of 1% w/v agarose hydrogel at day 3.

Migration Assay

As it was not possible to obtain any additional information from the tested stainings, it was important to ensure whether the cells were adhering on the DBS-$CONHNH_2$ hydrogel surface or migrating into the well and adhering on the well surface. For that purpose, a cell migration assay was performed by simply preparing DBS-$CONHNH_2$ hydrogels (100 µL, 80 µL and 60 µL to test different gel thickness) in transwell inserts and adding cells on top of the gel (Figure 4.41 a).[282,283] If the cells migrate through the gel they will cross the membrane and adhere to the bottom of the well, which can be followed by optical microscopy (Figure 4.41 b). Additionally, to ensure that the cells were not attached to the membrane, the gels were removed and the inserts rinsed with trypsin to detach any cells

that were attached to the membrane. For comparison, two different controls were prepared, one where cells were added into a transwell insert in the absence of gel, with medium added into the well, and another where cells where added directly into the well.

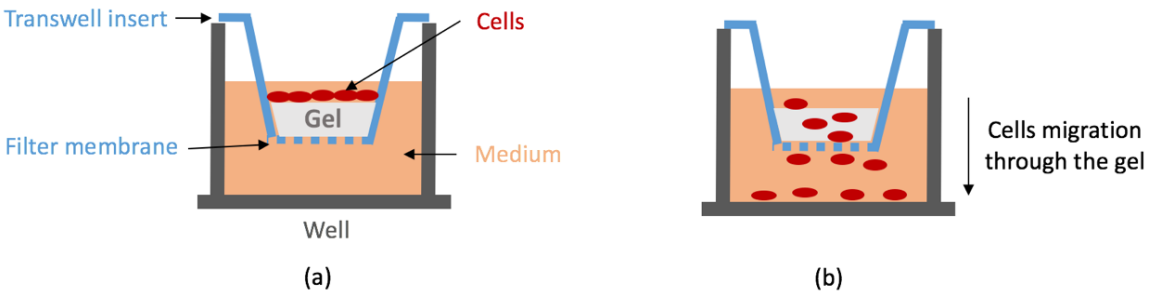

Figure 4.41. Schematic representation of the cell migration assay. (a) DBS-$CONHNH_2$ hydrogel was formed in the transwell insert and cells were added on top of the hydrogel. Medium was added in the well. (b) Cells migration through the gel network into the well. Adhesion of cells on the bottom of the well can be followed by optical microscopy.

After 1 day the plates were observed under the optical microscope but no cells were detected on the bottom of the wells, except for the control where cells were added directly into the well. After 7 days the same was observed and therefore, the gels were removed and the filters washed with trypsin. Again, no cells were observed in the wells where different volumes of DBS-$CONHNH_2$ hydrogels had been present (Figure 4.42). This result indicates that the cells do not migrate through DBS-$CONHNH_2$ hydrogel and therefore the results obtained for the metabolic activity correspond to the cells attached on the surface of DBS-$CONHNH_2$ hydrogels.

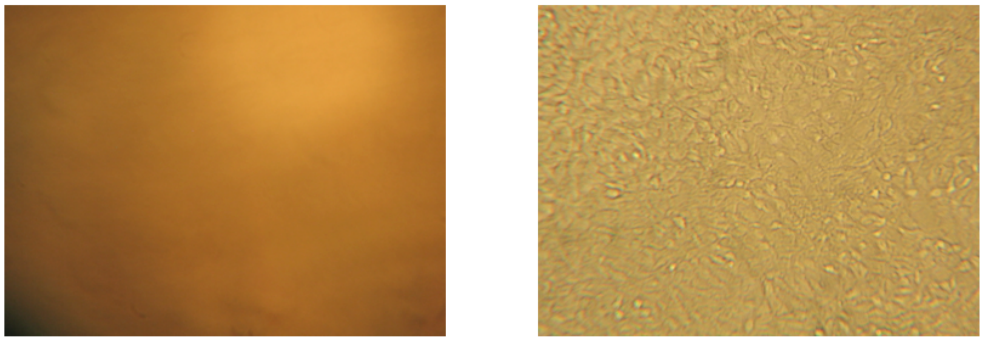

Figure 4.42. Example of an optical microscope image obtained on the migration assay for the well were DBS-$CONHNH_2$ hydrogels were present (left – no cells present) and control (right - cells added directly into the well and attached to the bottom of the well) after washing the membrane with trypsin, on day 7.

4.5.2. 2D Cell Culture in Transwells

DBS-$CONHNH_2$ hydrogels were then tested in transwells, with gels prepared in inserts, which were placed on top of medium, containing cells that were growing attached to the well plates. Initially, a cell density of 40000 cells/mL was used, but cells reached confluency before the end of the 7 days experiment (Figure 4.43). After optimization of the number of cells, a cell density of 10000 cell/mL was used. The cytocompatibility of DBS-$CONHNH_2$ hydrogels in the absence and the presence of heparin (50 µg/mL, 25 µg/mL and 10 µg/mL) was studied, as well as DBS-$CONHNH_2$ in the presence of C16-DAPMA, and the presence of heparin-C16-DAPMA aggregates. Furthermore, the cytocompatibility of the hydrid hydrogels composed of DBS-$CONHNH_2$ and agarose in the presence and absence of heparin was also studied.

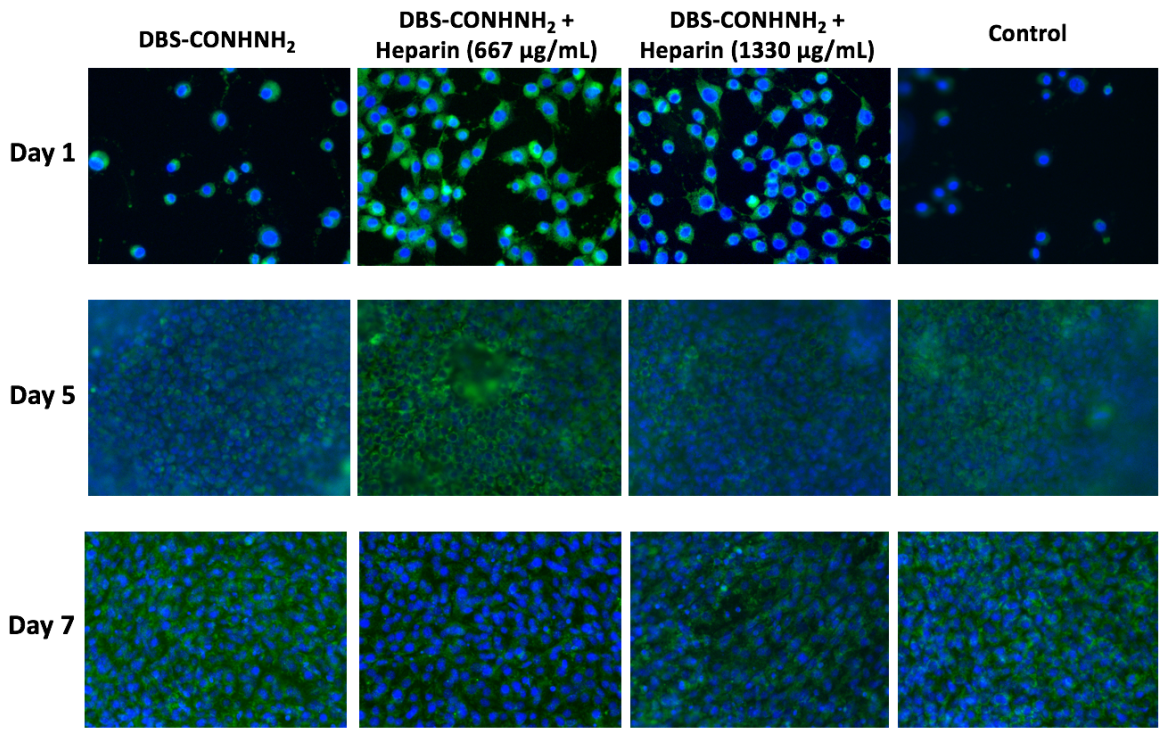

Figure 4.43. Fluorescence microscopy images of mitotraker/hoechst staining of DBS-$CONHNH_2$ hydrogels, DBS-$CONHNH_2$ hydrogels in the presence of heparin (667 µg/mL and 1330 µg/mL) and controls (medium with cells), in transwells, at day 1, 5 and 5. Cell density: 40000 cells/mL. Magnification: 20x.

Cell Morphology

Optical microscopy of cells with DBS-$CONHNH_2$ hydrogels in transwells allowed us to verify the elongation and the increase of the number of cells over one week, (Figure 4.44). This indicates that DBS-$CONHNH_2$ hydrogels do not appear to be toxic, as cells can adhere and grow when in contact with the LMWG hydrogel. Similar results were obtained for DBS-$CONHNH_2$ hydrogels with heparin and the hybrid hydrogels (Figure 4.45 and Figure 4.46, respectively), however, on day 3, cells were more elongated and stretched in the presence of heparin and in the hybrid hydrogels than for the DBS-$CONHNH_2$ hydrogels alone, which may indicate that these conditions can improve the biocompatibility of DBS-$CONHNH_2$ hydrogels for cells to adhere and proliferate. Additionally, when DBS-$CONHNH_2$ was incorporated with C16-DAPMA and heparin-C16-DAPMA aggregates, no cells were observed over the 7 days, indicating that the presence of C16-DAPMA is toxic and contributes to the death of the cells, which agrees with the lack of metabolic activity

observed on the previous experiment. Even when bound to heparin it is clear that C16-DAPMA is still exhibiting some toxicity.

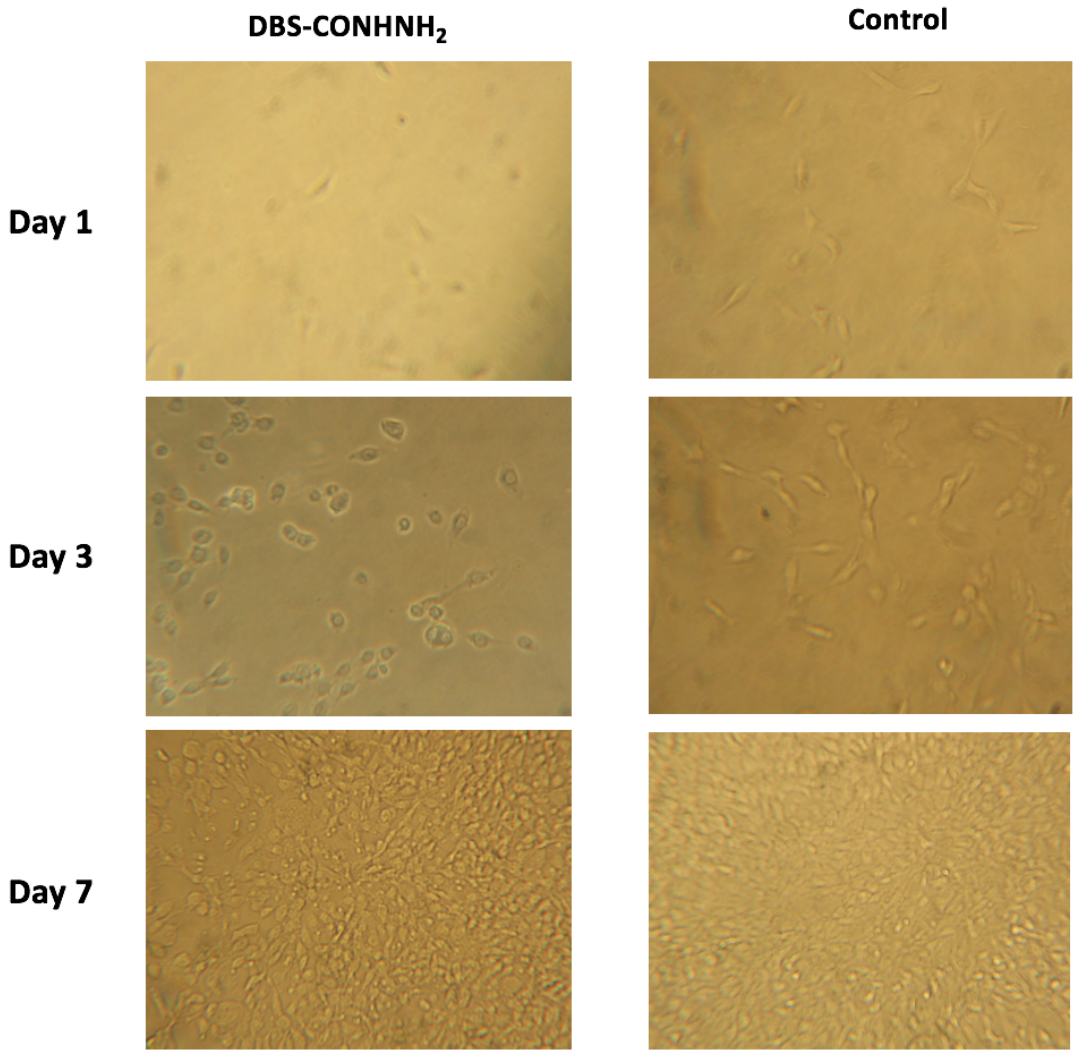

Figure 4.44. Optical microscopy images of DBS-CONHNH$_2$ hydrogels in transwells, at day 1 3 and 7 and control (medium with cells). Magnification: 20x.

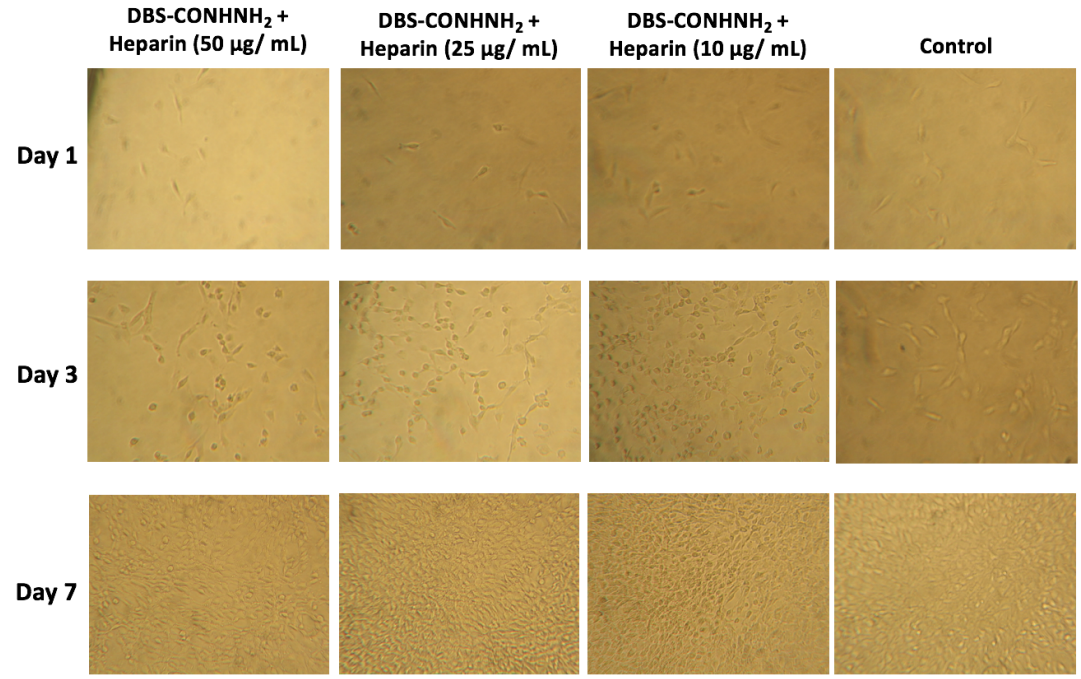

Figure 4.45. Optical microscopy images of DBS-$CONHNH_2$ hydrogels in the presence of heparin (50 µg/mL, 25 µg/mL and 10 µg/mL) and controls (medium with cells), in transwells, at day 1, 3 and 7. Magnifcation: 20x.

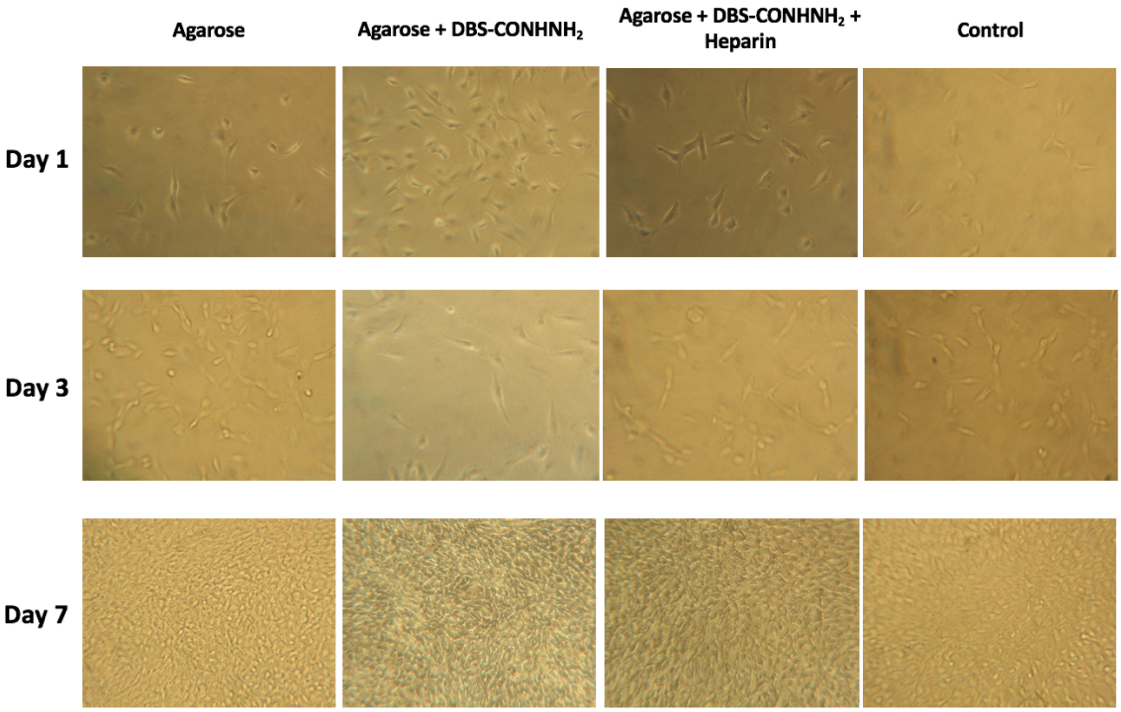

Figure 4.46. Optical microscopy images of agarose hydrogels, DBS-$CONHNH_2$ and agarose hybrid hydrogels and DBS-$CONHNH_2$ and agarose hybrid hydrogels in the presence of heparin (50 µg/mL) and controls (medium with cells), in transwells, at day 1, 3 and 7. Magnifcation: 20x.

Phalloidin/DAPI staining as shown in Figure 4.47, corresponds to the tests performed before the optimization of the cell density due to a malfunction of the computer connected to the fluorescence microscope when the optimised samples went for imaging. Nevertheless, the obtained images reveal the presence of stretched actin filaments on cells on day 1, from the DBS-$CONHNH_2$ hydrogel sample. On day 5 elongated filaments were also observed, together with cell confluency, as expected. This may indicate that DBS-$CONHNH_2$ hydrogels do not have a negative influence on cell growth, i.e., the hydrogels do not appear toxic to the cells, as they present a good adhesion and proliferation. Similar results were observed when heparin was incorporated within the gels (Figure 4.48).

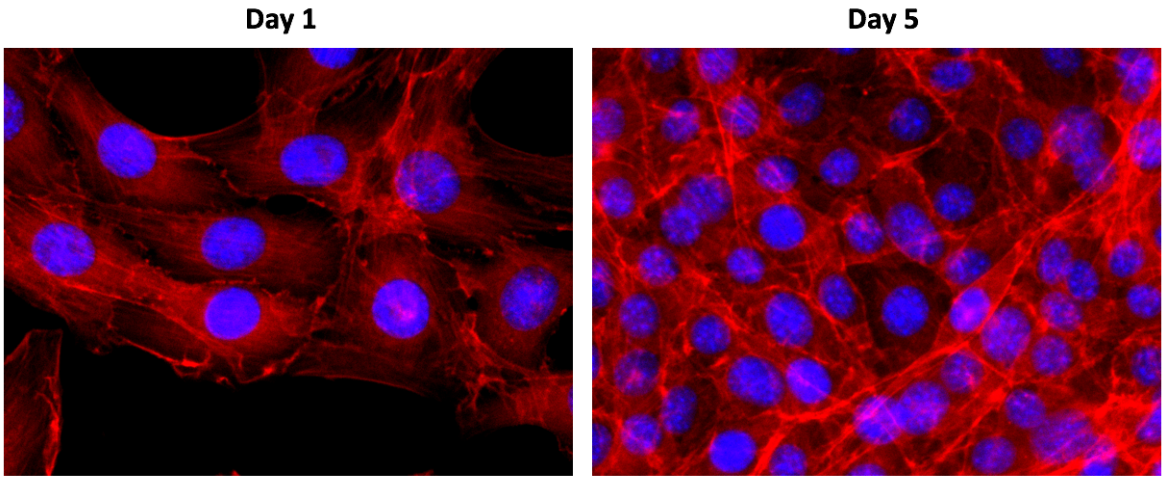

Figure 4.47. Fluorescence microscopy images of phalloidin/DAPI staining of DBS-$CONHNH_2$ hydrogels in transwells, at day 1 and 5. Magnification: 40x.

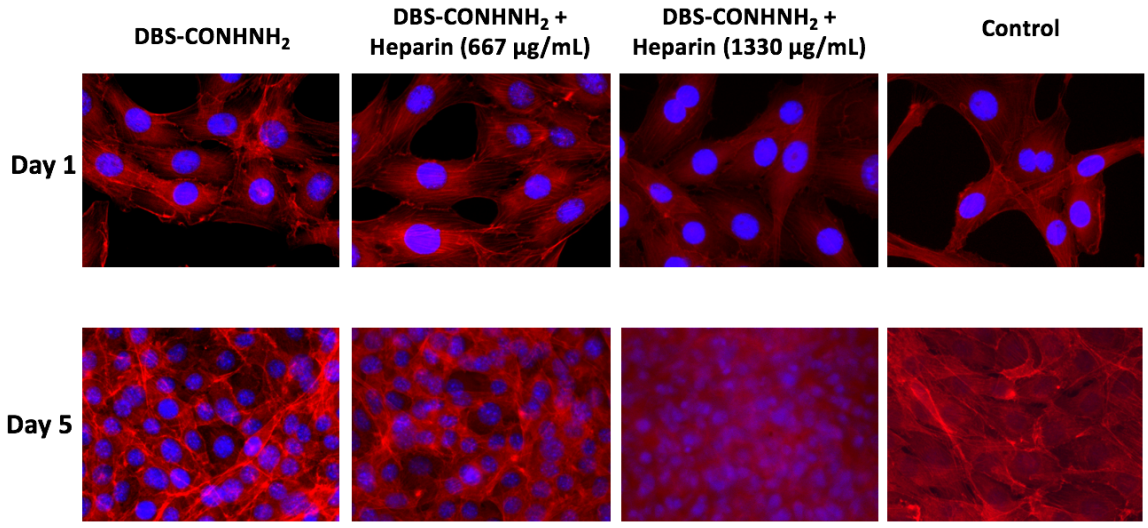

Figure 4.48. Fluorescence microscopy images of phalloidin/DAPI staining of DBS-$CONHNH_2$ hydrogels and DBS-$CONHNH_2$ hydrogels in the presence of heparin (667 µg/mL and 1330 µg/mL) in transwells at day 1 and 5. Magnification: 40x.

Live/Dead Staining

Live/dead staining images revealed the existence of viable cells on day 1, for DBS-$CONHNH_2$ hydrogels, DBS-$CONHNH_2$ hydrogels in the presence of heparin and for the hybrid hydrogels of DBS-$CONHNH_2$ and agarose (Figure 4.49, 4.50 and 4.51). On day 3, it was possible to observe elongated cells, as they were adhering to the well and proliferating. On day 7, the number of viable cells increased significantly, indicating that these conditions do not inhibit cell proliferation. However, once again when C16-DAPMA was present no cells were observed over the 7 days, corroborating the previously obtained results. Dead cells were not present or they were present in a very small number just in some samples, as they may had been washed off with the DPBS washes.

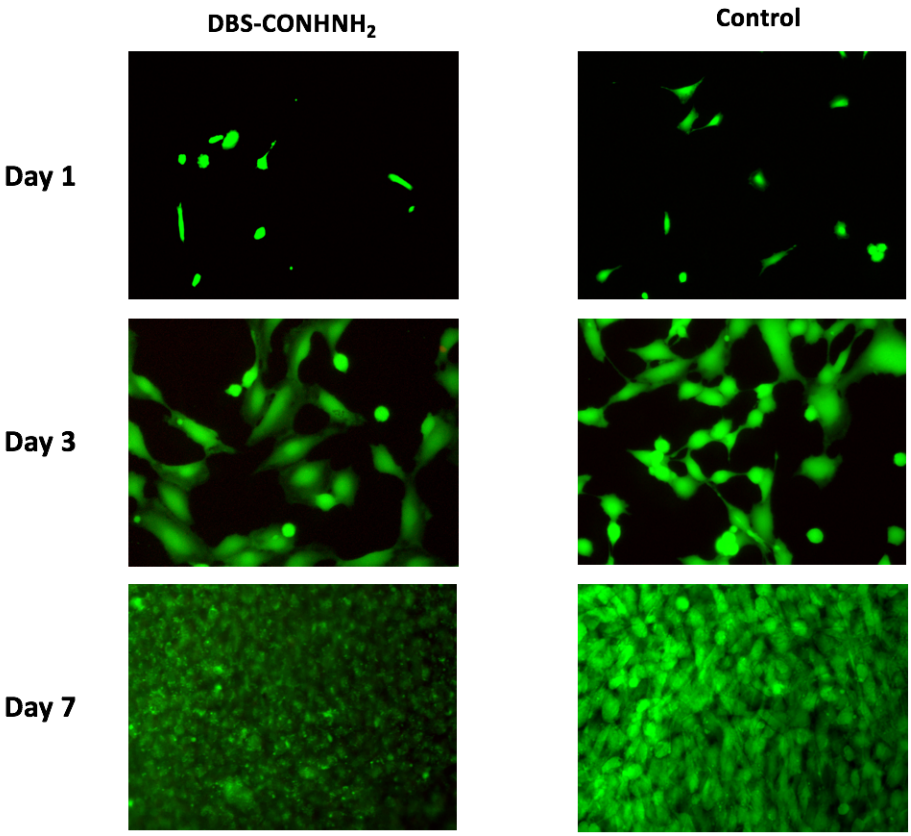

Figure 4.49. Fluorescence microscopy images of calcein-AM/PI staining of DBS-$CONHNH_2$ hydrogels (0.4% w/v) and controls (medium with cells), in transwells, at day 1, 3 and 7. Magnification: 20x.

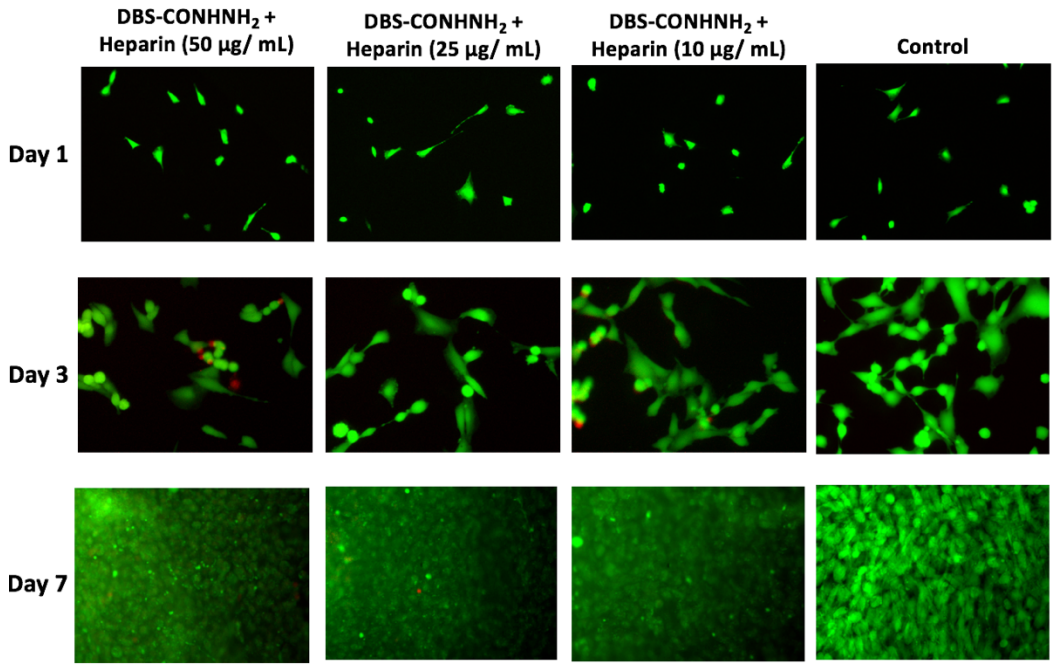

Figure 4.50. Fluorescence microscopy images of calcein-AM/PI staining of DBS-$CONHNH_2$ hydrogels in the presence of heparin (50 µg/mL, 25 µg/mL and 10 µg/mL) and controls (medium with cells), in transwells, at day 1, 3 and 7. Magnification: 20x.

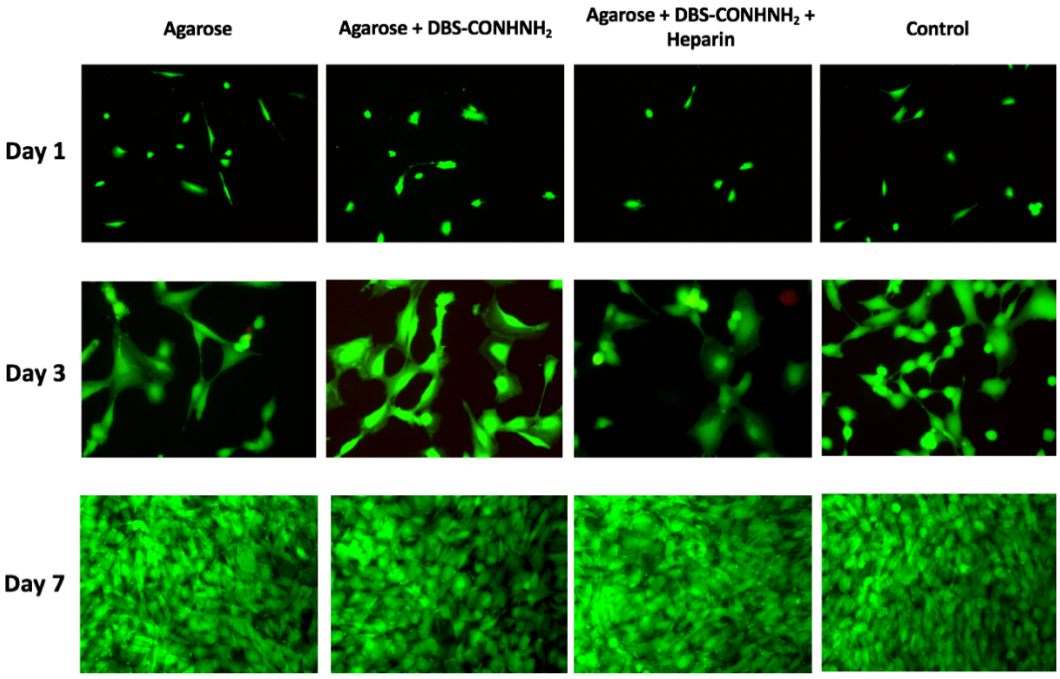

Figure 4.51. Fluorescence microscopy images of calcein-AM/PI staining of agarose hydrogels, DBS-$CONHNH_2$ and agarose hybrid hydrogels and DBS-$CONHNH_2$ and agarose hybrid hydrogels in the presence of heparin (50 µg/mL) and controls (medium with cells), in transwells, at day 1, 3 and 7. Magnification: 20x.

MitoTracker Staining

MitoTracker staining of cells in contact with DBS-$CONHNH_2$ hydrogels in transwells was obtained and is shown in Figure 4.52. Mitochondrial staining (green) was achieved over one week, indicating that DBS-$CONHNH_2$ hydrogels do not damage the mitochondria or reduce the membrane potential, otherwise the accumulation of the dye would not be possible. Similar results were observed when DBS-$CONHNH_2$ was incorporated with heparin (50 µg/mL, 25 µg/mL and 10 µg/mL) (Figure 4.53) and when cells were in contact with the hybrid hydrogels of DBS-$CONHNH_2$ and agarose in the presence and absence of heparin (Figure 4.54). Additionally, when C16-DAPMA was present within the gel network the presence of cells was not detected, confirming the toxicity of C16-DAPMA.

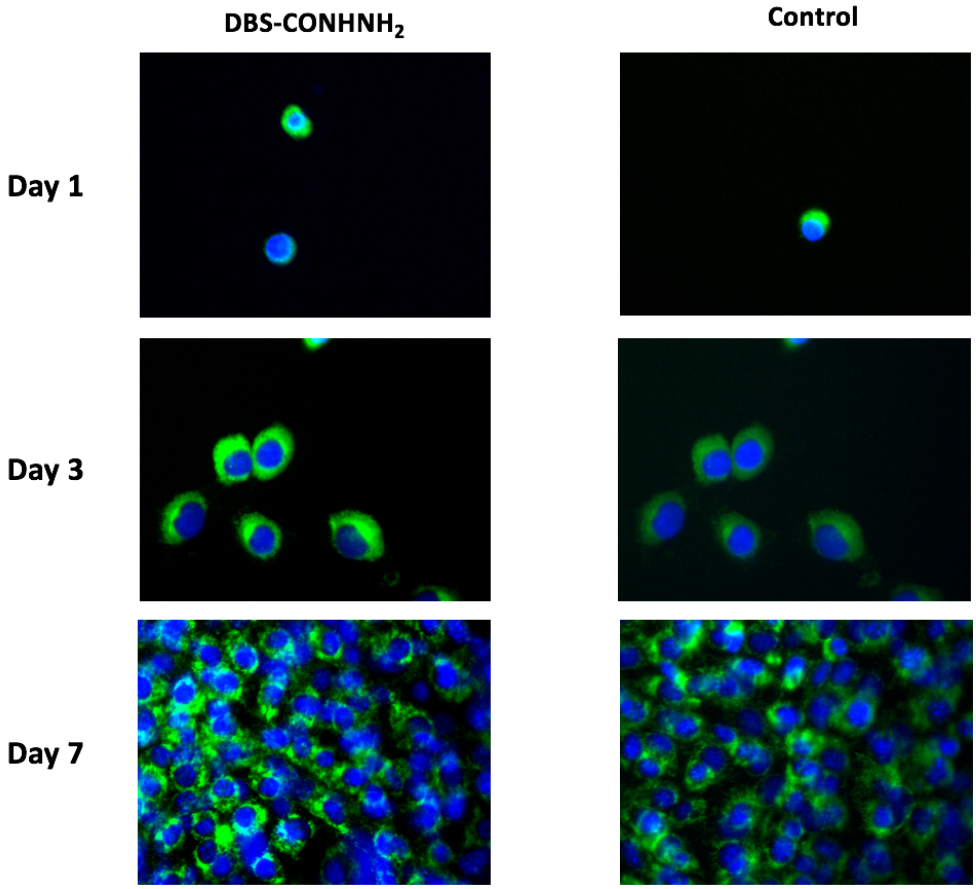

Figure 4.52. Fluorescence microscopy images of mitotraker/hoechst staining of DBS-$CONHNH_2$ hydrogels (0.4% w/v) and controls (medium with cells), in transwells, at day 1, 3 and 7. Magnification: 40x.

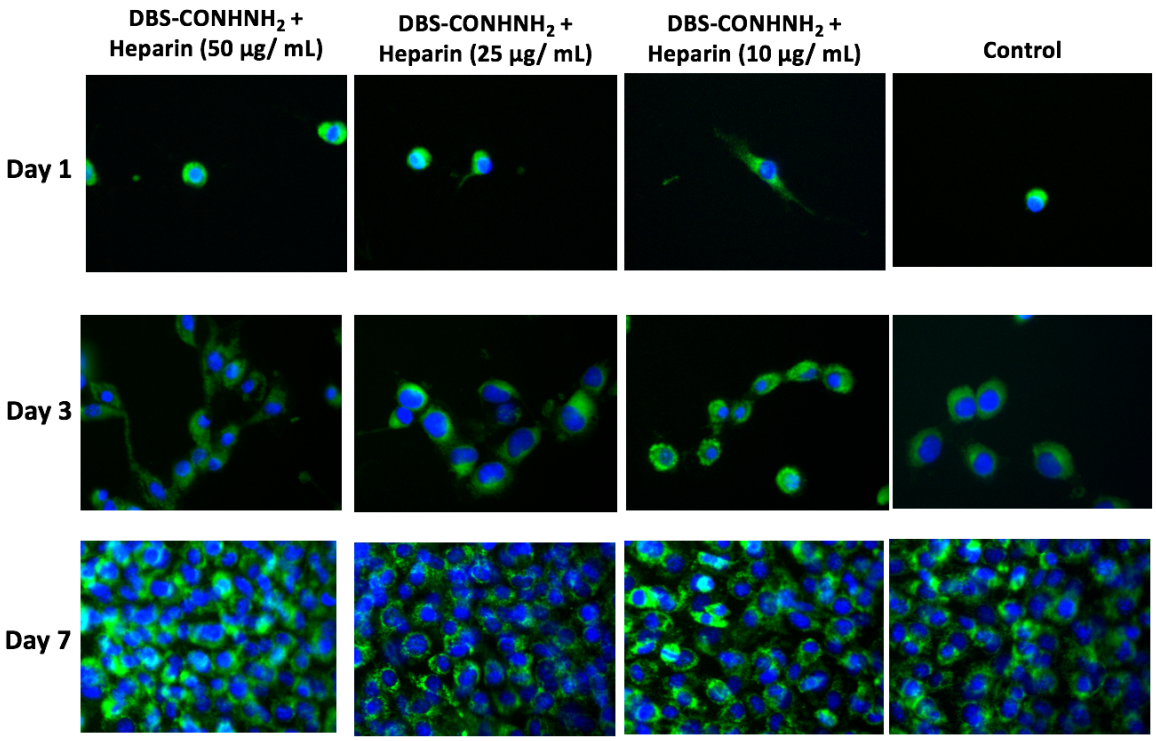

Figure 4.53. Fluorescence microscopy images of mitotraker/hoechst staining of DBS-$CONHNH_2$ hydrogels in the presence of heparin (50 µg/mL, 25 µg/mL and 10 µg/mL) and controls (medium with cells), in transwells, at day 1, 3 and 7. Magnification: 40x.

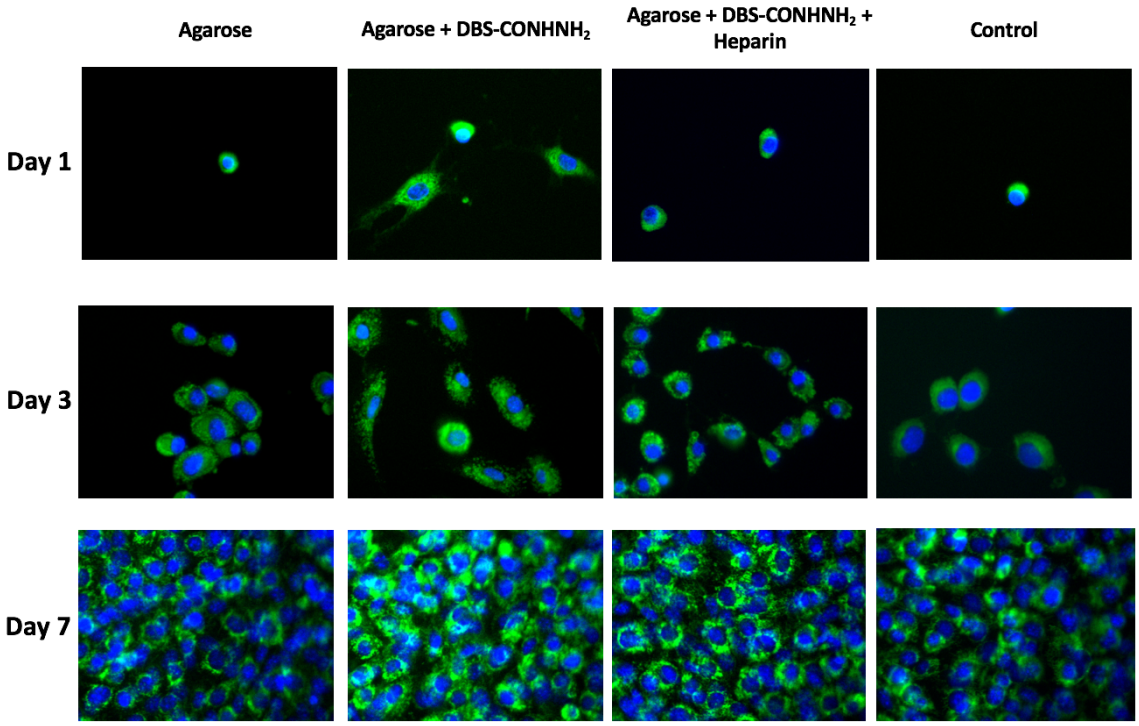

Figure 4.54. Fluorescence microscopy images of mitotraker/hoechst staining of agarose hydrogels, DBS-$CONHNH_2$ and agarose hybrid hydrogels and DBS-$CONHNH_2$ and agarose hybrid hydrogels in the presence of heparin (50 µg/mL) and controls (medium with cells), in transwells, at day 1, 5 and 7. Magnification: 40x.

Metabolic Activity

Metabolic activity of DBS-$CONHNH_2$ hydrogels (Figure 4.55) in transwells shows a slightly better metabolic activity after 7 days when heparin (50 µg/mL, 25 µg/mL and 10 µg/mL) is incorporated within DBS-$CONHNH_2$ hydrogels. In contrast, this assay clearly shows the toxicity of C16-DAPMA, as the absence of metabolic activity proves that no viable cells were present. Interestingly, the presence of agarose revealed good metabolic activity over one week. Comparing this result with the obtained metabolic activity when cells were added to the top of agarose, allows us to conclude that agarose is not toxic to cells, but despite being biocompatible, does not have adhesion moieties with which cells can adhere and proliferate.

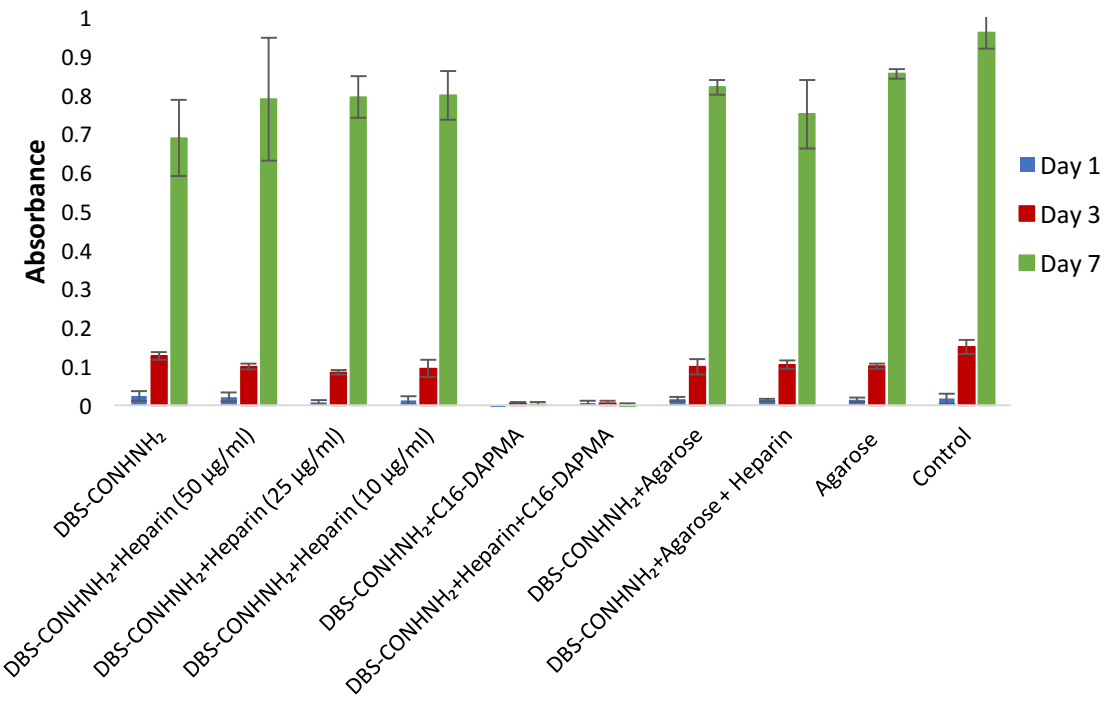

Figure 4.55. Absorbance of WST-1 reagent at 440 nm with (from left to right): DBS-$CONHNH_2$ hydrogels; DBS-$CONHNH_2$ hydrogels in the presence of heparin (50 µg/mL, 25 µg/mL and 10 µg/mL); DBS-$CONHNH_2$ hydrogels in the presence of C16-DAPMA (140 µg/mL); DBS-$CONHNH_2$ hydrogels in the presence of heparin (50 µg/mL) and C16-DAPMA (140 µg/mL); DBS-$CONHNH_2$ hydrogels with agarose (1% w/v); DBS-$CONHNH_2$ hydrogels with agarose (1% w/v) and heparin (50 µg/mL); agarose (1%) and control (medium with cells), in transwells, at day 1, 3 and 7.

For additional information, Figure 4.56 shows the metabolic activity before cell density optimization of DBS-$CONHNH_2$ hydrogels in the presence of higher concentrations of heparin (1 mM - 667 µg/mL and 2 mM - 1330 µg/mL). The significant higher concentrations of heparin resulted in a decrease of the metabolic activity when compared with DBS-$CONHNH_2$ hydrogels alone, after 7 days. This is in agreement with the lower metabolic activity obtained when the cells were on top of the hydrogels using the same heparin concentrations, indicating lower biocompatibility when heparin is used in excess. This confirms that the concentration of heparin incorporated in DBS-$CONHNH_2$ hydrogels is crucial to support and promote the growth of cells.

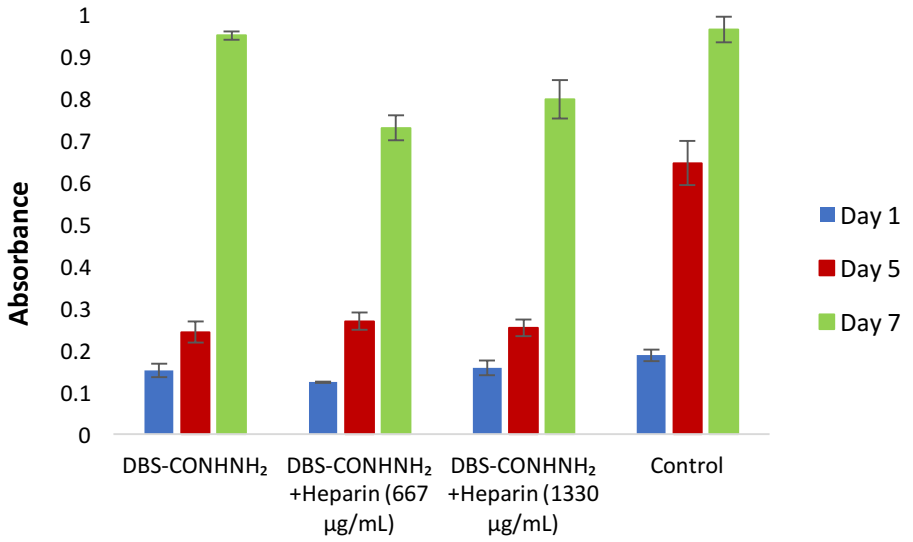

Figure 4.56. Absorbance of WST-1 reagent at 440 nm with (from left to right): DBS-$CONHNH_2$ hydrogels; DBS-$CONHNH_2$ hydrogels in the presence of heparin (667 µg/mL and 1330 µg/mL) and control (medium with cells), in transwells, at day 1, 5 and 7.

4.5.3. 3D Cell Culture

The preparation of DBS-$CONHNH_2$ gels involves the heating of samples at high temperatures (close to the boiling point of water) which creates harsh conditions for the cells to survive, with gelation occurring within seconds. Consequently, the heating and thereafter the transfer of the samples into the well plates and inserts had to be done outside the cell culture hood with subsequent sterilization by application of UV-light. The fact that the gels were prepared in non-sterile conditions, meant it was not possible to perform 3D cell encapsulation experiments in these DBS-$CONHNH_2$ hydrogels.

4.6. Summary, Conclusions and Future Work

To overcome the limitations of using DBS-COOH hydrogels as potential scaffolds for tissue engineering, DBS-$CONHNH_2$ LMWG was synthesised and its orthogonal self-assembly with heparin and C16-DAPMA was studied. The incorporation of these two components within the gel network did not inhibit gelation. Furthermore, the addition of heparin-C16-DAPMA aggregates into the DBS-$CONHNH_2$ hydrogels resulted in stable and uniform hydrogels using a charge raio +/- of 2 at different concentrations of heparin/binder, with a decrease of the charge ratio +/- only being observed for concentrations of heparin higher than 600

μM. Moreover, it was demonstrated that the presence of C16-DAPMA interacting with heparin in the hydrogel network had a significant effect on the thermal stability of the hydrogel, affecting also the CD signal intensity. IR spectra of the gel in the presence of binder and heparin showed overlap of the characteristic vibrations of C16-DAPMA, heparin and DBS-$CONHNH_2$ suggesting effective self-sorting at the molecular level. The use of MalB solution on top of the gel allowed us to prove that binder - heparin interactions appear to be unaffected when incorporating these two components within the gel. By using TEM and SEM the presence of aggregates characteristic of the C16-DAPMA interacting with heparin were observed, along with nanofibers but also needles which were not observed for the gel alone. This indicates that the C16-DAPMA-heparin aggregates influence the self-assembly of DBS-$CONHNH_2$ gel fibers, changing its morphology. The mechanical properties of the hydrogel were affected when C16-DAPMA alone was incorporated due to the formation of foam, while the presence of agarose contributed to the formation of stiffer and stronger gels, as expected. Additionally, this study provides evidence that when mixing heparin, C16-DAPMA or heparin-C16-DAPMA aggregates with DBS-$CONHNH_2$ into one single system, the individual function of each component is kept, hence the multi-component systems tested are orthogonal.

The release of heparin from DBS-$CONHNH_2$ hydrogels was achieved and the addition of agarose up to 1% w/v did not affect the maximum amount of heparin that can be released, while also allowing the formation of robust and stiffer gels. Furthermore, the presence of C16-DAPMA limited the release of heparin by binding to it and hence preventing its escape from the gel. The addition of borax/NaOH buffer (pH 10) on top of DBS-$CONHNH_2$ hydrogels incorporating heparin-C16-DAPMA aggregates, contributed to an increase of heparin released from the hydrogel, which can indicate that a triggered release is achievable by deprotonating the positively charged C16-DAPMA that consequently cannot interact electrostatically with heparin, allowing its release from the gel. Additionally, controlled release of heparin was achievable by changing the surface area of gel in contact with the release medium.

From the cytocompatibility studies performed, 3D cell culture assays could not be performed due to the preparation method of DBS-$CONHNH_2$ hydrogels which required high

temperatures. 2D cell culture assays revealed that DBS-$CONHNH_2$ hydrogels remained stable in the plates throughout the 7 days of experiment and no fluctuation of gels or disruption of the gel network was observed. Due to the high density of the gel it was difficult to obtain clear fluorescence microscopy images when the cells were put on top of the gels. However, the metabolic activity assay proved that cells were able to adhere and proliferate when on top of DBS-$CONHNH_2$ hydrogels, with a somewhat higher metabolic activity being obtain when 10-50 μg/mL of heparin was incorporated within the hydrogel. Additionally, migration studies proved that cells did not migrate through the gel and attach to the bottom of the plates, confirming that the obtained metabolic activity corresponded to the cells growing directly on top of DBS-$CONHNH_2$ hydrogels. Furthermore, when DBS-$CONHNH_2$ hydrogels were tested alone and in the presence of 10-50 μg/mL of heparin in transwells, clear fluorescence microscopy images were obtained, where it was possible to observe the presence of viable cells, able to adhere, stretch and proliferate over one week. In addition, cell proliferation assays confirmed that DBS-$CONHNH_2$ hydrogels are not cytotoxic, and again the presence of 10-50 μg/mL of heparin could improve the metabolic activity of the cells. In contrast, the use of higher concentrations of heparin (667 μg/mL and 1330 μg/mL) proved to have the opposite influence, with metabolic activity decreasing significantly, indicating that the concentration of heparin incorporated within the gel network is crucial to support and promote cell growth.

In respect to the hybrid hydrogels, we could conclude that agarose, although biocompatible, does not have adhesion moieties and therefore, cells are not able to adhere to the hybrid hydrogels as effectively as when only DBS-$CONHNH_2$ is present. The presence of C16-DAPMA as heparin binder within the gel network proved to be toxic to the cells, with no cells being detected using the fluorescence microscope and no metabolic activity being obtained, indicating that cells died when in contact with C16-DAPMA. Even when bound to heparin, the C16-DAPMA still had a negative influence on cell growth.

Additionally, for a less extensive and faster cytotoxicity study, the live/dead staining and the metabolic activity test in transwells should be prioritised as they will be sufficient to obtain conclusive and valid information.

As future work, further release studies could be performed in order to better understand the influence of pH of release medium in triggering heparin release from the gel. Additionally, the release assays could be adapted and designed in order to mimic the gel preparation needed in cell culture plates. It would be of great interest to test the cytotoxicity of DBS-$CONHNH_2$ hydrogels on different types of cells, namely primary cells (e.g. human adipose derived stem cells). Furthermore, as C16-DAPMA proved to be toxic, its replacement is crucial. Smith's group has since developed a cholesterol-based heparin binder which proved to have low cytotoxicity and could replace C16-DAPMA. Also, the use of gelatin or gelatin-agarose conjugates as PG to form the hybrid hydrogel with DBS-$CONHNH_2$ can overcome the limitation obtained with agarose hydrogels by incorporating cell adhesion moieties.[281,284] It is also worth noting that, DBS-$CONHNH_2$ and agarose hybrid hydrogels proved to be biocompatible so they could be used for different applications such as drug delivery. Controlled release of heparin has significant relevance in a clinical setting to avoid deep vein thrombosis.[285]

5. Orthogonal Self-Assembly of Cyclohexane-Based Low-Molecular-Weight Hydrogels

The following studies were performed on a placement at Delft University of Technology in Netherlands, as part of the SmartNet network.

5.1. Introduction

With the majority of the reported applications of hydrogels still using polymeric gelators, in fields such as biomedicine,[286–290] food[291,292] and cosmetics,[293–295] the use of responsive LMWGs as potential alternative to polymer gels has become an attractive subject. The van Esch research group has widely studied the use of LMWGs as a complement to or substitute for polymeric hydrogels.[296–307]In particular, they have designed a family of effective LMWGs consisting of a triamide cyclohexane gelating scaffold with the addition of amino acid substituents that contribute via the additional presence of hydrogen bonding and hydrophobic interactions to promote gelation (Figure 5.1). [296]

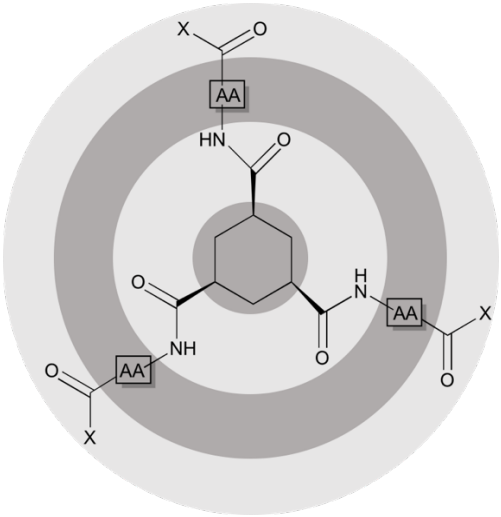

Figure 5.1. Chemical structure of cyclohexane-based LMWGs. Light grey: hydrophilic regions; dark grey: hydrophobic regions. AA: aminoacid; X: hydrophilic substituent.[296]

In this chapter, the assembly of a multi-component hybrid system using cyclohexane-based LMWGs with heparin and C16-DAPMA was studied. Figure 5.2 shows the LMWGs used for

this study that were previously synthesised by Vincent le Sage from Delft University of Technology.

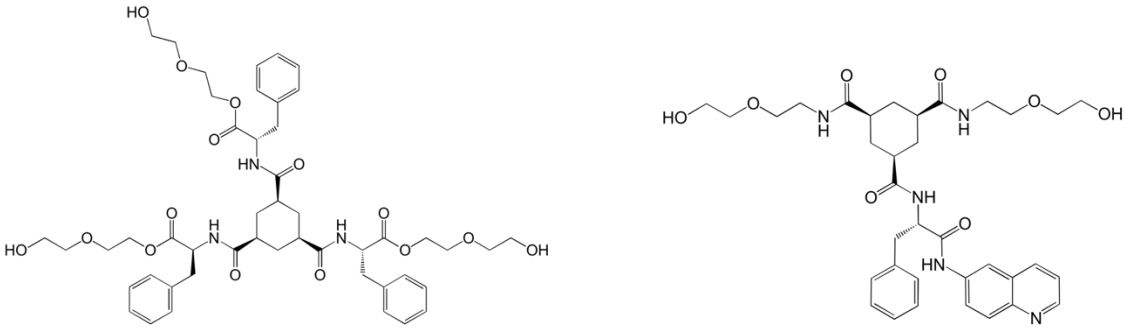

Figure 5.2. Chemical structure of cyclohexane-based hydrogelators. OG1: heat-cool gelator and OG2: pH responsive gelator.

Compound OG1 is a thermoreversible hydrogelator capable of forming stable gels at very low concentrations due to the presence of phenylalanine amino acids that provide hydrophobic interactions fundamental for the gelation of water.[296] OG2 was designed as a LMWG-drug conjugate system. Specifically, it is a pH responsive gelator connected to a phenylalanyl-aminoquinoline that can be enzymatically cleaved, releasing the aminoquinoline group, through the hydrolysis of the amide into an amine.[298] The OG2 gel forms on raising the pH as the protonated aminoquinoline is converted into the neutral free base form. Interestingly, the drug is protected from enzymatic action while the gel nanofibers are assembled. After applying a stimulus to disassemble the gel nanofibers (e.g. temperature, pH) the individual molecules can be enzymatically cleaved and the drug can be released (Figure 5.3). Both compounds have ethylene glycol chains connected in order to control the degree of hydrophobicity, introducing the degree of water solubility needed to form gels.[296,298,300]

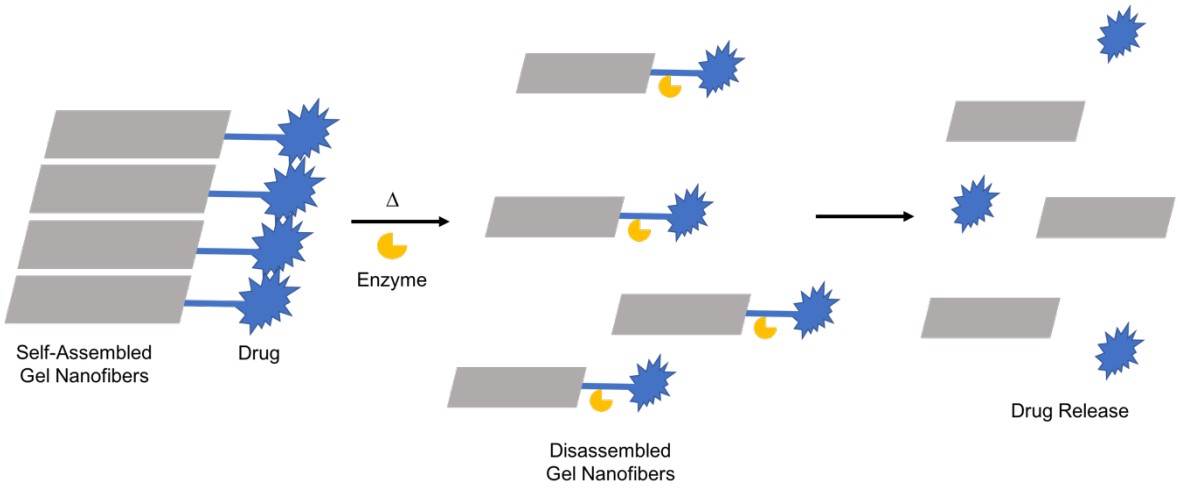

Figure 5.3. Schematic representation of a two-step release system with the dissociation of self-assembled nanofibers followed by enzymatic cleavage for OG2-drug conjugate hydrogels. Δ: trigger of gel-sol transition (temperature, pH).[Adapted from reference [298]]

The goal was to use self-assembled C16-DAPMA micelles to interact with heparin and study their coexistence within the OG1/ OG2 gel networks. Studies were performed in order to better understand this multi-component supramolecular system.

5.2. Orthogonal Self-Assembly of Cyclohexane Hydrogels with C16-DAPMA and Heparin

Firstly, heparin, C16-DAPMA and heparin-C16-DAPMA aggregates were incorporated within OG1 and OG2 hydrogels to understand if the addition of these components inhibited the formation of OG1 and OG2 gels. The gelation of OG1 in water was achieved by cooling heated solutions of 0.5% w/v of gelator. The final pH of the OG1 gel was 7. OG2 hydrogels were obtained by acidifying the gelator solution (0.5% w/v) in water, with HCl (1 M), to completely dissolve the gelator, followed by the neutralisation of the solution by rapid addition of NaOH (1 M). The final pH of the OG2 gel was between 8-9. Heparin, C16-DAPMA and heparin-C16-DAPMA aggregates were added to the LMWG solutions prior to heating for OG1 and prior to the addition of NaOH for OG2, as after heating and adding NaOH the hydrogels formed immediately. The final pH of OG1 and OG2 gels in the presence of additives was the same as for the hydrogels alone.

Gel Formation with the Incorporation of Different Concentrations of Heparin or C16-DAPMA

In order to test the influence of heparin on the formation of OG1 and OG2 hydrogels, different concentrations of heparin (38 μM; 150 μM; 300 μM; 400 μM; 600 μM; 1000 μM) were added to the gelator solutions. For all the different concentrations tested, stable and homogeneous gels were obtained, suggesting that the presence of heparin does not inhibit gel formation. The same was observed when different concentrations of C16-DAPMA (150 μM; 300 μM; 600 μM; 800 μM; 1000 μM; 1200 μM) were added to OG1 and OG2 gels, with stable and homogenous gels being formed in each case.

Gel Formation with Constant Concentrations of Heparin and Different Concentrations of C16-DAPMA

Gel formation was then tested by keeping the heparin concentration constant and varying C16-DAPMA concentration in order to verify the best charge ratio of these two molecules for the formation of stable gels. For the different heparin concentrations tested, an initial charge ratio (+/-) of 2 was used. If no stable/ homogeneous gels were formed, lower concentrations of C16-DAPMA were used for the same heparin concentration.

Table 5.1 shows the tested ratios of heparin and C16-DAPMA in OG1 hydrogels, where it is possible to verify that for a heparin concentration of 150 μM, the use of the maximum concentration of C16-DAPMA calculated lead to the formation of stable gels. For heparin concentrations above 300 μM, charge ratios below 2 were needed to allow the formation of stable gels. The higher the heparin concentration, the lower the charge ratio between heparin and C16-DAPMA needed to obtain stable and uniform gels. This may indicate that on increasing the heparin/C16-DAPMA concentration, more aggregates will be present and the dispersity of these aggregates destabilises the nanofiber gel network.

Table 5.1. Test of different heparin/ binder ratios on OG1 gel formation.

[Heparin] (μM)	[C16-DAPMA] (μM)	Gel Formation	Charge ratio +/-
150	Below 600	Stable gel	2
300	Above 1100	Non uniform gel	1.7
	Below 1000	Stable gel	
400	Above 900	Non uniform gel	1
	Below 800	Stable gel	
600	Above 1300	Non uniform gel	1
	Below 1200	Stable gel	

The incorporation of different heparin and C16-DAPMA ratios within OG2 hydrogels (Table 5.2) revealed that the use of a charge ratio of 2 for all the different heparin concentrations tested, resulted in the formation of stable gels. Unlike the OG1 hydrogels, the increase of the heparin/ C16-DAPMA concentrations within the OG2 network did not appear to affect gel stability, which may indicate a higher loading capacity of OG2 hydrogels than OG1 hydrogels, or less sensitivity to an excess of C16-DAPMA.

Table 5.2. Test of different heparin/ binder ratios in OG2 gel formation.

[Heparin] (μM)	[C16-DAPMA] (μM)	Gel Formation	Charge ratio +/-
150	Below 600	Stable gel	2
300	Below 1200	Stable gel	2
400	Below 1600	Stable gel	2
600	Below 2400	Stable gel	2

5.2.1. Thermal Stability and T_{gel} Determination

The thermal stability of the gels formed in the previous sections was tested by the "dropping ball method", where a steel ball is placed on top of the gel and the temperature monitored by placing the gels in a heating block (Figure 5.4).[308] The T_{gel} value was considered the temperature at which the steel ball started to fall through the gel. OG1 gel

(0.5% w/v) in water presented a T_{gel} value of 65 °C. The incorporation of different concentrations of heparin, C16-DAPMA and heparin/C16-DAPMA aggregates resulted in the observations of the same T_{gel} value, indicating that the presence of these different components had no effect on the thermal stability of the OG1 gel.

The OG2 gel (0.5% w/v) in water presented a T_{gel} value of 72 °C. The presence of heparin in the gel yielded materials with T_{gel} values of approximately 78 °C, that can be considered as the same T_{gel} range as for the gel alone, indicating that heparin does not appear to significantly affect the thermal stability of OG2 gels. When C16-DAPMA, or heparin bound to C16-DAPMA were incorporated within the gel, the T_{gel} values decreased to approximately 50 °C, indicating that C16-DAPMA and heparin/C16-DAPMA aggregates do influence the thermal stability of OG2 hydrogels.

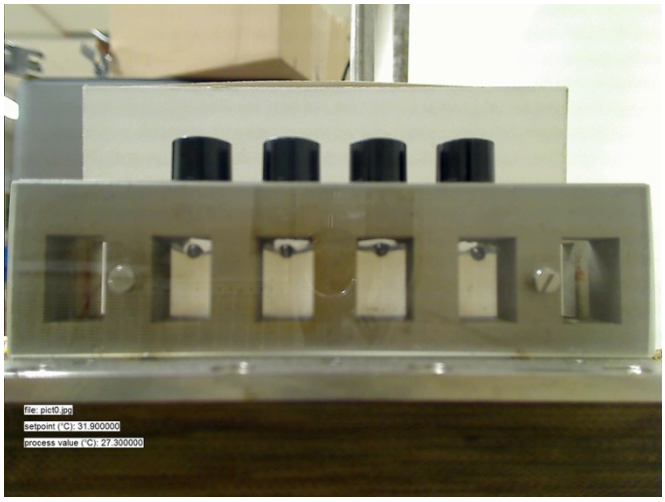

Figure 5.4. Dropping ball method: Steel balls are placed on top of gels, that subsequently are placed in a heating block, where the temperature is monitored and recorded.

5.2.2. Transmission Electron Microscopy

TEM images of the OG1 gel, the OG1 gel in the presence of heparin, as well as in the presence of C16-DAPMA and heparin-C16-DAPMA aggregates were obtained to gain a better understanding of the morphology of these different systems.

TEM images of the OG1 hydrogel (Figure 5.5) showed the presence unbranched nanofibers with a diameter of 13.6 $\pm$ 1.6 nm. In the presence of heparin (Figure 5.6), the OG1 hydrogel

showed a different morphology, with what appeared to be rigid alignment of the nanofibers (12.7 $\pm$ 1.0 nm) being induced by heparin, resulting in thicker structures that resemble needles. In addition, when C16-DAPMA is added into the OG1 hydrogels (Figure 5.7), it also appears to influence the self-assembly of OG1, contributing to the formation of significantly thinner (4.4 $\pm$ 0.4 nm in diameter) and longer unbranched nanofibers, when compared to the OG1 hydrogel alone.

Figure 5.8, shows the OG1 hydrogel in the presence of heparin bound to C16-DAPMA using phosphotungstic acid (4.2%) stain and a gold grid, where it is possible to see the presence of both nanofibers and the typical organised aggregates of heparin interacting with C16-DAPMA. However, it must be noted that these conditions for imaging did not result in very clear images. It was difficult to identify the gel nanofibers and for that reason, all the imaging was repeated using uranyl acetate stain in a copper grid as described in the experimental part. However, using this approach the stain did not set properly or reveal clear images. Nevertheless, it is possible to conclude that the incorporation of heparin-C16-DAPMA aggregates did not prevent the nanofiber assembly and the interactions between heparin and C16-DAPMA remain present, as the typical hierarchically-organised and aligned nanostructures of heparin-C16-DAPMA aggregates were observed.

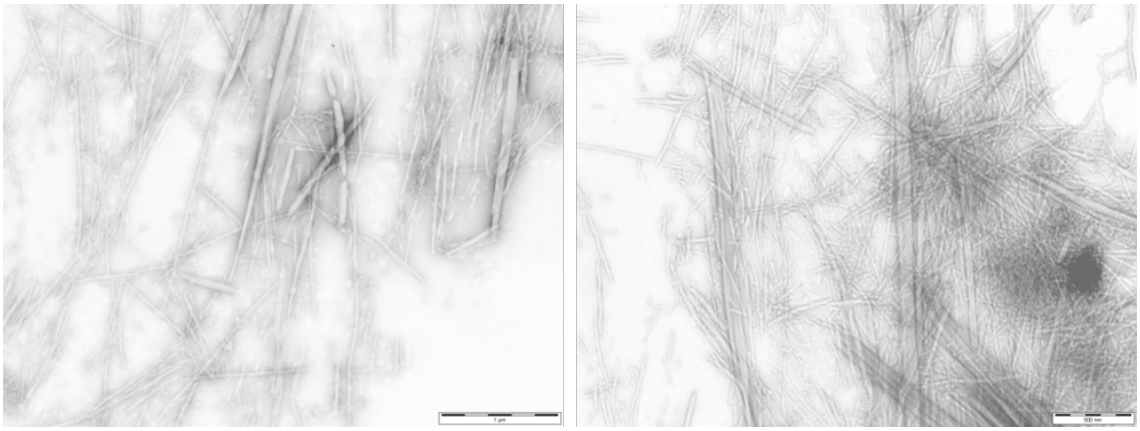

Figure 5.5. TEM images of OG1 (0.5% w/v) gel. Scale bars: 1 μm (left) and 500 nm (right).

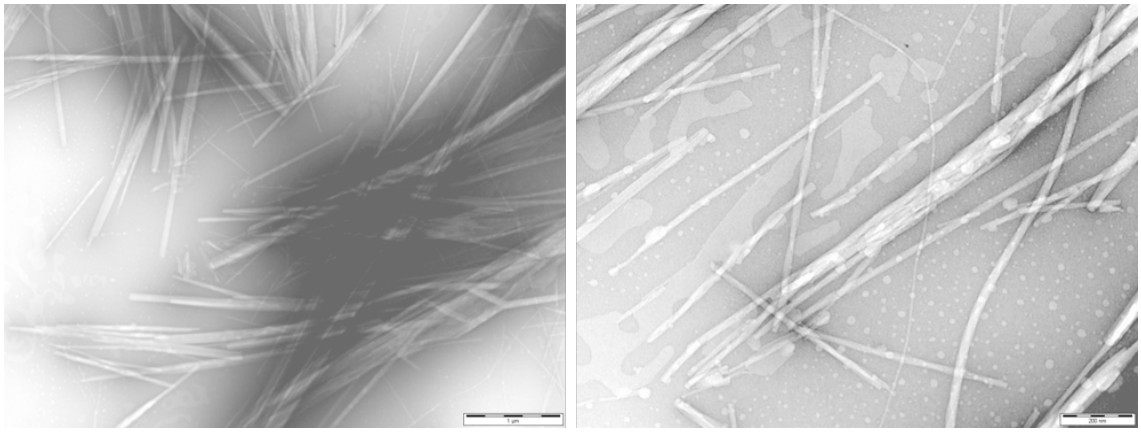

Figure 5.6. TEM images of OG1 (0.5% w/v) gel in the presence of heparin (38 μM). Scale bars: 1 μm (left) and 200 nm (right).

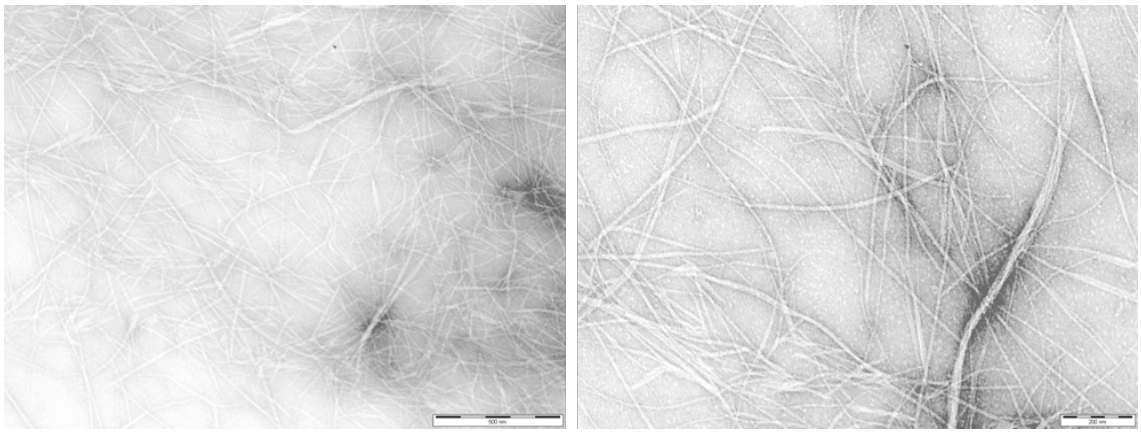

Figure 5.7. TEM images of OG1 (0.5% w/v) gel in the presence of C16-DAPMA (150 μM). Scale bars: 500 nm (left) and 200 nm (right).

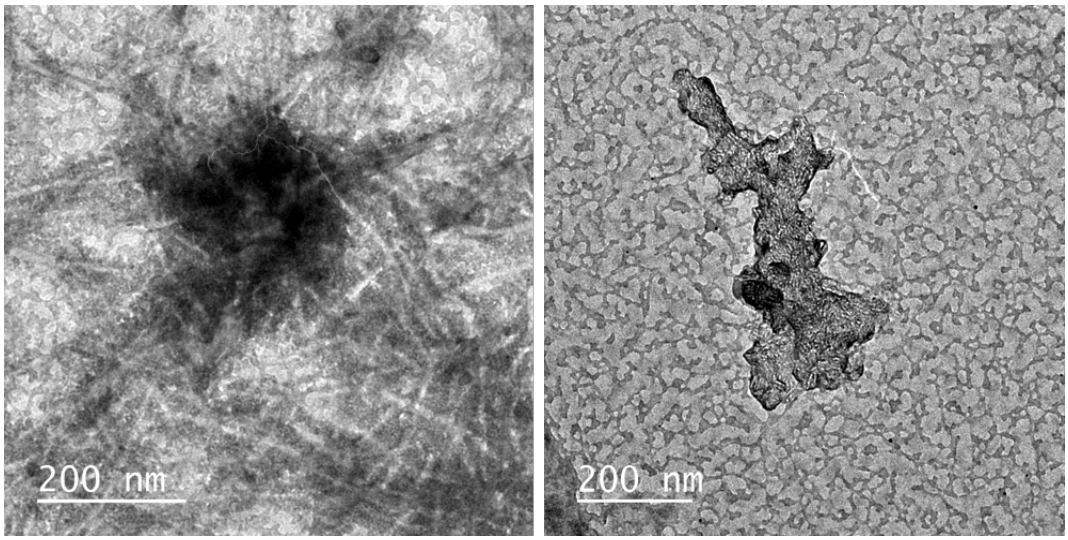

Figure 5.8. TEM images of OG1 (0.5% w/v) gel in the presence of heparin(38μM) and C16-DAPMA (150 μM).

The morphology of OG2 gels was also analysed by TEM imaging as shown in Figure 5.9, where it is possible to observe the presence of unbranched and long nanofibers with a diameter of 4.8 ± 0.3 nm, proving self-assembly of the gelator into 1D fibers in water. When heparin was present (Figure 5.10) it was possible to once again verify the presence of these long unbranched nanofibers (5.7 ± 0.5 nm in diameter) and unspecific polymer aggregates that may correspond to heparin. The morphology of the nanofibers does not appear to be significantly affected by the presence of heparin and no interactions are believed to be happening between the gelator and the heparin. On the other hand, when C16-DAPMA was incorporated into the OG2 gel network, two different nanofiber morphologies were identified, as shown in Figure 5.11, with no visible presence of the self-assembled C16-DAPMA micelles. While the unbranched long nanofibers were still present (5.2 ± 0.2 nm in diameter); branched and shorter nanofibers were also observed (9.2 ± 0.7 nm in diameter). This may indicate that the C16-DAPMA is not self-assembling into micelles and may coassemble with the OG2 molecules contributing to the different morphology being observed.[309] This is consistent with the observation that C16-DAPMA lowers the T_{gel} value of OG2 as described above and suggests this may be underpinned by a morphological change.

When both heparin and C16-DAPMA were incorporated within the gel network (Figure 5.12) it was possible to observe the presence of aggregates along with OG2 nanofibers (7.5 ± 1.2 nm in diameter). However, in these aggregates, the presence of the well-organized hierarchical nanostructures characteristic of C16-DAPMA interacting with heparin (as described in Chapter 2) were not observed, and it was therefore not possible to confirm that the interactions remain intact. Additionally, it is noticeable that the presence of the heparin/C16-DAPMA aggregates somewhat influenced the length of the fibers, that are significantly shorter than the typical long nanofibers of the self-assembled OG2 gelator. Once again this supports the observation of a lower T_{gel} value on this material.

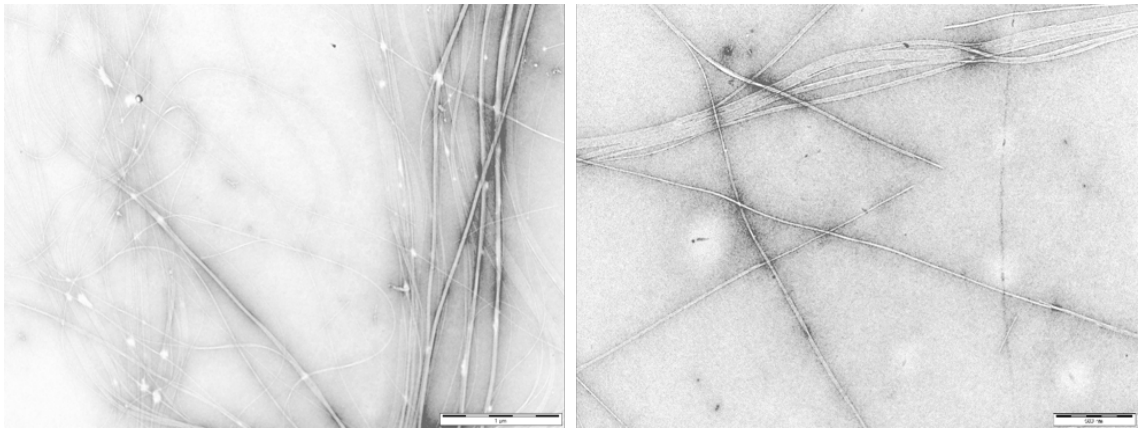

Figure 5.9. TEM images of OG2 (0.5% w/v) gel. Scale bars: 1 μm (left) and 500 nm (right).

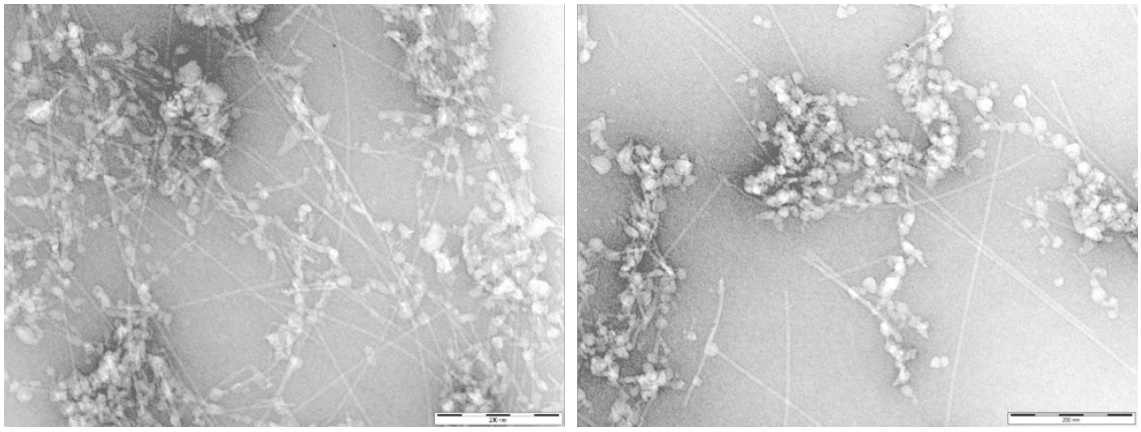

Figure 5.10. TEM images of OG2 (0.5% w/v) gel in the presence of heparin (38 μM). Scale bars: 500 nm (left) and 200 nm (right).

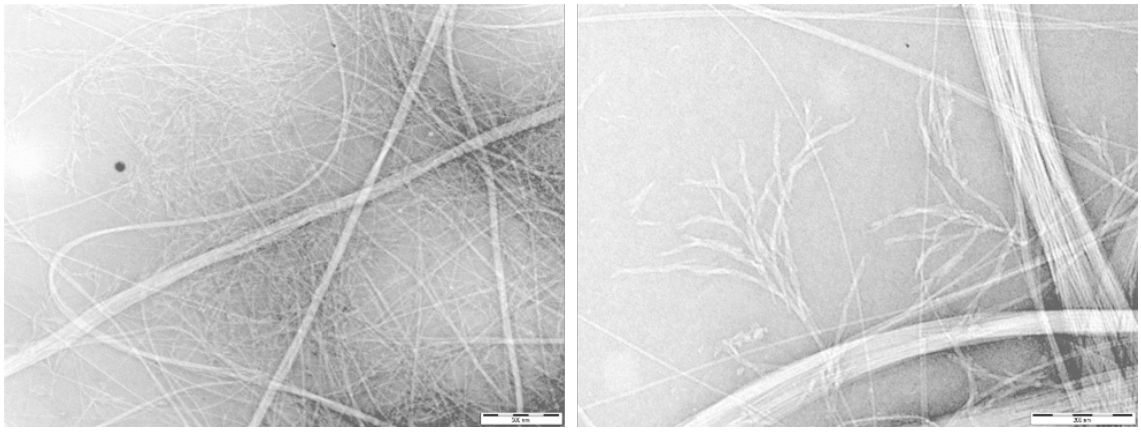

Figure 5.11. TEM images of OG2 (0.5% w/v) gel in the presence of C16-DAPMA (150 μM). Scale bars: 500 nm (left) and 200 nm (right).

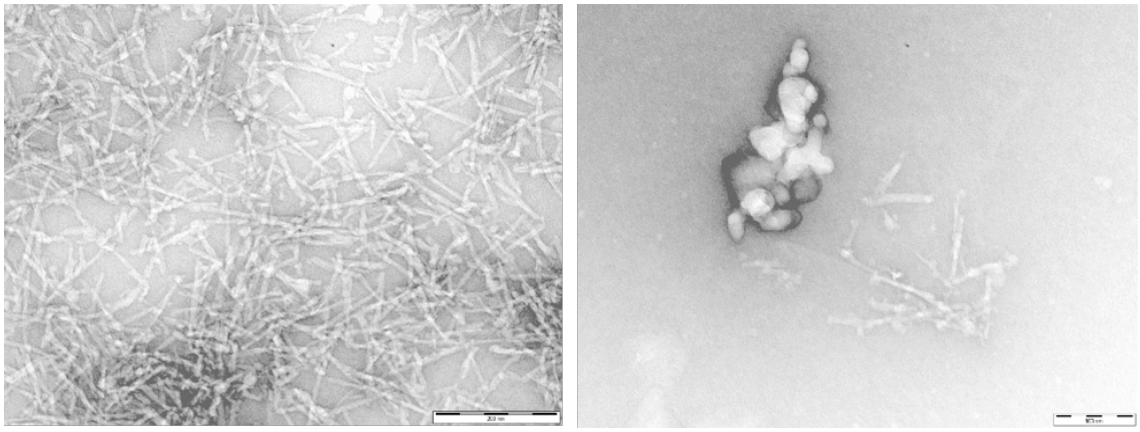

Figure 5.12. TEM images of OG2 (0.5% w/v) gel in the presence of heparin(38μM) and C16-DAPMA (150 μM). Scale bars: 200 nm (left) and 100 nm (right).

5.2.3. Rheology Studies

The influence of the incorporation of C16-DAPMA and heparin within the OG1 and OG2 gel networks was studied by rheology. For that purpose, the strain dependence of G' and G'' for 0.5% w/v OG1 hydrogels was measured and is presented on Figure 5.13. The incorporation of different components (0.3 mM of heparin, 1.2 mM of C16-DAPMA individually and bound) within the OG1 gel matrix did not significantly affect the stability of the gel and in each case a LVR up to approximately 1.3% of strain was obtained. This agrees with the earlier observation that the additives also have minimal impact on other macroscopic properties such as thermal stability.

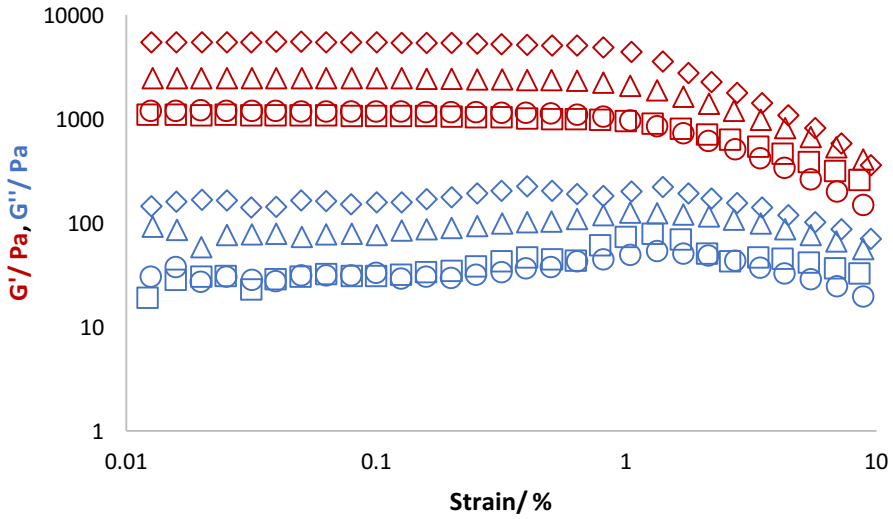

Figure 5.13. Strain amplitude dependence of the storage modulus (G') and loss modulus (G'') for OG1 gel (○), OG1 gel with heparin (△), OG1 gel with C16-DAPMA (◇) and OG1 gel with heparin and C16-DAPMA (□). Frequency = 1 Hz.

Figure 5.14 follows the change in rheological performance of OG1 over time and hence shows the gelation kinetics of OG1 hydrogels. As the gelation of OG1 occurs within seconds, when the measurement was started the gel was already formed and thus a constant G' value was obtained. Only for the sample containing heparin and C16-DAPMA was it possible to observe an increase of G' from 608 Pa at 0 minutes to 1281 Pa at 5 minutes, indicating that the incorporation of the hierarchical aggregates may slightly slow down the gelation kinetics of OG1 hydrogels. In addition, the presence of C16-DAPMA in the gel resulted in the highest G' value, meaning that the fibril network is stiffer when compared to the other tested conditions. This result corroborates the obtained TEM images, where the incorporation of C16-DAPMA molecules appeared to promote the self-assembly of the OG1 gelator into thinner and longer fibers that may result in a denser and stronger gel.

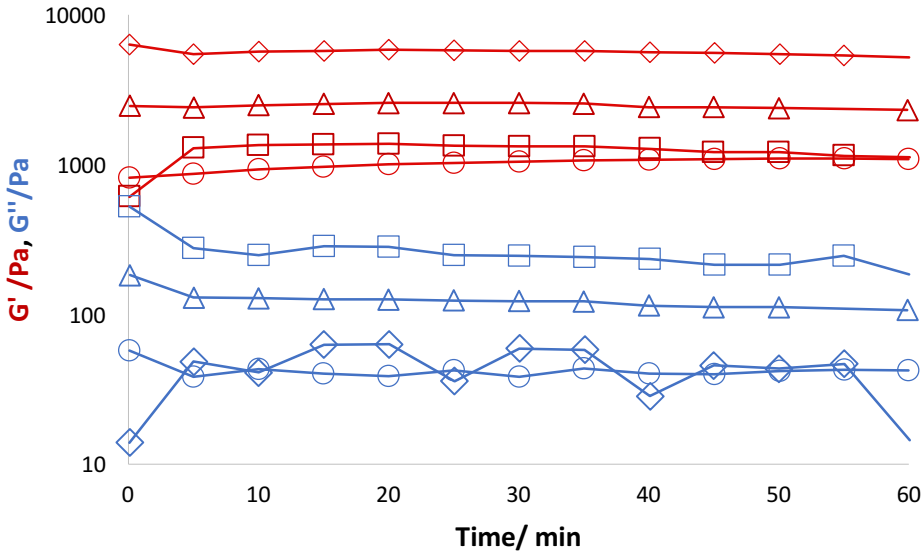

Figure 5.14. Time sweep oscillatory rheology measurements (frequency = 1Hz and 0.5% strain) for OG1 gel (○), OG1 gel with heparin (△), OG1 gel with C16-DAPMA (◇) and OG1 gel with heparin and C16-DAPMA (□).

Figure 5.15 shows the strain dependence of G' and G'' for 0.5% w/v OG2 hydrogels that exhibited a similar LVR when alone, incorporated with 0.3 mM of heparin and 0.3 mM of heparin bound to 1.2 mM of C16-DAPMA (up to approximately 1.8% of strain). However, when 1.2 mM of C16-DAPMA was present within the gel the LVR decreased to approximately 1% strain, indicating that the incorporation of C16-DAPMA contributes to a less stable gel. This is in agreement with TEM imaging which showed an impact of C16-DAPMA on OG2 nanofibre morphology, and is also in agreement with other macroscopic properties such as thermal stability.

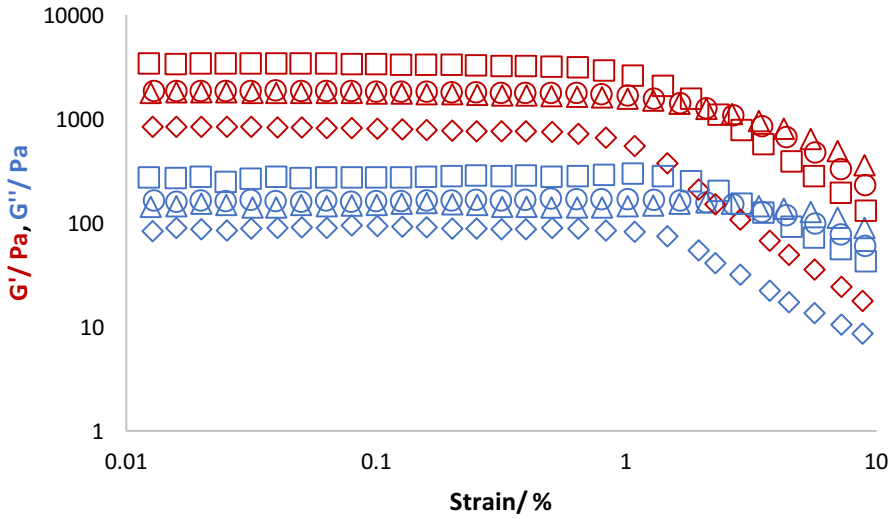

Figure 5.15. Strain amplitude dependence of the storage modulus (G') and loss modulus (G'') for OG2 gel (○), OG2 gel with heparin (△), OG2 gel with C16-DAPMA (◇) and OG2 gel with heparin and C16-DAPMA (□). Frequency = 1 Hz.

Figure 5.16 shows the kinetic rheological data for OG2 gelation. The OG2 hydrogel has a gradual increase of G' over 60 minutes, with the first 10 minutes showing the most significant increase (from 268 Pa at 0 min to 1072 Pa at 10 min). When heparin is added to the hydrogel a similar profile of gelation is obtained, with a slightly lower G' value after 60 minutes (1559 Pa compared to 2481 Pa from OG2 hydrogel alone). When heparin bound to C16-DAPMA is present, a faster gelation process appears to happen during the first 15 minutes (G' increases from 268 Pa at 0 min to 2243 Pa at 15 min), and after that G' becomes constant. After 60 minutes a similar G' to the OG2 hydrogel is obtained, indicating a faster gelation but the formation of materials with similar overall stifness. The incorporation of C16-DAPMA results in faster gelation, reaching the maximum G' value after 10 minutes, but the gel is significantly weaker (G' = 695 Pa at 60 minutes). Indeed, as observed by TEM, shorter nanofibers were formed when C16-DAPMA was added into the OG2 gel, explaining the fact that the gelation process is faster and the formation of branched nanofibers can contribute to a weaker gel, with lower thermal stability. The more rapid, but less effective assembly in the presence of C16-DAPMA suggests that this additive is intimately involved in the assembly process as described above.

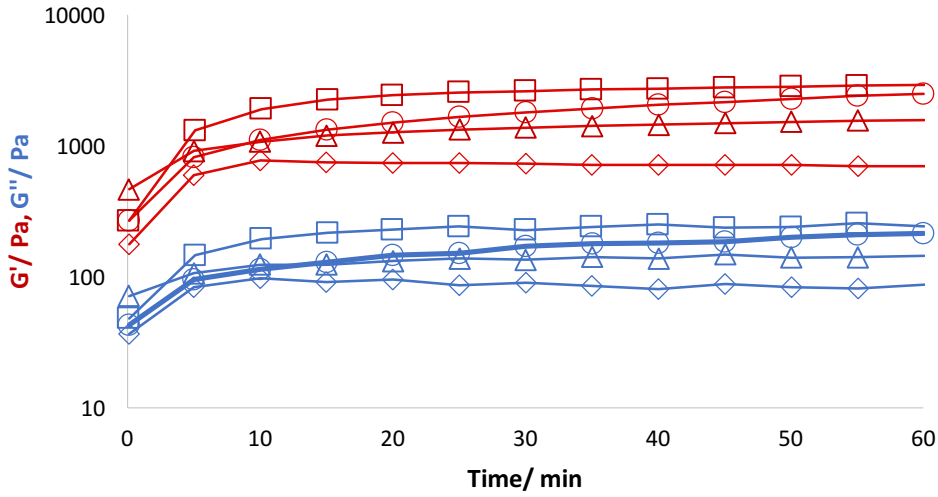

Figure 5.16. Time sweep oscillatory rheology measurements (frequency = 1Hz and 0.5% strain) for OG2 gel (○), OG2 gel with heparin (△), OG2 gel with C16-DAPMA (◇) and OG2 gel with heparin and C16-DAPMA (□).

5.3. Release Studies

The release of heparin from OG1 and OG2 hydrogels was then studied. Furthermore, the influence of agarose when added to OG1/OG2 hydrogelators to form hybrid gels and subsequently release heparin was also investigated. The same release experiments as described in Chapters 3 and 4 were performed for OG1 and OG2 hydrogels. Therefore, one experiment consisted on placing 10 mM Tris-HCl/ 150 mM NaCl buffer (1 mL) on top of the gel (3 mL) and collecting aliquots of buffer over time and the second experiment consisted of forming gel cylinders (1 mL) which requires the presence of agarose and placing them in a jar with buffer (35 mL) as receiving medium.

Heparin release from OG1 hydrogels

Figure 5.17 shows the release profile obtained for 0.5% w/v OG1 hydrogels containing either 1 mM of heparin or 1 mM of heparin with 2 mM of C16-DAPMA also present. When only heparin is present within the OG1 gel network it was possible to observe a gradual increase of heparin being released over the first 24 hours, with 56% of heparin released over that period of time. After 24 hours, the release of heparin is essentially complete, reaching a total of 59% release after 72h. When C16-DAPMA was interacting with heparin

within the gel network the release of heparin was inhibited as expected, with only 10% of heparin being released after 72h, clearly demonstrating the efficacy of C16-DAPMA binding to heparin even after being incorporated within OG1 gel network, and hence limiting heparin release.

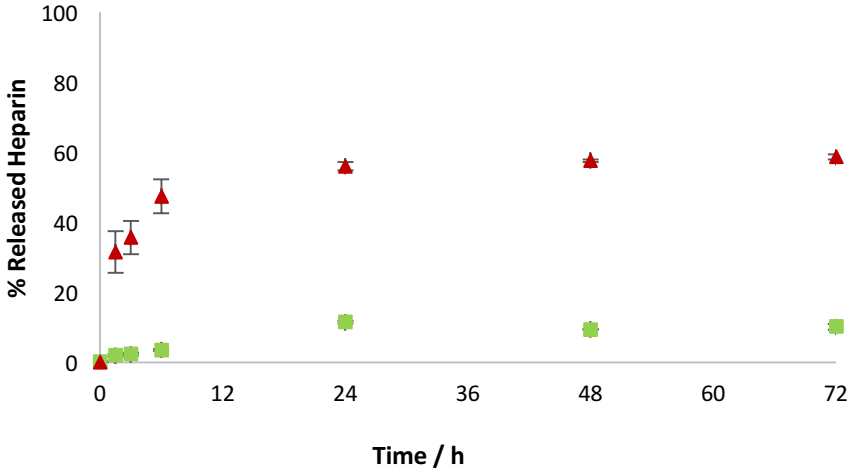

Figure 5.17. Heparin release from OG1 hydrogel (0.5% w/v) containing 1 mM of heparin (▲) and 1 mM of heparin with 2 mM of C16-DAPMA (■).

The same experiment was performed to verify how heparin release is affected when incorporated into a hybrid hydrogel consisting of 0.5% w/v OG1 as LMWG and 1% w/v agarose as PG. When comparing the release of heparin from OG1 hydrogel and OG1-agarose hybrid hydrogel (Figure 5.18), an identical release profile was obtained for both conditions, with 59% and 62% heparin released after 72 h, from OG1 hydrogel and OG1-agarose hybrid hydrogel, respectively. This indicates that the addition of 1% w/v of agarose to OG1 hydrogels allows to obtain a stiffer, more robust and manipulatable hydrogel, without adversely affecting the release of heparin.

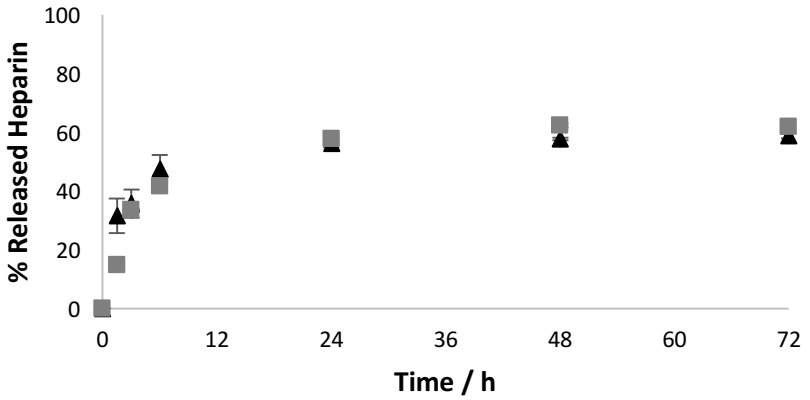

Figure 5.18. Heparin release from OG1 hydrogel (0.5% w/v) with 1 mM of heparin in the absence of agarose (▲) and in the presence of 1% w/v of agarose (■).

Figure 5.19 compares the release of heparin from 0.5% w/v OG1-agarose hybrid hydrogels containing 1 mM of heparin when buffer was placed on top of the gel, and when a gel cylinder was immersed in buffer. When using the OG1-agarose hybrid gel cylinder, the amount of released heparin increased to 97% after 72 hours, compared with 62% total release obtained with the previous method. This proves once again that the greater the surface area to volume ratio of the gel in contact with buffer, the more of the heparin can be released, suggesting that some of the heparin effectively becomes trapped within the gel nanostructure if it is too far away from the gel surface.

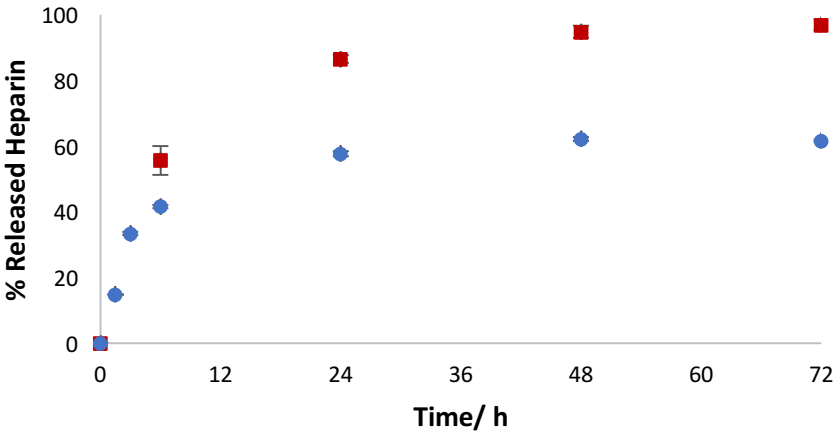

Figure 5.19. Different methods of heparin release from OG1 hydrogel (0.5% w/v). (●): Buffer on top of the gel. (■): Gel cylinder.

Heparin release from OG2 hydrogels

Heparin release from OG2 hydrogels with buffer added on top is shown on Figure 5.20. A gradual increase on the release of heparin was observed over time, reaching a maximum of 67% after 72 hours. Despite the fact that OG1 hydrogels, in the same conditions, resulted in a lower total release of heparin after 72 hours, it is worth noting that after 6 hours, 47% of heparin was released from the OG1 gels, instead of only 33% from the OG2 gel. This indicates a faster initial release of heparin in OG1 hydrogels but a lower total amount of heparin that can be released, when compared with OG2 gels. This indicates that the kinetics of release are better for OG1 but the thermodynamics of release are better for OG2. This may be a result of the change in morphology of the OG1 nanofibers in the presence of heparin observed by TEM, with the junction of the fibers into a needle shape contributing to a different heparin release profile and leading to more of the heparin becoming effectively permanently entrapped. Interestingly, when C16-DAPMA was present within the gel network, it did not inhibit the release of heparin, as expected, and a very similar release of heparin was obtained as when only heparin was present (Figure 5.20). This may be due to the fact that when $NaOH_{(aq)}$ is added to form the gel, after acidifying the sample, the pH of the hydrogel is not neutral but between 8-9 (measured by placing pH test paper inside the gel), which can contribute to the deprotonation of C16-DAPMA that can then no longer interact electrostatically with heparin. This agrees with the triggered release assay performed in Chapter 4, when a pH 10 buffer was added on top of the gel to obtain the release of heparin when C16-DAPMA was effectively binding to heparin. Additionally, this is supported by the fact that the well-organised hierarchical crystalline nanostructures characteristic of heparin interacting with C16-DAPMA could not be observed by TEM. We suggest that the agglomerates observed by TEM probably correspond to heparin alone and that C16-DAPMA in this system is intimately involved in OG2 assembly and does not get involved in heparin binding.

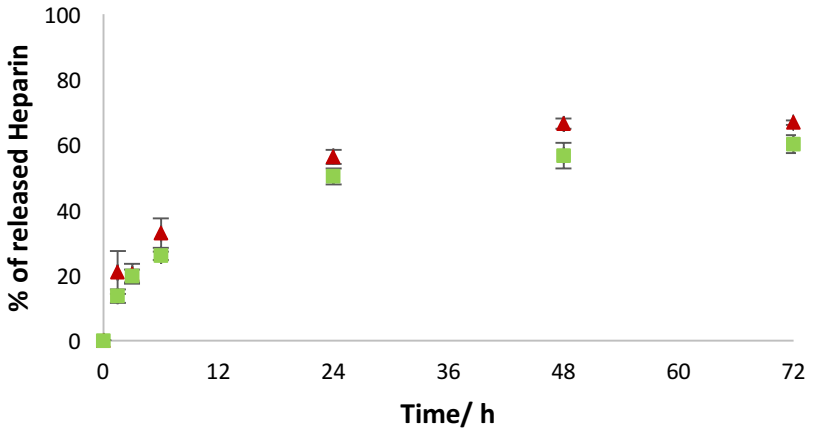

Figure 5.20. Heparin release from OG2 hydrogel (0.5% w/v) containing 1 mM of heparin (▲) and 1mM of heparin and 2 mM of C16-DAPMA (■).

Surprisingly, the use of agarose to prepare hybrid hydrogels with OG2 resulted in the formation of very unstable gels or partial gels. Therefore, it was not possible to obtain hybrid hydrogels using OG2 and agarose. It is believed that the fact that OG2 is a pH responsive gelator and needs to initially be acidified at pH 2 contributed to the hydrolysis of agarose and thus prevented the formation of uniform, stable and stiff hybrid gels.

5.4. Positively Charged Cyclohexane LMWG

A different approach to release heparin in a controlled manner involves the direct interaction of heparin with negatively charged nanofibers that can degrade or can be enzymatically cleaved. An example of heparin directly interacting with nanofibers was already described in Chapter 1 – Section 1.6.[195] Another example was reported by Xu and coworkers with the development of a heparinized $Cu(OH)_2$ nanofibrous membrane. It was confirmed that the negatively charged heparin was successfully immobilised onto positive charged $Cu(OH)_2$ nanofibers by electrostatic interactions. The system exhibited good hemocompatibility and very good antibacterial activities against *Escherichia coli* and *Staphyloccocus aureus*.[310] However, the release of heparin from the triggered degradation of self-assembled nanofibers was, to the best of our knowledge, not tested yet.

During the placement, a new hydrogelator was synthesised by Vincent le Sage (Figure 5.21) with a similar structure to OG2 but with one of the ethylene glycol chains changed in order

to add an amine group and obtain a positively charged gelator that can potentially interact directly with heparin. As the phenylalanyl-aminoquinoline can be enzymatically cleaved, the triggered release of heparin could then be easily achieved. Therefore, further characterisation and release assays were performed with this gelator to better understand the ability of this gelator to bind heparin and release it.

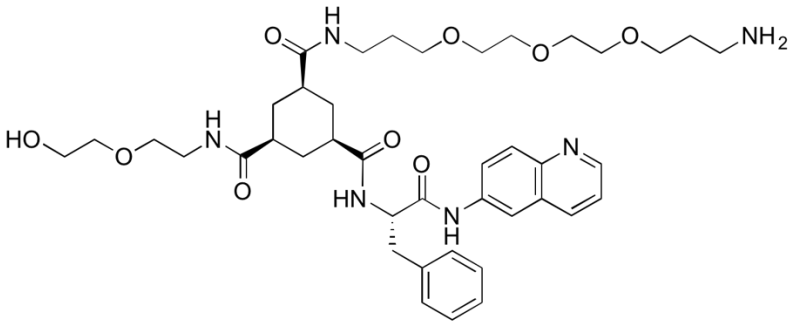

Figure 5.21. Positively charged cyclohexane gelator (OG+).

OG+ hydrogels (0.5% w/v) could be obtained using two different approaches, one by acidifying the gelator solution in water, with HCl (1 M), to completely dissolve the gelator, followed by neutralisation of the solution by NaOH (1 M) and the other by dissolving the gelator in DMSO and adding 0.1 M Tris-HCl buffer, pH 7.75 (mixture ratio of 1:9 DMSO:buffer).

TEM images of OG+ hydrogel and OG+ hydrogel in the presence of heparin were obtained using the first method of preparation described above, and are shown in Figure 5.22 and 5.23. OG+ nanofibers presented a similar morphology to OG2 nanofibers with unbranched and elongated nanofibers having a diameter of 6.8 $\pm$ 0.8 nm. When heparin was incorporated within the gel it was possible to observe the presence of needle-like semi-crystalline structures that may correspond to heparin (Figure 5.23 - top). When obtaining more detailed images of these nanostructures (Figure 5.23 - bottom) it was possible to clearly observe the presence of what appear to be nanofibers wrapped around larger fibrillar objects. In a first conclusion, it appears that these are OG+ nanofibers that effectively bind to heparin and may as well have an influence in the organization and packing of heparin into a needle-like morphology. This fascinating hierarchical nanoscale

architecture supports the view that interactions can be established between OG+ and heparin.

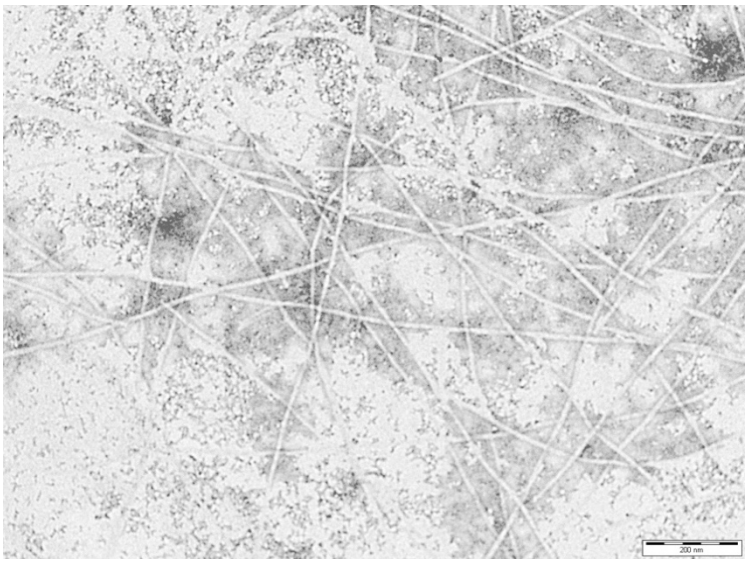

Figure 5.22. TEM image of OG+ (0.5% w/v) gel. Scale bar: 200 nm.

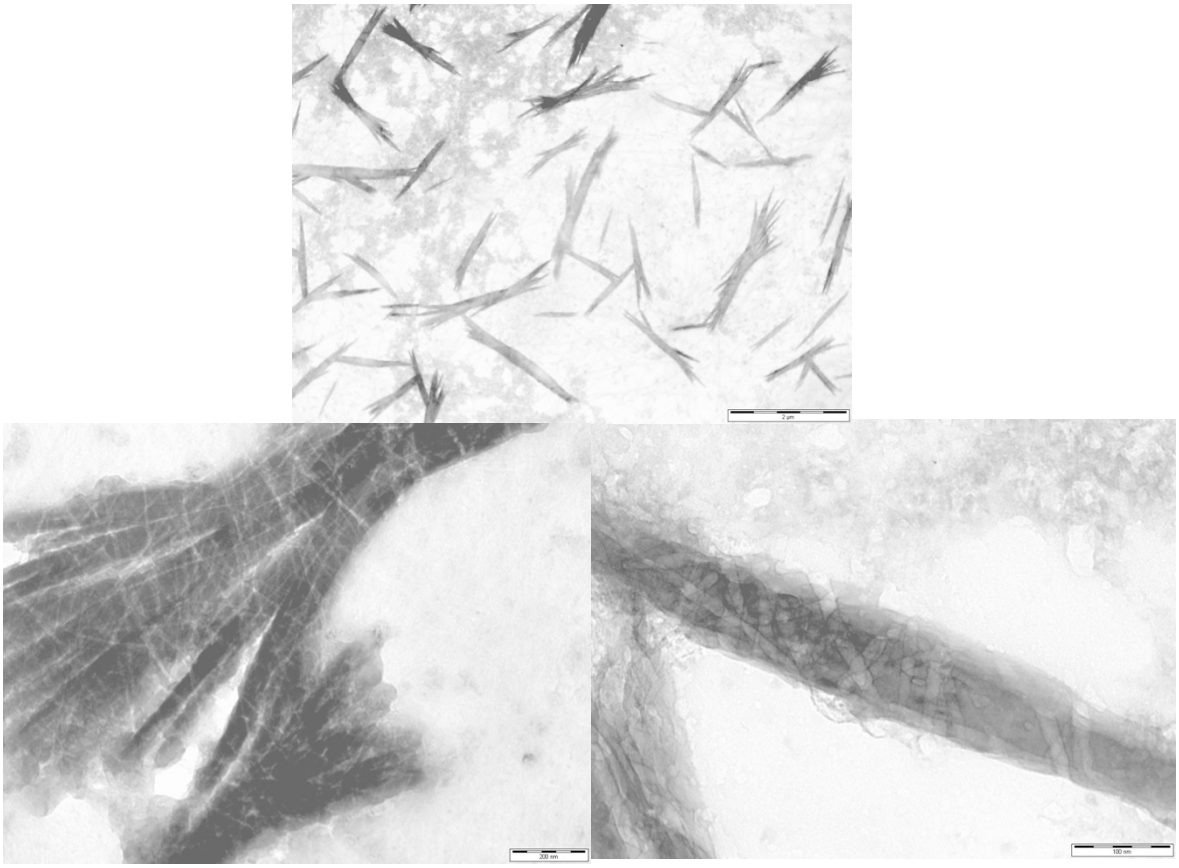

Figure 5.23. TEM images of OG+ gel (0.5% w/v) in the presence of heparin (78 µM). Scale bars: 2 µm (top); 200 nm (bottom left) and 100 nm (bottom right).

The OG+ gelator was designed so it can bind directly to heparin and be enzymatically cleaved by α-chymotrypsin (α-chy), resulting in the release of heparin. Therefore, heparin release from OG+ hydrogels was tested by using 1 mL of gel samples (1:9 DMSO:buffer preparation method) and placing 1 mL buffer on top of the hydrogels. Aliquots of buffer were collected over time and added to MalB to detect the presence of heparin (as described in Chapter 3). Three different conditions were tested and the obtained results are shown in Figure 5.24 (it should be noted that this experiment was performed with only one gel sample per condition and in the future, it should be repeated in triplicate).

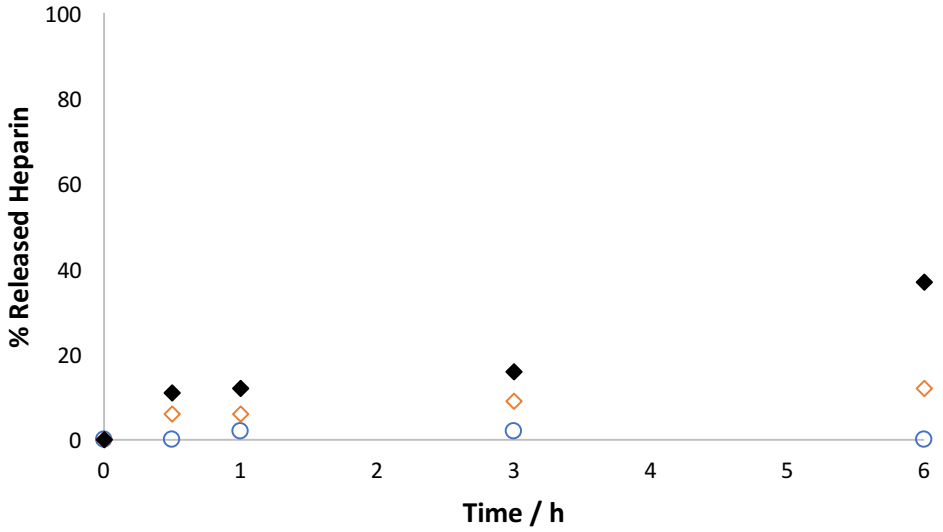

Figure 5.24. Heparin release from OG+ hydrogels: (○) OG+ hydrogel with heparin without α-chy; (◇) OG+ hydrogel with heparin and α-chy at room temperature; (◆) OG+ hydrogel with heparin and α-chy at 37 °C.

Firstly, OG+ hydrogel in the presence of 1 mM of heparin was monitored to confirm that the gel nanofibers were effectively binding to heparin and therefore, no release of heparin was being obtained by a possible excess of the concentration of heparin used. Over the period of 6 hours it was observed that no release of heparin was detected, indicating that OG+ effectively binds to heparin as previously seen in the TEM images. This is the first time in this thesis we have observed a gel which completely inhibits heparin release without the requirement for C16-DAPMA assemblies to be present. Moreover, as the heparin agglomerates appear to be wrapped by the gel nanofibers, the fact that a higher

concentration of heparin is being used when compared to the TEM samples, did not appear to affect the binding efficiency and no excess of heparin appears to be free within the gel network.

We then added 900 µL of α-chy in 0.1 M Tris-HCl buffer, pH 7.75 to 100 µL DMSO solution of OG+ gelator with heparin. The enzyme concentration after mixing with DMSO was 40 µM. As described in the introduction, α-chy needs a stimulus, such as temperature, to start the enzymatic cleavage and as reported by van Bommel at *al.*,[298] an increase in temperature contributes to an increase in enzymatic hydrolysis. Therefore, the experiment was performed by keeping one sample at room temperature (RT - 21-25 °C) and another at 37 °C to verify the effect of temperature in the activation of the enzymatic cleavage and consequently the release of heparin. When the gel was kept at room temperature a release of 12% of heparin was obtained after 6 hours. At 37 °C a significant increase in the release of heparin was obtained, with approximately double the percentage of heparin being release after 30 minutes (from 6% at RT to 11% at 37 °C) up to triple release after 6 hours (form 12% at RT to 37% at 37 °C). Therefore, the release of heparin from OG+ hydrogels was achieved through the enzymatic cleavage of the phenylalanyl-aminoquinoline moiety and by increasing the temperature a higher percentage of heparin is released. This therefore indicates that controlled breakdown of gel nanostructures can induce heparin release when the gel nanofibers and heparin are mutually interacting. This indicates the potential of well-defined hydrogels to achieve controlled heparin release.

5.5. Summary, Conclusions and Future Work

The orthogonal self-assembly of OG1 and OG2 hydrogelators with heparin and C16-DAPMA was investigated. With respect to the OG1 hydrogel, the presence of heparin and C16-DAPMA contribute to different nanofiber morphologies, however with no evident influence in the stability of the gels (similar T_{gel} and LVR values). On the other hand, the incorporation of C16-DAPMA or heparin bound to C16-DAPMA in OG2 hydrogels significantly changed the morphology of the nanofibers, affecting the mechanical properties of the nanofibrils and the gelation kinetics. It was proposed that C16-DAPMA is

intimately involved in OG2 assembly and that the pH of the gel prevents its interaction with heparin.

Release of heparin from both hydrogels was successfully demonstrated. Additionally, it was possible to obtain a hybrid hydrogel with OG1 and agarose with equivalent heparin release and thus controlling the release of heparin from OG1 hybrid hydrogels by changing the surface area to volume ratio. The presence of C16-DAPMA, switched off the release of heparin from OG1 hydrogels as expected.

Conversely, the use of agarose with OG2 gelators inhibited the formation of a stable gel and thus limited the use of different release assays. We proposed this was a result of the pH changes used to form the gel. Moreover, the presence of C16-DAPMA within OG2 hydrogels did not inhibit heparin release, confirming that C16-DAPMA is not interacting with heparin, probably due to the basic conditions of the hydrogel causing deprotonation of C16-DAPMA.

OG+, a positively charged LMWG proved to effectively and directly bind to heparin, with TEM images showing gel nanofibers wrapped around heparin aggregates. The release of heparin was inhibited by this gel-binding event and was only achievable by enzymatic cleavage of the gelator leading to breakdown of the gel nanofibers, with an increase in temperature contributing to a higher percentage of released heparin.

Future work could seek to test the release of heparin from OG2 hydrogels by enzymatic cleavage, using α-chy. Additionally, it would be interesting to test the release of heparin from OG+ using α-chy at different temperatures than the ones tested (between 25-45 °C), to obtain a release profile dependent on temperature. It would also be interesting to test the maximum loading capacity of heparin within OG+ hydrogels by simply testing at which concentration heparin starts being released to the buffer on top of the OG+ hydrogel using MalB. We suggest that a gelator such as OG+ has considerable potential for the controlled release of heparin for future applications in tissue engineering.

6. Conclusions and Future Work

6.1. Conclusions

Initially, a family of simple self-assembling surfactant molecules based on saturated fatty acids was reported and their ability to bind to heparin was investigated. Modifying the hydrophobic chain length offers a mechanism for tuning the ability of these compounds to self-assemble into micellar aggregates, with C16-DAPMA being the optimal system in terms of CMC. Furthermore, this compound is also the most effective heparin binder as determined by MalB displacement assays – it is suggested that this indicates the synergy between surfactant self-assembly and polyanion binding. For the first time, the nanoscale aggregates formed on binding between SAMul cationic spherical micelles and polyanionic cylindrical heparin were structurally characterised. In particular, C14-DAPMA and C16-DAPMA formed highly organised nanocrystalline assemblies as observed by TEM. Characterisation by mesoscale simulations and SAXS further confirmed that the micelles remained intact during hierarchical assembly and were packed in a face-centred cubic manner on contact with heparin. The assemblies formed by the most effective system, C16-DAPMA showed the highest degree of crystalline order revealed by the distinct diffraction peaks. These self-assembling micelles present high stability even when they form very strong electrostatic interactions with heparin, indicating they can be considered as distinct building blocks for nanoscale assembly even in very competitive conditions.

In Chapter 3, a simple multi-component approach to hybrid hydrogels with two self-assembling components (DBS-COOH and C16-DAPMA) and two polymeric components (heparin and agarose) was used and the impact of each component on the others was characterised. This is the first time such a detailed study has been performed in a multi-component gel of this complexity. The self-assembly of DBS-COOH is slightly modified on the nanoscale by heparin, completely disrupted by C16-DAPMA and unaffected by agarose. However, if the heparin is bound to self-assembled multivalent C16-DAPMA, then the assembly of DBS-COOH still takes place, and although the presence of the hierarchical heparin/C16-DAPMA aggregates has some minor impacts on gel performance, the components are largely orthogonal to one another. The PG reinforces all materials when

present, and dominates macroscopic behaviour. DBS-COOH retains pH responsiveness and can be disassembled in the presence of the other components introducing triggered response characteristics to these hybrid hydrogels. The release of heparin from the DBS-COOH gel network was achieved, with the presence of C16-DAPMA inhibiting it completely and the presence of the PG not affecting the release while contributing to the formation of a more robust gel network. Cytocompatibility studies revealed that DBS-COOH is not cytotoxic, hence promising for biological applications.

The same multi-component approach and characterisation was used in Chapter 4, using a different LMWG – DBS-$CONHNH_2$. The self-assembly of DBS-$CONHNH_2$ was unaffected by the incorporation of heparin, C16-DAPMA and agarose. However, if heparin is bound to C16-DAPMA the morphology of the gel fibers is affected, although the hierarchical organised nanostructures of heparin-C16-DAPMA aggregates remain intact within the gel network. When the PG is present, DBS-$CONHNH_2$ self-assembly is unaffected and it contributes to the formation of robust gels. The release of heparin from the DBS-$CONHNH_2$ gel network was achieved, and once again the presence of C16-DAPMA inhibited its release, while the presence of the PG did not affect release. A change in pH of the release medium contributed to triggered release of heparin. Cytocompatibility studies confirmed that DBS-$CONHNH_2$ hydrogels are not cytotoxic, and cells were able to adhere on to the gel surface and proliferate, with the metabolic activity of the cells being enhanced when 10-50 μg/mL of heparin was incorporated within the gel network. However, C16-DAPMA proved to be cytotoxic for cells, and agarose, although non-cytotoxic, does not present adhesion moieties for cells to adhere.

In Chapter 5, multi-component hydrogel systems using cyclohexane based LMWGs (OG1 and OG2) were reported. The self-assembly of OG1 is slightly affected by heparin and C16-DAPMA and unaffected by agarose, with the release of heparin from both OG1 hydrogel and OG1-agarose hybrid hydrogel successfully achieved and inhibited by the presence of C16-DAPMA. The self-assembly of OG2 is unaffected by heparin and SAMul C16-DAPMA, but was altered by the presence of heparin bound to C16-DAPMA, with changes in morphology, and inhibited by agarose. The release of heparin over time from OG2 hydrogel is achievable, however the presence of C16-DAPMA does not inhibit the release of heparin

due to deprotonation of the heparin binder as the gel is formed by basification. Additionally, a positively charged cyclohexane-based LMWG – OG+ was introduced. OG+ directly binds to heparin as a consequence of its positive charge, as demonstrated by TEM images, and its triggered release can be obtained by enzymatic cleavage of the OG+ hydrogel.

With these studies, it was possible to gain fundamental insights into multi-component systems and conclude that this strategy is a powerful way of formulating multi-functional materials and tuning desired characteristics for bioactive release of heparin and potential cell growth.

6.2. Future Work

As future work, triggered heparin release under physiologically relevant conditions and multi-component hybrid gels should be studied, which ultimately may have biomedical applications. Studies can proceed to further explore the pH responsiveness of DBS-COOH and OG2 hydrogels to release bioactive molecules by testing different bases or acids, respectively. Different heparin binders, such as cholesterol-based SAMul binders, can also be tested in order to optimise the cytocompatibility of the multi-component hybrid gel systems while enabling a triggered release response through degradation of the binders. DBS-$CONHNH_2$ and agarose hybrid hydrogels have good biocompatibility making them good candidates for topical drug delivery and therefore *in vitro* release testing (e.g. cells Franz diffusion) may be performed. To better understand their potential as 3D scaffolds for cell growth, different PGs should be tested along with different types of mammalian cells. Additionally, the release of heparin from OG+ hydrogel network by enzymatic cleavage should be performed in more detail in order to understand how temperature can tune the release of heparin from this gel system, and the impacts of this on cell growth.

7. Experimental

7.1. General Reagents and Methods

All reagents were purchased from commercial sources and used directly without any further purification, with the exception of MalB dye which was synthesised in the DKS laboratory following known methods.[225] Heparin, sodium salt, from porcine intestinal mucosa (MW 13,500-15,000 Da) was purchased from Merck. α-Chymotrypsin from bovine pancreas (MW 40,000 Da) was purchased from Sigma. Thin layer chromatography (TLC) was performed on Merck aluminium-backed plates coated with 0.25 nm silica gel 60. Preparative gel permeation chromatography (GPC) was performed on Biobeads SX-1 supplied by Bio-Rad. ESI mass spectra were recorded on a Bruker Daltonics Micro-Tof mass spectrometer. Fluorescence spectra were obtained with a Hitachi F-4500 fluorimeter. Infrared spectra were recorded on Shimadzu IRPrestige-21 FT-IR spectrometer. UV-Vis absorbance was recorded on a Shimadzu UV-2401PC spectrophotometer. TEM and SEM images were obtained by Meg Stark at Biology Technology Faculty, University of York, using a FEI Tecnai 12 Bio TWIN operated at 120 kV for the TEM images and a JEOL JSM-7600F operated at 3 kV for the SEM images. Thermal stability was recorded on a Huber Ministat 230 circulator oil bath. Kinetic studies were performed on a Bruker AV500 spectrometer (^{1}H 500 MHz) and a Jasco J810 CD spectrophotometer. DLS and zeta potential measurements were recorded on a Zetasizer Nano ZS. SAXS was performed by Ville Liljeström at the Department of Applied Physics, School of Science, Aalto University (Finland), using a SAXS setup consisting of a rotating anode microfocus X-ray source (Bruker), a Montel multilayer focusing monochromator (Incoatec) and four collimating slits (JJ X-ray). Rheology studies were performed on a Kinexus Pro+ rheometer from Malvern instruments, and on a AR-G2 rheometer from TA instruments. Optical microscopy images were recorded by a Nikon Eclipse TS100 inverted microscope. Fluorescence microscopy images were obtained using a Leica DMIL inverted microscope.

7.2. Synthesis

Synthesis of tert-Butyl 3-((3-aminopropyl)(methyl)amino)propyl carbamate (Mono Boc-Protected DAPMA)[311]

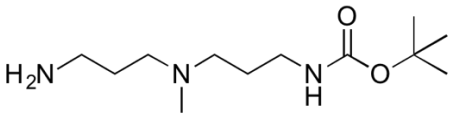

Molecular Formula: $C_{12}H_{27}N_3O_2$

Molecular Weight: 245.36

N,N-Di-(3-aminopropyl)-*N*-methylamine (50 mL, 310 mmol) was dissolved in 250 mL of THF and cooled to 0 °C. Di-(tert-butyl)dicarbonate (12.0 g, 55.0 mmol) was dissolved in THF and added drop wise over 2 h, to the previous solution. The reaction was then quenched with water (5 mL). The solvent was removed by rotary evaporation and the product was dissolved in $NaOH_{(aq)}$ (pH>10) and extracted with DCM. The organic layers were washed with citric acid, and the pH adjusted to 4-5. The aqueous layers were then basified with NaOH (5 M) pH>10 and the compound was extracted with DCM. The organic layers were dried with $MgSO_4$ and filtered. The final product was evaporated by rotary evaporation resulting in a colourless oil (4.9 g, 20.0 mmol, 36%).

^{1}H NMR (400 MHz, DMSO-d_6) δ: 6.77 (br t, *J* = 5.2 Hz, N*H*, 1H); 2.88 (q, CH_2NHCO, *J* = 6.8 Hz, 2H); 2.50 (t, CH_2NH$_2$, *J* = 6.4 Hz, 2H); 2.25-2.18 (m, CH_2N(CH$_3$), 4H); 2.04 (s, N(CH_3), 3H); 1.60-1.54 (m, CH_2CH$_2$NH$_2$, 2H); 1.49-1.39 (m, CH_2CH$_2$N(CH$_3$), 2H); 1.33 (s, C(CH_3), 9H). ^{13}C NMR (100 MHz, DMSO-d_6) δ: 156.09 (*C*ONH); 77.79 (*C*CH$_3$); 55.59, 55.42 (*C*H$_2$NCH$_3$); 42.34 (N*C*H$_3$); 38.89 (*C*H$_2$NHCO); 38.74 (*C*H$_2$NH$_2$); 31.16 (*C*H$_2$CH$_2$NHCO); 28.78 (C*C*H$_3$); 27.72 (*C*H$_2$CH$_2$NH$_2$). HRMS: Calcd. [M+H]$^+$ ($C_{12}H_{28}N_3O_2$) *m/z* = 246.2176. Found [M+H]$^+$ *m/z* = 246.2180.

Coupling of Myristic Acid and DAPMA (mono Boc-protected C14-DAPMA)

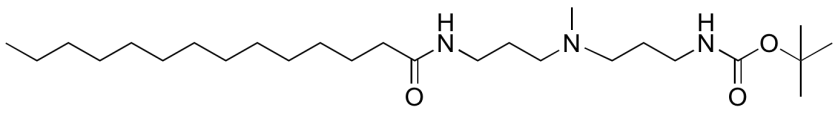

Molecular Formula: $C_{26}H_{53}N_3O_3$

Molecular Weight: 455.72

Myristic acid (1.00 g, 4.40 mmol) was dissolved in DCM (65 mL). O-(Benzotriazol-1-yl)-*N,N,N',N'*-tetramethyluronium tetrafluoroborate (TBTU) (1.41 g, 4.40 mmol) and triethylamine (5.4 mL) were added to the mixture and it was stirred for 5 min at room temperature. Mono Boc-protected DAPMA (1.08 g, 4.4 mmol) was dissolved in DCM (65 mL), added to the mixture and the reaction was stirred overnight. The solvent was removed by rotary evaporation and the product dissolved in EtOAc (50 mL) and washed with $NaHSO_4$ (2 x 15 mL, 1.33 M), $NaHCO_3$ (2 x 15 mL, saturated), deionised water (3 x 15 mL) and brine (15 mL, saturated). The organic layer was collected, dried with $MgSO_4$, filtered and dried under vacuum. The product was purified by GPC column (Bio-beads, 100% DCM). The obtained product was a beige solid (800 mg, 1.80 mmol, 41%).

R_f = 0.3 (90:10:1 DCM/MeOH/Et_3N). ^{1}H NMR (400 MHz, $CDCl_3$) δ: 6.81 (br s, N*H*, 1H); 5.12 (br s, N*H*Boc, 1H); 3.30 (q, C*H*$_2$NHCO, *J* = 6.0 Hz, 2H); 3.17 (q, C*H*$_2$NHBoc, *J* = 5.2 Hz, 2H); 2.55 (t, C*H*$_2$N(CH_3), *J* = 6.4 Hz, 4H); 2.31 (s, N(C*H*$_3$), 3H); 2.16 (t, C*H*$_2$CONH, *J* = 7.2 Hz, 2H); 1.75-1.69 (m, C*H*$_2$CH$_2$N(CH_3), 4H); 1.59-1.56 (m, C*H*$_2$CH$_2$CONH, 2H); 1.42 (s, C(C*H*$_3$)$_3$, 9H); 1.23 (s, CH_2C*H*$_2$$CH_2$, 20H); 0.86 (t, C*H*$_3$$CH_2$, *J* = 6.8 Hz, 3H). ^{13}C NMR (100 MHz, $CDCl_3$) δ: 176.75 (*C*ONH); 156.92 (O*C*ONH); 77.13 (*C*(CH_3)$_3$); 54.13, 53.86 (*C*H$_2$NCH$_3$); 39.22 (N*C*H$_3$); 36.16 (*C*H$_2$NHCO); 35.52 (CH_2CONH); 31.99, 29.74, 29.44 (all *C*H$_2$); 28.42 (C*C*H$_3$); 25.79, 24.84, 24.55, 22.76 (all *C*H$_2$); 14.20 (*C*H$_3$CH$_2$). ν_{max} (cm^{-1}) (solid): 3397*m*, 2924*s*, 1691*m*, 1633*m*, 1555*m*, 1514*m*, 1365*m*, 1172*m*, 1049*w*, 722*w*. HRMS: Calcd. $[M+H]^+$ ($C_{26}H_{54}N_3O_3$) *m/z* = 456.4160. Found $[M+H]^+$ *m/z* = 456.4162.

Coupling of Palmitic Acid and DAPMA (mono Boc-protected C16-DAPMA)

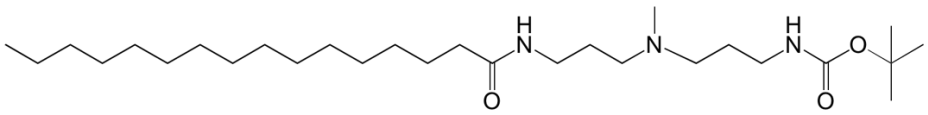

Molecular Formula: $C_{28}H_{57}N_3O_3$

Molecular Weight: 483.44

Palmitic acid (1.00 g, 3.90 mmol) was dissolved in DCM (65 mL). TBTU (1.25 g, 3.90 mmol) and triethylamine (5.4 mL) were added to the mixture and it was stirred for 5 min at room temperature. Mono Boc-protected DAPMA (950 mg, 3.90 mmol) was dissolved in DCM (65 mL), added to the mixture and the reaction was stirred overnight. The solvent was removed by rotary evaporation and the product dissolved in EtOAc (50 mL) and washed with $NaHSO_4$ (2 x 15 mL, 1.33 M), $NaHCO_3$ (2 x 15 mL, saturated), deionised water (3 x 15 mL) and brine (15 mL, saturated). The organic layer was collected, dried with $MgSO_4$, filtered and dried under vacuum. The product was purified by GPC column (Bio-beads, 100% DCM). The obtained product was an orange gummy solid (1.18 g, 2.40 mmol, 62%).

R_f = 0.3 (90:10:1 DCM/MeOH/Et_3N). ^{1}H NMR (400 MHz, $CDCl_3$) δ: 7.26 (br s, N*H*, 1H); 5.56 (br s, N*H*Boc, 1H); 3.41 (q, C*H*$_2$NHCO, *J* = 5.2 Hz, 2H); 3.32 (q, C*H*$_2$NHBoc, *J* = 4.8 Hz, 2H); 3.18 (t, C*H*$_2$N(CH_3), *J* = 6.4 Hz, 4H); 2.88 (s, N(C*H*$_3$), 3H); 2.32 (t, C*H*$_2$CONH, *J* = 7.6 Hz, 2H); 2.09-2.02 (m, C*H*$_2$$CH_2$N($CH_3$), 4H); 1.68-1.65 (m, C*H*$_2$$CH_2$CONH, 2H); 1.51 (s, C(C*H*$_3$)$_3$, 9H); 1.33 (s, CH_2C*H*$_2$$CH_2$, 24H); 0.96 (t, C*H*$_3$$CH_2$, *J* = 6.8 Hz, 3H). ^{13}C NMR (100 MHz, $CDCl_3$) δ: 176.36 (*C*ONH); 156.88 (O*C*ONH); 77.15 (*C*(CH_3)$_3$); 54.23, 53.98 (*C*$H_2$$NCH_3$); 39.41 (N*C*$H_3$); 36.21 (*C*$H_2$NHCO); 35.76 ($CH_2$CONH); 31.99, 29.78, 29.43 (all *C*H_2); 28.42 (C*C*H_3); 25.81, 24.98, 24.66, 22.75 (all *C*H_2); 14.19 (*C*$H_3$$CH_2$). ν_{max} (cm^{-1}) (solid): 3300*w,* 3017*w*, 2936*s*, 2845*s*; 1671*s*, 1647*s*, 1538*m*, 1456*m*, 1390*m*, 1272*m*, 1250*s*, 1171*s*, 1046*s*, 867*w*, 723*w*. HRMS: Calcd. $[M+H]^+$ ($C_{28}H_{58}N_3O_3$) *m/z* = 484.4473. Found $[M+H]^+$ *m/z* = 484.4474.

Coupling of Stearic Acid and DAPMA (mono Boc-protected C18-DAPMA)

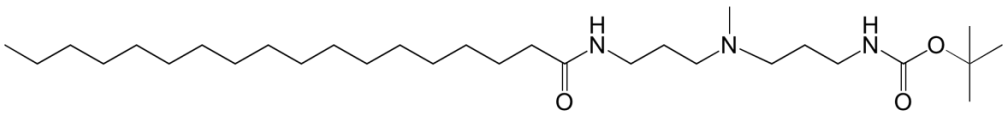

Molecular Formula: $C_{30}H_{61}N_3O_3$

Molecular Weight: 511.47

Stearic acid (1.00 g, 3.50 mmol) was dissolved in DCM (65 mL). TBTU (1.25 g, 3.90 mmol) and triethylamine (5.4 mL) were added to the mixture and it was stirred for 5 min at room temperature. Mono Boc-protected DAPMA (860 mg, 3.50 mmol) was dissolved in DCM (65 mL), added to the mixture and the reaction was stirred overnight. The solvent was removed by rotary evaporation and the product dissolved in EtOAc (50 mL) and washed with $NaHSO_4$ (2 x 15 mL, 1.33 M), $NaHCO_3$ (2 x 15 mL, saturated), deionised water (3 x 15 mL) and brine (15 mL, saturated). The organic layer was collected, dried with $MgSO_4$, filtered and dried under vacuum. The product was purified by GPC column (Bio-beads, 100% DCM). The obtained product was a light orange gummy solid (1.13 g, 2.20 mmol, 63%).

R_f = 0.3 (90:10:1 DCM/MeOH/Et_3N). ^{1}H NMR (400 MHz, $CDCl_3$) δ: 7.15 (br s, N*H*, 1H); 5.47 (br s, N*H*Boc, 1H); 3.30 (q, C*H*$_2$NHCO, *J* = 4.8 Hz, 2H); 3.20 (q, C*H*$_2$NHBoc, *J* = 4.4 Hz, 2H); 3.10 (t, C*H*$_2$N(CH_3), *J* = 6.4 Hz, 4H); 2.81 (s, N(C*H*$_3$), 3H); 2.22 (t, C*H*$_2$CONH, *J* = 8.0 Hz, 2H); 1.99-1.93 (m, C*H*$_2$CH$_2$N(CH_3), 4H); 1.55-1.54 (m, C*H*$_2$CH$_2$CONH, 2H); 1.40 (s, C(C*H*$_3$)$_3$, 9H); 1.22 (s, CH$_2$C*H*$_2$CH$_2$, 28H); 0.85 (t, C*H*$_3$CH$_2$, *J* = 6.8 Hz, 3H). ^{13}C NMR (100 MHz, $CDCl_3$) δ: 176.60 (*C*ONH); 156.93 (O*C*ONH); 77.15 (*C*(CH_3)$_3$); 54.14, 53.89 (*C*H$_2$N(CH_3)); 39.27 (N(*C*H$_3$)); 36.16 (*C*H$_2$NHCO); 35.59 (CH$_2$CONH); 31.99, 29.78, 29.43 (all *C*H$_2$); 28.42 (C(*C*H$_3$)$_3$); 25.80, 24.86, 24.57, 22.75 (all *C*H$_2$); 14.19 (*C*H$_3$CH$_2$). ν_{max} (cm^{-1}) (solid): 3404*m*, 2917*s*, 1649*m*, 1526*m*, 1467*m*, 1366*m*, 1170*m*, 1054*s*, 722*w*. HRMS: Calcd. $[M+H]^+$ ($C_{30}H_{62}N_3O_3$) *m/z* = 512.4798. Found $[M+H]^+$ *m/z* = 512.4786.

Boc Group Removal to yield C14-DAPMA

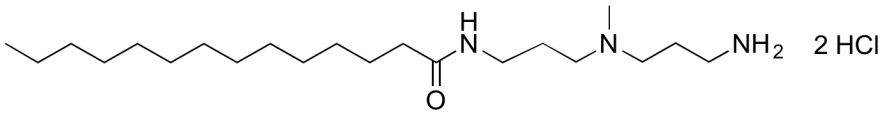

Molecular Formula: $C_{21}H_{47}Cl_2N_3O$

Molecular Weight: 428.52

Mono Boc-protected C14-DAPMA (800 mg, 1.80 mmol) was dissolved in MeOH (50 mL) and HCl gas was applied for approximately 15 seconds. The mixture was stirred for 3 hours and the solvent was removed by rotaty evaporation. The product C14-DAPMA was a beige solid (617 mg, 1.40 mmol, 78%).

R_f = 0.3 (90:10:1 DCM/MeOH/Et_3N). ^{1}H NMR (400 MHz, CD_3OD-d_4) δ: 4.96 (br s, N*H*, 1H); 3.65 (s, NH_2, 2H); 3.08 (t, CH_2N(CH_3), *J* = 7.2 Hz, 4H); 2.91 (s, NCH_3, 3H); 2.27 (t, CH_2CO, J = 7.2 Hz, 2H); 2.21-2.13 (m, CH_2CH_2N(CH_3), 4H); 2.04-1.96 (m, CH_2CH_2CO, 2H); 1.64-1.60 (m, CH_2CH_2CO, 2H); 1.32-1.29 (m, $CH_2CH_2CH_2$, 22H); 0.90 (t, CH_3CH_2, *J* = 6.8 Hz, 3H). ^{13}C NMR (100 MHz, CD_3OD-d_4) δ: 177.16 (*C*ONH); 55.29, 54.24 (*C*H_2N(CH_3)); 40.51 (N(*C*H_3)); 37.90 (*C*H_2CO); 37.31 (*C*H_2NHCO); 36.94 (*C*H_2NH_2); 33.05, 30.75, 30.46, 26.99, 25.44, 23.72, 23.43 (all *C*H_2); 14.51 (*C*H_3CH_2). ν_{max} (cm^{-1}) (solid): 3352*w*, 3306*w*, 2918*s*, 1638*m*, 1554*m*, 1470*m*, 1090*w*, 722*w*. HRMS: Calcd. $[M+H]^+$ ($C_{21}H_{46}N_3O$) *m/z* = 356.3635. Found $[M+H]^+$ *m/z* = 356.3623.

Boc Group Removal to yield C16-DAPMA

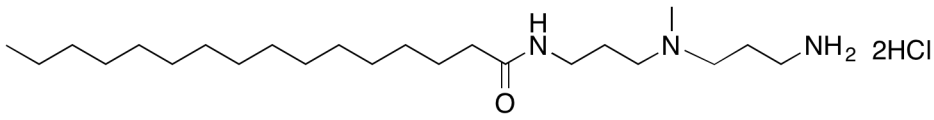

Molecular Formula: $C_{23}H_{51}Cl_2N_3O$

Molecular Weight: 456.58

MonoBoc-protected C16-DAPMA (750 mg, 1.60 mmol) was dissolved in MeOH (50 mL) and HCl gas was applied for approximately 15 seconds. The mixture was stirred for 3 hours and

the solvent was removed by rotaty evaporation. The product C16-DAPMA was a sticky orange solid (578 mg, 1.30 mmol, 82%).

R_f = 0.3 (90:10:1 DCM/MeOH/Et_3N). ^{1}H NMR (400 MHz, CD_3OD-d_4) δ: 4.99 (br s, N*H*, 1H); 3.35 (s, NH_2, 2H); 3.08 (t, CH_2N(CH_3), *J* = 7.2 Hz, 4H); 2.90 (s, NCH_3, 3H); 2.27 (t, CH_2CO, J = 7.6 Hz, 2H); 2.20-2.12 (m, CH_2CH_2N(CH_3), 4H); 2.03-1.96 (m, CH_2CH_2CO, 2H); 1.63-1.60 (m, CH_2CH_2CO, 2H); 1.32-1.28 (m, $CH_2CH_2CH_2$, 24H); 0.90 (t, CH_3CH_2, *J* = 6.8 Hz, 3H). ^{13}C NMR (100 MHz, CD_3OD-d_4) δ: 175.96 (*C*ONH); 54.02, 52.96 (*C*H_2N(CH_3)); 39.20 (N(*C*H_3)); 36.62 (*C*H_2CO); 35.93 (*C*H_2NHCO); 35.67 (*C*H_2NH_2); 31.77, 29.51, 29.18, 25.68, 24.18, 22.44, 22.13 (all *C*H_2); 13.22 (*C*H_3CH_2). ν_{max} (cm^{-1}) (solid): 3389*w*, 3254*w*, 2917*s*, 1634*m*, 1548*m*, 1468*m*, 1056*s*, 721*w*. HRMS: Calcd. $[M+H]^+$ ($C_{23}H_{50}N_3O$) *m/z* = 384.3948. Found $[M+H]^+$ *m/z* = 384.3961.

Boc Group Removal to yield C18-DAPMA

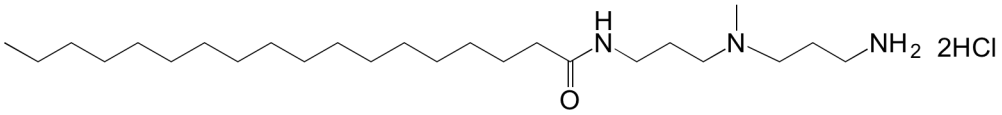

Molecular Formula: $C_{25}H_{55}Cl_2N_3O$

Molecular Weight: 484.64

MonoBoc-protected C18-DAPMA (800 mg, 1.60 mmol) was dissolved in MeOH (50 mL) and HCl gas was applied for approximately 15 seconds. The mixture was stirred for 3 hours and the solvent was removed by rotary evaporation. The product C18-DAPMA was a slightly sticky light orange solid (431 mg, 0.89 mmol, 57%).

R_f = 0.3 (90:10:1 DCM/MeOH/Et_3N). ^{1}H NMR (400 MHz, CD_3OD-d_4) δ: 4.91 (br s, N*H*, 1H); 3.31 (s, NH_2, 2H); 3.08 (t, CH_2N(CH_3), *J* = 7.6 Hz, 4H); 2.90 (s, NCH_3, 3H); 2.25 (t, CH_2CO, *J* = 7.6 Hz, 2H); 2.17-2.09 (m, CH_2CH_2N(CH_3), 4H); 1.99-1.92 (m, CH_2CH_2CONH, 2H); 1.65-1.54 (m, CH_2CH_2CO, 2H); 1.35-1.21 (m, $CH_2CH_2CH_2$, 28H); 0.90 (t, CH_3CH_2, *J* = 6.8 Hz, 3H). ^{13}C NMR (100 MHz, CD_3OD-d_4) δ: 177.89 (*C*ONH); 55.23, 54.26 (*C*H_2N(CH_3)); 40.47 (N(*C*H_3)); 37.90 (*C*H_2NHCO); 37.74 (*C*H_2NH_2); 36.55 (*C*H_2CO); 33.08, 30.81, 30.64, 27.02, 25.22, 23.74, 23.45 (all *C*H_2); 14.50 (*C*H_3CH_2). ν_{max} (cm^{-1}) (solid): 3385*w*, 3243*w*, 2916*s*, 1641*m*, 1543*m*, 1468*m*, 1059*s*, 721*w*. HRMS: Calcd. $[M+H]^+$ ($C_{25}H_{54}N_3O$) *m/z* = 412.4261. Found $[M+H]^+$ *m/z* = 412.4267.

Synthesis of 1,3:2,4-dibenzylidene-D-Sorbitol-p,p'-dimethylester (DBS-COOCH$_3$)[87]

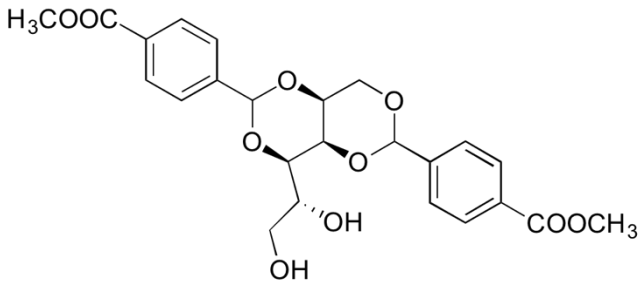

Molecular Formula: $C_{24}H_{26}O_{10}$
Molecular Weight: 474.15

D-Sorbitol (3.08 g, 16.9 mmol), cyclohexane (35 mL) and methanol (10 mL) were mixed, and stirred for 20 min, at 50 °C under N_2 atmosphere. Methyl 4-formylbenzoate (4.71 g, 28.7 mmol) and p-toluene sulfonic acid hydrate (1.00 g) were dissolved in methanol (20 mL) and stirred for 20 min (RT). The mixture was added drop wise to the D-sorbitol solution. The reaction temperature was then increased to 70 °C and stirred for approximately 3 h. The product was washed with methanol (3 x 100 mL), dried under vacuum for approximately 1 h and then air-dried overnight. To ensure that mono and tri-substitued derivates were removed, the compound was washed with boiling water (4 x 100 mL) and DCM. The obtained product was a white powder (6.10 g, 12.9 mmol, 89%).

^{1}H NMR (400 MHz, DMSO-d_6) δ: 8.00-7.97 (m, Ar*H*, 4H); 7.61 (t, Ar*H*, *J* = 8.4 Hz, 4H); 5.76 (s, ArC*H*, 2H); 4.91 (d, CHO*H*, *J* = 5.2Hz, 1H); 4.46 (br, CHO*H*, 1H); 4.22-4.15 (m, sugar, 3H (overlap)); 3.91 (m, sugar, 1H); 3.88 (m, sugar, 1H); 3.85 (s, OC*H*$_3$, 6H); 3.78 (br, sugar, 1H); 3.63-3.61 (m, sugar, 1H); 3.50-3.45 (m, sugar, 1H). ^{13}C NMR (100 MHz, DMSO-d_6) δ: 166.52 (*C*OO); 143.84 (Ar-*C*); 143.57 (Ar-*C*); 130.28 (Ar-*C*); 130.22 (Ar-*C*); 129.56 (Ar-*C*); 129.47 (Ar-*C*); 127.02 (Ar-*C*); 99.05 (Acetal-*C*); 98.97 (Acetal-*C*); 78.08 (*C*H); 70.69 (*C*H); 69.83 (*C*H$_2$); 69.04 (*C*H); 68.10 (*C*H); 63.14 (*C*H$_2$); 52.74 (*C*H$_3$). ν_{max} (cm^{-1}) (solid): 3249*m*, 2954*m*, 1724*s*, 1616*w*, 1580*w*, 1512*w*, 1278*s*, 1018*s*, 856*m*, 836*m*, 750*s*, 708*m*. HRMS: Calcd. [M+Na]$^+$ ($C_{24}H_{26}O_{10}$) *m/z* = 497.1418. Found [M+Na]$^+$ *m/z* = 497.1416.

***Synthesis of 1,3:2,4-dibenzylidene-D-Sorbitol-p,p'-dicarboxylic acid (DBS-COOH)*[87]**

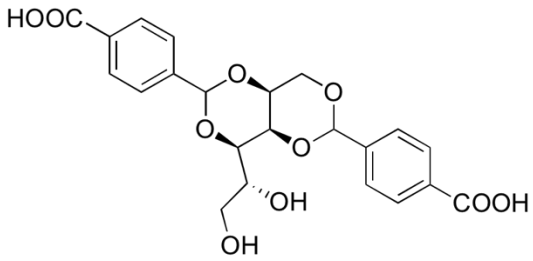

Molecular Formula: $C_{22}H_{22}O_{10}$
Molecular Weight: 446.41

DBS-$COOCH_3$ (1.20 g, 2.50 mmol) was dissolved in methanol (35 mL). $NaOH_{(aq)}$ (35 mL, 1 M) was added to the solution and the mixture was heated overnight at 80 °C under reflux. The solvent was removed by rotary evaporation, and 50 mL of water were added. The mixture was acidified to pH 3 using $NaHSO_4$, resulting in the formation of a white gel. The product was then filtered, washed with deionised water (4 x 100 mL) and dried under high vacuum oven at 50 °C for 1 day. The obtained product was a white powder (0.82 g, 1.80 mmol, 73%).

^{1}H NMR (400 MHz, DMSO-d_6) δ: 12.99 (br s, COO*H*, 2H); 7.98 (d, Ar*H*, *J* = 6.8 Hz, 4H); 7.59 (t, Ar*H*, , *J* = 8.4 Hz, 4H); 5.74 (s, ArC*H*, 2H); 4.25-4.17 (m, sugar, 3H (overlap)); 4.00 (s, sugar, 1H); 3.90 (d, sugar, *J* = 9.2 Hz,1H); 3.81-3.79 (m, sugar, 1H); 3.64 (d, sugar, *J* = 10.8 Hz, 1H); 3.49-3.48 (m, sugar, 1H). ^{13}C NMR (100 MHz, DMSO-d_6) δ: 167.12 (*C*OOH); 142.91 (Ar-*C*); 142.64 (Ar-*C*); 130.97 (Ar-*C*); 130.91 (Ar-*C*); 129.17 (Ar-*C*); 129.08 (Ar-*C*); 126.31 (Ar-*C*); 98.65 (Acetal-*C*); 98.57 (Acetal-*C*); 77.58 (*C*H); 70.16 (*C*H); 69.32 (CH_2); 69.04 (*C*H); 68.51 (*C*H); 67.62 (*C*H); 62.58 (CH_2). ν_{max} (cm^{-1}) (solid): 3394*m*, 2865*m*, 1689*s*, 1613*w*, 1577*w*, 1511*w*, 1290*m*, 1091*s*, 856*m*, 832*m*, 751*m*, 703*m*. HRMS: Calcd. $[M+Na]^+$ ($C_{22}H_{22}O_{10}$) *m/z* = 469.1105. Found $[M+Na]^+$ *m/z* = 469.1118.

Synthesis of 1,3:2,4-dibenzylidene-D-Sorbitol-p,p'-dihydrazide (DBS-CONHNH$_2$)[88]

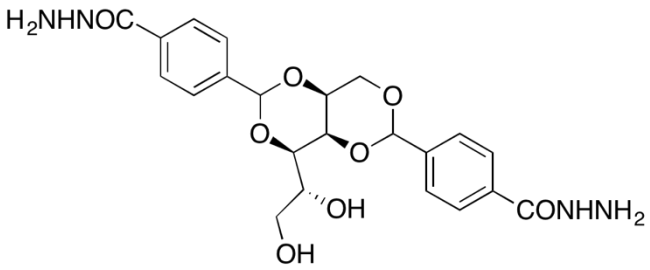

Molecular Formula: $C_{22}H_{26}N_4O_8$
Molecular Weight: 474.46

DBS-$COOCH_3$ (1.10 g, 2.32 mmol) was dissolved in tetrahydrofuran (40 mL). Hydrazine monohydrate (6.19 g, 0.12 mol) was added to the solution and the mixture was heated overnight at 65 °C under reflux. The product was then filtered, washed with deionised water (3 x 100 mL) and dried under high vacuum oven at 80 °C and pulverized. The obtained product was a white powder (0.88 g, 1.85 mmol, 80%) .

^{1}H NMR (400 MHz, DMSO-d_6) δ: 9.81 (s, CON*H*NH_2, 2H); 7.83 (d, Ar*H*, , *J* = 6.8 Hz, 4H); 7.52 (t, Ar*H*, , *J* = 8.8 Hz, 4H); 5.71 (s, ArC*H*, 2H); 4.93 (d, *J* = 6.0 Hz, CHO*H*, 1H); 4.51 (s, CONHNH_2, 4H); 4.47 (t, *J* = 11.6 Hz, CH_2O*H*, 1H); 4.23-4.16 (m, sugar, 3H (overlap)); 3.98 (s, sugar, 1H); 3.87 (d, *J* = 9.6 Hz, sugar, 1H); 3.78-3.77 (m, sugar, 1H); 3.63-3.59 (m, sugar, 1H); 3.47-3.44 (m, sugar, 1H). ^{13}C NMR (100 MHz, DMSO-d_6) δ: 165.66 (C=O); 141.25 (Ar-*C*); 140.98 (Ar-*C*); 133.50 (Ar-*C*); 133.42 (Ar-*C*); 126.77 (Ar-*C*); 126.69 (Ar-*C*); 126.06 (Ar-*C*); 98.76 (Acetal-*C*); 98.69 (Acetal-*C*); 77.56 (*C*H); 70.12 (*C*H); 69.32 (*C*H_2); 68.47 (*C*H); 67.67 (*C*H); 62.61 (*C*H_2). ν_{max} (cm^{-1}) (solid): 3294*m*, 2869*w*, 1664*s*, 1506*w*, 1163*m*, 1093*s*, 848*m*, 830*m*, 754*m*.HRMS: Calcd. $[M+Na]^+$ ($C_{22}H_{26}N_4O_8$) *m/z* = 497.1643. Found $[M+Na]^+$ *m/z* = 497.1670.

7.3. Chapter 2 – Characterisation and Assay Methods

Nile Red Assay[223]

Nile Red solution (2.5 mM) was prepared in ethanol. A blank solution was prepared by placing 1 mL of phosphate buffer saline, PBS (0.01 M, pH 7.4) into a cuvette and adding 1 µL of Nile Red solution. A stock solution of binder was prepared in PBS. Different amounts of stock solution (1000 µL; 900 µL; 800 µL; 700 µL; 600 µL; 500 µL; 400 µL; 300 µL; 200 µL;

100 µL) were added to cuvettes and the volume was made up to 1 mL with PBS. 1 µL of Nile Red was added to all the cuvettes. The fluorescence was recorded with an excitation wavelength of 550 nm and an emission wavelength of 635 nm. The procedure was performed for C14-DAPMA (stock solution concentration: 225 µM), C16-DAPMA (stock solution concentration: 100 µM) and C18-DAPMA (stock solution concentration: 175 µM). The data were obtained in triplicate for each binder.

MalB Assay[226]

MalB (25 µM) solution was prepared in Tris-HCl (10 mM) and NaCl (150 mM), wrapped with foil to avoid contact with direct light and incubated at 50 °C for 24 hours. Heparin (27 µM) was added to the MalB solution, after it cooled down. 2 mL of MalB (25 µM), heparin (27 µM) solution in Tris-HCl (10 mM) and NaCl (150 mM) was placed in a cuvette and titrated with binder stock solution to give a suitable charge ratio for the binder and heparin in the cuvette. Binder stock solution consisted of the solution of MalB and heparin in Tris-HCl (10 mM) and NaCl (150 mM) with a concentration of binder that resulted in a cuvette charge ratio (+ : -) of 0.1, after the addition of 10 µL of binder stock solution. After each addition of the binder stock solution, the cuvette was stirred to ensure mixing and the absorbance recorded at 615 nm. This procedure was performed in triplicate for each binder.

Dynamic Light Scattering (DLS) and Zeta Potential

The binder (1 mg/mL) was dissolved in 10 mM Tris-HCl/ 150 mM NaCl (pH 7.4). 1 mL of the sample was filtered using a syringe filter PTFE 0.45 µM and placed in a disposable cuvette. DLS measurements were carried out at 25 ^{o}C, in triplicate with 11-15 runs per single measurement. The procedure was performed for C14-DAPMA, C16-DAPMA without sonication and C18-DAPMA after sonicated for 30 minutes. The same procedure was also performed for each binder in the presence of heparin (charge ratio +/-: 2) (Table 7.1).

Table 7.1. Binder/Heparin ratios used in DLS measurements.

Sample	Concentration (mM)
C14-DAPMA/Heparin	2.33/0.580
C16-DAPMA/Heparin	2.19/0.550
C18-DAPMA/Heparin	2.06/0.520

Zeta potential measurements were obtained using the samples previously prepared for DLS. The samples were transferred to a zeta capillary cell (DTS1070) until the electrodes were fully covered with the solution and ensuring that no air bubbles were formed. An electric field was applied using a 4 mW He-Ne laser at 633 nm and the experiments were performed in triplicate with 11-15 runs per single measurement.

TEM Imaging

In order to obtain TEM images, 10 µL of each sample (Table 7.2) in ultra-pure H_2O was placed on a copper grid (standard) with Formvar and carbon support film. Excess sample was removed with filter paper then the sample was allowed to stand for 5 minutes. A negative stain (1% uranyl acetate) was applied to the grid while wet to allow the stain to run across the grid. The grid was then left to rest for 20 minutes before recording images.

Table 7.2. Concentrations of C14-DAPMA, C16-DAPMA, C18-DAPMA with and without heparin used to record TEM images in water.

Sample	Concentration (µM)
C14-DAPMA	200
C16-DAPMA	150
C18-DAPMA	150
C14-DAPMA / Heparin	200/50
C16-DAPMA / Heparin	150 / 38
C18-DAPMA / Heparin	150 / 38

SAXS

A sample of C16-DAPMA with heparin was prepared by mixing 10 µl of C16-DAPMA (7.36 mg/ml) in 10 mM Tris-HCl/ 150 mM NaCl with 10 µl of heparin (2.64 mg/ml) also in 10 mM Tris-HCl/ 150 mM NaCl. The sample formed a white precipitate and SAXS was measured from the precipitate. C14-DAPMA with heparin was prepared by mixing 15 µl of C14-DAPMA (7.08 mg/ml) in 10 mM Tris-HCl/ 150 mM NaCl with 15 µl of heparin (2.92 mg/ml) in 10 mM Tris-HCl/ 150 mM NaCl. The sample formed a white precipitate and SAXS was measured from the precipitate.

The wet precipitate was sealed between two Kapton foils during SAXS measurements. The sample environment was evacuated in order to reduce scattering from air. The final spot size at the sample position was roughly 1 mm in diameter. The scattered intensity was collected using a Hi-Star 2D area detector (Bruker). Sample-to-detector distance was 0.59 m, and silver behenate standard sample was used for calibration of the length of the scattering vector q. One-dimensional SAXS data were obtained by azimuthally averaging the 2D scattering data. The magnitude of the scattering vector q is given by $q=\frac{4\pi \sin(\theta)}{\lambda}$, where 2θ is the scattering angle.

Degradation Assay - Mass Spectrometry

C14-DAPMA and C16-DAPMA were dissolved in in ammonium carbonate (10 mM, pH 7.5) to give a concentration of 450 µM and 200 µM, respectively. 250 µL of this binder solution was combined with 250 µL of a Gly-Ala standard (1 mM, in 10 mM ammonium carbonate) for mass spectrometric analysis. Following incubation of the binder solution for 24 hours at 37 °C, the same analysis was repeated.

Degradation Assay - Fluorescence[206]

C14-DAPMA and C16-DAPMA were dissolved in 10 mM Tris-HCl/ 150 mM NaCl buffer to give a concentration of 225 µM and 100 µM, respectively. In a cuvette, an aliquot (1 mL) of each solution was mixed with Nile red (1 µL, 2.5 mM in ethanol). Following inversion to ensure mixing, fluorescence intensity at 635 nm was recorded over time using a 550 nm excitation wavelength. For the degradation experiment in the presence of heparin, the

binder stock solution was additionally endowed with a heparin concentration corresponding to a +/- charge ratio of 2. This procedure was performed in triplicate for each binder.

7.4. Chapters 3 and 4 – Characterisation and Assay Methods

DBS-COOH and DBS-CONHNH$_2$ Gel Formation

DBS-COOH gel was prepared with different gelator concentrations (0.1% w/v; 0.15% w/v; 0.2% w/v) in 10 mM Tris-HCl/ 150 mM NaCl buffer, pH 7.4. 0.5 mL of solvent was added to DBS-COOH powder (0.50 mg; 0.75 mg; 1.0 mg, respectively) and sonicated. 20 µL of 0.5 M NaOH(aq) was added to dissolve all the solid. The solution was then transferred to a vial with GdL (4 mg, 44.9 mM), followed by shaking to dissolve. The vials were allowed to stand overnight.

DBS-CONHNH$_2$ gel was prepared in 10 mM Tris-HCl/ 150 mM NaCl buffer, pH 7.4. 0.5 mL of solvent was added to DBS-CONHNH$_2$ powder (2 mg) and sonicated for 20 minutes. The solution was heated until complete dissolution of the gelator and a transparent solution was observed. The sample was allowed to cool down at room temperature.

DBS-COOH and DBS-CONHNH$_2$ – Agarose Hybrid Gel Formation

The required amount of DBS-COOH (2 mg) were added to 10 mM Tris-HCl/ 150 mM NaCl, pH 7.4 (1 mL) and sonicated for 10 minutes. 30 µL of 0.5 M NaOH(aq) was added to dissolve all the solid. The solution was transferred to a vial containing agarose (10 mg), heated to 90 °C in a thermoregulated oil bath to dissolve agarose, cooled to 50 °C, and then transferred to a vial containing GdL (8 mg, 44.9 mM), followed by shaking to dissolve. The vials were allowed to stand overnight.

The required weight of agarose (5 mg) and DBS-CONHNH$_2$ (2 mg) were jointly dissolved in 10 mM Tris-HCl/ 150 mM NaCl, pH 7.4 (0.5 mL). After sonicating the mixture, the solution was heated until complete dissolution of the gelators and a transparent solution was observed. The sample was allowed to cool down at room temperature.

DBS-COOH and DBS-CONHNH$_2$ Gel Formation with Different Concentrations of Heparin and C16-DAPMA

DBS-COOH gel was prepared with a minimum concentration of heparin (38 μM) and C16-DAPMA (150 μM) in order to verify the influence on gel formation and the best order of addition. DBS-COOH gel was prepared in 10 mM Tris-HCl/ 150 mM NaCl, pH 7.4. 0.5 mL of solvent was added to DBS-COOH powder (2.0 mg) and sonicated. 30 μL of 0.5 M $NaOH_{(aq)}$ was added to dissolve all solid. Solutions of C16-DAPMA and heparin were prepared with three times higher concentration than the intended final concentration, to allow for subsequent dilutions. 0.5 mL of C16-DAPMA solution (600 μM) was then added to 0.5 mL of heparin solution (152 μM) and stirred to ensure the binding. The previous mixture was added in different orders to the DBS-COOH solution: 1) The DBS-COOH solution was transferred to a vial with GdL (8 mg, 44.9 mM), followed by shaking to dissolve and 0.5 mL of the solution of C16-DAPMA and heparin was added after approximately 20 minutes; 2) 0.5 mL of the solution of C16-DAPMA and heparin was added to the DBS-COOH solution, stirred to ensure mixing and transferred to a vial with GdL (8 mg, 44.9 mM), followed by shaking to dissolve; 3) The DBS-COOH solution was transferred to a vial with GdL (8 mg, 44.9 mM), followed by shaking to dissolve and 0.5 mL of the solution of C16-DAPMA and heparin was immediately added. The vials were allowed to stand overnight. Addition order 3) was used in the following sections.

DBS-COOH gel was prepared with different concentrations of heparin (38 μM; 50 μM; 100 μM; 150 μM; 300 μM; 400μM; 500 μM) in 10 mM Tris-HCl/ 150 mM NaCl, pH 7.4. 0.5 mL of 10 mM Tris-HCl/ 150 mM NaCl was added to DBS-COOH powder (2.0 mg) and sonicated. 30 μL of 0.5 M $NaOH_{(aq)}$ was added to dissolve all solid. Solutions of heparin were prepared with double the intended final concentration, to allow for subsequent dilution. The DBS-COOH solution was transferred to a vial with GdL (8 mg, 44.9 mM), followed by shaking to dissolve and 0.5 mL of heparin solution was immediately added and stirred to ensure mixing. The vials were allowed to stand overnight.

DBS-$CONHNH_2$ gel was prepared with different concentrations of heparin (38 μM; 150 μM; 300 μM; 400 μM; 600 μM) in 10 mM Tris-HCl/ 150 mM NaCl buffer. DBS-$CONHNH_2$ powder (2 mg) was mixed with 0.25 mL of buffer and sonicated for 20 min. Solutions of heparin

were prepared with double the intended final concentration, to allow for subsequent dilution. 0.25 mL of heparin solution was added into the DBS-$CONHNH_2$ solution, followed by heating and shaking until a clear solution was obtained. The sample was allowed to cool down at room temperature.

DBS-COOH and DBS-$CONHNH_2$ gels were prepared with different concentrations of C16-DAPMA (150 μM; 300 μM; 600 μM; 800 μM; 1000 μM; 1200 μM) in 10 mM Tris-HCl/ 150 mM NaCl buffer. This followed the procedure explained above.

DBS-COOH gel was prepared with solutions containing a fixed concentration of heparin (150 μM) and different C16-DAPMA concentrations (100 μM; 150 μM; 200 μM; 250 μM; 300 μM; 350 μM; 400 μM; 450 μM; 500 μM; 600 μM). 0.5 mL of 10 mM Tris-HCl/ 150 mM NaCl (pH 7.4) was added to DBS-COOH powder (2.0 mg) and sonicated. 30 μL of 0.5 M $NaOH_{(aq)}$ was added to dissolve all solid. A solution of C16-DAPMA and heparin was prepared with three times the intended final concentration, to allow for subsequent dilutions. 0.5 mL of C16-DAPMA solution was then added to 0.5 mL of heparin solution and stirred to ensure binding. The DBS-COOH solution was transferred to a vial with GdL (8 mg, 44.9 mM), followed by shaking to dissolve and 0.5 mL of C16-DAPMA/heparin solution was immediately added and stirred to ensure mixing.

DBS-$CONHNH_2$ gel was prepared with solutions containing a fixed concentration of heparin (150 μM) and different C16-DAPMA concentrations (150 μM; 300 μM; 400 μM; 500 μM; 600 μM). 0.25 mL of 10 mM Tris-HCl/ 150 mM NaCl (pH 7.4) was added to DBS-$CONHNH_2$ powder (2.0 mg) and sonicated for 20 min. A solution of C16-DAPMA and heparin was prepared with three times the intended final concentration, to allow for subsequent dilutions. 0.25 mL of C16-DAPMA solution was then added to 0.25 mL of heparin solution and stirred to ensure binding. C16-DAPMA/heparin solution (0.25 mL) was added into the DBS-$CONHNH_2$ solution and stirred to ensure mixing. The sample was heated until a clear solution was observed and allowed to cool down at room temperature. The same study was performed for both gelators with double the concentration of heparin (300 μM) and different C16-DAPMA concentrations (500 μM; 800 μM; 1000 μM; 1100 μM; 1200 μM), as well as for 400 μM of heparin with different concentrations of C16-DAPMA (500 μM; 900

μM; 1000 μM; 1200 μM; 1500 μM; 1600 μM) and 600 μM of heparin with the following concentrations of C16-DAPMA: 1400 μM; 1500 μM; 1600 μM; 1800 μM; 2000 μM; 2200 μM; 2400 μM.

C16-DAPMA Stability at High Temperatures

C16-DAPMA (1 mg/mL) was dissolved in 10 mM Tris-HCl/ 150 mM NaCl (pH 7.4). 1 mL of the sample was filtered using a syringe filter (PTFE 0.45 μM) and placed in a disposable cuvette. DLS measurements were carried at 25°C and 70 °C, in triplicate with 11-15 runs per single measurement. Zeta potential measurements were obtained using the samples previously prepared for DLS. The samples were transferred to a zeta capillary cell (DTS1070) until the electrodes were fully covered with the solution and ensuring that no air bubbles were formed. An electric field was applied using a 4 mW He-Ne laser at 633 nm and the experiments were performed in triplicate with 11-15 runs per single measurement.

MalB (25 μM) solution was prepared as previously described. A solution of C16-DAPMA (2.4 mM) in 10 mM Tris-HCl/ 150 mM NaCl buffer was heated to 85 °C for 10 min. The binder solution (100 μL) was added to the MalB solution containing 100 μL of heparin (0.6 mM) and the absorbance was measured.

A solution of 1.2 mM of C16-DAPMA and 0.3 mM of heparin was prepared in buffer and heated at 85 °C for 10 min. An aliquot (200 μL) was added into the MalB solution and the absorbance recorded.

Thermal Stability and T_{gel} Determination

Thermal stability and T_{gel} values for DBS-COOH and DBS-$CONHNH_2$ were obtained by reproducible tube inversion methodology. All the samples with different concentrations of heparin, C16-DAPMA and heparin-C16-DAPMA aggregates that resulted in gel formation were placed into a thermo-controlled oil bath, with an initial temperature of 25 °C. The temperature was set to rise until 100 °C. After each increase of ca. 5 °C, the tubes were removed from the bath and turned upside down. The stability of the gels was observed and the T_{gel} was considered as the temperature when the gel started to run down the sides of the vial.

Infrared

DBS-COOH (Table 7.3) and DBS-$CONHNH_2$ (Table 7.4) gel samples were prepared for infrared by removing solvent from the samples under high vacuum. The resulting powder was placed into the infrared spectrometer and the spectra recorded.

Table 7.3. Concentrations of DBS-COOH, C16-DAPMA and heparin used to record infrared spectra.

Sample	Concentration (mM)
DBS-COOH	4.5
DBS-COOH/Heparin	4.5/0.3
DBS-COOH/Heparin/C16-DAPMA	4.5/0.30/0.80

Table 7.4. Concentrations of DBS-$CONHNH_2$, C16-DAPMA and heparin used to record infrared spectra.

Sample	Concentration (mM)
DBS-$CONHNH_2$	8.4
DBS-$CONHNH_2$/Heparin	8.4/0.3
DBS$CONHNH_2$/C16-DAPMA	8.4/1.2
DBS-$CONHNH_2$/Heparin/C16-DAPMA	8.4/0.3/1.2

NMR Characterisation of DBS-COOH Kinetics

DBS-COOH gel was prepared by adding D_2O (0.7 mL) to DBS-COOH (1.4 mg) and sonicating. 20 µL of $NaOH_{(aq)}$ (0.5 M) was added to dissolve all solid and DMSO (1.4 µL) was added as an internal standard. The solution was then transferred to a vial containing GdL (5.6 mg, 44.9 mM), followed by shaking. The sample was then immediately transferred to a NMR tube and placed in the spectrometer, with spectra recorded every 30 minutes for 10 hours. The kinetics of DBS-COOH gel formation with 300 µM heparin were obtained by adding D_2O (0.5 mL) to DBS-COOH (2.0 mg) and sonicating. 30 µL of $NaOH_{(aq)}$ (0.5 M) was added to

dissolve all solid and DMSO (2.0 µL) was added as an internal standard. The solution was then transferred to a vial containing GdL (8 mg, 44.9 mM), followed by shaking. 0.5 mL of heparin (600 µM) in D_2O was added to the DBS-COOH solution, stirred and immediately transferred to a NMR tube and placed in a spectrometer, with spectra recorded every 30 minutes for 10 hours. The same procedure was performed for the kinetics of DBS-COOH with 300 µM of heparin and 800 µM of C16-DAPMA.

Circular Dichroism

The DBS-COOH CD sample was prepared by adding 10 mM Tris-HCl/ 150 mM NaCl (500 µL) to DBS-COOH (0.2 mg) and sonicating. 5 µL of $NaOH_{(aq)}$ (0.5 M) was added to dissolve all solid and then the solution was transferred to a vial containing GdL (1 mg), followed by shaking. 400 µL of sample were immediately transferred to a CD cuvette (1 mm pathlength) and placed in the CD spectrometer, with spectra recorded every 5 minutes for 5 hours and a further reading after 6 hours. The same procedure was performed in the presence of 38 µM of heparin and 150 µM of C16-DAPMA/ 38 µM heparin.

The DBS-$CONHNH_2$ CD sample was prepared by adding 10 mM Tris-HCl/ 150 mM NaCl (500 µL) to DBS-$CONHNH_2$ (0.6 mg) and sonicating. The sample was heated until a clear solution was formed and 400 µL of sample were immediately transferred to a 1 mm quartz cuvette (incubated in a cell holder at 90 °C) and placed in the spectrometer. The temperature was set to cool down to 20 °C (5 °C/min ramp) while spectra were recorded every 30 seconds for 15 minutes. The same procedure was performed in the presence of 38 µM of heparin, 150 µM of C16-DAPMA and 150 µM of C16-DAPMA/ 38 µM heparin.

MalB Diffusion Assay

DBS-COOH gel (0.2% w/v) or DBS-$CONHNH_2$ gel (0.3% w/v) with 38 µM heparin, 150 µM C16-DAPMA and 38 µM heparin and DBS-$CONHNH_2$ gel (0.3% w/v) with 150 µM C16-DAPMA were prepared in 10 mM Tris-HCl/ 150 mM NaCl. 3 mL of 25 µM MalB solution were carefully placed on top of the gels and the absorbance measured at different times (0h, 1h, 2h, 3h, 4h, 5h, 6h, 7h, 24h, 48h, 72h, 168h) by collecting 2 mL of the MalB solution and replacing it after the measurement. Data were obtained in triplicate. A calibration curve of MalB was plotted and the obtained UV-Vis absorbance at 615 nm fitted against it.

Electron Microscopy

DBS-COOH (Table 7.5) and DBS-$CONHNH_2$ (Table 7.6) gel samples for TEM images were prepared in ultra-pure H_2O and images obtained by adding one microspatula of each sample on a copper grid (standard) with Formvar and carbon support film. The excess sample was removed with filter paper then allowed to set for 5 minutes. A negative stain (1% uranyl acetate) was applied to the grid while wet to allow the stain to run across the grid. The grid was left to rest for 30 minutes before taking images.

To obtain SEM images (Table 7.5 and 7.6), the gels were freeze fried on bits of copper shim. After mounting the samples on stubs they were sputter coated with approximately 5 nm of Au/Pd and the images recorded.

Table 7.5. Concentrations of DBS-COOH, C16-DAPMA and heparin used to record TEM and SEM images of gels prepared in ultra-pure H_2O.

Sample	Concentration (mM)
DBS-COOH	4.5
DBS-COOH/Heparin	4.5/0.038
	4.5/0.30
DBS-COOH/Heparin/C16-DAPMA	4.5/0.038/0.15
	4.5/0.30/0.80

Table 7.6. Concentrations of DBS-$CONHNH_2$, Heparin and C16-DAPMA used to record TEM and SEM images of gels prepared in ultra-pure water.

Sample	Concentration (mM)
DBS-$CONHNH_2$	8.4
DBS-$CONHNH_2$/Heparin	8.4/0.038
DBS$CONHNH_2$/C16-DAPMA	8.4/0.15
DBS-$CONHNH_2$/Heparin/C16-DAPMA	8.4/0.038/0.15

Rheology

The following measurements were performed in a Malvern Instrument Kinexus pro+ rheometer.

DBS-COOH (0.2% w/v) and DBS-$CONHNH_2$ (0.4% w/v) hydrogels were prepared in 10 mM Tris-HCl/ 150 mM NaCl buffer (d = 20 mm, h = 0.5 cm) on the lower plate of the equipment with a bottomless vial as template to obtain the intended gel dimensions. The viscoelastic properties were measured by applying dynamic strain sweeps (f = 1 Hz), dynamic frequency sweeps (Y = 0.1%) and temperature variation (f = 1 Hz, Y = 0.1%). The measurements were carried out with a parallel geometry plate (d = 20 mm) and a gap of 0.5 mm. The same procedure was performed for DBS-COOH and DBS-$CONHNH_2$ hydrogels incorporating heparin (1 mM), C16-DAPMA (2 mM), heparin/C16-DAPMA aggregates and agarose (1% w/v).

Release Studies

- Release Assay - Aliquots

DBS-COOH (0.2% w/v, 2% w/v, 5% w/v and 10% w/v) and DBS-$CONHNH_2$ (0.4% w/v) hydrogels (3 mL) containing 1 mM of heparin; 1 mM of heparin and 2 mM of C16-DAPMA; and agarose (0.5% w/v and 1% w/v) with heparin (1 mM) were prepared in 10 mM Tris-HCl/ 150 mM NaCl buffer (pH 7.4), followed by the addition of 1 mL of buffer on top. Aliquots of 65 µL of buffer were collected over time, added into 1935 µL of MalB solution (25.84 µM) and the UV-Vis absorbance recorded. The data were obtained in triplicate. A calibration curve of heparin was obtained by adding 65 µL of known heparin concentrations into 1935 µL of MalB solution and the absorbance spectra obtained. The same procedure was followed for the release of heparin (1 mM) from agarose gels (2.5% w/v, 5.0% w/v, 7.5% w/v and 10% w/v).

- Release Assay - Gel Cylinder

DBS-COOH (2% w/v) and DBS-$CONHNH_2$ (0.4% w/v) hydrogels were prepared with 1% w/v of agarose in 10 mM Tris-HCl/ 150 mM NaCl buffer incorporating 17 mM of heparin. The gel cylinders (approx. dimensions: radius 5 mm, height 14 mm) were removed from the vial carefully using a spatula and placed into a glass jar (100 mL). Buffer solution was added (35

mL, 10 mM Tris-HCl/ 150 mM NaCl) to the jar and aliquots of 65 μL of buffer were collected over time after gently swirling of the solution and added into 1935 μL of MalB solution (25.84 μM) for UV-Vis absorbance measurement. The data were obtained in triplicate. A calibration curve of heparin was obtained by adding 65 μL of known heparin concentrations into 1935 μL of MalB solution and the absorbance spectra obtained.

7.5. Chapter 3 and 4 - Cytocompatiblity Studies

Cell Line (3T3 cells: mouse embryonic fibroblasts)

Mouse fibroblast 3T3 cells were expanded in a T75 flask with Dulbecco's Modified Eagle's Medium (89% DMEM – high glucose and 3.7 g/L $NaHCO_3$), 10% fetal bovine serum (FBS) and 1% Penicillin/Streptomycin. To obtain the cells, the medium was removed from the T75 flask and the cells washed with 10 mL Dulbecco's phosphate buffered saline (DPBS) warmed at 37 °C. Trypsin/EDTA (1.5 mL) was added and the cells incubated at 37 °C for approximately 5 min. When cell detachment was observed (by optical microscopy), trypsin was neutralised with 3.5 mL of DMEM, 10% FBS, 1% P/S and the cell suspension collected into a 50 mL tube. The cells were counted in a Neubauer Chamber by mixing 20 μL of cell suspension with 180 μL of trypan blue by optical microscopy.

DBS-COOH Gel Preparation

DBS-COOH gel was prepared by adding 2 mg of gelator to 1 mL of 10 mM Tris-HCl/ 150 mM NaCl (pH 7.4), followed by sonication. 30 μL of 0.5 M NaOH(aq) was added to dissolve all solid. The solution was then transferred to a vial with GdL (8 mg, 44.9 mM), followed by shaking to dissolve. The solution was immediately transferred into the well plates (50 μL in each well of the 96 well plates and 100 μL in the inserts). The same procedure was followed to prepare the gels with 1 mM and 2 mM of heparin, by adding a solution of heparin in 10 mM Tris-HCl/ 150 mM NaCl with the appropriate concentration.

DBS-CONHNH$_2$ Gel Preparation

DBS-$CONHNH_2$ gel was prepared in 10 mM Tris-HCl/ 150 mM NaCl buffer (pH 7.4). 0.5 mL of buffer was added to DBS-$CONHNH_2$ powder (2 mg). The solution was heated until complete dissolution of the gelator and a transparent solution was observed. The solution

was immediately transferred into the well plates (50 μL in each well of the 96 well plates and 100 μL in the inserts). The same procedure was done to prepare the gels with different concentrations of heparin, C16-DAPMA and agarose, by adding a solution of heparin or C16-DAPMA in 10 mM Tris-HCl/ 150 mM NaCl with the appropriate concentration and by weighing agarose together with DBS-$CONHNH_2$ powder.

2D Cell Culture: Gels with Cells on Top

Gels were prepared in 96 well plates (50 μL of gel/ well) and sterilised by applying UV light for 20 min. After gelation, the cells were seeded on top of the gels. The desired number of cells (to obtain the following cell density: 50000 cells/mL or 25000 cells/ml after optimisation) was added into a 2 mL Eppendorf and centrifuged at 1800 rpm for 6 min at 25 °C, followed by the removal of the supernatant. The cells were re-suspended in DMEM - 10% FBS - 1% P/S and 100 μL added on top of each gel in the well.

2D Cell Culture: Gels in Transwells

Gels were prepared in the inserts (100 μL of gel/ insert) and sterilised by applying UV light for 20 min. After gelation, the cells were seeded on the bottom of the wells and both compartments (well and inserts) were filled with medium.

The desired number of cells (to obtain the following cell density: 40000 cells/mL or 10000 cells/mL after optimisation) was added into a 2 mL Eppendorf and centrifuged at 1800 rpm for 6 min at 25 °C, followed by the removal of the supernatant. The cells were re-suspended in DMEM - 10% FBS - 1% P/S and 500 μL added to each well.

Cell Morphology: Optical Microscopy

The morphology of the cells placed on top of the gels and with gels in transwells was followed by placing the 96 plates and the transwell plates under the optical microscope and recording images over the days of the experiment.

Cell Morphology: Phalloidin/ DAPI Staining

The medium was removed from the culture wells. Paraformaldehyde (PFA) was added to each well (100 μL or 200 μL into 96 well plates or 24 well plates, respectively) and incubated at room temperature for 1 h. PFA was removed and the samples washed twice with DPBS

for approximately 15 min. Triton-X100 (0.5% in PBS - 100 µL or 200 µL into 96 well plates or 24 well plates, respectively) was added to each well and incubated at room temperature for 1h. Triton-X100 was removed and the samples washed twice with DPBS for approximately 15 min. The plates were incubated overnight at 4 °C with 100 µL or 200 µL of phalloidin - tetramethylrhodamine B isothiocyanate (TRITC) diluted in PBS 1:23. The samples were washed twice with DPBS for approximately 15 min and incubated with 100 µL or 200 µL (96 well plates or 24 well plates, respectively) of 5 µg/mL DAPI in DPBS for 45 min at room temperature. The samples were washed twice with DPBS for approximately 15 min and the images collected from a fluorescence microscope.

Live/Dead Staining

The medium was removed from the culture wells. The plates were incubated with 13.3 µM calcein- acetoxymethyl (AM) and 4.8 µM propidium iodide (PI) in cell culture medium for 60 min at 37 °C. The staining solution was removed and the samples washed twice with DPBS for approximately 15 min. Some gels/cells were fixed with 100 µL or 200 µL (96 well plates or 24 well plates, respectively) of 4% PFA in PBS (0.01 M, pH 7.4) for 1h. The samples were washed twice with DPBS for approximately 15 min and the pictures were collected from a fluorescence microscope.

MitoTracker Staining

The medium was removed from the culture wells. The plates were incubated with 0.4 µM of MitoTracker Green and 10.8 µM of Hoechst diluted in culture medium, for 90 min at 37 °C. The staining solution was removed and the samples washed with DPBS for 30 min at room temperature. DPBS (twice the sample volume) was added to the cells and the images collected from a fluorescence microscope.

Metabolic Activity

WST-1 (4-[3-(4-Iodophenyl)-2-(4-nitrophenyl)-2H-5-tetrazolio]-1,3-benzene disulfonate) was added to each well (10% of the total volume – 5 µL for gels in 96 well plates and 10 µL for gels in transwells), followed by incubation of the plates at 37 °C for 2 h. The gels were then disrupted by pipetting them up and down, transferred into Eppendorfs and frozen. Later, the samples were thawed (protecting them from light) and homogenized. The

samples were centrifuged at 13800 rpm, for 5 min. The supernatant (80 μL) was collected and added into a new 96 well plate. The absorbance was measured at 440 nm.

Migration Assay

Different volumes (100 μL, 80 μL and 60 μL) of DBS-$CONHNH_2$ hydrogels (0.4% w/v) in transwells were prepared as described above. Cells (cell density: 10000 cells/mL) were added on top of the gels (double the volume of the gels). Two different controls were prepared: 200 μL of cells in medium was added to the insert, or 200 μL of cells in medium was added directly to the bottom of the well without the presence of the insert. The inserts were washed with trypsin to detach any cells from the membrane. The presence of cells on the bottom of the wells was followed by optical microscopy over 7 days.

7.6. Chapter 5 – Characterisation and Assay Methods

OG1 and OG2 Gel Formation[78,298]

The OG1 gel was prepared by adding 1 mL of water into 5 mg of gelator powder. The solution was heated until the gelator was dissolved and allowed to cool down at room temperature. The final pH of the OG1 gel was 7.

The OG2 gel was prepared by adding 0.8 mL of water into 5 mg of gelator powder and 0.1 mL of HCl (1 M) was added to completely dissolve the gelator. The solution was then neutralised by adding 0.1 mL of NaOH (1 M) and gently shaken. The gel formation was observed immediately after the neutralisation of the gelator solution (final pH 8-9).

OG1 and OG2 Gel Formation with Different Concentrations of Heparin and C16-DAPMA

OG1 and OG2 gels were prepared with different concentrations of heparin (38 μM; 150 μM; 300 μM; 400 μM; 600 μM; 1000 μM) in water. The OG1 gel was prepared by adding 1 mL of heparin solution into 5 mg of gelator powder. The solution was heated until the gelator dissolved and allowed to cool down at room temperature. The OG2 gel was prepared by adding 0.8 mL of heparin solution into 5 mg of gelator powder and 0.1 mL of HCl (1 M) to completely dissolve the gelator. The solution was then neutralised by adding 0.1 mL of NaOH (1 M) and gently shaken. Gel formation was observed immediately after

neutralisation of the gelator solution. Dilutions from the addition of the acid and base were taken into account when preparing the heparin solutions, in order to have the appropriate final concentration.

OG1 and OG2 gels were prepared with different concentrations of C16-DAPMA (150 μM; 300 μM; 600 μM; 800 μM; 1000 μM; 1200 μM) in water. The same procedure explained above was followed.

OG1 and OG2 gels were prepared with solutions containing a fixed concentration of heparin and different C16-DAPMA concentrations. An initial charge ratio (+/-) of 2 was tested and if no stable/ homogeneous gels were formed, lower concentrations of C16-DAPMA were used for the same heparin concentration. As explained above, all calculations for the concentrations used took into account the dilutions needed for the gel preparation.

OG1 and OG2 "Dropping Ball" Method for T_{gel} Determination[298]

A stainless steel ball (65 mg, 2.5 mm in diameter) was placed on top of the gel, previously prepared in a 2 mL glass vial. The vial was subsequently placed in a heating block and monitored by a CCD camera. The temperature of the heating block was increased by 1°C/min and the T_{gel} value was considered to be the temperature at which the steel ball started to fall through the gel.

OG1 and OG2 Transmission Electron Microscopy

OG1 and OG2 gel samples for TEM images (Table 7.7) were prepared in ultra-pure H_2O and obtained by adding one microspatula of each sample on a copper grid (standard) with Formvar and carbon support film. The excess of sample was removed with filter paper then allowed to set for 5 minutes. A negative stain (1% uranyl acetate) was applied to the grid while wet to allow the stain to run across the grid. The grid was left to rest for 30 minutes before taking images.

Table 7.7. Concentrations of OG1, OG2, Heparin and C16-DAPMA used to obtain TEM images of gels prepared in ultra-pure water.

Components	Concentration (mM)
OG1	5.9
OG2	7.5
Heparin	0.038
C16-DAPMA	0.15
Heparin/C16-DAPMA	0.038 / 0.15

OG1 and OG2 Rheology

The following measurements were performed in a TA Instruments AR2000 rheometer. OG1 gelator (5 mg) was added to water (1 mL) and transfered with a pipette to the lower plate of the rheometer that was previously heated. The sample was heated on the rheometer plate, followed by decreasing the temperature to 25°C.

OG2 hydrogels (0.5% w/v) were prepared by addition of 0.8 mL of water into a vial containing the gelator powder, that was then completely dissolved by the addition of 0.1 mL of HCl (1 M). NaOH (0.1 mL, 1 M) was added into a syringe, followed by the addition of the dissolved gelator solution and the mix immediately added into the lower plate of the equipment, to ensure a homogeneous mixture of the base with the acidic gelator solution. The measurements started immediately after sample loading.

The viscolelastic properties of OG1 and OG2 hydrogels were measured by applying a dynamic strain sweep (f = 1Hz) and a dynamic time sweep (f = 1 Hz, Y = 0.5%). The measurements were carried out with a parallel geometry plate (d = 40 mm) and a gap of 0.8 mm. The same procedure was performed for OG1 and OG2 hydrogels incorporating heparin (0.3 mM), C16-DAPMA (1.2 mM) and heparin (0.3 mM)/C16-DAPMA (1.2 mM) aggregates.

OG1 and OG2 Release Assays

The release of heparin from OG1 and OG2 hydrogels was performed following the same procedures described for the DBS-COOH and DBS-$CONHNH_2$ hydrogels.

OG+ Gel Formation

OG+ gel formation was obtained using two different approaches. One method consisted in adding 0.8 mL of water into 5 mg of gelator powder and 0.1 mL of HCl (1 M) was added to completely dissolve the gelator. The solution was then neutralised by adding 0.1 mL of NaOH (1 M) and gently shaken. The gel formation was observed immediately after the neutralisation of the gelator solution. In a second approach, 5 mg of gelator was dissolved in 0.1 mL of DMSO, followed by the addition of 0.9 mL of 0.1 M Tris-HCl buffer, pH 7.75 (mixture ratio of 1:9 DMSO:buffer). Gel formation was observed immediately after the addition of the buffer solution.

OG+ Gel Formation with Heparin

OG+ gel was prepared by adding 0.8 mL of heparin solution (0.078 or 1 mM) into 5 mg of gelator powder and 0.1 mL of HCl (1 M) to completely dissolve the gelator. The solution was then neutralised by adding 0.1 mL of NaOH (1 M) and gently shaken. Gel formation was observed immediately after the neutralisation of the gelator solution. Dilutions from the addition of the acid and base were taken into account when preparing the heparin solutions, in order to have the appropriate final concentration.

Alternatively, 0.1 mL of heparin (0.078 or 1 mM) dissolved in DMSO was added to 5 mg of gelator, followed by the addition of 0.9 mL of 0.1 M Tris-HCl buffer, pH 7.75 (mixture ratio of 1:9 DMSO:buffer). Gel formation was observed immediately after the addition of the buffer solution.

OG+ Transmission Electron Microscopy

OG+ hydrogels (0.5% w/v) were prepared using the first method described above and following the same procedure as described for the TEM images of OG1 and OG2. When in the presence of heparin, a heparin concentration of 0.078 mM was used.

OG+ Release Assays

OG+ hydrogels were prepared following the second method of gel preparation previously described. Buffer solution (1 mL of 10 mM Tris-HCl/ 150 mM NaCl) was placed on top of 1 mL of OG+ hydrogels (0.5% w/v) containing 1 mM of heparin. Release assays of OG+ hydrogels in the presence of α-chy enzyme (from bovine pancreas, type II, $\geq$ 40 units/mg protein) were conducted using 1 mL samples that were prepared by adding enzyme stock solution (900 µL, α-chy in 0.1 M Tris-HCl buffer, pH 7.75) to a DMSO solution of OG+ with heparin (1 mM in 1 mL of sample). 1 mL of 10 mM Tris-HCl/ 150 mM NaCl was placed on top of the gels. The experiment using the enzyme was performed at room temperature and at 37 °C. Aliquots (65 µL) of buffer were removed over time and added to MalB solution (1935 µL) and the absorbance at 615 nm obtained.

Abbreviations

1D	One-dimensional
2D	Two-dimensional
3D	Three-dimensional
α-chy	α- chymotrypsin
A	Alanine
AgNPs	Silver nanoparticles
AM	Acetoxymethyl
ASC	Adipose tissue derived stem cells
AuNPs	Gold nanoparticles
BMP-2	Bone morphogenic protein-2
Boc	tert-Butyl Dicarbonate
br	broad (NMR)
CD	Circular Dichroism
CE_{50}	Charge excess
CGC	Critical Gelation Concentration
ChS-F	Chondroitin sulfate
CMC	Critical Micelle Concentration
CN	Cavernous nerve
D	Aspartic acid
d	doublet (NMR)
DAPI	4',6-diamidino-2-phenylindole
DAPMA	*N,N*-Di-(3-aminopropyl)-*N*-methylamine
DBS	1,3:2,4-dibenzylidene-D-Sorbitol
DBS-$COOCH_3$	1,3:2,4-dibenzylidene-D-Sorbitol-*p,p'*-dimethylester
DBS-COOH	1,3:2,4-dibenzylidene-D-Sorbitol-*p,p'*-dicarboxylic acid
DBS-$CONHNH_2$	1,3:2,4-dibenzylidene-D-Sorbitol-*p,p'*-dihydrazide
DCM	Dichloromethane
DLS	Dynamic Light Scattering
DMEM	Dulbecco's Modified Eagle's Medium

DOPC	Dioleoylphosphocholine
DPBS	Dulbecco's phosphate buffered saline
DPD	Dissipative Particle Dynamics
E	Glutamic Acid
EC_{50}	Effective concentration
ECM	Extracellular matrix
EGF	Epidermal growth factor
FBS	Fetal bovine serum
FDM	Fibroblast-derived extracellular matrix
FGF	Fibroblast growth factor
FGFR	Fibroblast growth factor receptor
Fmoc	9-fluorenylmethoxycarbonyl
Fmoc-FF	Fmoc-diphenylalanine
G'	Storage or elastic modulus
G''	Loss or viscous modulus
GAG	Glycosaminoglycans
GdL	Glucono-δ-lactone
GF	Growth factors
GNF	Glycosyl-nucleosyl-fluorinated
GPC	Gel permeation chromatography
HCEC	Human corneal endothelial cells
HUVEC	Human umbilical vein endothelial cells
IR	Infrared
K	Lysine
LMWG	Low molecular weight gelator
LMWH	Low-molecular-weight heparin
LVR	Linear viscoelastic region
m	medium (IR)
m	multiplet (NMR)
MalB	Mallard Blue
MDP	Multidomain peptide
NIR	Near-infrared

NMR	Nuclear Magnetic Resonance
PA	Peptide amphiphile
PBS	Phosphate buffer saline
PdI	Polydispersity index
PEG	Poly(ethylene glycol)
PEG-AMI	Maleimide-terminated poly(ethylene glycol)
PEGDM	Poly(ethylene glycol) dimethacrylate
PFA	Paraformaldehyde
PG	Polymer gelator
PlGF-1	Placental growth factor-1
P/S	Penicillin/Streptomycin
p-TsOH	*p*-Toluenesulfonic acid
q	quartet (NMR)
RGD	Arginine-glycine-aspartic acid
s	strong (IR)
s	singlet (NMR)
SAMul	Self-assembling multivalency
SAXS	Small Angle X-Ray Scattering
SDS	Sodium dodecylsulfonate
SDBS	Dodecylbenzenesulfonate
SEM	Scanning Electron Microscopy
SHH	Sonic hedgehog
t	triplet (NMR)
TBTU	O-(Benzotriazol-1-yl)-*N*,*N*,*N'*,*N'*-tetramethyluronium tetrafluoroborate
TEM	Transmission Electron Microscopy
T_{gel}	Critical gelation temperature
TGFβ	Transforming growth factor beta
TLC	Thin layer chromatography
TRITC	Tetramethylrhodamine B isothiocyanate
V	Valine

VEGF	Vascular endothelial growth factor
w	weak (IR)
WST-1	Tetrazolium salt

References

1 S. S. Babu, V. K. Praveen and A. Ajayaghosh, *Chem. Rev.*, 2014, **114**, 1973–2129.

2 A. R. Hirst, B. Escuder, J. F. Miravet and D. K. Smith, *Angew. Chem. Int. Ed.*, 2008, **47**, 8002–8018.

3 J.-M. Lehn, *Angew. Chem. Int. Ed. Engl.*, 1990, **29**, 1304–1319.

4 M. J. Webber, E. A. Appel, E. W. Meijer and R. Langer, *Nat. Mater.*, 2015, **15**, 13–26.

5 E. Mattia and S. Otto, *Nat. Nanotechnol.*, 2015, **10**, 111–119.

6 V. Gauba and J. D. Hartgerink, *J. Am. Chem. Soc.*, 2007, **129**, 2683–2690.

7 G. Du, E. Moulin, N. Jouault, E. Buhler and N. Giuseppone, *Angew. Chem. Int. Ed.*, 2012, **51**, 12504–12508.

8 S. Hamieh, V. Saggiomo, P. Nowak, E. Mattia, R. F. Ludlow and S. Otto, *Angew. Chem. Int. Ed.*, 2013, **52**, 12368–12372.

9 V. I. Martín, F. J. Ostos, M. Angulo, A. M. Márquez, P. López-Cornejo, M. López-López, A. T. Carmona and M. L. Moyá, *J. Colloid Interface Sci.*, 2017, **491**, 336–348.

10 J. W. Steed, D. R. Turner and K. J. Wallace, *Core Concepts in Supramolecular Chemsitry and Nanochemistry*, Wiley, 2007.

11 G. Whitesides, J. Mathias and C. Seto, *Science*, 1991, **254**, 1312–1319.

12 L. F. Lindoy and I. M. Atkinson, *Self Assembly in Supramolecular Systems*, Royal Society of Chemistry, Cambridge, 2000.

13 D. Philp and J. F. Stoddart, *Angew. Chem. Int. Ed. Engl.*, 1996, **35**, 1154–1196.

14 W. Pfeifer and B. Saccà, *ChemBioChem*, 2016, **17**, 1063–1080.

15 D. Chandler, *Nature*, 2005, **437**, 640–647.

16 X. Chi, A. J. Guerin, R. A. Haycock, C. A. Hunter and L. D. Sarson, *Chem. Commun.*, 1995, 2563–2565.

17 J. N. Israelachvili, D. J. Mitchell and B. W. Ninham, *J. Chem. Soc., Faraday Trans. 2*, 1976, **72**, 1525–1568.

18 K. J. M. Bishop, *Angew. Chem. Int. Ed.*, 2016, **55**, 1598–1600.

19 J. P. Mathias and J. F. Stoddart, *Chem. Soc. Rev.*, 1992, **21**, 215–225.

20 A. R. Hirst and D. K. Smith, *Chem. Eur. J.*, 2005, **11**, 5496–5508.

21 L. Raehm and J.-P. Sauvage, *Struct. Bond.*, 2001, **99**, 55–78.

22 V. K. Praveen, C. Ranjith, E. Bandini, A. Ajayaghosh and N. Armaroli, *Chem. Soc. Rev.*, 2014, **43**, 4222–4242.

23 Y. Li, H. Zhou, J. Chen, S. Anjum Shahzad and C. Yu, *Biosens. Bioelectron.*, 2016, **76**, 38–53.

24 V. Kalaparthi, S. Palantavida, N. E. Mordvinova, O. I. Lebedev and I. Sokolov, *J. Colloid Interface Sci.*, 2017, **491**, 133–140.

25 D. J. Lloyd and J. Alexander, *Colloid Chem. Chem. Cat. Co New York*, 1926, **1**, 767.

26 J. W. Steed, *Chem. Commun.*, 2011, **47**, 1379–1383.

27 X. Yang, G. Zhang and D. Zhang, *J. Mater. Chem.*, 2012, **22**, 38–50.

28 M. reza Saboktakin and R. M. Tabatabaei, *Int. J. Biol. Macromol.*, 2015, **75**, 426–436.

29 G. Yu, X. Yan, C. Han and F. Huang, *Chem. Soc. Rev.*, 2013, **42**, 6697–722.
30 D. K. Smith, *Self-Assembling Fibrillar Networks - Supramolecular Gels in Supramolecular Chemistry*, John Wiley & Sons, Ltd, 2012.
31 M. A. Rogers and J. H. J. Kim, *Food Res. Int.*, 2011, **44**, 1447–1451.
32 D. Pasini and A. Kraft, *Curr. Opin. Solid State Mater. Sci.*, 2004, **8**, 157–163.
33 P. Matricardi, C. Di Meo, T. Coviello, W. E. Hennink and F. Alhaique, *Adv. Drug Deliv. Rev.*, 2013, **65**, 1172–1187.
34 Y. Zhao, M. Tanaka, T. Kinoshita, M. Higuchi and T. Tan, *J. Control. Release*, 2010, **147**, 392–399.
35 F. Zhao, M. L. Ma and B. Xu, *Chem. Soc. Rev.*, 2009, **38**, 883–891.
36 M. C. Branco and J. P. Schneider, *Acta Biomater.*, 2009, **5**, 817–831.
37 P. Jonkheijm, P. van der Schoot, A. P. H. J. Schenning and E. W. Meijer, *Science*, 2006, **313**, 80–3.
38 R. G. Weiss, *J. Am. Chem. Soc.*, 2014, **136**, 7519–7530.
39 K. Hanabusa and M. Suzuki, *Polym. J.*, 2014, **46**, 776–782.
40 S. Kiyonaka, K. Sugiyasu, S. Shinkai and I. Hamachi, *J. Am. Chem. Soc.*, 2002, **124**, 10954–10955.
41 R. Dong, Y. Pang, Y. Su and X. Zhu, *Biomater. Sci.*, 2015, **3**, 937–954.
42 X. Ma, N. Zhou, T. Zhang, W. Hu and N. Gu, *Mater. Sci. Eng. C*, 2017, **73**, 357–365.
43 M. Xue, D. Gao, X. Chen, K. Liu and Y. Fang, *J. Colloid Interface Sci.*, 2011, **361**, 556–564.
44 V. K. Praveen, C. Ranjith and N. Armaroli, *Angew. Chem. Int. Ed.*, 2014, **53**, 365–368.
45 P. Bairi, B. Roy and A. K. Nandi, *Chem. Commun.*, 2012, **48**, 10850–10852.
46 H. Jia, H. Wang, C. Liu, C. Li, J. Yang, X. Xu, J. Feng, X. Zhang and R. Zhuo, *Soft Matter*, 2012, **8**, 6906–6912.
47 C. Wang, D. Zhang and D. Zhu, *J. Am. Chem. Soc.*, 2005, **127**, 16372–16373.
48 J. W. Sadownik, J. Leckie and R. V. Ulijn, *Chem. Commun.*, 2011, **47**, 728–730.
49 M.-O. M. Piepenbrock, G. O. Lloyd, N. Clarke and J. W. Steed, *Chem. Rev.*, 2010, **110**, 1960–2004.
50 R. Gortner and W. Hoffman, *J. Am. Chem. Soc.*, 1921, **43**, 2199–2202.
51 F. M. Menger and K. L. Caran, *J. Am. Chem. Soc.*, 2000, **122**, 11679–11691.
52 J. D. Hartgerink, E. Beniash and S. I. Stupp, *Science*, 2001, **294**, 1684–1688.
53 H. Cui, M. J. Webber and S. I. Stupp, *Biopolymers*, 2010, **94**, 1–18.
54 Z. Xie, A. Zhang, L. Ye and Z. Feng, *Soft Matter*, 2009, **5**, 1474–1482.
55 R. Helen Zha, Y. S. Velichko, R. Bitton and S. I. Stupp, *Soft Matter*, 2016, **12**, 1401–1410.
56 Y. Shi, J. Wang, H. Wang, Y. Hu, X. Chen and Z. Yang, *PLoS One*, 2014, **9**, e106968.
57 R. Li, C. C. Horgan, B. Long, A. L. Rodriguez, L. Mather, C. J. Barrow, D. R. Nisbet and R. J. Williams, *RSC Adv.*, 2015, **5**, 301–307.
58 S. Fleming and R. V. Ulijn, *Chem. Soc. Rev.*, 2014, **43**, 8150–8177.
59 A. M. Smith, R. J. Williams, C. Tang, P. Coppo, R. F. Collins, M. L. Turner, A. Saiani and

R. V. Ulijn, *Adv. Mater.*, 2008, **20**, 37–41.
60 W. Helen, P. de Leonardis, R. V. Ulijn, J. Gough and N. Tirelli, *Soft Matter*, 2011, **7**, 1732–1740.
61 W. T. Truong, Y. Su, D. Gloria, F. Braet and P. Thordarson, *Biomater. Sci.*, 2015, **3**, 298–307.
62 Y. Liu, X.-D. Xu, J.-X. Chen, H. Cheng, X.-Z. Zhang and R.-X. Zhuo, *Colloids Surfaces B Biointerfaces*, 2011, **87**, 192–197.
63 J. Raeburn, C. Mendoza-Cuenca, B. N. Cattoz, M. A. Little, A. E. Terry, A. Zamith Cardoso, P. C. Griffiths and D. J. Adams, *Soft Matter*, 2015, **11**, 927–935.
64 Y. Zhang, H. Gu, Z. Yang and B. Xu, *J. Am. Chem. Soc.*, 2003, **125**, 13680–13681.
65 V. Jayawarna, M. Ali, T. A. Jowitt, A. F. Miller, A. Saiani, J. E. Gough and R. V. Ulijn, *Adv. Mater.*, 2006, **18**, 611–614.
66 C. Tang, A. M. Smith, R. F. Collins, R. V. Ulijn and A. Saiani, *Langmuir*, 2009, **25**, 9447–9453.
67 J. Raeburn, G. Pont, L. Chen, Y. Cesbron, R. Lévy and D. J. Adams, *Soft Matter*, 2012, **8**, 1168–1174.
68 L. Chen, K. Morris, A. Laybourn, D. Elias, M. R. Hicks, A. Rodger, L. Serpell and D. J. Adams, *Langmuir*, 2010, **26**, 5232–5242.
69 F. Rodríguez-Llansola, D. Hermida-Merino, B. Nieto-Ortega, F. J. Ramírez, J. T. L. Navarrete, J. Casado, I. W. Hamley, B. Escuder, W. Hayes and J. F. Miravet, *Chem. Eur. J.*, 2012, **18**, 14725–14731.
70 B. C. Baker, A. L. Acton, G. C. Stevens and W. Hayes, *Tetrahedron*, 2014, **70**, 8303–8311.
71 A. J. Kleinsmann, N. M. Weckenmann and B. J. Nachtsheim, *Chem. Eur. J.*, 2014, **20**, 9753–9761.
72 D. K. Kumar, D. A. Jose, A. Das and P. Dastidar, *Chem. Commun.*, 2005, 4059–4061.
73 N. N. Adarsh, D. K. Kumar and P. Dastidar, *Tetrahedron*, 2007, **63**, 7386–7396.
74 K. Liu and J. W. Steed, *Soft Matter*, 2013, **9**, 11699–11705.
75 G. O. Lloyd and J. W. Steed, *Soft Matter*, 2011, **7**, 75–84.
76 M.-O. M. Piepenbrock, G. O. Lloyd, N. Clarke and J. W. Steed, *Chem. Commun.*, 2008, 2644–2646.
77 S. J. James, A. Perrin, C. D. Jones, D. S. Yufit and J. W. Steed, *Chem. Commun.*, 2014, **50**, 12851–12854.
78 M. de Loos, A. Friggeri, J. van Esch, R. M. Kellogg and B. L. Feringa, *Org. Biomol. Chem.*, 2005, **3**, 1631–1639.
79 G. John, J. H. Jung, M. Masuda and T. Shimizu, *Langmuir*, 2004, **20**, 2060–2065.
80 Q. Chen, Y. Lv, D. Zhang, G. Zhang, C. Liu and D. Zhu, *Langmuir*, 2010, **26**, 3165–3168.
81 H. Surya Prakash Rao, M. Kamalraj, J. Swain and A. K. Mishra, *RSC Adv.*, 2014, **4**, 12175–12181.
82 J. Li, K. Fan, L. Niu, Y. Li and J. Song, *J. Phys. Chem. B*, 2013, **117**, 5989–5995.
83 S. Sun, J. Song, Z. Shan and R. Feng, *J. Electroanal. Chem.*, 2012, **676**, 1–5.

84 B. O. Okesola, V. M. P. Vieira, D. J. Cornwell, N. K. Whitelaw and D. K. Smith, *Soft Matter*, 2015, **11**, 4768–4787.
85 E. A. Wilder, R. J. Spontak and C. K. Hall, *Mol. Phys.*, 2003, **101**, 3017–3027.
86 Y. Lan, M. G. Corradini, X. Liu, T. E. May, F. Borondics, R. G. Weiss and M. A. Rogers, *Langmuir*, 2014, **30**, 14128–14142.
87 D. J. Cornwell, B. O. Okesola and D. K. Smith, *Soft Matter*, 2013, **9**, 8730–8736.
88 B. O. Okesola and D. K. Smith, *Chem. Commun.*, 2013, **49**, 11164–11166.
89 D. K. Kumar and J. W. Steed, *Chem. Soc. Rev.*, 2014, **43**, 2080–2088.
90 J. Raeburn and D. J. Adams, *Chem. Commun.*, 2015, **51**, 5170–5180.
91 L. E. Buerkle and S. J. Rowan, *Chem. Soc. Rev.*, 2012, **41**, 6089–6102.
92 C. Colquhoun, E. R. Draper, E. G. B. Eden, B. N. Cattoz, K. L. Morris, L. Chen, T. O. McDonald, A. E. Terry, P. C. Griffiths, L. C. Serpell and D. J. Adams, *Nanoscale*, 2014, **6**, 13719–13725.
93 E. R. Draper, E. G. B. Eden, T. O. McDonald and D. J. Adams, *Nat Chem*, 2015, **7**, 848–852.
94 K. Sugiyasu, S. I. Kawano, N. Fujita and S. Shinkai, *Chem. Mater.*, 2008, **20**, 2863–2865.
95 Z. Shen, T. Wang and M. Liu, *Chem. Commun.*, 2014, **50**, 2096–2099.
96 Z. Shen, T. Wang and M. Liu, *Langmuir*, 2014, **30**, 10772–10778.
97 D. J. Cornwell and D. K. Smith, *Mater. Horiz.*, 2015, **2**, 279–293.
98 D. J. Cornwell, B. O. Okesola and D. K. Smith, *Angew. Chem. Int. Ed.*, 2014, **53**, 12461–12465.
99 Q. Wei, M. Xu, C. Liao, Q. Wu, M. Liu, Y. Zhang, C. Wu, L. Cheng and Q. Wang, *Chem. Sci.*, 2016, **7**, 2748–2752.
100 A. R. Hirst, J. F. Miravet, B. Escuder, L. Noirez, V. Castelletto, I. W. Hamley and D. K. Smith, *Chem. Eur. J.*, 2009, **15**, 372–379.
101 Q. Xue, H. Ren, C. Xu, G. Wang, C. Ren, J. Hao and D. Ding, *Sci. Rep.*, 2015, **5**, 8764.
102 A. Brizard, M. Stuart, K. van Bommel, A. Friggeri, M. de Jong and J. van Esch, *Angew. Chem. Int. Ed.*, 2008, **47**, 2063–2066.
103 A. Heeres, C. Van Der Pol, M. Stuart, A. Friggeri, B. L. Feringa and J. Van Esch, *J. Am. Chem. Soc.*, 2003, **125**, 14252–14253.
104 A. M. Brizard, M. C. A. Stuart and J. H. van Esch, *Faraday Discuss.*, 2009, **143**, 345–357.
105 E. R. Draper, M. Wallace, R. Schweins, R. J. Poole and D. J. Adams, *Langmuir*, 2017, **33**, 2387–2395.
106 X. Zhang, S. Malhotra, M. Molina and R. Haag, *Chem. Soc. Rev.*, 2015, **44**, 1948–1973.
107 E. Pazos, E. Sleep, C. M. Rubert Pérez, S. S. Lee, F. Tantakitti and S. I. Stupp, *J. Am. Chem. Soc.*, 2016, **138**, 5507–5510.
108 B. O. Okesola, S. K. Suravaram, A. Parkin and D. K. Smith, *Angew. Chem. Int. Ed.*, 2016, **55**, 183–187.
109 S. C. Lee, I. K. Kwon and K. Park, *Adv. Drug Deliv. Rev.*, 2013, **65**, 17–20.

110 P. Gupta, K. Vermani and S. Garg, *Drug Discov. Today*, 2002, **7**, 569–579.
111 M. Goldberg, R. Langer and X. Jia, *J. Biomater. Sci. Polym. Ed.*, 2007, **18**, 241–268.
112 O. Ozay, *J. Appl. Polym. Sci.*, 2014, **131**, 39660.
113 N. C. Wickremasinghe, V. A. Kumar and J. D. Hartgerink, *Biomacromolecules*, 2014, **15**, 3587–3595.
114 L. Yin, S. Xu, Z. Feng, H. Deng, J. Zhang, H. Gao, L. Deng, H. Tang and A. Dong, *Biomater. Sci.*, 2017, **5**, 698–706.
115 L. Qin, P. Duan, F. Xie, L. Zhang and M. Liu, *Chem. Commun.*, 2013, **49**, 10823–10825.
116 F. Qiu, Y. Chen, C. Tang, J. Zhang, M. Gong and B. Su, *Int. J. Nanomedicine*, 2015, **10**, 847–858.
117 K. J. C. van Bommel, A. Friggeri, M. C. A. Stuart, B. L. Feringa and J. van Esch, *J. Control. Release*, 2005, **101**, 287–408.
118 S. Zhang, J. Ermann, M. D. Succi, A. Zhou, M. J. Hamilton, B. Cao, J. R. Korzenik, J. N. Glickman, P. K. Vemula, L. H. Glimcher, G. Traverso, R. Langer and J. M. Karp, *Sci. Transl. Med.*, 2015, **7**, 300ra128.
119 M. B. Mellott, K. Searcy and M. V. Pishko, *Biomaterials*, 2001, **22**, 929–941.
120 A. Bertz, S. Wöhl-Bruhn, S. Miethe, B. Tiersch, J. Koetz, M. Hust, H. Bunjes and H. Menzel, *J. Biotechnol.*, 2013, **163**, 243–249.
121 H. Komatsu, S. Matsumoto, S. Tamaru, K. Kaneko, M. Ikeda and I. Hamachi, *J. Am. Chem. Soc.*, 2009, **131**, 5580–5585.
122 S. Sutton, N. L. Campbell, A. I. Cooper, M. Kirkland, W. J. Frith and D. J. Adams, *Langmuir*, 2009, **25**, 10285–10291.
123 P. L. Ritger and N. A. Peppas, *J. Control. Release*, 1987, **5**, 23–36.
124 F. Rodríguez-Llansola, J. F. Miravet and B. Escuder, *Chem. Commun.*, 2009, 7303–7305.
125 F. Rodríguez-Llansola, J. F. Miravet and B. Escuder, *Chem. Commun.*, 2011, **47**, 4706–4708.
126 N. L. Angeloni, C. W. Bond, Y. Tang, D. A. Harrington, S. Zhang, S. I. Stupp, K. E. McKenna and C. A. Podlasek, *Biomaterials*, 2011, **32**, 1091–1101.
127 S. Choe, C. W. Bond, D. A. Harrington, S. I. Stupp, K. T. McVary and C. A. Podlasek, *Nanomedicine*, 2017, **13**, 95–101.
128 D. G. Fatouros, D. A. Lamprou, A. J. Urquhart, S. N. Yannopoulos, I. S. Vizirianakis, S. Zhang and S. Koutsopoulos, *ACS Appl. Mater. Interfaces*, 2014, **6**, 8184–8189.
129 S. P. Patil, S.-H. Kim, J. R. Jadhav, J. Lee, E. M. Jeon, K.-T. Kim and B. H. Kim, *Bioconjug. Chem.*, 2014, **25**, 1517–1525.
130 J. O. Radler, *Science*, 1997, **275**, 810–814.
131 R. Langer and J. P. Vacanti, *Science*, 1993, **260**, 920–926.
132 T. Dvir, B. P. Timko, D. S. Kohane and R. Langer, *Nat. Nanotechnol.*, 2011, **6**, 13–22.
133 P. Bernhard and B. Sangeeta, *Tissue Engineering*, Pearson Prentice Hall Bioengineering, 2004.
134 M. P. Lutolf and J. Hubbell, *Nat. Biotechnol.*, 2005, **23**, 47–55.

135 H. T. Aiyelabegan and E. Sadroddiny, *Biomed. Pharmacother.*, 2017, **88**, 956–970.
136 E. S. Place, N. D. Evans and M. M. Stevens, *Nat. Mater.*, 2009, **8**, 457–470.
137 F. Guilak, D. L. Butler, S. A. Goldstein and F. P. T. Baaijens, *J. Biomech.*, 2014, **47**, 1933–1940.
138 P. M. Kharkar, K. L. Kiick and A. M. Kloxin, *Chem. Soc. Rev.*, 2013, **42**, 7335–7372.
139 A. Vallés-Lluch, M. Arnal-Pastor, C. Martínez-Ramos, G. Vilariño-Feltrer, L. Vikingsson, C. Castells-Sala, C. E. Semino and M. Monleón Pradas, *Acta Biomater.*, 2013, **9**, 9451–9460.
140 M. B. Chen, S. Srigunapalan, A. R. Wheeler and C. a Simmons, *Lab Chip*, 2013, **13**, 2591–2598.
141 V. Jayawarna, M. Ali, T. A. Jowitt, A. F. Miller, A. Saiani, J. E. Gough and R. V. Ulijn, *Adv. Mater.*, 2006, **18**, 611–614.
142 G. A. Silva, C. Czeisler, K. L. Niece, E. Beniash, D. A. Harrington, J. A. Kessler and S. I. Stupp, *Science*, 2004, **303**, 1352–1355.
143 J. L. Drury and D. J. Mooney, *Biomaterials*, 2003, **24**, 4337–4351.
144 K. Y. Lee and D. J. Mooney, *Chem. Rev.*, 2001, **101**, 1869–1879.
145 W. S. Toh and X. J. Loh, *Mater. Sci. Eng. C*, 2014, **45**, 690–697.
146 N. J. Hogrebe, J. W. Reinhardt and K. J. Gooch, *J. Biomed. Mater. Res. Part A*, 2017, **105**, 640–661.
147 S. A. Fisher, R. Y. Tam and M. S. Shoichet, *Tissue Eng. Part A*, 2014, **20**, 895–898.
148 S. Reed and B. Wu, *Ann. Biomed. Eng.*, 2014, **42**, 1528–1536.
149 I. L. Kim, R. L. Mauck and J. A. Burdick, *Biomaterials*, 2011, **32**, 8771–8782.
150 N. Eslahi, M. Abdorahim and A. Simchi, *Biomacromolecules*, 2016, **17**, 3441–3463.
151 E. J. Berns, Z. Álvarez, J. E. Goldberger, J. Boekhoven, J. A. Kessler, H. G. Kuhn and S. I. Stupp, *Acta Biomater.*, 2016, **37**, 50–58.
152 T. Suga, S. Osada, T. Narita, Y. Oishi and H. Kodama, *Mater. Sci. Eng. C*, 2015, **47**, 345–350.
153 S. Ziane, S. Schlaubitz, S. Miraux, A. Patwa, C. Lalande, I. Bilem, S. Lepreux, B. Rousseau, J. F. Le Meins, L. Latxague, P. Barthélémy and O. Chassande, *Eur. Cells Mater.*, 2012, **23**, 147–160.
154 X. Bai, S. Lü, Z. Cao, C. Gao, H. Duan, X. Xu, L. Sun, N. Gao, C. Feng and M. Liu, *Chem. Eng. J.*, 2016, **288**, 546–556.
155 J. E. Babensee, L. V. McIntire and A. G. Mikos, *Pharm. Res.*, 2000, **17**, 497–504.
156 K. Lee, E. A. Silva and D. J. Mooney, *J. R. Soc. Interface*, 2011, **8**, 153–170.
157 V. E. Santo, M. E. Gomes, J. F. Mano and R. L. Reis, *Tissue Eng. Part B Rev.*, 2013, **19**, 327–352.
158 M. Lovett, K. Lee, A. Edwards and D. L. Kaplan, *Tissue Eng. Part B Rev.*, 2009, **15**, 353–370.
159 J. Boekhoven and S. I. Stupp, *Adv. Mater.*, 2014, **26**, 1642–1659.
160 R. B. Montero, X. Vial, D. T. Nguyen, S. Farhand, M. Reardon, S. M. Pham, G. Tsechpenakis and F. M. Andreopoulos, *Acta Biomater.*, 2012, **8**, 1778–1791.

161 S. E. Sakiyama-Elbert and J. A. Hubbell, *J. Control. Release*, 2000, **69**, 149–158.
162 J. A. Beamish, L. C. Geyer, N. A. Haq-Siddiqi, K. Kottke-Marchant and R. E. Marchant, *Biomaterials*, 2009, **30**, 6286–6294.
163 L. M. Mullen, S. M. Best, R. A. Brooks, S. Ghose, J. H. Gwynne, J. Wardale, N. Rushton and R. E. Cameron, *Tissue Eng. Part C Methods*, 2010, **16**, 1439–1448.
164 M. S. Lee, T. Ahmad, J. Lee, H. K. Awada, Y. Wang, K. Kim, H. Shin and H. S. Yang, *Biomaterials*, 2017, **124**, 65–77.
165 S. Mehrotra, D. Lynam, R. Maloney, K. M. Pawelec, M. H. Tuszynski, I. Lee, C. Chan and J. Sakamoto, *Adv. Funct. Mater.*, 2010, **20**, 247–258.
166 D. Lynam, C. Peterson, R. Maloney, D. Shahriari, A. Garrison, S. Saleh, S. Mehrotra, C. Chan and J. Sakamoto, *Carbohydr. Polym.*, 2014, **103**, 377–384.
167 D. R. Griffin, J. L. Schlosser, S. F. Lam, T. H. Nguyen, H. D. Maynard and A. M. Kasko, *Biomacromolecules*, 2013, **14**, 1199–1207.
168 K. Kim, J. Lam, S. Lu, P. P. Spicer, A. Lueckgen, Y. Tabata, M. E. Wong, J. A. Jansen, A. G. Mikos and F. K. Kasper, *J. Control. Release*, 2013, **168**, 166–178.
169 S. Lu, J. Lam, J. E. Trachtenberg, E. J. Lee, H. Seyednejad, J. J. J. P. van den Beucken, Y. Tabata, M. E. Wong, J. A. Jansen, A. G. Mikos and F. K. Kasper, *Biomaterials*, 2014, **35**, 8829–8839.
170 E. H. Nguyen, M. R. Zanotelli, M. P. Schwartz and W. L. Murphy, *Biomaterials*, 2014, **35**, 2149–2161.
171 C. J. Newcomb, S. Sur, S. S. Lee, J. M. Yu, Y. Zhou, M. L. Snead and S. I. Stupp, *Nano Lett.*, 2016, **16**, 3042–3050.
172 N. C. Wickremasinghe, V. Kumar, S. Shi and J. D. Hartgerink, *ACS Biomater. Sci. Eng.*, 2015, **1**, 845–854.
173 N. C. Rivron, J. Liu, J. Rouwkema, J. De Boer and C. A. Van Blitterswijk, *Eur. Cells Mater.*, 2008, **15**, 27–40.
174 K. W. Lee, J. J. Yoon, J. H. Lee, S. Y. Kim, H. J. Jung, S. J. Kim, J. W. Joh, H. H. Lee, D. S. Lee and S. K. Lee, *Transplant. Proc.*, 2004, **36**, 2464–2465.
175 M. Ishihara, K. Obara, T. Ishizuka, M. Fujita, M. Sato, K. Masuoka, Y. Saito, H. Yura, T. Matsui, H. Hattori, M. Kikuchi and A. Kurita, *J. Biomed. Mater. Res.*, 2003, **64A**, 551–559.
176 A. Radulescu, H. Y. Zhang, C. L. Chen, Y. Chen, Y. Zhou, X. Yu, I. Otabor, J. K. Olson and G. E. Besner, *J. Surg. Res.*, 2011, **171**, 540–550.
177 A. Yayon, M. Klagsbrun, J. D. Esko, P. Leder and D. M. Ornitz, *Cell*, 1991, **64**, 841–848.
178 N. L. Leong, A. Arshi, N. Kabir, A. Nazemi, F. A. Petrigliano, B. M. Wu and D. R. McAllister, *J. Orthop. Res.*, 2015, **33**, 229–236.
179 F. Reyes-Ortega, G. Rodríguez, M. R. Aguilar, M. Lord, J. Whitelock, M. H. Stenzel and J. San Román, *J. Mater. Chem. B*, 2013, **1**, 850–860.
180 I. Capila and R. J. Linhardt, *Angew. Chem. Int. Ed.*, 2002, **41**, 391–412.
181 J. Hirsh and R. Raschke, *Chest*, 2004, **126**, 188S–203S.
182 D. L. Rabenstein, *Nat. Prod. Rep.*, 2002, **19**, 312–331.

183 A. Y. Y. Lee, *J. Clin. Oncol.*, 2009, **27**, 4895–4901.
184 F. Peysselon and S. Ricard-Blum, *Matrix Biol.*, 2014, **35**, 73–81.
185 T. H. Nguyen, S.-H. Kim, C. G. Decker, D. Y. Wong, J. a Loo and H. D. Maynard, *Nat. Chem.*, 2013, **5**, 221–227.
186 C. Dos Santos, C. Blanc, R. Elahouel, M. Prescott, G. Carpentier, A. Ori, J. Courty, Y. Hamma-Kourbali, D. G. Fernig and J. Delbé, *Biochimie*, 2014, **107**, 350–357.
187 F. Alam, S. W. Chung, S. R. Hwang, J. young Kim, J. Park, H. T. Moon and Y. Byun, *J. Appl. Toxicol.*, 2015, **35**, 104–115.
188 N. B. Skop, F. Calderon, S. W. Levison, C. D. Gandhi and C. H. Cho, *Acta Biomater.*, 2013, **9**, 6834–6843.
189 L. Gilmore, S. Rimmer, S. L. Mcarthur, S. Mittar, D. Sun and S. Macneil, *Biotechnol. Bioeng.*, 2013, **110**, 296–317.
190 Y. Su and G. E. Besner, *J. Surg. Res.*, 2014, **189**, 222–231.
191 Y. Zhao, M. S. Lord and M. H. Stenzel, *J. Mater. Chem. B*, 2013, **1**, 1635–1643.
192 Y. Arisaka, J. Kobayashi, M. Yamato, Y. Akiyama and T. Okano, *Biomaterials*, 2013, **34**, 4214–4222.
193 S. Prokoph, E. Chavakis, K. R. Levental, A. Zieris, U. Freudenberg, S. Dimmeler and C. Werner, *Biomaterials*, 2012, **33**, 4792–4800.
194 C. Loira-Pastoriza, A. Sapin-Minet, R. Diab, J. L. Grossiord and P. Maincent, *Int. J. Pharm.*, 2012, **426**, 256–262.
195 K. Rajangam, M. S. Arnold, M. A. Rocco and S. I. Stupp, *Biomaterials*, 2008, **29**, 3298–3305.
196 I. D'Angelo, O. Oliviero, F. Ungaro, F. Quaglia and P. A. Netti, *Acta Biomater.*, 2013, **9**, 7389–7398.
197 N. R. Johnson and Y. Wang, *J. Control. Release*, 2013, **166**, 124–129.
198 G. Niu, J.-S. Choi, Z. Wang, A. Skardal, M. Giegengack and S. Soker, *Biomaterials*, 2014, **35**, 4005–4014.
199 P. Du, M. P. Hwang, Y. K. Noh, R. Subbiah, I. G. Kim, S. E. Bae and K. Park, *J. Control. Release*, 2014, **194**, 122–129.
200 A. Watarai, L. Schirmer, S. Thones, U. Freudenberg, C. Werner, J. C. Simon and U. Anderegg, *Acta Biomater.*, 2015, **25**, 65–75.
201 E. Foster, J. You, C. Siltanen, D. Patel, A. Haque, L. Anderson and A. Revzin, *Eur. Polym. J.*, 2015, **72**, 726–735.
202 T. Fernández-Muiños, L. Recha-Sancho, P. López-Chicón, C. Castells-Sala, A. Mata and C. E. Semino, *Acta Biomater.*, 2015, **16**, 35–48.
203 B. Peña, R. Shandas and D. Park, *J. Biomed. Mater. Res. - Part A*, 2015, **103**, 2102–2108.
204 Y. Liang and K. L. Kiick, *Acta Biomater.*, 2014, **10**, 1588–1600.
205 K. Rajangam, H. A. Behanna, M. J. Hui, X. Han, J. F. Hulvat, J. W. Lomasney and S. I. Stupp, *Nano Lett.*, 2006, **6**, 2086–2090.
206 S. M. Bromfield, P. Posocco, C. W. Chan, M. Calderon, S. E. Guimond, J. E. Turnbull,

S. Pricl and D. K. Smith, *Chem. Sci.*, 2014, **5**, 1484–1492.
207 A. C. Rodrigo, A. Barnard, J. Cooper and D. K. Smith, *Angew. Chem. Int. Ed.*, 2011, **50**, 4675–4679.
208 M. Mammen, S.-K. Choi and G. M. Whitesides, *Angew. Chem. Int. Ed.*, 1998, **37**, 2754–2794.
209 G. M. Pavan, A. Danani, S. Pricl and D. K. Smith, *J. Am. Chem. Soc.*, 2009, **131**, 9686–9694.
210 J. Huskens, A. Mulder, T. Auletta, C. A. Nijhuis, M. J. W. Ludden and D. N. Reinhoudt, *J. Am. Chem. Soc.*, 2004, **126**, 6784–6797.
211 S. Miyamoto, S. Akiyama and K. Yamada, *Science*, 1995, **267**, 883–885.
212 Y. Lim, K.-S. Moon and M. Lee, *Chem. Soc. Rev.*, 2009, **38**, 925–934.
213 D. J. Welsh and D. K. Smith, *Org. Biomol. Chem.*, 2011, **9**, 4795–4801.
214 S. P. Jones, N. P. Gabrielson, D. W. Pack and D. K. Smith, *Chem. Commun.*, 2008, 4700–4702.
215 A. Barnard, P. Posocco, S. Pricl, M. Calderon, R. Haag, M. E. Hwang, V. W. T. Shum, D. W. Pack and D. K. Smith, *J. Am. Chem. Soc.*, 2011, **133**, 20288–20300.
216 P. Posocco, S. Pricl, S. Jones, A. Barnard and D. K. Smith, *Chem. Sci.*, 2010, **1**, 393–404.
217 S. M. Bromfield and D. K. Smith, *J. Am. Chem. Soc.*, 2015, **137**, 10056–10059.
218 L. E. Fechner, B. Albanyan, V. M. P. Vieira, E. Laurini, P. Posocco, S. Pricl and D. K. Smith, *Chem. Sci.*, 2016, **7**, 4653–4659.
219 H. Ihre, A. Hult, J. M. J. Fréchet and I. Gitsov, *Macromolecules*, 1998, **31**, 4061–4068.
220 S. M. Bromfield, E. Wilde and D. K. Smith, *Chem. Soc. Rev.*, 2013, **42**, 9184–9195.
221 S. Balalaie, M. Mahdidoust and R. Eshaghi-Najafabadi, *J. Iran. Chem. Soc.*, 2007, **4**, 364–369.
222 P. Greenspan, E. P. Mayer and S. D. Fowler, *J. Cell Biol.*, 1985, **100**, 965–973.
223 M. C. A. Stuart, J. C. Van De Pas and J. B. F. N. Engberts, *J. Phys. Org. Chem.*, 2005, **18**, 929–934.
224 E. Kunio and U. Minoru, *Structure-Performance Relationships in Surfactants*, 2003.
225 S. M. Bromfield, A. Barnard, P. Posocco, M. Fermeglia, S. Pricl and D. K. Smith, *J. Am. Chem. Soc.*, 2013, **135**, 2911–2914.
226 S. M. Bromfield, P. Posocco, M. Fermeglia, S. Pricl, J. Rodríguez-López and D. K. Smith, *Chem. Commun.*, 2013, **49**, 4830–4832.
227 A. J. Konop and R. H. Colby, *Langmuir*, 1999, **15**, 58–65.
228 H. Schiessel, M. D. Correa-Rodríguez, S. Rudiuk, D. Baigl and K. Yoshikawa, *Soft Matter*, 2012, **8**, 9406–9411.
229 B. Jachimska, M. Wasilewska and Z. Adamczyk, *Langmuir*, 2008, **24**, 6866–6872.
230 U. Kätzel, M. Vorbau, M. Stintz, T. Gottschalk-Gaudig and H. Barthel, *Part. Part. Syst. Charact.*, 2008, **25**, 19–30.
231 E. Kizilay, A. D. Dinsmore, D. A. Hoagland, L. Sun and P. L. Dubin, *Soft Matter*, 2013, **9**, 7320–7332.

232 J. E. Laaser, Y. Jiang, S. R. Petersen, T. M. Reineke and T. P. Lodge, *J. Phys. Chem. B*, 2015, **119**, 15919–15928.
233 S. M. Bromfield, P. Posocco, M. Fermeglia, J. Tolosa, A. Herreros-López, S. Pricl, J. Rodríguez-López and D. K. Smith, *Chem. Eur. J.*, 2014, **20**, 9666–9674.
234 E. M. Terentjev and D. A. Weitz, *The Oxford Handbook of Soft Condensed Matter*, 2015.
235 V. Liljeström, J. Mikkilä and M. a Kostiainen, *Nat. Commun.*, 2014, **5**, 4445.
236 V. Liljeström, J. Seitsonen and M. A. Kostiainen, *ACS Nano*, 2015, **9**, 11278–11285.
237 J. Mikkilä, E. Anaya-Plaza, V. Liljeström, J. R. Caston, T. Torres, A. de la Escosura and M. A. Kostiainen, *ACS Nano*, 2016, **10**, 1565–1571.
238 N. M. Sangeetha and U. Maitra, *Chem. Soc. Rev.*, 2005, **34**, 821–836.
239 M. W. Tibbitt, B. W. Han, A. M. Kloxin and K. S. Anseth, *J. Biomed. Mater. Res. A*, 2012, **100 A**, 1647–1654.
240 T. Diab, E. M. Pritchard, B. A. Uhrig, J. D. Boerckel, D. L. Kaplan and R. E. Guldberg, *J. Mech. Behav. Biomed. Mater.*, 2012, **11**, 123–131.
241 A. Zieris, K. Chwalek, S. Prokoph, K. R. Levental, P. B. Welzel, U. Freudenberg and C. Werner, *J. Control. Release*, 2011, **156**, 32–40.
242 T. R. Hoare and D. S. Kohane, *Polymer*, 2008, 49, 1993–2007.
243 N. A. Liechty, W. B., Kryscio, D.R., Slaughter, B. V. and Peppas, *Annu. Rev. Chem. Biomol. Eng.*, 2010, **1**, 149–173.
244 J. Li and D. J. Mooney, *Nat. Rev. Mater.*, 2016, **1**, 16071.
245 R. J. Wade and J. A. Burdick, *Mater. Today*, 2012, **15**, 454–459.
246 M. S. Rehmann and A. M. Kloxin, *Soft Matter*, 2013, **9**, 6737–6746.
247 D. Seliktar, *Science*, 2012, **336**, 1124–1128.
248 P. Li, X.-Q. Dou, C.-L. Feng and D. Zhang, *Soft Matter*, 2013, **9**, 3750–3757.
249 P. Li, Z. Yin, X. Q. Dou, G. Zhou and C. L. Feng, *ACS Appl. Mater. Interfaces*, 2014, **6**, 7948–7952.
250 J. Wang, X. Miao, Q. Fengzhao, C. Ren, Z. Yang and L. Wang, *RSC Adv.*, 2013, **3**, 16739–16746.
251 J. Wang, Z. Wang, J. Gao, L. Wang, Z. Yang, D. Kong and Z. Yang, *J. Mater. Chem.*, 2009, **19**, 7892–7896.
252 S. Middeldorp, *Thromb. Res.*, 2008, **122**, 753–762.
253 M. R. Matanovic, I. Grabnar, M. Gosenca and P. A. Grabnar, *Int. J. Pharm.*, 2015, **488**, 127–135.
254 Y. M. Abul-Haija and R. V. Ulijn, *Biomacromolecules*, 2015, **16**, 3473–3479.
255 M. K. Włodarczyk-Biegun, C. J. Slingerland, M. W. T. Werten, I. A. van Hees, F. A. de Wolf, R. de Vries, M. A. C. Stuart and M. Kamperman, *Biomacromolecules*, 2016, **17**, 2063–2072.
256 S. Ikeda and K. Nishinari, *J. Agric. Food Chem.*, 2001, **49**, 4436–4441.
257 J. Raeburn, A. Zamith Cardoso and D. J. Adams, *Chem. Soc. Rev.*, 2013, **42**, 5143–5156.

258 E. R. Draper, L. L. E. Mears, A. M. Castilla, S. M. King, T. O. McDonald, R. Akhtar and D. J. Adams, *RSC Adv.*, 2015, **5**, 95369–95378.
259 Y. Abidine, V. M. Laurent, R. Michel, A. Duperray, L. I. Palade and C. Verdier, *Eur. Lett.*, 2015, **109**, 38003.
260 A. Counotte-Potman and H. C. Van Der Plas, *J. Heterocycl. Chem.*, 1983, **20**, 1259–1261.
261 A. Awadhiya, S. Tyeb, K. Rathore and V. Verma, *Eng. Life Sci.*, 2017, **17**, 204–214.
262 S. M. Goldman and G. A. Barabino, *J. Tissue Eng. Regen. Med.*, 2017, **11**, 572–581.
263 H. Hemeda, J. Kalz, G. Walenda, M. Lohmann and W. Wagner, *Cytotherapy*, 2013, **15**, 1174–1181.
264 A. Papathanasopoulos, D. Kouroupis, K. Henshaw, D. McGonagle, E. A. Jones and P. V. Giannoudis, *J. Orthop. Res.*, 2011, **29**, 1327–1335.
265 G. Matziolis, C. Perka, A. Disch and H. Zippel, *Calcif. Tissue Int.*, 2003, **73**, 370–379.
266 A. B. Schreiber, J. Kenney, W. J. Kowalski, R. Friesel, T. Mehlman and T. Maciag, *Proc. Natl. Acad. Sci. U.S.A*, 1985, **82**, 6138–6142.
267 D. L. M. Hickson-Bick, G. C. Sparagna, L. M. Buja and J. B. McMillin, *Am. J. Physiol. Heart Circ. Physiol.*, 2002, **282**, 656–664.
268 M. Artwohl, A. Lindenmair, V. Sexl, C. Maier, G. Rainer, A. Freudenthaler, N. Huttary, M. Wolzt, P. Nowotny, A. Luger and S. M. Baumgartner-Parzer, *J. Lipid Res.*, 2008, **49**, 2627–2640.
269 Z. H. Lu, Y. M. Mu, B. A. Wang, X. L. Li, J. M. Lu, J. Y. Li, C. Y. Pan, T. Yanase and H. Nawata, *Biochem. Biophys. Res. Commun.*, 2003, **303**, 1002–1007.
270 M. C. Rho, K. Ah Lee, S. Mi Kim, C. Sik Lee, M. Jeong Jang, Y. Kook Kim, H. Sun Lee, Y. Hyun Choi, B. Yong Rhim and K. Kim, *Toxicol. Appl. Pharmacol.*, 2007, **220**, 311–319.
271 W. El-Assaad, J. Buteau, M. L. Peyot, C. Nolan, R. Roduit, S. Hardy, E. Joly, G. Dbaibo, L. Rosenberg and M. Prentki, *Endocrinology*, 2003, **144**, 4154–4163.
272 J. E. de Vries, M. M. Vork, T. H. Roemen, Y. F. de Jong, J. P. Cleutjens, G. J. van der Vusse and M. van Bilsen, *J. Lipid Res.*, 1997, **38**, 1384–1394.
273 D. Dyntar, M. Eppenberger-Eberhardt, K. Maedler, M. Pruschy, H. M. Eppenberger, G. A. Spinas and M. Y. Donath, *Diabetes*, 2001, **50**, 2105–2113.
274 L. L. Listenberger, D. S. Ory and J. E. Schaffer, *J. Biol. Chem.*, 2001, **276**, 14890–14895.
275 T. Furuno, T. Kanno, K. Arita, M. Asami, T. Utsumi, Y. Doi, M. Inoue and K. Utsumi, *Biochem. Pharmacol.*, 2001, **62**, 1037–1046.
276 K. A. Harvey, C. L. Walker, T. M. Pavlina, Z. Xu, G. P. Zaloga and R. A. Siddiqui, *Clin. Nutr.*, 2010, **29**, 492–500.
277 I. Ojea-Jimenez, L. Garcia-Fernandez, J. Lorenzo and V. F. Puntes, *ACS Nano*, 2012, **6**, 7692–7702.
278 F. Schweizer, *Eur. J. Pharmacol.*, 2009, **625**, 190–194.
279 Y. Wang, Y. Tang, Z. Zhou, E. Ji, G. P. Lopez, E. Y. Chi, K. S. Schanze and D. G. Whitten, *Langmuir*, 2010, **26**, 12509–12514.
280 R. Imani, S. H. Emami, P. R. Moshtagh, N. Baheiraei and A. M. Sharifi, *J. Macromol.*

Sci. B, 2012, **51**, 1606–1616.
281 S. Sakai, I. Hashimoto and K. Kawakami, *J. Biosci. Bioeng.*, 2007, **103**, 22–26.
282 K. I. Hulkower and R. L. Herber, *Pharmaceutics*, 2011, **3**, 107–124.
283 N. Kramer, A. Walzl, C. Unger, M. Rosner, G. Krupitza, M. Hengstschläger and H. Dolznig, *Mutat. Res. Mutat. Res.*, 2013, **752**, 10–24.
284 H. Lin, A. W. Cheng, P. G. Alexander, A. M. Beck and R. S. Tuan, *Tissue Eng. Part A*, 2014, **20**, 2402–2411.
285 M. Dvorak, M. Vlasin, M. Dvorakova, P. Rauser, L. Lexmaulova, Z. Gregor and R. Staffa, *Vet. Med.*, 2010, **55**, 523–546.
286 M. Vishnu Priya, M. Sabitha and R. Jayakumar, *Carbohydr. Polym.*, 2016, **136**, 609–617.
287 A. Alhalafi, *Oman J. Ophthalmol.*, 2017, **10**, 3–8.
288 T. Thambi, V. H. G. Phan and D. S. Lee, *Macromol. Rapid Commun.*, 2016, **37**, 1881–1896.
289 S. Ashraf, H.-K. Park, H. Park and S.-H. Lee, *Macromol. Res.*, 2016, **24**, 297–304.
290 A. Kumar and S. S. Han, *Int. J. Polym. Mater. Polym. Biomater.*, 2017, **66**, 159–182.
291 E. Dickinson, *Trends Food Sci. Technol.*, 2015, **43**, 178–188.
292 M. Davidovich-Pinhas, S. Barbut and A. G. Marangoni, *Annu. Rev. Food Sci. Technol.*, 2016, **7**, 65–91.
293 R. V. Contri, I. C. Kulkamp-Guerreiro, S. J. da Silva, L. A. Frank, A. R. Pohlmann and S. S. Guterres, *AAPS Pharm. Sci. Tech.*, 2016, **17**, 863–871.
294 C. M. Crane and A. Fonolla-Moreno, *US Patent*, 9364399 B2, 2016.
295 E. Akabane and C. Hayakawa, *US Patent*, 20160262991 A1, 2016.
296 K. J. C. van Bommel, C. van der Pol, I. Muizebelt, A. Friggeri, A. Heeres, A. Meetsma, B. L. Feringa and J. van Esch, *Angew. Chem. Int. Ed.*, 2004, **43**, 1663–1667.
297 A. Friggeri, B. L. Feringa and J. Van Esch, *J. Control. Release*, 2004, **97**, 241–248.
298 K. J. C. van Bommel, M. C. a Stuart, B. L. Feringa and J. van Esch, *Org. Biomol. Chem.*, 2005, **3**, 2917–2920.
299 J. Boekhoven, A. M. Brizard, K. N. K. Kowlgi, G. J. M. Koper, R. Eelkema and J. H. Van Esch, *Angew. Chem. Int. Ed.*, 2010, **49**, 4825–4828.
300 J. Boekhoven, M. Koot, T. A. Wezendonk, R. Eelkema and J. H. van Esch, *J. Am. Chem. Soc.*, 2012, **134**, 12908–12911.
301 C. Maity, W. E. Hendriksen, J. H. Van Esch and R. Eelkema, *Angew. Chem. Int. Ed.*, 2015, **54**, 998–1001.
302 V. Le Sage, V. Lakshminarayanan, E. Mendes, R. Eelkema and J. Van Esch, *Chem. Today*, 2014, **32**, 62–66.
303 J. S. Foster, J. M. Żurek, N. M. S. Almeida, W. E. Hendriksen, V. A. A. le Sage, V. Lakshminarayanan, A. L. Thompson, R. Banerjee, R. Eelkema, H. Mulvana, M. J. Paterson, J. H. van Esch and G. O. Lloyd, *J. Am. Chem. Soc.*, 2015, **137**, 14236–14239.
304 N. Singh, K. Zhang, C. A. Angulo-Pachón, E. Mendes, J. H. van Esch and B. Escuder, *Chem. Sci.*, 2016, **7**, 5568–5572.

305 J. M. Poolman, C. Maity, J. Boekhoven, L. van der Mee, V. A. A. le Sage, G. J. M. Groenewold, S. I. van Kasteren, F. Versluis, J. H. van Esch and R. Eelkema, *J. Mater. Chem. B*, 2016, **4**, 852–858.

306 N. Singh, C. Maity, K. Zhang, C. A. Angulo-Pachón, J. H. van Esch, R. Eelkema and B. Escuder, *Chem. Eur. J.*, 2017, **23**, 2018–2021.

307 J. Boekhoven, A. M. Brizard, M. C. A. Stuart, L. Florusse, G. Raffy, A. Del Guerzo and J. H. van Esch, *Chem. Sci.*, 2016, **7**, 6021–6031.

308 A. Takahashi, M. Sakai and T. Kato, *Polym. J.*, 1980, **12**, 335–341.

309 K. L. Morris, L. Chen, J. Raeburn, O. R. Sellick, P. Cotanda, A. Paul, P. C. Griffiths, S. M. King, R. K. O'Reilly, L. C. Serpell and D. J. Adams, *Nat. Commun.*, 2013, **4**, 1480.

310 L.-J. Zhu, L.-P. Zhu, Z. Yi, J.-H. Jiang, B.-K. Zhu and Y.-Y. Xu, *Colloids Surf. B Biointerfaces*, 2013, **110**, 36–44.

311 A. P. Krapcho and C. S. Kuell, *Synth. Commun.*, 1990, **20**, 2559–2564.